

ARL 69-0078

MAY 1969



AD 692742

Aerospace Research Laboratories

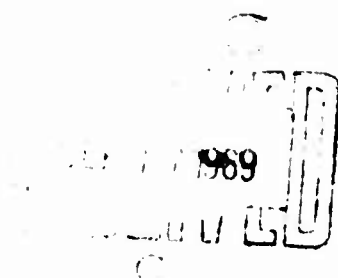
PROCEEDINGS OF UNIVERSITY OF MIAMI SYMPOSIUM ON OPTICAL PROPERTIES OF ORBITING SATELLITES

**DOUGLAS DUKE
UNIVERSITY OF MIAMI
MIAMI, FLORIDA**

**KENNETH KISSELL
GENERAL PHYSICS RESEARCH LABORATORY**

Contract No. F33615-67-C-1870
Project No. 7114

This document has been approved for public release and sale;
its distribution is unlimited.



**OFFICE OF AEROSPACE RESEARCH
United States Air Force**



235

ARL 69-0078

**PROCEEDINGS OF UNIVERSITY OF MIAMI
SYMPOSIUM ON OPTICAL PROPERTIES OF
ORBITING SATELLITES**

EDITED BY

**DOUGLAS DUKE
UNIVERSITY OF MIAMI
MIAMI, FLORIDA**

AND

**KENNETH E. KISSELL
GENERAL PHYSICS RESEARCH LABORATORY**

MAY 1969

Contract No. F33615-67-C-1870
Project No. 7114
Task II

This document has been approved for public release and sale;
its distribution is unlimited.

**AEROSPACE RESEARCH LABORATORIES
OFFICE OF AEROSPACE RESEARCH
UNITED STATES AIR FORCE
WRIGHT-PATTERSON AIR FORCE BASE, OHIO**

FOREWORD

This final technical report was prepared under contract F33615 67C 1870, University of Miami, Florida. The symposium covered herein was accomplished on Project 7114 under the technical cognizance of Dr. Kenneth E. Kissell, Director of the General Physics Research Laboratory, Aerospace Research Laboratories.

TABLE OF CONTENTS

	<u>Page</u>
Foreword	ii
"Ten Years of Optical Satellite Observations" Dr. Douglas Duke, University of Miami	v
"Optical and Infrared Characteristics of Satellite Surface Materials", Stanley Greenberg, Lockheed Co.	2-3
"Reflectometer Experiment", J. P. Corrigan, NASA, D. McDowell and J. Holloway, Electro-optical Systems	4-30
"The Determination of the Orientation of a Tumbling Cylinder from the Shape of the Light Curve", J. G. Williams, North American Aviation	31-39
"Time Varying Reflection from Rotating Convex Surfaces", D. O. Carhoun, Mitre Corporation	40-41
"Interpretation of Photometric Signatures from Satellites", M. Hansburg, Goodyear Aerospace Corporation	42-65
"Investigations into a Method for the Optical Estimation of the Rotation Axis of Artificial Satellites", R. H. Giese, University of Bochum, West Germany	66-122
"Optical Studies of Spacecraft from the Cloudcroft Facility", E. T. Tyson, Cloudcroft, New Mexico	123-124
"The Design and Operation of Some Devices for Photoelectric and Photographic Registration of Artificial Satellites", Kenneth Fea, University of London, England	125-126
"Results of Photometric and Polarimetric Measurements for Various Satellites Using NASA's Mobile Photometric Observatory", R. H. Emmons and R. J. Preski, Goodyear Aerospace Corporation, Akron, Ohio	127-138

"An Approximate Method of Estimating the Reflection Characteristics of A Spherical Satellite", D. E. Smith, RSRS, Slough, England	139-156
"Design of Telescope Optical Systems for Visual Observations of Orbiting Satellites", A. S. Leonard, University of California	157-166
"Theory and Observation of the Rotational Motion of the Pegasus Satellites", R. L. Holland and M. B. Barkley, NASA Marshall Spaceflight Center	167-173
"Attitude Determination of the Ariel III Satellite" R. B. Bent, RSRS, Slough, England	174-190
"Czechoslovak Contribution to Satellite Photometry" F. Link, Onerejov Astronomical Institute	191-200
"Wide Band (Visual Spectrum) Photoelectric Photometry of PAGEOS During its First Fifteen Months in Orbit", R. C. Vanderburgh, USAF, Aerospace Research Laboratories	201-226

TEN YEARS OF OPTICAL SATELLITE OBSERVATIONS

Douglas Duke
University of Miami

It is not generally known that within a matter of weeks after the launching of the first two earth satellite vehicles by Russia late in 1957, large scale photographs were made of these objects at the Air Force Missile Test Center at Cape Kennedy, Florida. Even the very earliest photographs allowed a reasonably accurate measurement of the size of these objects and their orientation changes (tumbling rate). Much experimentation was carried out during the first six months in an effort to obtain the clearest possible photographs. Various combinations of exposure times, focal lengths and film speeds were tried. Methods for rapid acquisition and the smoothest possible tracking were developed.

Despite all these efforts, even the clearest photographs made in 1958 did not have sufficient resolution to allow the determination of structural details below approximately 5 feet in extent. While some improvement might be expected from increasing the telescope aperture to more than the 24 inch instruments then available, such improvement would be nominal since the best observed resolution was several times the diffraction limit of the 24 inch instruments. As is the case in all astronomical observations where high resolution is desirable, the problem lay in the distortion of the optical wavefronts produced by the refractive index turbulence in the earth's atmosphere.

Two independent and complementary actions were called for to improve this problem of atmospheric seeing. The first was to design tracking telescopes with apertures and driving mechanisms optimized for satellite observations and to locate these at high elevation sites so as to minimize the atmospheric transmission path and the resulting distortion. This consideration resulted in the construction of the Cloudcroft Electro-Optical Facility by the Air Force and the Mount Haleakala Facility by the Advanced Research Projects Agency.

BLANK PAGE

The second indicated action was a comprehensive program of study and experimentation for the purpose of improving our knowledge of the exact nature of the atmospheric distortions so as to attempt to devise new devices and techniques reducing their effect. Unfortunately the pleas and urgings of the author fell on deaf ears for almost five years. Finally in 1963 the increased realization in the possibility of optical methods due to the new attention being paid to the laser caused a revival of interest.

For the past 18 months a group under the direction of the author and with the support of the Air Force Avionics Laboratory and the Air Force Eastern Test Range has been working on these problems of atmospheric distortion to optical images. To date the results have been modest, principally due to the difficult nature of the phenomena being investigated and the need to design and construct entirely new registration and measurement devices. It is felt that only a beginning has been made and that real results will take several additional years.

OPTICAL AND INFRARED CHARACTERISTICS OF
SATELLITE SURFACE MATERIALS

S. A. Greenberg
Lockheed Palo Alto Research Laboratory
Palo Alto, California

ABSTRACT

OPTICAL AND INFRARED CHARACTERISTICS OF
SATELLITE SURFACE MATERIALS

S. A. Greenberg, Research Scientist

LOCKHEED PALO ALTO RESEARCH LABORATORY
PALO ALTO, CALIFORNIA

The optical properties of typical spacecraft surface materials are discussed. The four basic classes of materials (solar absorbers, solar reflectors, flat absorbers and flat reflectors) are described in terms of directional spectral reflectance in the wavelength region 0.2 - 30 microns. The concept of remote spectral scanning of satellites for identification of surface materials is examined in relation to identification of vehicle origin, temperature, mission and lifetime. Environmentally induced degradation of optical properties of spacecraft coatings is discussed in reference to signature characteristics. Methods of remote sensing of surface temperatures are proposed, based on the temperature variation of optical absorption edges of semiconductor materials. The limitations of remote optical characterization of orbiting spacecraft are outlined and requirements for closer coordination of designers and observers are emphasized.

REFLECTOMETER EXPERIMENT

AN

APPLICATIONS TECHNOLOGY SATELLITE SCIENTIFIC PAPER

J. P. Corrigan - NASA/Goddard

D. McDowell - EOS

J. Holloway - EOS

CONTENTS

INTRODUCTION

EXPERIMENT OBJECTIVES

REFLECTOMETER DESIGN

- a. Optics
- b. Reflectometer Sampling
- c. Mechanical Subsystem
- d. Electronics Subsystem

SUMMARY OF OPERATION

REFERENCES

APPENDIX I - ATS REFLECTOMETER SAMPLES

ILLUSTRATIONS

- 1 The Reflectometer Experiment
- 2 Reflectometer Optical Schematic
- 3 Spectrum of the Tungsten Lamp
- 4 Mechanical Subsystem
- 5 Electronics Subsystem
- 6 Format, Reflectivity Data

INTRODUCTION

Late in 1967, the National Aeronautics and Space Administration will launch the third satellite in the ATS series, the spin-stabilized synchronous orbit ATS-C. Among the several experiments carried by this spacecraft will be the Reflectometer Experiment, an experiment designed primarily for obtaining engineering data necessary for the design of spacecraft solar power systems and other reflective optical systems.

Power systems for advanced space missions are recognized to be one of the most critical problem areas in space technology. The two basic energy sources apparently showing the most promise of meeting space power requirements are solar energy and nuclear energy. One critical component of the solar energy system is the solar concentrator, which depends upon geometrical accuracy and spectral and specular reflectance of the concentrator surface. The efficiency is directly related to the specular reflectivity of its mirrored surface.

Considerable effort has already been expended in developing fabrication techniques for obtaining the essential geometric accuracies, and in investigating materials which demonstrate in a laboratory environment the high specular reflectivity required for space solar systems. However, almost without exception, data regarding the performance and the useful life of highly reflective surfaces in a space environment is not available. As technological advances in power systems are made, knowledge about the durability of materials used in all types of optical systems is not only desirable but indispensable.

Essential to the design of solar space power systems and other systems requiring the use of specularly reflective surfaces in space is the determination of how reflective surfaces are affected when exposed for prolonged periods to a space environment.

The difficulty in estimating specular reflectance loss in a space environment results from the following conditions. First, the mechanism and environmental influences which cause reflectance are understood only hypothetically. Second, flux-intensity levels of possible degrading factors in space generally have not been determined directly but have only been estimated from extrapolation of other measurements. Third, because of the uncertainties regarding the degrading mechanisms themselves and the character of the space environment, it simply has not been practical to simulate reflective-surface degradation in the laboratory.

The hostile aspects of the space environment which have significant effects on reflective surfaces have been determined to be micrometeoroids, charged particles, ultraviolet radiation, temperature, and the inherent vacuum of space. In space, measurement of the total effect of these environmental factors is essential to the development of various systems and instruments which depend upon specularly reflecting surfaces to insure adequate performance throughout the planned lifetime of the system or instrument.

One example of a degrading mechanism is micrometeorites. Most space measurements made to date have been concerned with the penetration of pressure vessels (such as space power-system radiators and pressured space vehicles) by large particles. As a result, most micrometeorite instrumentation has been designed to detect encounters with these larger particles in space. With reflective surfaces, however, the problem is not penetration but gradual erosion and roughening of the surface layer by the continual impact of smaller particles which cause no major structural damage such as penetration. This effect can be especially pronounced in samples having interference-type surface coatings which are especially sensitive to changes in thickness. In extreme cases, the entire reflective coating may be worn away, exposing the reflective substrate material.

Although many attempts have been made to simulate various space-environment factors, there is not only uncertainty as to what factor to simulate, but to what degree. The micrometeorite conditions suspected to exist in space involve large flux levels of micron-sized particles moving at 20 to 70 kilometers per second relative to the surface of the spacecraft. It has been impossible to simulate small particles at high speeds simultaneously in the laboratory. Slow moving large particles with the equivalent kinetic energy do not have the same effect and the validity of the extrapolation of these parameters to simulate space effects is the subject of much controversy.

Much of the same sort of argument applies to other degrading influences assumed to exist in space. An area of uncertainty even greater than that associated with the individual effects of erosion mechanisms is their combined effect. All these uncertainties taken together weigh heavily in favor of the direct measure of reflective degradation in space.

The data obtained from the reflectometer experiment will be directly and immediately applicable to solar-concentrators and related power system designs and to all optical systems dependent upon reflective surfaces in space. Examples of types of systems and instruments which will benefit greatly from the data gathered by the reflectometer experiment are: solar-energy converters, space telescopes, optical communication systems--including laser systems--and specularly reflective thermal control surfaces.

Although the minimum desired lifetime of the reflectometer experiment is one year, every effort will be made to assure an instrument life of three years, the expected life of ATS-C, the space platform for the reflectometer experiment.

EXPERIMENT OBJECTIVES

The objective of the reflectometer experiment is to test in a space environment, for an extended period (one to three years) the durability of specularly reflective surface materials. The experiment is designed primarily to obtain engineering data necessary for spacecraft optical systems.

A secondary aim is to obtain data of scientific value relating to the degradation process. However, this objective is pursued only to the extent that the primary objective is not compromised. For this reason, no direct systematic measurement of the environment is planned.

Ideally it would be desirable to make the acquisition of scientific data the primary aim in order to gain a thorough scientific understanding of the space environment. From this more complete set of test data, it would be possible to deduce engineering data for any application. But fulfillment of this objective would require a large number of space flights and many more experiments. Therefore, the experiment is primarily aimed at obtaining much needed engineering data only.

The reflectometer experiment will provide data consisting of measurements of both the magnitude of reflectivity and spectral characteristics of reflectivity; analysis of data will provide insight into the cause and extent of indicated damage to sample surfaces. To further pinpoint the cause of surface erosion an effort will be made to separate the effects on various surfaces by selectively shielding particular samples.

The surface samples will be mounted in pairs and one member of each pair will be partially protected from the space environment by a clear quartz crystal. The quartz shield will effectively block most of the charged particles and micrometeorites except for a very short interval during which data is recorded. The quartz shield will permit passage of ultraviolet radiation, however. The other member of the sample pair will be continually exposed to the entire space environment.

The reflectivity of each of the samples will be determined by sequentially projecting a beam of light from a tungsten filament light bulb onto the sample and measuring the amount reflected. The intensity of the return beam will be measured by a "white" light photodetector, and the spectral composition of the reflected beam will be analyzed by a low resolution spectrometer, measuring the reflectivity in each of the four spectral bands.

A more complete reflectometer experiment might include other environmental measurements in order to correlate cause and effect data. However, the complexity of the space environment would make the complete measurement and cataloging of all environmental parameters an expensive undertaking. Thus, the success of the reflectometer experiment will depend upon correlation with the data from other sources such as the previously flown ATS-1 and other satellite and space probes. In addition, evaluation of other data collected during the active lifetime of the ATS-C reflectometer experiment--such as solar storm activity and critical on-board temperature measurements--will be extremely valuable.

Since most optical systems are primarily concerned with the use of specular rather than diffuse reflecting surfaces, no attempt will be made to evaluate diffuse reflectivity.

REFLECTOMETER DESIGN

Figure 1 is an overall view of the reflectometer and its location in the ATS-C spacecraft. The essential elements of the reflectometer experiment are: the optics, internal light source, light detectors, test sample configuration, the electric and mechanical subsystems, and the telemetry and command interfaces.

a. Optics

Figure 2 illustrates the reflectometer optical schematic. Radiant energy from one of the two incandescent tungsten lamps is passed through (or

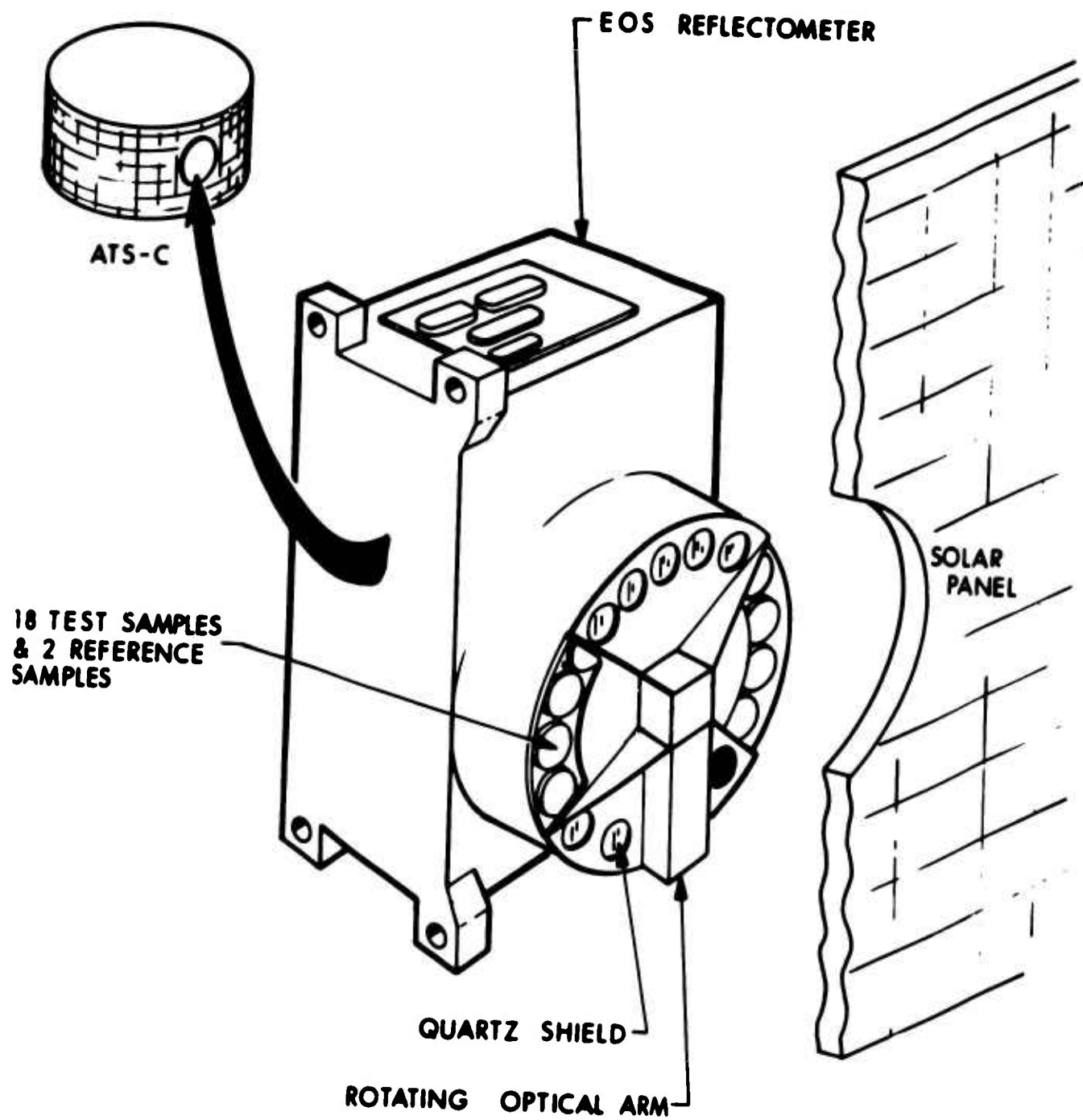


Figure 1. The Reflectometer Experiment

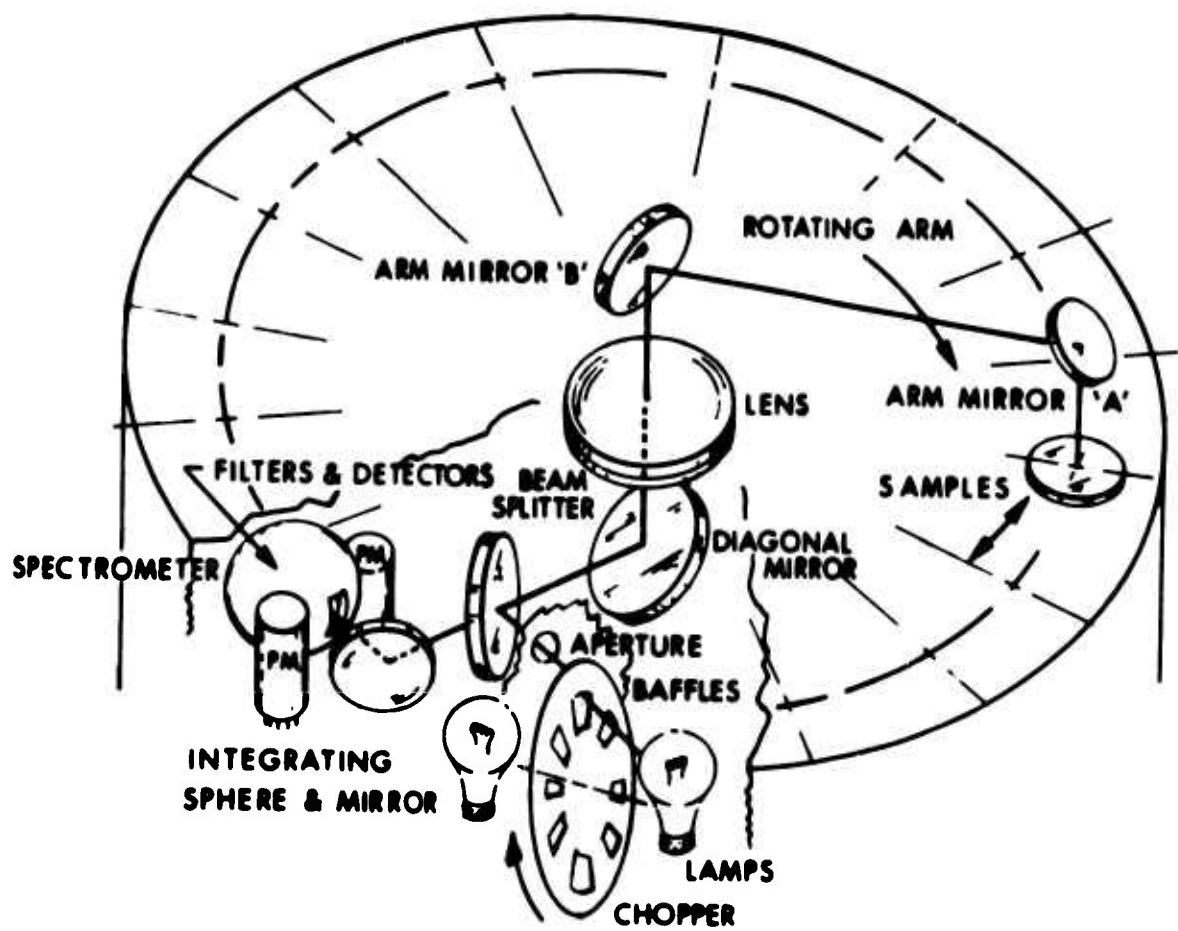


Figure 2. Reflectometer Optical Schematic

reflected from, depending upon the lamp in use) a mechanical chopper driven at 2400 rpm producing a pulse rate of 480 Hz. An aperture stop limits the light beam passing to the beam splitter lens to 0.2 inch. The beam splitter projects 30 percent of the source light into the telecentric optical system. The remaining light is reflected out of the system.

The optical path to the reflectometer sample consists of two 0.3 inch diameter lens elements and two mirrors which are an integral part of the rotating arm. The two-element mirror arrangement focuses the light onto the sample surface. The light is subsequently reflected off the sample surface and returned along the same mirror and lens system to the beam splitter. Seventy percent of the light is dissipated and the remaining 30 percent is reflected via another mirror into an integrating sphere spectrometer.

Two lead sulphide photoconductors, one silicon photoconductor, and two photomultiplier tubes (P-M tubes) are mounted at apertures on the integrating sphere. Mounted in front of three of the five detectors are different spectral filters forming a system capable of providing a nominal breakdown of the entire tungsten lamp spectrum. The spectrum from 0.3 to 0.65 microns is detected by the two P-M tubes ("seeing" 0.3 to 0.4, and 0.3 to 0.65 microns, respectively). The 0.65 to 1.2 micron spectral band is detected by an unfiltered silicon detector. The first of the lead sulfide detectors senses the 1.2 to 3 micron range of reflected light, and the other detector examines the entire (unfiltered) visible spectrum.

The effective optical efficiencies in the five spectral detection domains of the reflectometer are determined by a large number of factors, including the operating temperature of the tungsten lamp, the beam splitter efficiency, the various lens transmissivities, the mirror chromatic vignetting, and finally the bandpass characteristics of the various filter-detector combinations.

A simple tungsten filament incandescent bulb has been chosen as the light source for the reflectometer, being the best trade-off between reliability and lamp lifetime, and the desired lamp response in the ultraviolet range. The lamp will be operated at a voltage as close as possible to that of sunlight in space. Figure 3 shows the electromagnetic spectrum of both the tungsten lamp and the sun. From this, it can be seen that the lamp does provide a satisfactory range, with the possible exception of too little radiation in the ultraviolet region.

The usable output, which extends from less than 0.3 micron into the 3 micron region, compares favorably with the solar spectrum in which 98 percent of the solar energy is found. The solar spectrum extends somewhat beyond that of a lamp operating at 2800°K . (The tungsten lamp has little output below 0.35 micron or above 2.0 microns.)

At the lower end of the spectrum 9 percent of the solar energy is below 0.4 micron and 1.2 percent is below 0.3 micron. The tungsten lamp exhibits less than 0.08 percent of its total energy at wavelengths less than 0.4 micron when operated at 2800°K . Assuming 80 percent of the 2-watt input to the lamp is radiated, about 4 milliwatts of light energy with wavelengths below 0.45 micron will be available to the optical system.

The problem of tungsten lamp reliability was solved by using two especially rugged lamps and by operating them below rated voltage. The lamps are low-voltage, high-intensity devices which operate with 0.65 amp at 3.2 volts. Should the primary lamp fail, the backup lamp can be commanded into action from the ground.

The partial aluminum coating on a Vycor substrate of the beam splitter gives it nearly neutral reflectance-transmittance characteristics.

Two sets of ghosts are formed by the beam splitter. One set is formed by the outgoing bundle and the other set by the return bundle. The

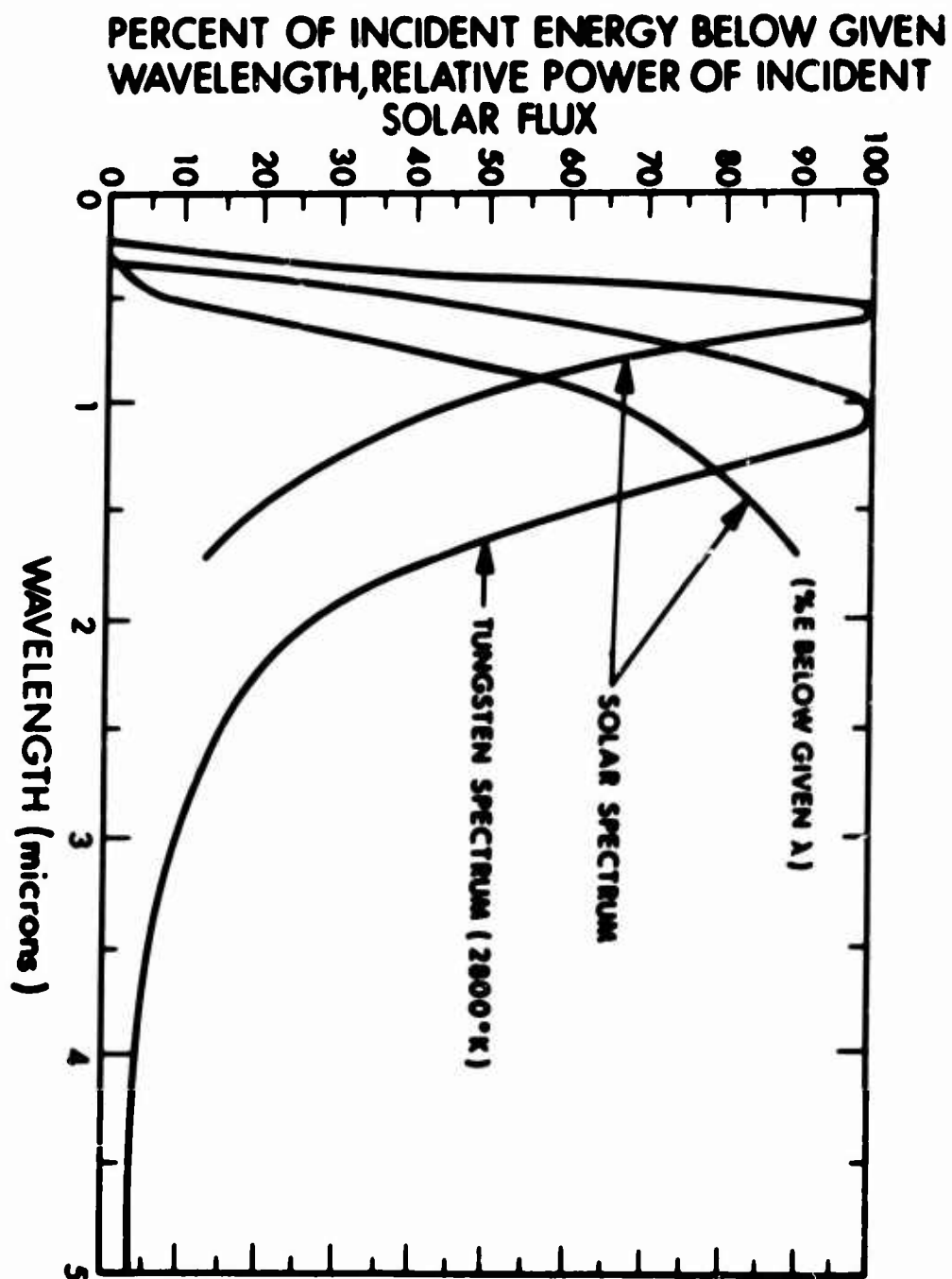


Figure 3. Spectrum of the Tungsten Lamp

ghosts formed by the outgoing rays are vignetted mostly by the optical system and the ghosts formed by the return rays are formed near the primary image at the integrating sphere entrance window.

To reduce the sensitivity to sample misalignment the optics are designed to focus the filament image on the sample. This image is then reimaged by the lens onto the detector plane through the beam divider. Angular movement of the sample does not change the position of the image. In order to avoid an energy change as the sample is tilted the lens diameter is substantially larger than the input beam diameter of 0.2 inch.

The slit through which the reflected rays enter the spectrometer is 1.1 mm x 0.284 mm, large enough to permit the beam to enter regardless of the optical aberrations and geometrical uncertainties. The lens diameter is 0.5 inch with a focal length of 2.73 inches. Although most spectrometric designs are extremely sensitive to image movement, the use of an integrating sphere allows the optical beam to wander in the aperture without affecting the output.

After penetrating the sphere aperture, the beam strikes a diffusely MgO reflecting interior surface. This results in an infinite number of reflections producing a constant power density and spectral content on any internal point. The photodetectors, with their respective bandpass filters are located on the surface of the integrating sphere spectrometer.

The major shortcoming of the spectrometer is its power efficiency which is proportional to the reflectance of the interior coating and to the ratio of the detector area to the total surface area of the coating. The spectrometer's low power efficiency requires high light power and highly sensitive photodetectors.

The system uses three types of light detectors. One type is a lead sulfide photoconductive device whose electrical resistance is inversely proportional to the impinging light level. PbS detectors have a broad

response spectrum extending from 0.3 micron to about 3.0 microns. Their response falls off rapidly at the near-ultraviolet wavelengths. The PbS detector responsivity, on the order of 100 microvolts per microwatt, is an order of magnitude better than other solid-state or photoconductive devices. They also operate at a fairly low voltage dc bias.

Lead sulfide photodetectors are extremely temperature-sensitive, having a dc resistivity temperature change on the order of 4 percent per degree centigrade. To reduce the problems caused by extreme temperature sensitivity, a combination of temperature monitoring and gain sensitivity compensation is used.

Another undesirable characteristic of lead sulfide is that its responsivity diminishes with age. To compensate for this and changes due to temperature, the signal conditioning electronics include ground-controlled range switching.

The second type of light detector is a silicon photodetector whose output current is proportional to the impinging light level. The silicon photodiode responsivity is on the order of 0.5 microampere per microwatt. This type photodetector has a broad response spectrum from approximately 0.32 micron to 1.2 microns. By combining the spectral output of the tungsten source and the spectral response of the silicon photodetector the capability to detect the 0.65 to 1.2 micron spectrum was established.

In a manner similar to that of the lead sulfide detector the silicon photodetector operates at a relatively low dc bias level. The silicon diode is not as temperature sensitive as the lead sulfide detectors; however, ground-controlled range switching is also provided in this channel.

The third type of light detector, a photomultiplier tube, RCA 8571, is used to monitor the near ultraviolet end of the reflected spectrum.

Its responsivity is in the order of 10^5 microamps per microwatt. The PMT overall spectral response is much narrower than that of the PbS detectors, but high in the near ultraviolet region. However, the tube does require a high-voltage bias of between 500 and 1,000 volts.

b. Reflectometer Sampling

Figure 1 illustrates the arrangement of the samples in the reflectometer instrument. Exposure of the samples to the space environment is made possible by allowing the reflectometer sample disc to protrude through a 7-inch diameter hole in the ATS-C solar panel. By means of the two reflecting mirrors in the rotating arm, the beam from the tungsten lamp is directed onto the surface of the sample, returns to the optical path and finally enters the spectrometer where it is quantitatively examined.

The experiment includes 20 samples, 10 of which are unshielded, 8 of which are shielded with quartz inserts, and 2 of which are reference samples (one full scale and one zero). The reference surfaces are carefully and continuously shielded at all times in order to maintain their calibrated reflectivity.

Since the number of surfaces to be tested was limited, considerable effort was devoted to selection of materials currently of interest to the space environment experimenters. Joint conferences between NASA experimenters, private industrial researchers, and ATS program management personnel resulted in selection of materials which, from most points of view, offered the best promise of resisting the erosion forces encountered in a space environment.

Appendix I lists the number and kind of materials selected for reflectometer test surfaces. The reflective materials have as substrates either nickel, aluminum, epoxy, or quartz. The reflective surfaces are either aluminum or silver. The various over-and-under-coatings are derivatives of the silicon oxide family. The samples themselves are quite small, three-quarters of an inch in diameter.

Certain geometrical reactions can be expected from thermally induced structural stresses. To reduce the number of uncontrolled variables and increase the reliability of the instruments and the validity of the data, every effort is made to prevent geometrical changes in the samples being tested. It is imperative that sample mounts be insensitive to distortion and temperature gradients. To accomplish the latter, a material with maximum conductivity is used. The sample mount will have a spherical recess at the center, such that the sample can be adjusted in any direction. To minimize the creep problem, metal inserts are used under the mounting bolt heads to redistribute the loading. The plate upon which the test samples are mounted is designed such that it is a rigid section.

The arm containing two mirrors to direct the tungsten beam on each of the 20 samples rotates at a rate of about an eighth of a revolution per minute sampling each reflective surface at a very slow rate. Arm rotation is not synchronized with the 100 rpm rotation rate of the spin stabilized ATS-C spacecraft. This permits data readout independent of the sending rate of the telemetry system or the spin rate of the spacecraft.

c. Mechanical Subsystem

Figure 4 shows the mechanical subsystem which includes a housing for the optical system and electronics and provides the drive system which rotates the optical scanner arm.

The housing, machined from a solid block, provides structural support for the various components and, as a sealed container, shields reflectometer components against the hostile space environment. Most of the mechanical elements are inside the hermetically sealed enclosure with the exception of two gears and a pair of bearings. The gears and bearings which serve to mount the arm assembly and which are exposed to the space environment are expected to operate without difficulty. The housing also acts as a conductive heat path between scanner arm, samples, and spacecraft to maintain a minimum temperature gradient.

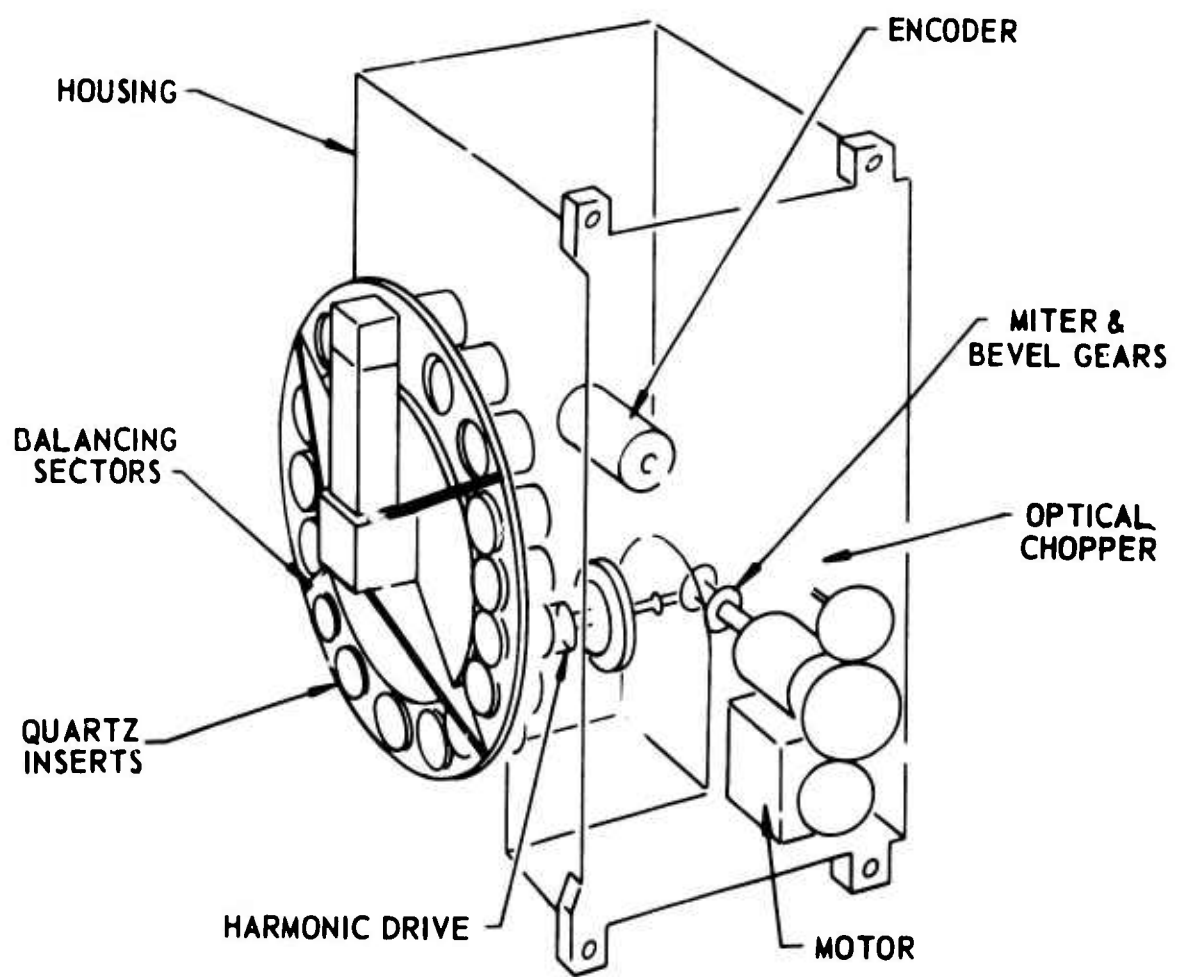


Figure 4. Mechanical Subsystem

The source of power for the drive system is a brushless 24 volt dc motor operating at 2400 rpm. Power is transferred through a 100:1 speed-reducer to a harmonic drive assembly which provides an effective dynamic coupling through the hermetically sealed housing enclosure. The optical chopper wheel is driven at 1:1 speed ratio through a spur gear train. The in-line branch of the miter gear train drives the output shaft of a 180:1 speed reducer, which in turn drives the scanner arm position encoder through a 1:1 spur gear train.

The 90° branch of the miter gear is directly coupled to the 72:1 harmonic reducer. The harmonic drive provides the rotary interference between the vacuum of space and the sealed housing. The output of the harmonic drive with a speed reduction 72:1 drives the reflectometer rotary scanner arm through a spur gear train.

In order to produce chopping frequency as high as practicable, the chopper wheel is driven at the motor speed of 2400 rpm. Spacecraft inertial properties and gyroscopic couple specification considerations have forced a chopper wheel design of essentially a flat disc with twelve equally spaced sharp-edged slots.

A parallel path via a speed reducer to the encoder translates mechanical angular position of the scanner arm into a digital electrical signal. The digital encoder reads out the position of the scanner arm with 8-bit resolution, allowing detection of minor local variations in sample damage.

The hard vacuum of space, which at ATS-C synchronous altitude is about 10^{-12} torr, poses a problem for the moving parts contained in the instrument. The most susceptible elements in the mechanical system are those moving at high speed or under a heavy load. Thus, as far as possible, the critical moving parts are located inside the hermetically sealed enclosure. This includes the brushless dc motor, the gear box speed reducer, the digital shaft-position encoder, the bulk of the optics, and all the electronics. Dry film lubricants (MoS_2 -Teflon) are employed for

the few bearings and gears which operate outside the hermetic housing in the space vacuum.

d. Electronics Subsystem

Figure 5 is the block diagram of the electronic subsystem. It is purposely a simple system to maintain the high reliability needed to assure a three-year lifetime in the experiment.

There are three principal electrical interfaces with the spacecraft: spacecraft power, the command system, and digital and analog telemetry systems.

Bias voltages for the photodetectors, high voltage for the photomultiplier, transistor bias for the signal conditioning, and the highly regulated voltage required for the tungsten lamps are all supplied by dc-to-dc converters in the reflectometer.

The high voltage converters are adjustable over the range of 500 to 1000 volts in order to set the peak output of the associated photomultiplier tube at 2 microamps. Limiting the P-M tube anode current to 2 microamps tends to minimize photomultiplier drift and instability.

Electrical power for the lamp's 3.2 volts dc at 650 milliamps each is developed by a single low voltage dc-to-dc converter. The output of the lamp interface circuits is used to activate highly reliable, subminiature relays which in turn direct power to the selected lamps. Since measurement of all bias voltages is essential for data reduction and correlation, analog values of the bias voltages are supplied to the spacecraft telemetry system.

Of the four command channels, one is used to start the motors, two others select and apply power to the desired lamp, and a fourth changes the gain of the signal conditioning.

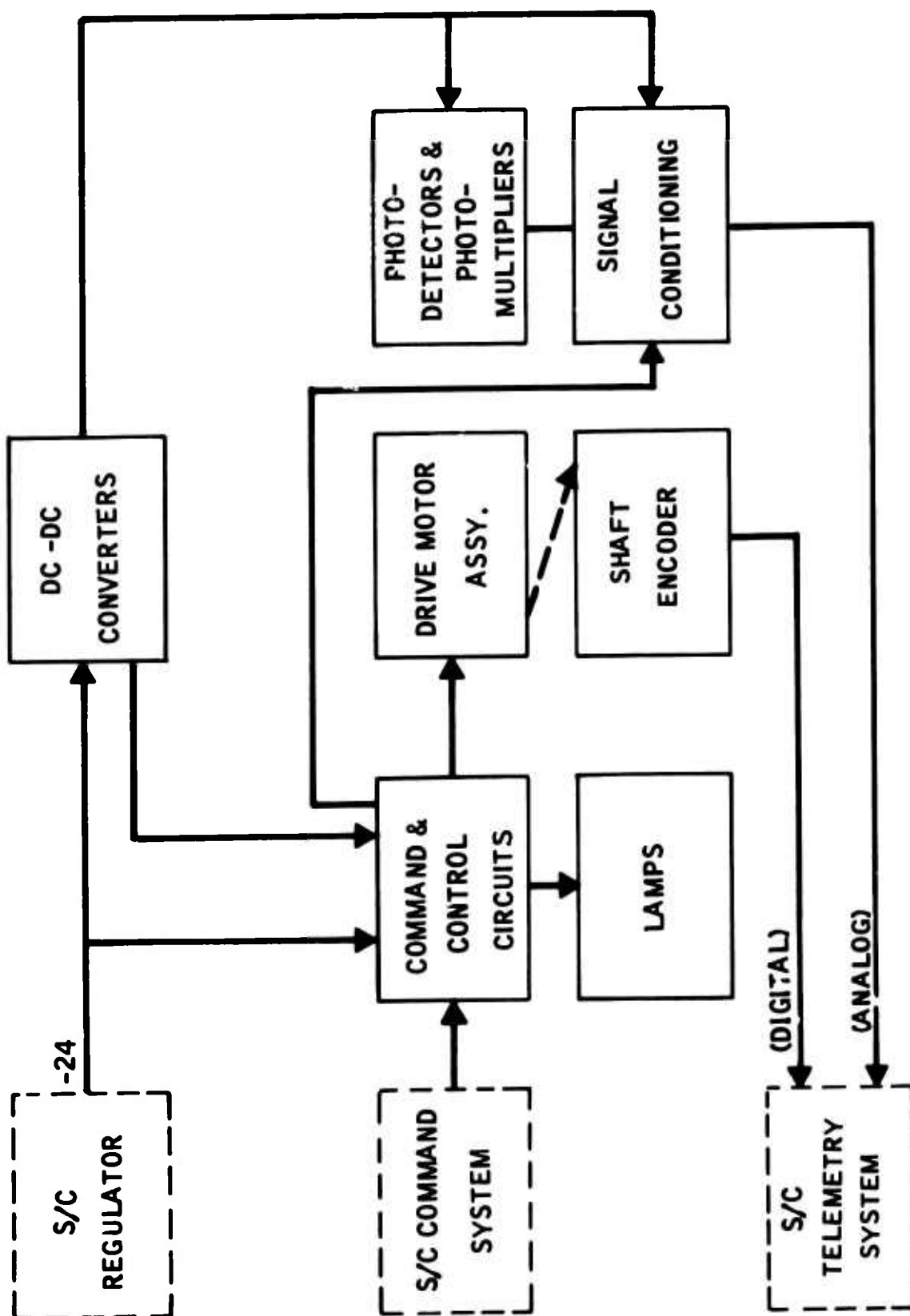


Figure 5. Electronics Subsystem

The brushless dc motor is operated from the spacecraft regulator bus at $-24V \pm 2\%$ through the motor control interface circuit.

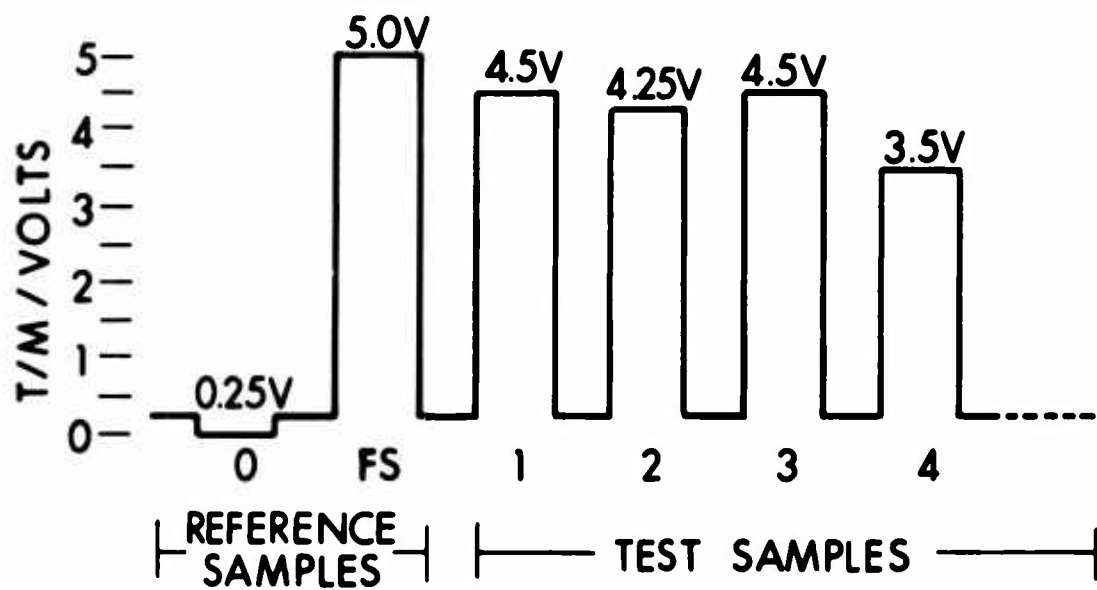
The power conversion subsystem of the reflectometer consists of two adjustable high voltage power supplies and a single, multiple-output, low voltage dc-to-dc converter.

There are basically two signal processing circuit designs, one associated with the lead sulfide and silicon detectors and one associated with the P-M tube detectors. These circuits consist of an FET buffer amplifier, an integrated-circuit amplifier as a bandpass filter, and a signal demodulator and impedance matching buffer circuit. A multiple-range feature is included in the photodetector signal conditioning channels to compensate for the undesirable features of the lead sulfide and silicon detectors, viz. temperature sensitivity and unpredictable performance degradation with age.

The primary telemetry data consists of:

- a. Five measurements of reflectivity (one broadband channel covering the entire tungsten spectrum--nominally from 0.3 to 3 microns--and four spectral reflectivity channels extending from 0.30 to 0.40, 0.30 to 0.65, 0.65 to 1.2, and 1.2 to 3 microns)
- b. Digital encoder readout (of the scanner arm position) with 8-bit resolution
- c. Temperature of lead sulfide detector, necessary to determine absolute detector sensitivity at any given time
- d. Record of photomultiplier high voltage to determine PMT gain
- e. Record of the tungsten lamp voltage, to determine stability of the light output

Figure 6 is an analog representation of the telemetry data. With time as the ordinate, the voltage level shown between sample spaces is an analog of the reflectivity of the instrument from between the samples. It represents the reflected light from the intersample space. Nominally and ideally, the zero reference is zero volts because the "zero reference" represents a black cavity.



SAMPLE REFLECTIVITY EQUATION = $\frac{V_1 - V_0}{V_{FS} - V_0} =$

$$\frac{4.5 - 0.25}{5.0 - 0.25} = 0.89$$

Figure 6. Format, Reflectivity Data

The full-scale (FS) sample although not necessarily 100 percent reflective, is known and calibrated. The system in turn is scaled so that the signal from the full-scale reference sample represents full-scale and all other samples are relative to it. The test sample voltage levels represent typical real numbers associated with particular samples. The reflectivity of a given sample is determined by the equation shown.

$$R_s = \frac{V_s - V_o}{V_{fs} - V_o} \quad \text{where } R_s = \text{test sample reflectivity}$$

V_s = applicable test sample reflectivity signal voltage (volts)
 V_{fs} = applicable full-scale sample reflectivity signal voltage (volts)
 V_o = applicable zero samples reflectivity signal voltage (volts)

End-to-end system calibration is performed by measuring the zero and full-scale reflectivity samples each time reflectivity data is recorded. This alleviates or controls the parameters likely to contribute to system decay. In this way the reflectivity measurement of a given test sample does not depend upon absolute reflectance measurement but upon a relative measurement and comparison with the reference samples. The scanner arm contains the shield assembly which protects the reference samples since confident use of reference samples requires that the samples be shielded from the space environment.

SUMMARY OF OPERATION

The following is a description of the normal operating cycle of the reflectometer.

The first ground command turns on the spacecraft voltage regulator. This is followed by a warmup period that permits dc-to-dc converters to stabilize. Stable voltages are essential for proper operation of the detectors and P-M tubes. The telemetry is then activated to verify the scanner arm position and critical parameters.

The drive motor is then started and during the next eight minutes the scanner arm is pivoted at the center of the array, scanning each of the 20 samples in turn. The arm projects the beam of light from the tungsten lamp onto the sample being tested. The portion of the light that is reflected returns through the arm down into the body of the reflectometer to the detectors and electronics. The return beam is analyzed by a "white" light detector as well as by a low resolution spectrometer which analyzes the return radiation in each of four spectral bands. The scanner arm stops automatically when it returns to the initial position. Finally the critical parameters are again checked and the spacecraft voltage regulator is de-energized.

The frequency of operation will depend upon the quality of data obtained. For the first month or two, the reflectometer will be interrogated frequently to procure initial trend data on some of the dielectric coatings which may be particularly susceptible to ultraviolet damage. Once initial trends have been established, data acquisition will be less frequent, possibly only once a month.

The total actual operating time of the reflectometer--over a three-year period, the lifetime of ATS-C--is anticipated to be no more than 50 hours total.

REFERENCES

Bartholomew, Hank. The Reflectometer Experiment, Paper presented at the
ATS Systems Engineer Training Program, August 22, 1966. Goddard
Space Flight Center, Greenbelt, Maryland.

Reflectometer Experiment for Applications Technology Satellite. Monthly
reports (various): Electro-Optical Systems, Inc., Pasadena,
California.

APPENDIX I
ATS REFLECTOMETER SAMPLES

ATS Reflectometer Samples

Item	Quantity Per Instrument	Position On Instrument	A Substrate	B Undercoat	C Reflective Coating	D Overcoat	Reflective Coating Thickness	Supplied By (Letters refer to table columns)
1	1	1 (100%)	--	--	Second Surface Reflection-Quartz	--	--	A, B, C, D-EOS
2	2	2, 4	Ni	Cr/SiO	Al	SiO	1700Å	A, B, C, D-EOS
3	1	3 (0%)	--	--	Black Anodize	--	--	--
4	2	5, 11	Ni	Cr/SiO	Al	None	--	A, B, C, D-EOS
5	1	6	Al	None	1/2 Mil Mylar	None	--	A-EOS B, C, D-NASA-Langley
6	2	7, 12	Ni	Cr/SiO	Al	SiO ₂	12λ/4 (550 mμ)	A, B-EOS C, D-NASA-GSFC
7	2	8, 10	Ni	Cr	Ag	MgF ₂	2λ/4 (550 mμ)	A-EOS B, C, D-NASA-GSFC
8	2	9, 15	Mg + Epoxy	SiO(250Å)	Al (1000Å)	(Si ₂ O ₃)x	12,000Å	A, B, C, D-NASA-Lewis
9	2	13, 14	Ni	None	Alzak	None	302 x 10 ⁴ Å	A, B, C, D-NASA-GSFC
10	1	16	Al	SiO	Al ₂ O ₃	Al ₂ O ₃	12λ/4 (550 mμ)	A-EOS B, C, D-NASA-GSFC
11	2	17, 20	Quartz	SiO	Al	SiO ₂	12λ/4 (550 mμ)	A-EOS B, C, D-NASA-GSFC
12(c)	2	18, 19	Al	SiO	Al	SiO Split Coating	1700Å	A, B, C, D-EOS

NOTES (a) Where a quantity of two samples per instrument are indicated, one is provided with a quartz shield.

(b) EOS supplies all sample mounts.

(c) Each sample is one-half overcoated with no overcoating on the other half.

THE DETERMINATION OF THE ORIENTATION OF A
TUMBLING CYLINDER FROM THE SHAPE OF
THE LIGHT CURVE

J. G. Williams
North American Aviation, Downey, California and
U. C. L. A., Los Angeles, California

THE DETERMINATION OF THE ORIENTATION OF A TUMBLING CYLINDER FROM THE SHAPE OF THE LIGHT CURVE

J. G. Williams

UCLA

Department of Planetary and Space Science
North American Rockwell Corp.
Space Division

Introduction

The problem to be treated here is the nature of the light curve of a tumbling, diffusely reflecting cylindrical satellite under various orientations of the spin axis. Several assumptions are made: the reflecting surface obeys the Lambert law, the cylinder tumbles end over end, and the angular velocity of the satellite with respect to the star field is small compared to the angular rate of spin. This latter assumption restricts the problem to one where the changing geometry of the sun, observer, and satellite has negligible effect on one cycle of the light curve. It will be indicated how the method of solution can also handle the case of a precessing cylinder and the case of cylinders with end pieces of various simple shapes.

Discussion

The expression for the apparent magnitude of a satellite may be conveniently written as¹

$$M = -26.50 - 2.5 \log(AYF) + 5 \log(R)$$

where γ is the albedo, A is the cross-sectional area of the cylinder as seen from the side, and R is the slant range of the satellite. The brightness function F for a diffusely reflecting cylinder obeying Lambert's law of reflection is given by^{1,2}

$$(1) \quad F = \frac{\sin \varphi_1 \sin \varphi_2}{4\pi} [(\pi - \theta) \cos \theta + \sin \theta].$$

In Equation (1) spherical coordinates are used which are fixed in the rotating body so that the symmetry axis points in the direction of the coordinate pole. The sun and the observer have polar angles which are given by φ_1 and φ_2 while θ measures the difference in their azimuthal angles.

Among the three quantities φ_1 , φ_2 and θ there are only two independent variables since the three quantities are related by means of the equation for the phase angle β :

$$(2) \quad \cos \theta = \cos \varphi_1 \cos \varphi_2 + \sin \varphi_1 \sin \varphi_2 \cos \theta.$$

A change of coordinates from the spinning system to an inertial system is now made. The new system of polar coordinates (Figure 1) is chosen to take advantage of the symmetries in the brightness function which will become apparent. The great circle joining the sun and observer directions defines the zero azimuth angle, and the point midway between the sun and observer directions is the equator. In this new system the polar angle will be called Λ and the azimuthal angle is Γ .

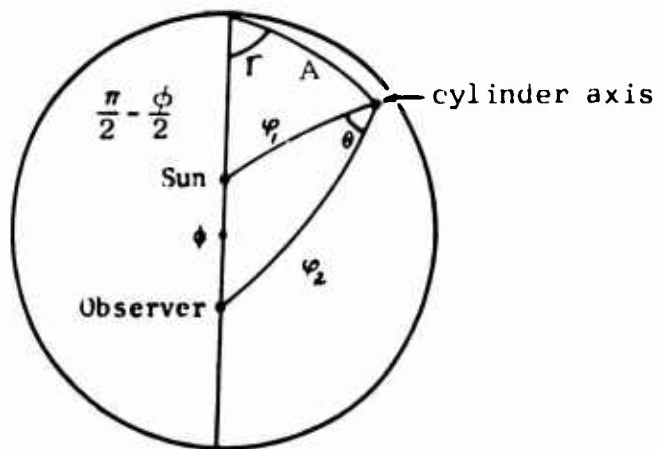


FIGURE 1

Solving for the brightness function in terms of these new coordinates yields

$$F_1 = \sin \theta |\sin \Gamma| \sin \Lambda$$

$$F_2 = \cos^2 \frac{\theta}{2} - \sin^2 \Lambda (\sin^2 \frac{\theta}{2} + \cos^2 \frac{\theta}{2} \cos^2 \Gamma)$$

$$(3) \quad F(\Lambda, \Gamma) = \frac{1}{4\pi} [(\pi - \tan^{-1}(F_1/F_2))F_2 + F_1].$$

Figure 2 is a sketch of the brightness function in the Λ, Γ system. When the cylinder's axis points in the direction of the pole the object has maximum brightness. When pointing toward the arc joining the sun and observer no light is received from the object. Saddle points are located on the equator at azimuths $\pm\pi/2$.

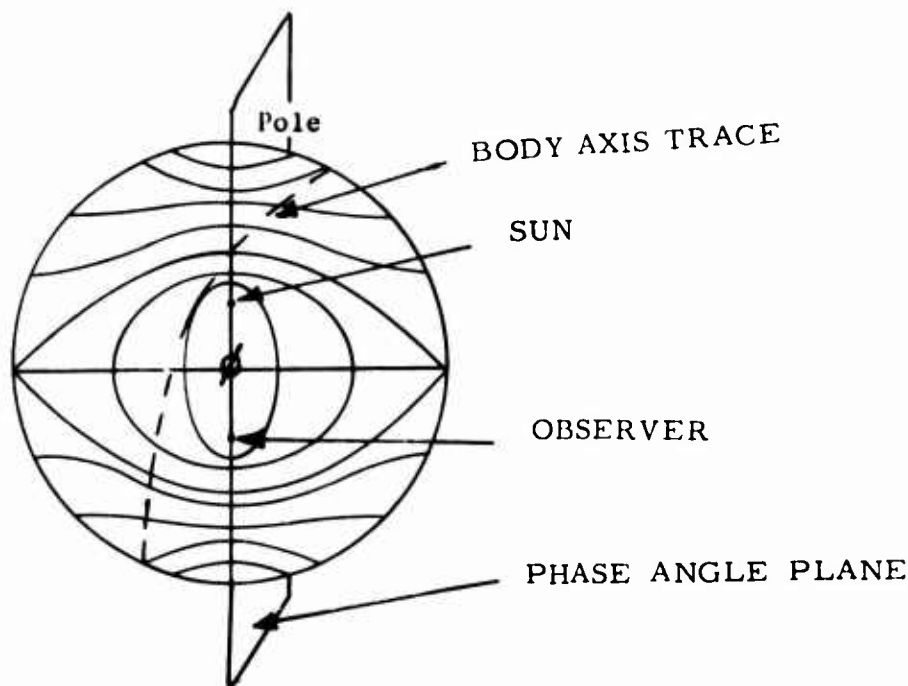


FIGURE 2

This problem is so highly symmetrical that the brightness function for one octant is repeated for each of the other seven octants. These symmetries are best thought of as two mutually perpendicular planes of mirror symmetry plus a point symmetry. A brief discussion of the origins of these symmetries will shed some light on what is to be expected in less simple problems. The mirror symmetry $F(A, \Gamma) = F(A, -\Gamma)$ will result for any object with cylindrical symmetry. The point symmetry $F(A, \Gamma) = F(\pi - A, \pi + \Gamma)$ results from the fact that a cylinder has a plane of mirror symmetry perpendicular to its symmetry axis. Thus a cylinder with dissimilar end caps would break this symmetry. The other mirror symmetry $F(A, \Gamma) = F(\pi - A, \Gamma)$ comes from the use of Lambert's law of reflection. It would result for any reflection law where the angles of incidence and reflection are treated identically.

For a tumbling object we now wish to know the location and brightness of the maxima and minima and their relation to the location of the spin axis. The straightforward approach of setting up the equation of the brightness function in terms of the coordinates of the spin axis and a parameter measuring the rotation, setting the derivative equal to zero, and solving for the location of the extrema is disappointing. The transcendental equation which must be solved is extremely difficult, if not impossible, to solve. However, the reverse problem, that of finding the location of the spin axis once the location of the maxima are known, is solvable.

The solution is effected by noting that the great circle swept out by the rotating cylinder is tangent to the isophotes at the extrema. There is one exception to this rule, a minimum which has zero intensity. First the equation for the brightness function will be set up in terms of the slope of the isophotes at the point tangency, then the slope of the isophotes will be calculated directly from the expression for the brightness function. The resulting expression for F is in terms of a measurable parameter, the fractional rotation from a maximum or a minimum.

The location of the extremum is designated Λ_0, Γ_0 . The great circle swept out by the tumbling cylinder has a slope of σ with respect to the line of constant colatitude. The angle X measures the angle of rotation away from the extremum. All of this may be visualized with the aid of Figure 3. Solving the relevant spherical triangles allows Equations (3) to be written as

$$F_1 = \sin \theta [\cos \Gamma_0 \cos \sigma \sin X + \sin \Gamma_0 (\cos X \sin A_0 + \cos A_0 \sin \sigma \sin X)]$$

$$F_2 = \cos^2 \frac{\theta}{2} - (\cos X \sin A_0 + \cos A_0 \sin X \sin \sigma)^2 \left(\sin^2 \frac{\theta}{2} + \cos^2 \frac{\theta}{2} \cos^2 \Gamma_0 \right)$$

$$- \sin^2 X \cos^2 \sigma \left(\sin^2 \frac{\theta}{2} + \cos^2 \frac{\theta}{2} \sin^2 \Gamma_0 \right)$$

$$+ 2 \cos^2 \frac{\theta}{2} \sin \Gamma_0 \cos \Gamma_0 \sin X \cos \sigma (\cos X \sin A_0 + \cos A_0 \sin X \sin \sigma)$$

$$(4) \quad F(X) = \frac{1}{4\pi} [(\pi - \tan^{-1}(F_1/F_2))F_2 + F_1].$$

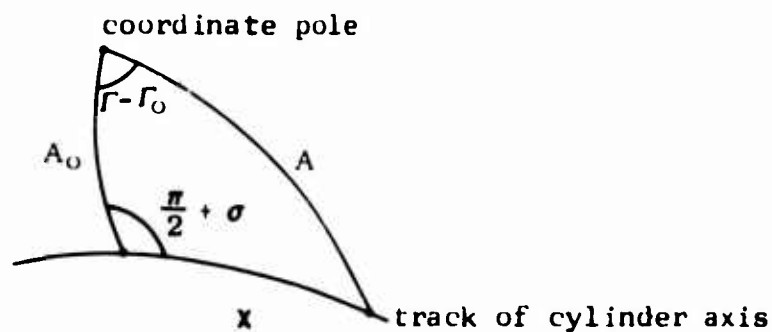


FIGURE 3

The slope of the isophotes, σ , is calculated from Equations (3) by means of

$$(5) \quad \tan \sigma(\Gamma, \Lambda) = \frac{1}{\sin \Lambda} \frac{\partial F}{\partial \Gamma} / \left(-\frac{\partial F}{\partial \Lambda} \right).$$

Evaluating (5) at the extrema gives

$$\begin{aligned}
 (6) \quad \tan \sigma(\Gamma_0, \Lambda_0) = & \frac{\sin \Gamma_0 \cos \Gamma_0}{\cos \Lambda_0} \left\{ 8\pi F(\Gamma_0, \Lambda_0) \left[\left(\cos^2 \frac{\theta}{2} \right. \right. \right. \\
 & - \sin^2 \Lambda_0 \left(1 - \cos^2 \frac{\theta}{2} \sin^2 \Gamma_0 \right) \left. \right)^2 \\
 & + \sin^2 \Gamma_0 \sin^2 \theta \sin^2 \Lambda_0 \left. \right] \cos^2 \frac{\theta}{2} \\
 & + |\sin \Gamma_0| \sin^3 \theta \sin \Lambda_0 \left[\cos^2 \frac{\theta}{2} \right. \\
 & \left. \left. - \sin^2 \Lambda_0 \left(1 + \cos^2 \frac{\theta}{2} \sin^2 \Gamma_0 \right) \right] \right\} / \\
 & \left\{ 8\pi F(\Gamma_0, \Lambda_0) \left[\left(\cos^2 \frac{\theta}{2} - \sin^2 \Lambda_0 \left(1 - \cos^2 \frac{\theta}{2} \sin^2 \Gamma_0 \right) \right)^2 \right. \right. \\
 & + \sin^2 \Gamma_0 \sin^2 \theta \sin^2 \Lambda_0 \left. \right] \left(\cos^2 \frac{\theta}{2} \cos^2 \Gamma_0 + \sin^2 \frac{\theta}{2} \right) \\
 & - |\sin^3 \Gamma_0| \sin^3 \theta \sin \Lambda_0 \left[\cos^2 \frac{\theta}{2} \right. \\
 & \left. \left. - \sin^2 \Lambda_0 \left(\cos^2 \frac{\theta}{2} \sin^2 \Gamma_0 - 1 \right) \right] \right\} .
 \end{aligned}$$

The slope angle from (6) is to be used in Equations (4). This gives the result which is sought.

The quantities Γ_0 , Λ_0 , and $\sigma(\Gamma_0, \Lambda_0)$ easily related to the coordinates of the spin axis Γ_1 , Λ_1 . Solving the proper spherical triangle (Figure 4) yields

$$(7) \quad \cos \Lambda_1 = \sin \Lambda_0 \cos \sigma$$

$$\tan(\Gamma_1 - \Gamma_0) = \sin \sigma / (-\cos \Lambda_0 \cos \sigma)$$

Rotation of these coordinates into right ascension and declination can be done by conventional means.

The extension of the above method to the more complex situation follows. For end caps on the cylinder the appropriate brightness functions for the end caps would have to be added onto the cylinder's brightness function. There would be a constant multiplying the term for the end caps relating the cylinder's diameter to its length. For a precessing cylinder there would be an angle of precession to be determined. The great circle path of the cylinder axis used in Equations (4) would have to be replaced by the path of the precessing axis. The important point to note is that at each point of the foregoing analysis these additional complexities can be added without preventing the method from yielding an expression for the brightness function in terms of the fraction of the rotation between the maxima or minima.

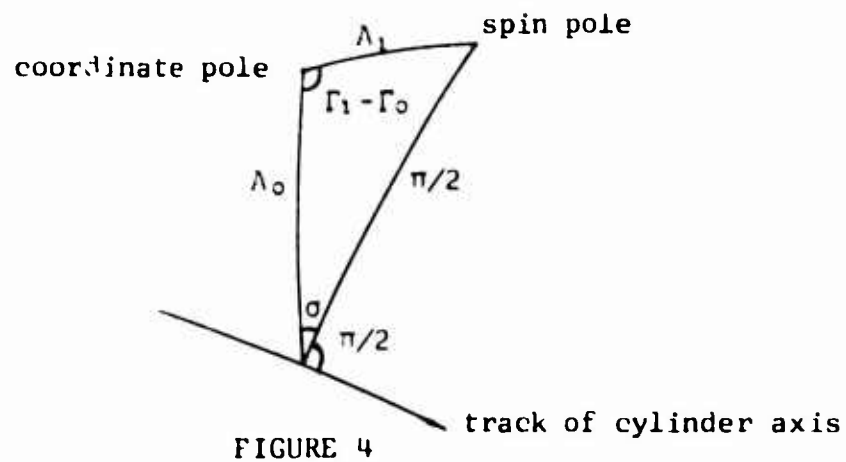
One simple case with end caps can be done. The case with two diffuse or specular, hemispherical end caps would only increase the brightness function F by a constant amount; the slope equation (6) remains unchanged (interpreting the $\Gamma(A_0, \Gamma_0)$ in it as the result without end caps). The constant added amount would depend upon the phase angle ϕ for the diffuse end caps.

For the simple case of the cylinder only two unknowns are involved in getting the spin axis location. With precession and end caps added an additional unknowns must be solved for. In addition the product of albedo and area of the body can be derived from the absolute magnitude of the maxima.

A sample tabulation is shown for the case of the cylinder. For a given value of phase angle and various values of Γ_0, A_0 , there is tabulated the value of the brightness function $F(\Gamma_0, A_0)$, the difference in magnitude for three equally spaced, intermediate points, and the location of the spin axis Γ_1, A_1 . Due to the symmetries of $F(\Gamma_0, A_0)$ inherent in the simple case, the determination of the proper octant for the spin axis would require light curves for several different points across the sky.

In the sample table a 100 or -100 has been printed whenever the magnitude of a quantity of zero intensity is involved. For slopes which are indeterminate, σ was set equal to $\pi/2$. We note that a great variety of light curves are represented, for example at $A_0 = 70^\circ, \Gamma_0 = 80^\circ$ the tumbling cylinder would appear constant which means that the isophote $F(A_0, \Gamma_0)$ is nearly a great circle. There are symmetrical light curves such as $A_0 = 0, \Gamma_0 = \text{anything}$. There are strongly unsymmetrical curves such as $A_0 = 20^\circ, \Gamma_0 = 80^\circ$ or $A_0 = 70^\circ, \Gamma_0 = 10^\circ$. It is noted that for $\phi = 90^\circ$ when the spin axis lies half way between the observer and the sun then $A_0 = 0, \Gamma_0 = 0$ and the variation amounts to .5 magnitude.

In practice the reduction of light curves by means of the above model or the more complex analogues would be best done by means of a least-squares procedure. Since the unknowns in Equations (4) and (6), Γ_0 and A_0 , are explicitly given, the least-squares procedure could be carried out in a straightforward manner. This advantage should carry over into the more complex models.



References

1. J.G. Williams and G.A. McCue, An Analysis of Satellite Optical Characteristics Data, Planetary and Space Science, 14, 839 (1966).
2. R.H. Giese, Attitude Determination from Specular and Diffuse Reflection by Cylindrical Artificial Satellites, Smithsonian Astrophysical Observator Special Report No. 127.

TABLE I: SAMPLE TABULATION FOR CYLINDER"

PHASE ANGLE = 90. DEGREES										
A	0.0	10.	20.	30.	40.	50.	60.	70.	80.	90.
GAMMA = 0.0	0.125000	0.117462	0.095756	0.062500	0.021706	0.0	0.0	0.0	0.0	0.0
	0.500	0.270	0.139	-0.178	-1.138	-100.000	-100.000	-100.000	-100.000	-100.000
	0.900	0.423	0.201	-0.262	-1.411	-100.000	-100.000	-100.000	-100.000	-100.000
	0.300	0.270	0.139	-0.178	-1.138	-100.000	-100.000	-100.000	-100.000	-100.000
	180. 90.0 180. 80.0 180. 70.0 180. 60.0 180. 50.0 90. 90.0 90. 90.0 90. 90.0 90. 90.0									
GAMMA = 1.0	0.125000	0.117579	0.096234	0.063695	0.025660	0.004129	0.001288	0.000757	0.000591	0.000549
	0.512	0.259	0.115	-0.192	-1.336	-1.336	-1.330	-1.484	-1.952	-3.230
	0.901	0.434	0.214	-0.239	-1.233	-2.934	-4.359	-5.274	-5.748	-5.893
	0.312	0.293	0.180	-0.129	-1.118	-3.497	-4.749	-5.038	-4.658	-3.230
	180. 90.0 180. 80.0 184. 70.1 181. 60.3 186. 52.5 122. 66.2 107. 78.5 102. 83.7 101. 87.1 100. 90.0									
GAMMA = 2.0	0.125000	0.117927	0.097731	0.067683	0.035498	0.015113	0.007777	0.005268	0.004317	0.004060
	0.532	0.263	0.118	-0.139	-0.509	-0.801	-0.948	-1.110	-1.385	-1.891
	0.923	0.465	0.249	-0.175	-0.902	-1.805	-2.597	-3.216	-3.596	-3.721
	0.332	0.320	0.220	-0.089	-0.854	-1.967	-2.691	-2.878	-2.561	-1.891
	190. 90.0 189. 80.2 186. 70.5 190. 61.6 161. 56.7 135. 62.9 121. 72.4 114. 79.4 111. 85.0 110. 90.0									
GAMMA = 3.0	0.125000	0.118480	0.100163	0.073944	0.047367	0.028834	0.019233	0.014717	0.012698	0.012117
	0.570	0.262	0.139	-0.068	-0.309	-0.509	-0.654	-0.791	-0.962	-1.207
	0.902	0.519	0.302	-0.078	-0.616	-1.197	-1.719	-2.147	-2.432	-2.534
	0.370	0.369	0.264	-0.026	-0.574	-1.211	-1.639	-1.736	-1.523	-1.207
	190. 90.0 194. 80.4 189. 71.2 180. 63.5 163. 60.1 145. 63.6 132. 70.4 125. 77.3 121. 83.9 120. 90.0									
GAMMA = 4.0	0.125000	0.119177	0.103250	0.081374	0.059812	0.043676	0.033696	0.028110	0.025320	0.024473
	0.594	0.319	0.176	0.003	-0.172	-0.322	-0.443	-0.552	-0.665	-0.795
	0.718	0.605	0.379	0.039	-0.375	-0.792	-1.164	-1.474	-1.689	-1.771
	0.394	0.431	0.319	0.058	-0.340	-0.746	-1.013	-1.059	-0.945	-0.795
	205. 90.0 199. 80.6 193. 72.1 182. 65.5 168. 62.9 153. 65.1 142. 70.3 135. 76.6 131. 83.3 130. 90.0									
GAMMA = 5.0	0.125000	0.119934	0.105563	0.086940	0.071810	0.058349	0.049158	0.043473	0.040425	0.039467
	0.594	0.336	0.231	0.076	-0.063	-0.190	-0.291	-0.378	-0.458	-0.534
	0.720	0.750	0.496	0.179	-0.162	-0.487	-0.774	-1.013	-1.185	-1.252
	0.394	0.520	0.400	0.160	-0.149	-0.438	-0.617	-0.651	-0.605	-0.534
	211. 90.0 206. 80.9 198. 72.9 187. 67.1 174. 65.0 161. 66.5 152. 70.8 145. 76.5 141. 83.1 140. 90.0									
GAMMA = 6.0	0.125000	0.120657	0.107687	0.095782	0.082402	0.071549	0.063693	0.058537	0.055646	0.054717
	0.730	0.510	0.323	0.164	0.029	-0.082	-0.175	-0.252	-0.316	-0.365
	0.791	1.017	0.701	0.373	0.058	-0.226	-0.476	-0.685	-0.836	-0.897
	0.394	0.694	0.541	0.302	0.028	-0.212	-0.323	-0.401	-0.397	-0.365
	221. 90.0 214. 81.0 206. 73.3 194. 68.0 182. 65.9 171. 67.0 162. 70.7 155. 76.2 151. 82.8 150. 90.0									
GAMMA = 7.0	0.125000	0.121252	0.112220	0.101201	0.090707	0.082037	0.075543	0.071128	0.068585	0.067757
	1.101	0.761	0.510	0.316	0.162	0.037	-0.067	-0.153	-0.219	-0.260
	1.230	1.293	1.148	0.746	0.393	0.083	-0.191	-0.425	-0.597	-0.665
	0.394	1.045	0.896	0.580	0.279	0.024	-0.138	-0.229	-0.267	-0.260
	234. 90.0 227. 80.8 218. 72.9 207. 67.2 195. 64.5 183. 65.0 173. 68.4 166. 74.2 161. 81.7 160. 90.0									
GAMMA = 8.0	0.125000	0.121844	0.113867	0.104672	0.096005	0.088785	0.083280	0.079465	0.077235	0.076502
	1.365	1.321	0.963	0.698	0.488	0.309	0.146	-0.007	-0.137	-0.202
	1.510	1.542	1.242	0.907	0.611	0.411	0.244	-0.009	-0.390	-0.533
	0.394	1.301	1.116	0.746	0.477	0.274	0.074	0.003	-0.161	-0.202
	241. 90.0 236. 80.3 230. 71.3 229. 63.6 218. 58.2 204. 56.2 191. 56.5 180. 65.6 172. 76.7 170. 90.0									
GAMMA = 9.0	0.125000	0.121760	0.114433	0.105867	0.097827	0.091114	0.085967	0.082379	0.080272	0.079578
	1.5214	1.424	1.043	0.746	0.477	0.287	0.153	0.064	0.013	-0.184
	1.6700	1.600	1.242	0.907	0.611	0.411	0.244	-0.009	-0.390	-0.490
	0.394	1.5214	1.242	0.907	0.611	0.411	0.244	-0.009	-0.390	-0.490
	250. 90.0 240. 80.0 230. 70.0 220. 60.0 210. 50.0 200. 40.0 200. 30.0 270. 20.0 270. 10.0 180. 90.0									

TIME-VARYING REFLECTION FROM ROTATING
CONVEX SURFACES

Dean O. Carhoun
MITRE Corporation
Bedford, Massachusetts

Time-Varying Reflection from Rotating Convex Surfaces

A method is presented for determining the time variation of the photometric flux density received in the far field by diffuse Lambert reflection from the surfaces of rotating objects of different shapes. The surfaces discussed are restricted to the class of convex quadric surfaces which can be identified with coordinate surfaces of systems of orthogonal, curvilinear coordinates in euclidean 3-space. The relative motion between the object and observer, and object and source is described by rotation with three degrees of freedom. Formulas permitting calculation of the received flux density by routine substitution are presented. The results for some of the more general quadric surfaces can be obtained by simple extension of the results for conical surfaces.

INTERPRETATION OF PHOTOMETRIC
SIGNATURES FROM SATELLITES

M. Hansburg
Goodyear Aerospace Corporation
Akron, Ohio

ABSTRACT

A satellite photometric signature is a record of the variations in intensity of sunlight reflected either diffusely or specularly from an orbiting satellite. The variations in photometric intensity that arise from precessing cylindrical satellites are considered in this paper. Procedures are described for extracting satellite attitude, as a function of time, and satellite size, in terms of a length-times-diameter product, from photometric signatures. Results from the analysis of representative rocket-body signatures are given.

1. INTRODUCTION

a. Usefulness of Optical Data

The measurable characteristics of sunlight reflected from a satellite can provide significant information concerning the satellite. Instantaneous attitude and position, the satellite's size, shape, and exterior coating properties, may all be determined by an analysis of the reflected sunlight. Optical monitoring of satellites is relatively inexpensive, and can be a valuable supplement to radar monitoring.

b. Description of Optical Data

Optical data are acquired through a telescope that tracks the satellite in its transit across the sky. The data can be either photometric signatures or sequences of photographic images on film. Tracking is done before sunrise or after sunset so that the brightness of the sky background is well below that of the satellite. The capability to track optically extends well into the evening hours and may last through most of the night if the satellite is sufficiently high. For example, Echo 1 satellite at about 900 mi can be seen throughout the night at northern latitudes near the period of the summer solstice.

The photometric signature is the recorded analog output of the changes in intensity of the received, reflected sunlight from the orbiting satellite. The satellite (unless it is a uniform sphere) exhibits changes in apparent brightness as it tumbles; or if stabilized, the satellite exhibits changes in apparent brightness as it changes aspect angle with respect to the observer. The photoelectric photometer, when placed at the focus of the telescope, records these changes in brightness as a change in electrical output, which in turn provides a trace or analog of light intensity versus time. This record is calibrated by recording the photometric intensity of stars of known magnitude during a given observational period.

If an image orthicon camera or photographic film is placed at the telescope's focus, an image of the telescope-tracked satellite is obtained.

USAF Avionics Laboratory Observatory at Sulphur Grove, near Dayton, Ohio, first acquired photometric data in mid-1962. Two additional facilities at Cloudcroft, New Mexico (Air Force), and at Hawaii (ARPA) are now being made available. These facilities are described in Reference 1. Goodyear Aerospace recently completed a NASA-sponsored, truck-mounted portable 24-in. telescope for the photometric examination of satellites.^{2*}

Although GAC has analyzed satellite imagery as well as the photometric signature, the emphasis has been placed on photometry. This paper will be restricted to the interpretation of photometric signatures. Techniques will be presented for the determination of attitude and size from the photometric signature of rocket bodies; results of the application of these techniques to representative signatures will also be given.

c. Description of Photometric Signatures

The photometric signature of an orbiting satellite is made up of either specular or diffuse reflection components, or a combination of the two. Typical specular and diffuse signatures for rocket bodies are shown in Figure 1. Specular (mirror-like) reflection from a given satellite surface is observed only if the normal to the surface bisects the angle between the sun-pointing (S) and observer-pointing (O) vectors. The proper specular geometry for a rocket body (cylinder) occurs briefly, twice per tumbling cycle, to yield for each cycle a pair of specular flashes, as in the Agena (upper) signature of Figure 1.

* Superior numbers in the text refer to items in the List of References.

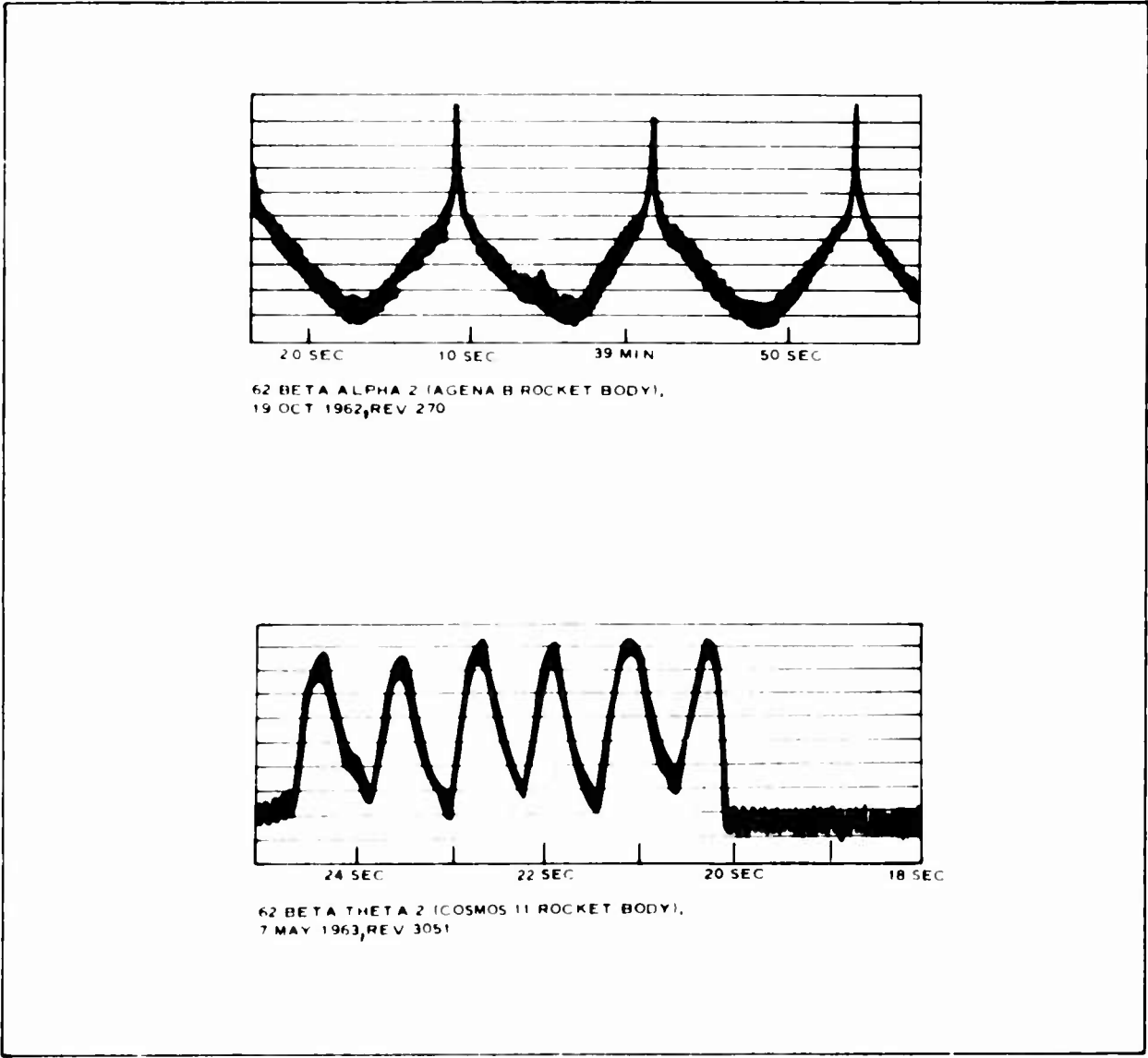


Figure 1 - Typical Photometric Signatures

A diffusely-reflecting surface point may be viewed anywhere along a hemispheric solid angle that is forward of the surface point. Outside this solid angle, the point will be in shadow. Variations in the diffuse signature (the lower signature of Figure 1) occur as portions of the cylinder's illuminated surface enter and leave shadow, and as the cylinder-to-observer aspect angle varies.

d. Interpretation of Photometric Signatures

The variations in the aspect angle or attitude of an orbiting satellite produce (unless the satellite is a uniformly reflecting sphere) corresponding variations in the amplitude of the received photometric signature. The changes in satellite attitude, which result whether the satellite is stable or is tumbling, are identified by matching, in the least-squares sense and over the entire transit, the satellite's photometric signature with a properly generated theoretical equivalent. The attitude history, from which the "best-matched" theoretical signature has been generated, characterizes the attitude history that is associated with the orbiting satellite.

Mathematical models have been developed by Goodyear Aerospace that describe the diffuse and specular reflection from such simple shapes as cylinders, cones, and spheres, and from plates that are flat or have symmetrical curvature. These models are expressed as a function of the to-be-determined satellite attitude and amplitude parameters, and are used to generate the theoretical signatures that are then matched, as described in the previous paragraph, with the acquired experimental signature. The best matches, in the least squares sense, determine values for the desired satellite parameters.

The theoretically generated diffuse signature predicts at each instant of time the intensity of the received diffusely reflected sunlight. However,

the specularly reflected light contribution, because it occurs only briefly at irregularly spaced instants of time, is handled differently. In the specular case, the satellite parameters are used to generate the different attitudes of the vehicle that exist at the times of the received flashes. The generated attitude for each flash is then matched with the corresponding vehicle attitude that is required by specular geometry to generate each flash. The desired parameter set is then determined when the best match has occurred.

The attitude parameter solution in the specular case, since it requires only the measurement of time and is independent of amplitude, will be more accurate than the corresponding diffuse reflection solution. However, since the diffuse albedo is more reliably known, and since the diffuse return represents an averaged reflection from a large portion of the vehicle, the diffuse signature provides a more accurate indication of vehicle size.

The size of the satellite is determined from the now known satellite aspect geometry as a function of the properly calibrated (in terms of stellar magnitudes) amplitude of the photometric signature. In the case of the cylinder, the computed "size" is in reality an albedo-times-length-times-diameter product. If the albedo is known or is assumed from experience obtained with typical spacecraft coatings, then the length-times-diameter product can be determined.

2. MATHEMATICAL MODEL FOR DESCRIPTION OF SATELLITE ATTITUDE

The instantaneous attitudes of a tumbling or precessing satellite are defined by the orientations of the satellite's longitudinal axis \underline{L}_t^* and are determined

* The axis vectors, \underline{L}_t and $\underline{\Omega}$, are assumed to be of unity magnitude.

over the entire transit of the satellite. The assumption is made that the ends of the cylinder do not reflect light and that during the time the satellite is being observed the precession axis and precession angle remain constant. Accordingly, all possible orientations of \underline{L}_t lie on the surface of a conic (see Figure 2), the axis of which is the precession axis $\underline{\Omega}^*$ (with right ascension R_Ω and declination D_Ω). The precession angle is obtained from the scalar product $(\underline{\Omega}, \underline{L}_t)$, namely $\cos^{-1}(\underline{\Omega}, \underline{L}_t)$. Two additional scalars, the rotation period T_p and an initial phase angle Ω_{1r} , are required to determine within this locus of possible positions of \underline{L}_t the exact position at any time t .

A desired attitude or position \underline{L}_t is determined as follows. The rotation of a vector about an axis has been extensively described in the literature (Reference 3, see page 9). The position \underline{L}_t , after a rotation of Ω_t about an axis $\underline{\Omega}$ and from a reference position \underline{L}_0 , is given by

$$\underline{L}_t = \underline{L}_0 \cos \Omega_t + (\underline{\Omega} \times \underline{L}_0) \sin \Omega_t + (\underline{\Omega})(\underline{\Omega}, \underline{L}_0)(1 - \cos \Omega_t) . \quad (1)$$

The rotation angle Ω_t is defined, in terms of the rotation period T_p and an initial phase angle Ω_{1r} , by

$$\Omega_t = \Omega_{1r} + \frac{2\pi t}{T_p} . \quad (2)$$

The reference position \underline{L}_0 lies on the acceptable locus of positions of \underline{L}_t as defined by the given scalar product $(\underline{\Omega}, \underline{L}_t)$.

* The axis vectors, \underline{L}_t and $\underline{\Omega}$, are assumed to be of unity magnitude.

SATELLITE ATTITUDE MODEL

$$\underline{L}_t = \underline{L}_0 \cos \Omega_t + (\underline{\Omega} \times \underline{L}_0) \sin \Omega_t + \underline{\Omega} (\underline{\Omega} \cdot \underline{L}_0) (1 - \cos \Omega_t)$$

$$\Omega_t = \Omega_{1r} + \frac{2\pi t}{T_p}$$

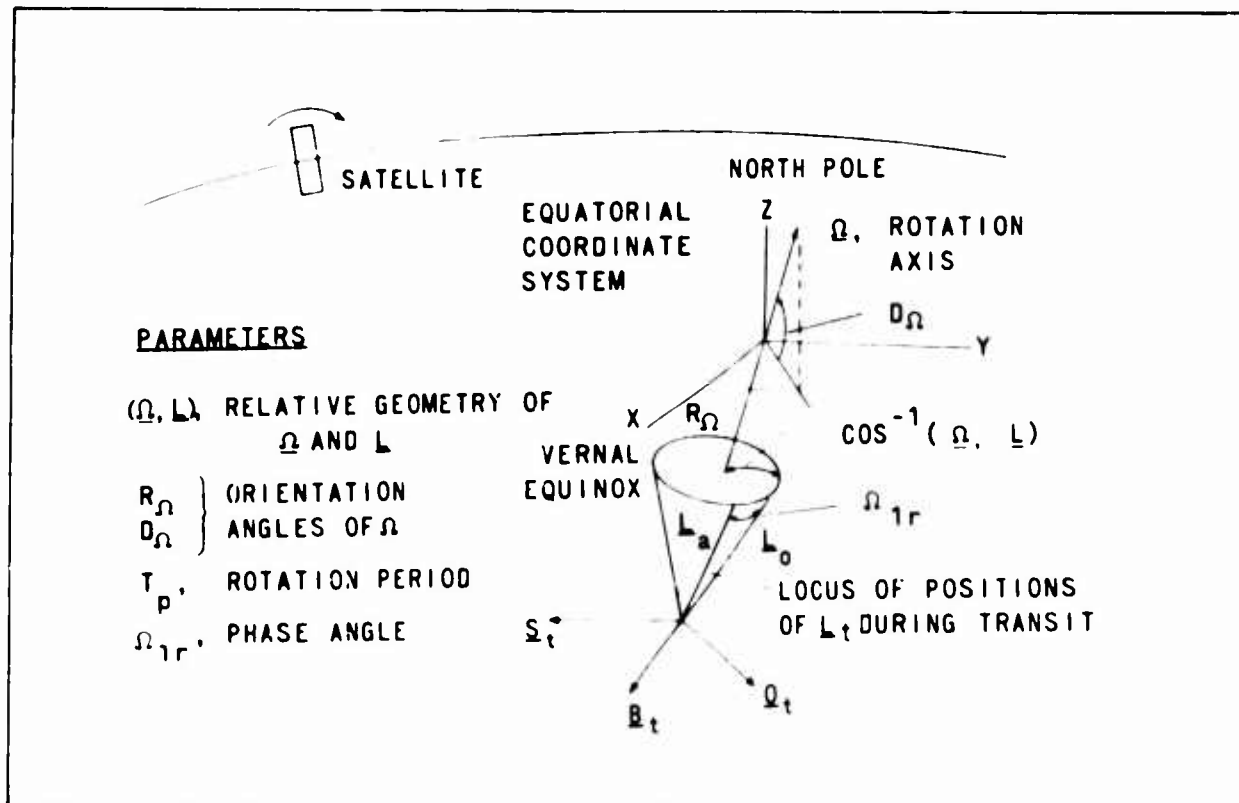


Figure 2 - Satellite Attitude

3. INTERPRETATION OF DIFFUSE SIGNATURES FOR CYLINDERS

a. Mathematical Model of Diffuse Signature

The received illuminance E_d , diffusely reflected from a cylinder, is described⁴ by

$$\frac{E_d}{E_c} = \left(\frac{A_d H_c R_c}{2\pi R_r^2} \right) (\cos \theta_{ot} \cos \theta_{st}) \left[(\pi - X_t) (\cos X_t) + \sin X_t \right] . \quad (3)$$

The terminology entering into the amplitude (the first factor of Equation 3) of the received illuminance ratio E_d/E_c is:

A_d = diffuse albedo of cylinder reflecting surface,

E_c = illuminance (lumens per unit area) from the sun, and

$H_c R_c$ = height and radius, respectively, of the cylinder.

The time-dependent orientation angles (θ_{ot} , θ_{st} , and X_t), which determine the remainder of Equation 3, are related to the instantaneous positions of the cylinder axis vector \underline{L}_t , of the sun-pointing vector (\underline{S}_t), and of the observer-pointing vector (\underline{O}_t). Physically the angles are defined as follows. In a coordinate system (Figure 3) where the axis position \underline{L}_t is made to coincide with the Z (vertical) axis, the angles θ_{ot} and θ_{st} define the elevation, from the coordinate system's horizontal plane, of \underline{O}_t and \underline{S}_t , respectively, while the azimuthal absolute difference angle between \underline{O}_t and \underline{S}_t is given by X_t .

The instantaneous axis position \underline{L}_t is available from Equation 1; the instantaneous positions of the sun (\underline{S}_t) and observer (\underline{O}_t) vectors are determined respectively from tables⁵ and from the orbital elements of the satellite.

SIGNATURE MODEL

$$\frac{E_d}{E_c} = \left(\frac{A_d H_c R_c}{2\pi R_r^2} \right) (\cos \theta_{ot} \cos \theta_{st}) \left[(\pi - X_t) (\cos X_t) + \sin X_t \right]$$

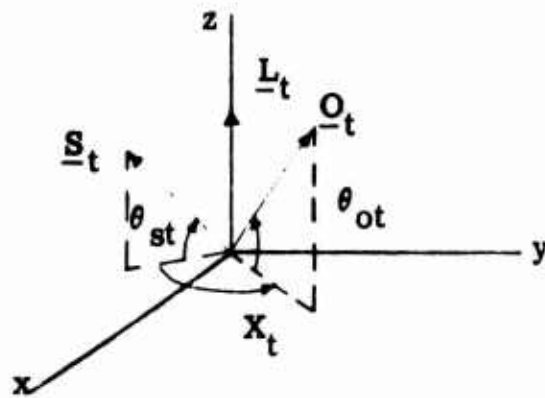


Figure 3 - Signature Model in the Interpretation of Cylinder Diffuse Signatures

b. Matching of Theoretical and Experimental Diffuse Signatures

The variations, that occur in the received photometric diffuse signature, result from the contribution of G_t , defined from Equation 3 as

$$G_t = (\cos \theta_{ot} \cos \theta_{st}) \left[(\pi - X_t) (\cos X_t) + \sin X_t \right]. \quad (4)$$

The following amplitude matching procedure permits extraction of the cylinder's attitude and size from the variations in the signature.

The received photometric signature, covering the entire observed transit of the satellite, is suitably sampled at from 50 to 150 points; and the resulting sample amplitudes are normalized with respect to the amplitude and satellite range that exist at a signature reference point.*

The normalized signature amplitudes J_t are matched with the theoretical amplitudes G_t , each of which is computed from Equation 4 at the time of the corresponding sample point J_t . A least squares matching of the amplitudes G_t and J_t is carried out.

An amplitude J_p , inserted so that the amplitude scales of G_t and J_t can be properly compared, represents the actual contribution of the " G_t " term at the signature reference point.

The various computed values of G_t are functions of the five attitude model parameters described in Item 2. These parameters, in addition to the amplitude scalar, J_p , are varied until a minimum difference between G_t and J_t is achieved. The values of the five attitude parameters and of the signature reference amplitude J_p , that correspond to this minimum, characterize the reflection conditions of the orbiting satellite cylinder, and

*The selection of the signature reference point is arbitrary; usually the maximum-valued signature amplitude is made the reference point.

permit the computation of its attitude and size (in terms of a length times diameter product).

4. INTERPRETATION OF SPECULAR SIGNATURE FOR CYLINDERS

a. Specular Reflection Requirements

Specularly reflected illuminance from a given surface is received if the bisector \underline{B}_t of the sun and observer vectors \underline{S}_t and \underline{O}_t coincides with the normal to the given reflecting surface. Specular reflection from a cylinder thus requires

$$(\underline{L}_t, \underline{B}_t) = 0 \quad . \quad (5)$$

The geometry of specular reflection is illustrated in Figure 4. The intersection of the " $(\underline{L}, \underline{B}) = 0$ " plane and the locus of \underline{L}_t define for each tumbling cycle the two cylinder attitudes (\underline{L}_a and \underline{L}_b in Figure 4) from which specular reflection is observed as a pair of specular flashes. In addition, specular reflection requires that the " $(\underline{L}_t, \underline{B}_t) = 0$ " plane and the \underline{L}_t locus be sufficiently close to one another to intersect.

In a similar manner, the requirements for specular reflection from a conic reflecting surface are determined (see Figure 4).

b. Extraction of Attitude Information, General Method

The times of occurrence of the specular flashes provide an excellent description of the attitude history of the reflecting satellite. For example, as a satellite cylinder moves across the sky, the orientation of the bisector (of \underline{S}_t and \underline{O}_t) vector \underline{B}_t and therefore the required cylinder specular attitudes, \underline{L}_a and \underline{L}_b in Figure 4, are continually changing. The times of specular flash occurrence, which are irregularly spaced to accommodate the continually changing specular attitudes, thus determine the attitude history of the reflecting cylinder and therefore permit the determination of the five attitude parameters.

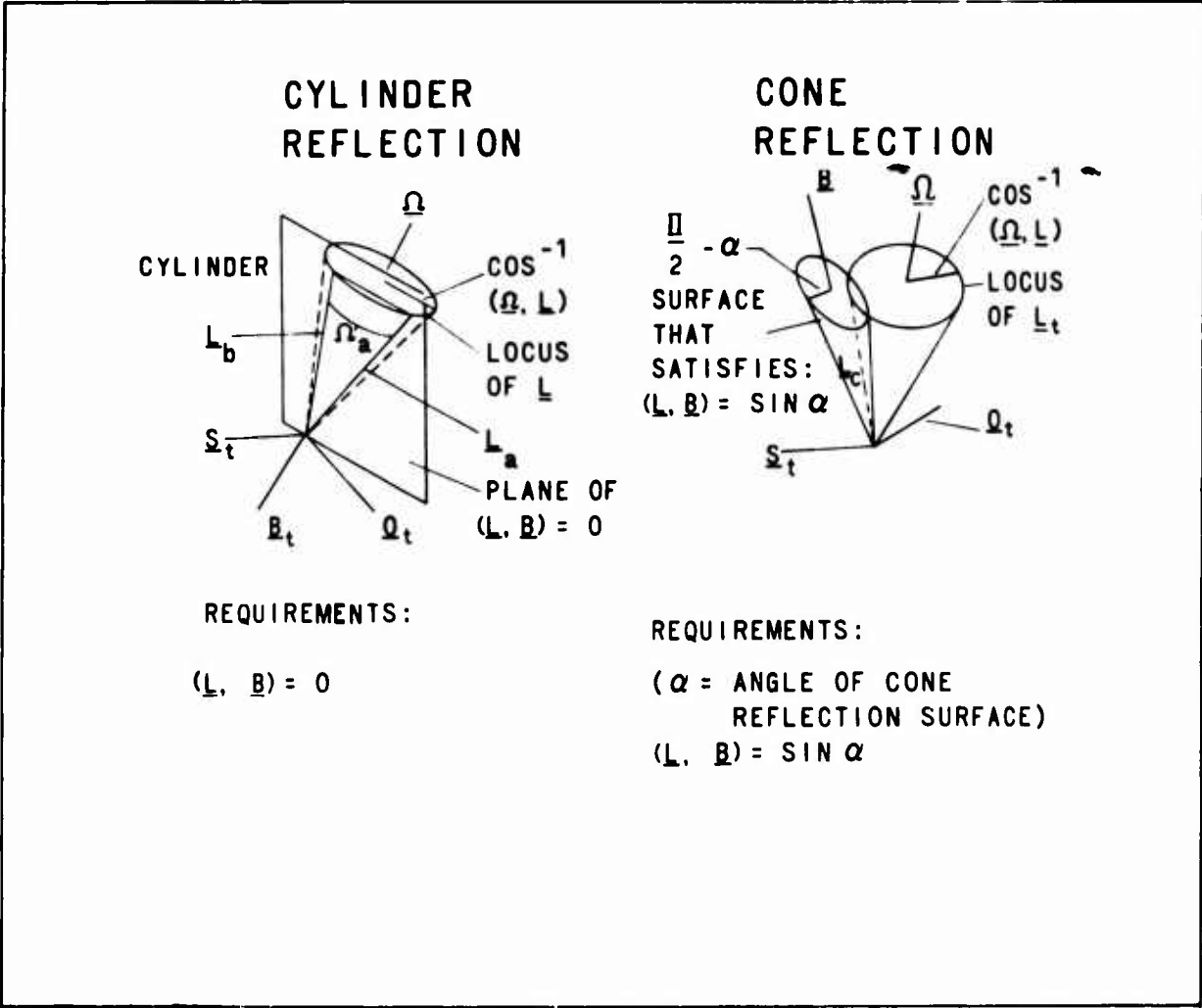


Figure 4 - Specular Reflection Requirements

c. Angular Separation γ_h between Required and Generated Cylinder Attitudes

The matching of the required (\underline{L}_{ah}) and generated (\underline{L}_{th}) cylinder attitudes is accomplished by minimizing the angles γ_h that separate the two cylinder attitudes that occur at each of the specular-flash times. The generated attitude (\underline{L}_{th}) is obtained at time t_h for a given set of five attitude parameters from the attitude Equations 1 and 2. The reference attitude \underline{L}_0 corresponds to the time ($t = 0$) of the first flash.

The required specular flash attitude \underline{L}_{ah} is also obtained from Equations 1 and 2 upon insertion of the constraint, $(\underline{L}_{ah}, \underline{B}_{ah}) = 0$.

The angle γ_h , separating \underline{L}_{th} and \underline{L}_{ah} , lies along the surface of the conic locus of \underline{L}_t and is determined from Equation 1.

The separation angle γ_h is restricted to the range

$$-\pi \leq \gamma_h \leq \pi .$$

d. Evaluation of Cylinder Attitude

The proper set of five attitude parameters, which defines the actual attitude history of the specularly reflecting cylinder, occurs when the required attitude \underline{L}_{ah} and the generated attitude \underline{L}_{th} coincide at all the specular flashes; or γ_h is minimum.

5. MINIMIZATION OF SQUARE DIFFERENCE EXPRESSION

Minimization of the square difference (SD) expressions in the diffuse and specular reflection cases is required to determine the proper values of the five attitude parameters and of the amplitude parameter when its solution is applicable. The adopted minimization procedure is general and applies not only to the two SD expressions already developed for cylinders but can

be used with other expressions of SD to be developed for signatures of other shapes.

The minimization of SD is accomplished in an iterated procedure through proper incrementing of the attitude (and amplitude) parameters. A Taylor's series approximation of SD is used to facilitate the determination of the proper parameter increments at each iteration. Constraints are introduced in the procedure to insure that the increments selected are sufficiently small so that the Taylor's series approximation of SD is reasonably accurate and converges.

6. SIGNATURE ANALYSIS RESULTS

a. Computation of Specular Signature

The specular solution described in Item 4 has been applied to eight pairs of specular flashes from an Agena rocket body (62 β a2) signature that was obtained during a 22 July 1965 orbit.

Computer solutions of the specular signature require initial estimates of the input parameters, of which all but the two orientation angles of $\underline{\Omega}$ can be furnished. Ten arbitrary values of $\underline{\Omega}$ that are randomly spaced within the equatorial coordinate system are inserted as initial estimates of $\underline{\Omega}$. One half of the above initial estimates of $\underline{\Omega}$ converged to two near-zero minimums of SD (Item II of Figure 5) - Solution A and Solution B; the other half converged to local minimums and were discarded.

Other data are necessary to resolve the ambiguity between the two near-zero Solutions A and B. In the present case, Solution B was determined to be correct through use of specular flashes from a conic reflecting surface portion of the rocket body. The spacing between these flashes provided an approximate but independent solution of $\underline{\Omega}$ (see Item III of Figure 5).

I. INPUT PARAMETER VALUES							
ALL TRIALS: $(\Omega, L) = 0, T_p = 0.60358, \Omega_{1r} = 0$							
TRIALS 1 TO 4: $R_\Omega = 0, 120, 180, 240; D_\Omega = +45 \text{ DEG}$							
TRIALS 5 AND 6: $R_\Omega = 90, 270; D_\Omega = -45 \text{ DEG}$							
TRIALS 7 THROUGH 10: $R_\Omega = 0, 90, 180, 270; D_\Omega = 0 \text{ DEG}$							
II. SPECULAR SIGNATURE SOLUTIONS:							
SOLUTION	SUCCESSFUL TRIALS	(Ω, L)	R_Ω (DEG)	D_Ω (DEG)	T_p	Ω_{1r} (DEG)	$\sqrt{\langle \gamma_h^2 \rangle}$ (DEG)
A	2,3,4	0.00039	233.96	59.20	0.60261	0.01	0.143
B	8,9	0.00002	119.74	-13.03	0.59225	0.192	0.563
III. INDEPENDENT SOLUTION USING CONIC FLASHES							
1. $(\Omega, L) = 0, R_\Omega = 117.4 \text{ DEG}, D_\Omega = -7.5 \text{ DEG}$							
2. COMPUTED ROCKET BODY CONE ANGLE = 16 DEG							

Figure 5 - Computation of Agena Rocket Body (62βα2) Specular Signature (Input Signature Data, USAF Sulphur Grove Observatory)

Additional sources of data that could be used to resolve the solution ambiguity are available from the accompanying diffuse reflection portion of the vehicle's signature or from the specular data from other orbits of the same vehicle.

The last column in Item II gives an estimate of the average angular deviation γ_h , between the required and generated attitudes of \underline{L}_t . The deviation of 0.563 deg found for Solution B is equivalent to an average uncertainty in the times of the flashes of about 0.05 sec.

b. Diffuse Reflection Computer Program Results

Diffuse reflection signatures of several orbits of two rocket bodies were analyzed; simultaneous matching of three or four selected cycles from each signature was obtained.

The solutions for the attitude parameters ($\underline{\Omega}$, \underline{L}), R_Ω , D_Ω , and T_p (see Item 2) are shown in Table I for each rocket body. The resulting value of SD, when the minimal solution is obtained, provides an estimate of the degree of mismatch between theory and experiment.

The actual theoretical and experimental sample point values are plotted in Figures 6 and 7.

c. Error Analysis of Diffuse-Reflection Computations

An error analysis of the diffuse-reflection computations has been carried out.

The following input errors were considered in the error analysis: $\Delta E_d/E_d$, photometric signature amplitude; $\Delta R_r/R_r$, satellite range; Δt , time of photometric measurements; and ΔR_o and ΔD_o the right ascension and declination of the observer vector. Expressions have been obtained that describe the effects of these errors upon the computed orientations of the cylinder axis, \underline{L}_t , and of the tumbling axis $\underline{\Omega}$ and upon the computed cylinder size or

Table I - Diffuse Reflection Computer Program Results

Rocket body	Date of orbit	Precession		Rotation axis orientation		Mismatch $\sqrt{\text{SD}}$
		angle (deg) $\cos^{-1}(\underline{\Omega}, \underline{L})$	Rotation period (sec)	Right ascension (deg)	Declin- ation (deg)	
Satellite 1092	3 Dec 1966	90.29	10.2468	283.480	7.855	0.088
	24 Sep 1966	87.33	9.2552	256.027	5.679	0.058
	8 Sep 1966	89.61	9.0486	236.357	-15.417	0.042
Satellite 1950	9 Mar 1966	89.98	0.43986	83.12	-77.87	0.075

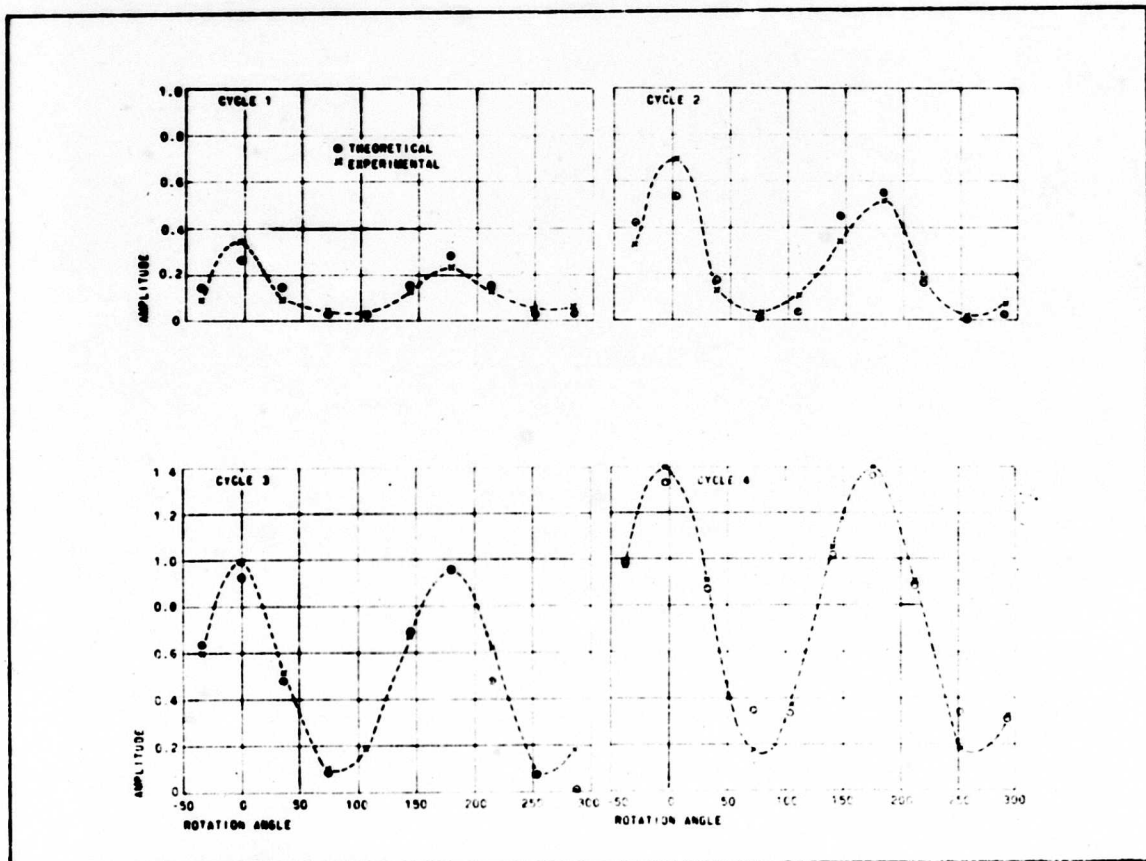


**Figure 6 - Comparison of Experimental and Theoretical Diffuse Cycles.
Satellite 1092 (3 Dec 1966 Orbit) (Input Signature Data,
USAF Sulphur Grove Observatory)**

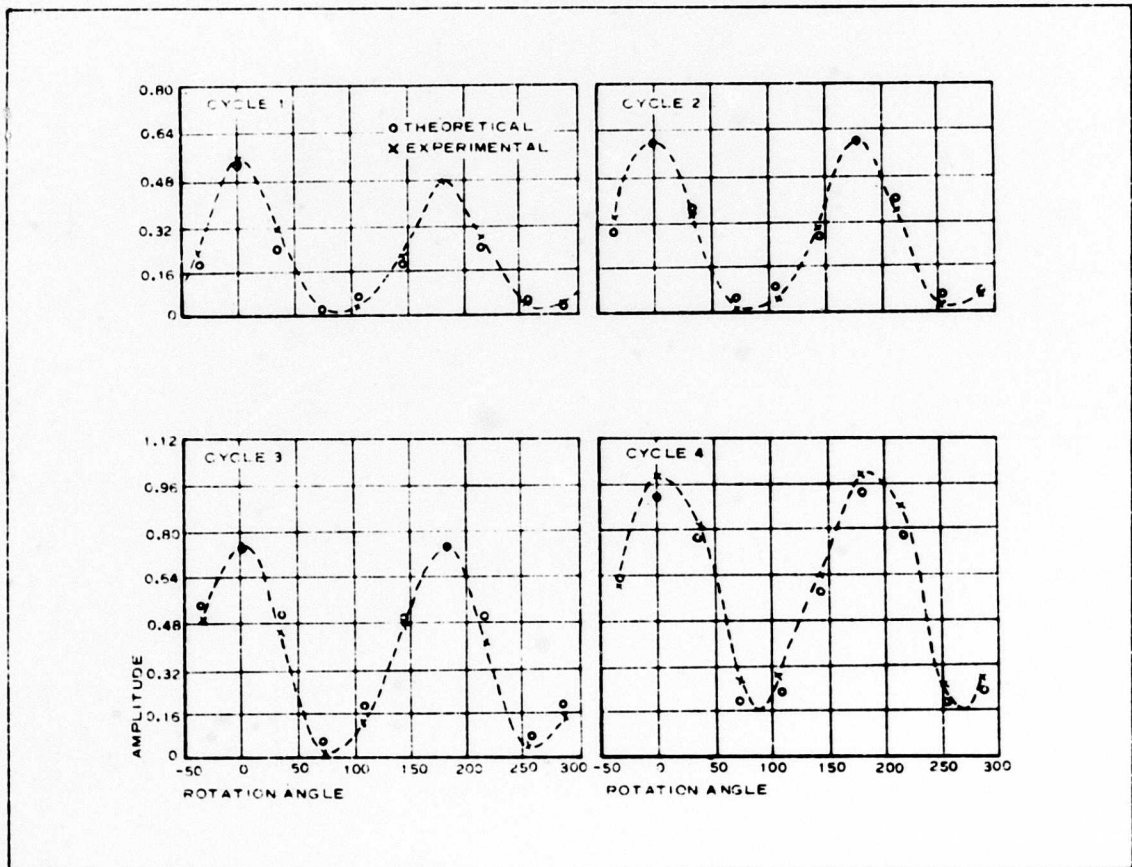


Figure 7 - Comparison of Experimental and Theoretical Diffuse Cycles. Satellite 1950 (Input Signature Data, USAF Sulphur Grove Observatory)

length times diameter product. The orientation inaccuracies, $\Delta \underline{L}_t$ and $\Delta \underline{\Omega}$, are given as the degrees of separation between the corresponding true and "noisy" vectors; while the size inaccuracy appears as $\Delta S/S$.

The above three errors ($\Delta \underline{L}_t$, $\Delta \underline{\Omega}$, and $\Delta S/S$) have been determined for the four diffuse-signatures analyzed in Table I, and are tabulated in Table II. The assumed distribution of input errors also appears in Table II.

7. CONCLUSIONS AND FUTURE EFFORTS

A technique for analyzing the specularly and diffusely reflecting optical signatures of cylindrical satellites, to provide satellite attitude and size (as a length-times-diameter product), has been presented.

Payloads in general have shapes that may be derived, singly or in combination, from cones, spheres, and plates (curved or flat) as well as from cylinders. The technique of matching corresponding experimental and theoretical data samples may be extended to signatures received from such payloads. Also, the analysis of stabilized bodies, in which the observed aspect angle of the stabilized body is varying continually because of the satellite's orbital motion, is possible with this technique. Future efforts will be directed toward obtaining the necessary computer programs, based upon the derived theoretical models, that will permit the extraction of useful information from the signatures of such payloads.

Consideration should be given to other information available in the optical signature. For example, the optical signature can be used to monitor the in-flight variations in albedo of a given satellite reflection coating. If the dimensions of the satellite are known, the albedo of its reflection coating may be determined very accurately through an analysis of the satellite's optical signature. Thus, the in-flight performance and changes with exposure time of various satellite coatings may be determined by painting

Table II - Accuracies of Diffuse Computer Program Results

Rocket body	Date of orbit	Axis orientation errors*		Size error*, †	
		ΔL_t (deg)	$\Delta \Omega$ (deg)	$\frac{\Delta S}{S}$	W^*
Satellite 1092	3 Dec 1966	2.02	1.94	0.046	1.64
	24 Sep 1966	2.42	2.29	0.059	1.25
	8 Sep 1966	1.04	1.04	0.031	0.925
Satellite 1950	9 Mar 1966	1.23	1.08	0.038	1.21

* The tabulated errors are based upon the following assumed distribution of input errors: $\Delta E_d/E_d = .10$, $\Delta R_r/R_r = .01$, $\Delta t = .002$ seconds, and $\Delta R_o = \Delta D_o = .015$ radians. The input error distribution is weighted by the value of W , which is obtained from the actual degree of mismatch between the theoretical and experimental signature. A unity value for W would indicate a correspondence between the assumed input errors and the output mismatch.

† The size error does not include the uncertainty that exists in the value assumed for the diffuse-reflection albedo.

rocket bodies that are used for other purposes and observing these bodies photometrically over periods of months or years.

8. LIST OF REFERENCES

1. "Restoration of Atmospherically Degraded Images" Volume I. Woods Hole Summer Study, July 1966, National Academy of Sciences; National Research Council; Washington, D. C.
2. GER-12703S1, S2: Ground-Based Photometric Surveillance of the Passive Geodetic Satellite (U). Akron, Ohio, Goodyear Aerospace Corporation, 15 July 1966.
3. Whittaker, E. T.: Analytical Dynamics (U). 4th Edition, Cambridge, England, University Press, 1937.
4. Stiles, G. J.: Prediction of Apparent Magnitude of Distant Missiles in Sunlight. Memorandum Report No. 1008, Aberdeen Proving Ground, Maryland, Ballistic Research Laboratories, June 1956.
5. Nautical Almanac. U.S. Naval Observatory, U.S. Government Printing Office, Washington, D. C.

9. ACKNOWLEDGEMENTS

Thanks are given to Messrs. K. E. Kissell and R. C. Vanderburgh of the USAF Sulphur Grove Observatory for their making available all the signature data that were analyzed in this report. Special appreciation is due Mr. Kissell for giving so generously of his time during discussions that stimulated many of the ideas used in this report.

Early phases of the study reported in this paper were performed under contract to the Air Force.

INVESTIGATIONS INTO A METHOD FOR THE
OPTICAL ESTIMATION OF THE ROTATION AXIS
OF ARTIFICIAL SATELLITES

R. H. Giese
University of Bochum
Bochum, W. Germany

ROYAL AIRCRAFT ESTABLISHMENT

Library Translation 1212

January 1967

INVESTIGATIONS INTO A METHOD FOR THE OPTICAL ESTIMATION OF THE
ROTATION AXIS OF ARTIFICIAL SATELLITES

(UNTERSUCHUNGEN ÜBER EINE METHODE ZUR OPTISCHEN BESTIMMUNG DER
ROTATIONSACHSE KÜNSTLICHER SATELLITEN)

by

R. H. Giese

Deutsche Gesellschaft für Ortung und Navigation E.V. Düsseldorf.

Technical paper presented at the meeting of Committee 7

on 10th November 1964 in Berlin

Translated by

Barbara Crossland

Translation edited by

D. W. Scott

TRANSLATION EDITOR'S SUMMARY

A method is described for determining the orientation of the rotation axis of a spin-stabilized satellite, fitted with reflecting surfaces parallel to the axis, from observations of flashes of reflected sunlight. The conditions in which such flashes may be observed are set out, and some typical visibility patterns have been worked out and are shown in the form of maps.

The errors to be expected are discussed in detail, and for most cases the direction of the spin axis may be determined to within $\pm 0.5^\circ$.

<u>CONTENTS</u>		<u>Page</u>
1	INTRODUCTION	3
	1.1 Techniques for determining the orientation in space of artificial satellites	3
	1.2 Co-ordinate systems, symbols, conversion formulae	5
2	DETERMINING THE ORIENTATION IN SPACE	8
	2.1 Determining the normal to the reflecting surface	8
	2.2 Determining the axis of rotation	9
3	VISIBILITY OF LIGHT FLASHES	10
	3.1 Reflection cone	10
	3.2 A sufficient condition for the avoidance of reflection flashes	11
	3.3 Conditions for the appearance of light flashes	13
	3.4 Programme for the calculation of flash curves	14
	3.5 Results	15
4	ACCURACY OF THE TECHNIQUE	17
	4.1 Errors in the normal to the reflecting surface	17
	4.2 Errors in the determination of the axis	18
	4.3 The normal angle	20
	4.4 Effect of the finite diameter of the sun's disc	23
5	CONCLUSIONS	28
	Acknowledgments	28
	Tables 1-6	29-35
	References	36
	List of Illustrations	38
	Illustrations	Figures 1 - 12
	Detachable abstract cards	-

1 INTRODUCTION

1.1 Techniques for determining the orientation in space of artificial satellites

For numerous problems in space research, it is necessary to control actively, or at least to establish passively, the orientation in space of the satellites used. In the case of large astronomical satellites such as the American Orbiting Astronomical Observatory, it is aimed to achieve, where optical orientation in relation to reference stars is concerned, an active control of the position of the space vehicle and a stability of the adjustment of the instruments to within ± 0.1 second of arc. Unlike these heavy satellites, with their complicated position-control systems, small satellites are spin-stabilized by rotation about their axis with the greatest moment of inertia. As a result of the forces exerted on the satellites by the earth's magnetic field and the gradient of the gravitational field, the axis of rotation precesses slowly. For the satellites Explorer IV and Explorer XI, which, like propellers, rotate about a lateral axis, the direction of the axis changes by about 10° per day^{11, 12}. On the other hand, in the case of satellites Tiros I (Ref.1), Explorer VIII (Ref.13), Telstar I (Ref.9) and Explorer VII (Ref.13), the average precession rate of the rotation axis is only about 3° (Tiros) to 0.2° (Explorer VII) per day. The satellites last mentioned are so constructed and balanced that their axis of symmetry, which is also the axis of the greatest moment of inertia, affords a stable, nutation-free (nutation damping) rotation. The spatial orientation of such a satellite is determined by the direction of the axis of rotation and by the angle of rotation in relation to a fixed reference direction in the plane of rotation. The following devices are frequently used to obtain information concerning these factors:

(a) Horizon sensors

These devices respond to the difference in radiation intensity between the background of the sky and the earth's surface (or atmosphere). They rotate with the satellite and indicate, through a telemetry system, the moment at which their line of sight points to the boundary line between earth and sky. This direction can, in practice, be measured to an accuracy of $\pm 2^\circ$; however, an accuracy of $\pm 0.1^\circ - 0.2^\circ$ is obtainable in principle^{10, 7}.

(b) Solar-aspect measuring devices

These devices work on a photoelectric principle, and give the angle between the direction of the sun and a reference direction of the satellite. Using this principle, the accuracy of angular measurements is, for Explorer VIII, about $\pm 1^\circ$ (Ref.13) and for Telstar I, about $\pm 0.5^\circ$ (Ref.9).

(c) Television cameras

With satellites, such as weather satellites, which carry television cameras on board, it is possible to deduce the position of the camera or satellite axis from the positions of known geographical points on the television picture. The accuracy of the estimate of this direction for Tiros I is a few degrees⁴.

(d) Antennae with directional characteristics

If the satellite has a transmitting antenna with non-isotropic characteristics, field strength variations occur at the receiver which have a period corresponding to the natural rotation of the satellite. As a result of this phenomenon, Naumann was able to estimate the rotation axis of Explorer IV (rotating dipole) to within $\pm 20^\circ$ (Ref.11) and that of Explorer XI to within $\pm 3^\circ$ (Ref.12).

(e) Reflecting surfaces

If the sun's light is reflected by mirrors on the satellite to an observing station, information can be gained regarding the position of the normals to the reflecting surface from the flash of light reflected; on an astronomical scale of brightness, this reflected light is several times greater than the light reaching the observer in other ways. The present paper deals with a technique based on this principle.

The possibility of estimating the orientation of a satellite using the reflection law has already been investigated (in 1957) by Davis and others³. Their technique, however, was at first applied only to satellites of cylindrical shape, whose rotation is not discernible and which have a reflective coating, and to cases involving practically simultaneous observation by two stations. The problem of estimating the axis of rotation of such a satellite by rotation about an axis perpendicular to the axis of symmetry was solved by Zessewich¹⁹, also by Notni and Oleak¹⁴ for the booster rocket of Sputnik III (accuracy 5°). A system with reflectors, whose normals are inclined at 68° and 95° to the axis of symmetry, was recently satisfactorily developed (accuracy $>0.5^\circ$) for the communication satellite Telstar (Hill 1963, Ref.8). With this system, the position of the axis of rotation can be calculated from the times of two flashes of reflected sunlight as sections of two cones. Working independently, Giese, at the Smithsonian Astrophysical Observatory (Cambridge, Mass.), during investigations into the possibility of estimating the spatial orientation from Baker-Nunn camera photographs or from visual observations⁵ found a similar, but simpler, technique⁶. If one furnishes a spin-stabilized satellite with one or more mirrors, in such a way, that the normal to the mirrors lies perpendicular to the axis of rotation, the latter can be determined as lines of intersection

of two planes, providing that the observed position of two (suitable) reflection flashes in relation to the stellar background is known. The times of the observations need be known only approximately and, depending on the precession velocity of the axis of the satellite, may be separated by hours or days. The technique will be described again briefly in Section 2. The main point of the investigation here however, concerns the positions of the sun, satellite orbit and satellite axis at which, in general, light flashes are to be expected when these positions are observed from the earth (Section 3) and the accuracy with which the position in space of the rotation axis can be determined (Section 4) under different geometrical conditions. The estimation of the angle of rotation and the period of rotation has already been dealt with in other papers^{1,4,5}, and will not be discussed further in this investigation.

1.2 Co-ordinate systems, symbols, conversion formulae

Since it is necessary in this work to use co-ordinate systems when carrying out calculations, let us first summarize the systems used, the definitions and conversion formulae.

Co-ordinate systems:

The equatorial system (Fig.1)

The equatorial system is an inertial cartesian system, rotating clockwise in relation to the direction of its axis, with the unit vectors $\vec{C}_1, \vec{C}_2, \vec{C}_3$. The equatorial plane is parallel to the datum plane bounded by \vec{C}_1, \vec{C}_2 ; \vec{C}_1 points towards a fixed, particular direction in this plane (vernal equinox) and \vec{C}_3 is directed towards the celestial north pole. A polar co-ordinate system, with the direction angles α (right ascension, here in degrees or radians) and δ (declination) is associated with the equatorial system. According to whether the origin of the system is at the centre of the earth, at the place of observation or at the centre of mass of the satellite, the system is termed a geocentric or topocentric one or one referred to the satellite.

The orbital system (Fig.2)

The orbital system has as its datum plane the orbital plane of the satellite. The position of this plane in relation to the equatorial plane is fixed by the angle Ω (right ascension of the ascending node) and i (inclination). The unit vectors of the corresponding cartesian system are $\vec{C}'_1, \vec{C}'_2, \vec{C}'_3$ (clockwise-rotating system). \vec{C}'_1 then points to the ascending node and \vec{C}'_3 to the northern celestial hemisphere. In a manner analogous to that described above, angles of direction α' and δ' , corresponding to $\vec{C}'_1, \vec{C}'_2, \vec{C}'_3$ are

associated with the orbital system. The angle u' (corresponding to α') is used specifically to indicate the position of the satellite in the orbit. The origin of the orbital system is the centre of the earth.

The spin axis system (see Fig.6)

The spin axis system has as its datum plane the plane in which the natural rotation of the satellite occurs. Its axis unit vectors are \vec{C}_1'' , \vec{C}_2'' , \vec{C}_3'' (cartesian system). \vec{C}_1'' points towards the ascending node between the celestial equator and the plane of rotation of the satellite; \vec{C}_3'' points in the direction of the spin axis. If, during any period of time considered any precession and nutation of the spin axis can be disregarded, then the system \vec{C}_1'' , \vec{C}_2'' , \vec{C}_3'' can, within this time interval, be considered fixed in space relative to the direction of its axes. The origin of the spin axis system is the centre of the satellite.

The auxiliary plane system

This cartesian system is fixed by the unit vectors \vec{E}_1 , \vec{E}_2 , \vec{E}_3 , and has as its datum plane a plane normal to the position vector from the centre of the earth to the satellite. \vec{E}_3 points in the direction of this vector. \vec{E}_1 has the same direction as that of the component of the axis vector of the satellite which lies in the datum plane. Further details are given in Section 4.4.

Definitions

Vectors will always be indicated by arrows written above their symbols. Unit vectors will be written in large letters, other vectors in small ones. Components of vectors will be represented by the letters X, Y, Z, for unit vectors, by x, y, z, in other cases. Above or below is indicated the characteristic symbol for the vector or the co-ordinate system. No apostrophe signifies an equatorial system, the symbol ' an orbital system and the symbol '' a spin axis system.

The following vectors are used particularly frequently (Fig.3):

- \vec{x} (unit vector \vec{X} ; value r)
position vector from the centre of the earth to the satellite;
- \vec{x}_B (unit vector \vec{X}_B ; value ρ)
vector from the observer to the satellite;
- \vec{x}_R (unit vector \vec{X}_R ; value R)
vector from the centre of the earth to the observer;

\vec{X}_0 Unit vector, from satellite to sun

$\vec{X}_A \equiv \vec{C}_3$ Unit vector in the direction of the spin axis, independent of the direction of rotation of the satellite in the hemisphere facing the sun;

\vec{A} Unit vector with the direction of the vector of the angular velocity of the spin motion. Depending on the direction of rotation, known from the launching conditions,

$$\vec{A} = \vec{X}_A \text{ or } \vec{A} = -\vec{X}_A$$

Conversion formulae:

For the conversion of the equatorial system into an orbital one, the following equation applies:-

$$\begin{pmatrix} x' \\ y' \\ z' \end{pmatrix} = \begin{pmatrix} \cos \Omega & \sin \Omega & 0 \\ -\sin \Omega \cos i & \cos \Omega \cos i & \sin i \\ \sin \Omega \sin i & -\cos \Omega \sin i & \cos i \end{pmatrix} \begin{pmatrix} x \\ y \\ z \end{pmatrix} \quad (1)$$

The components of the vector \vec{x} are in the orbital system:-

$$\begin{pmatrix} x' \\ y' \\ z' \end{pmatrix} = \begin{pmatrix} r \cos u' \\ r \sin u' \\ 0 \end{pmatrix} \quad (2)$$

in the equatorial system:-

$$\begin{pmatrix} x \\ y \\ z \end{pmatrix} = \begin{pmatrix} r \cdot (\cos u' \cos \Omega - \sin u' \cos i \sin \Omega) \\ r \cdot (\cos u' \sin \Omega + \sin u' \cos i \cos \Omega) \\ r \cdot \sin u' \sin i \end{pmatrix} \quad (3)$$

A unit vector in the direction defined by α and δ has the components:-

$$\begin{pmatrix} X \\ Y \\ Z \end{pmatrix} = \begin{pmatrix} \cos \delta \cos \alpha \\ \cos \delta \sin \alpha \\ \sin \delta \end{pmatrix} \quad (4)$$

2 DETERMINING THE ORIENTATION IN SPACE

2.1 Determining the normal to the reflecting surface

In Fig.4 let \vec{x}_B be the vector from the observer to the satellite and let \vec{x}_0 be the unit vector from the satellite to the sun (see 1.2). If reflection of the sunlight is observed in a reflecting element of the satellite surface, then, on the basis of the laws of reflection, a vector \vec{n} at right angles to the reflecting surface can be determined. This is given by:-

$$\vec{n} = -\vec{x}_B + \vec{x}_0, \quad (5)$$

since \vec{n} lies in the plane of $-\vec{x}_B$ and \vec{x}_0 and, in addition, halves the angle included by these two unit vectors. The unit vector in the direction of \vec{n} will, in future, be denoted by \vec{N} .

The vector \vec{x}_0 can, for the time of the observation, be calculated from the vector from the centre of the earth to the sun and from the geocentric position vector \vec{x} from the centre of the earth to the satellite. For earth satellites, however, a very close approximation can be obtained by substituting solely the geocentric unit vector to the sun, given in astronomical ephemerides. The resulting deviation in direction for satellites at a distance of 1.1, 2.0, or 10 earth-radii from the centre of the earth is only 9.6, 18 or 88 seconds of arc respectively. If only the time t_1 of a reflection flash is recorded, the unit vector \vec{x}_B can be found from the known vector $\vec{x}_R(t_1)$ from the centre of the earth to the observer and from $\vec{x}(t_1)$ with the help of orbital determination programmes:-

$$\vec{x}_B = \frac{\vec{x}(t_1) - \vec{x}_R(t_1)}{|\vec{x}(t_1) - \vec{x}_R(t_1)|} \quad (6)$$

It is much simpler mathematically to calculate \vec{x}_B directly from photographs or visual observations of the position of the reflection flash relative to known reference stars in the sky. From the observed angular directions α_B and δ_B of the reflection flash in the topocentric equatorial system, one obtains in cartesian equatorial co-ordinates:-

$$\vec{x}_B = \begin{pmatrix} \cos \delta_B \cos \alpha_B \\ \cos \delta_B \sin \alpha_B \\ \sin \delta_B \end{pmatrix} \quad (7)$$

\vec{N} can then be calculated using equation (5) and it is assumed from now on that this is known.

2.2 Determining the axis of rotation

For the practical estimation of the rotation axis of a satellite, the cases represented in Figs.5 and 6 may be of particular importance. The first of these figures illustrates the geometrical conditions for the case of an elongated cylinder rotating about its transverse axis (tumbling motion) with reflecting plane surfaces; the second figure represents a squat cylinder rotating about the axis of symmetry (spinning motion) which has a plane mirror fixed to its casing. The first example corresponds in principle to the motion of a satellite such as Explorer XI, the second example to a type such as Tiros. If \vec{A} is to be calculated for such a satellite from reflection flashes, one observation alone is not sufficient. The condition $\vec{N} \perp \vec{A}$ gives only one plane, that in which A lies. In order to determine the axis of rotation itself, a second observation must be made in order to obtain a further normal vector \vec{N}_2 ($\vec{N}_1 \neq \vec{N}_2$), which fixes another plane through the axis of rotation, and hence A as the intersection line of the two planes. This gives:-

$$\vec{A} = \pm \frac{[\vec{N}_1, \vec{N}_2]}{|[\vec{N}_1, \vec{N}_2]|} \quad (8)$$

(see 1.2 for choice of sign). Of course, when deciding on the times at which observations are to be made, care should be taken to ensure that the time interval $\Delta t = t_2 - t_1$ between the two flash observations taken is sufficiently small for any precession of the spin axis to be negligible. If Δt is of the order of a few periods of rotation, this provision becomes a rule, (c.f. 1.1).

From the angular directions α_{B1} , δ_{B1} and α_{B2} , δ_{B2} of the reflection flashes directly observed in the topocentric equatorial system, one obtains:-

$$[\vec{n}_1, \vec{n}_2] = \begin{vmatrix} \vec{C}_1 & \vec{C}_2 & \vec{C}_3 \\ X_{Q1} - \cos \delta_{B1} \cos \alpha_{B1} & Y_{Q1} - \cos \delta_{B1} \sin \alpha_{B1} & Z_{Q1} - \sin \delta_{B1} \\ X_{Q2} - \cos \delta_{B2} \cos \alpha_{B2} & Y_{Q2} - \cos \delta_{B2} \sin \alpha_{B2} & Z_{Q2} - \sin \delta_{B2} \end{vmatrix} \quad \dots (9)$$

and

$$\vec{A} = \pm \frac{[\vec{n}_1, \vec{n}_2]}{|[\vec{n}_1, \vec{n}_2]|} \quad (10)$$

When only moderate accuracy is required (± 30 minutes of arc), it is sufficient to take, from a map of the stars, (e.g. Bonner catalogue), the observed positions of two appropriate reflection flashes, and to substitute for vectors X_{01} and X_{02} the geocentric unit vector to the sun for time t_1 and t_2 given in ephemerides. Since this vector varies in direction only by about 2.5 seconds of arc per minute and since t is not otherwise necessary for evaluating equation (9), only an approximate (\pm a few minutes) knowledge of the observation time is necessary. For the determination of \vec{A} from measurements of the direction of the reflection flashes, the instrumental expenditure is limited to a telescope, a map of the stars, a table of the sun from an astronomical almanac and a pocket watch. Even the simple mathematical evaluation of equation (9) can be carried out directly by a smaller station, such as that set up by an expedition. On the other hand, to determine \vec{A} from equation (6), not only is accurate measurement of the times t_1 and t_2 respectively of the reflection flashes necessary, but also the calculation of the orbit $\vec{x}(t_1)$ must be carried out⁸.

3 VISIBILITY OF LIGHT FLASHES

3.1 Reflection cone

For the spin axis system (see 1.2) illustrated in Fig.6, the reflection condition of equation (5) gives:-

$$\vec{n} = \begin{pmatrix} \cos \delta_0'' \cos \alpha_0'' - \cos \delta_B'' \cos \alpha_B'' \\ \cos \delta_0'' \sin \alpha_0'' - \cos \delta_B'' \sin \alpha_B'' \\ \sin \delta_0'' \quad \quad \quad - \sin \delta_B'' \end{pmatrix} \quad (11)$$

Since, with the orientation considered in this paper, the reflecting surface \vec{n} is always perpendicular to \vec{X}_A , the component of \vec{n} in the direction of \vec{C}_3'' disappears. Then:-

$$\sin \delta_B'' = \sin \delta_0'' \quad (12)$$

so that, on the basis of the geometrical conditions defined in Fig.6, clearly $\delta_B'' = \delta_0''$. From the relationship between the two other components:

$$\tan \alpha_n'' = \frac{\sin \alpha_0'' - \sin \alpha_B''}{\cos \alpha_0'' - \cos \alpha_B''} \quad (13)$$

Thus, for each illuminated position α_n'' of the mirror which rotates with the satellite, there is a corresponding reflection beam with the angular directions α_B'' and δ_B'' . During the rotation of the satellite, α_n'' and hence α_B'' vary periodically with time, whereas $\delta_B'' = \delta_\theta''$ and α_θ'' remain constant. Since the dimensions of the satellite can be disregarded in comparison with ρ , the totality of all reflected rays lies in very close approximation to the part of the surface of a double cone which is turned away from the sun; the generator of this double cone forms an angle δ_θ'' with the plane of rotation and its vertex lies at the centre of the satellite. The semi-vertex angle $(90^\circ - \delta_\theta'')$ of the cone then corresponds to the angle between \vec{X}_A (see Section 1.2) and \vec{X}_θ . This angle will, in future, be referred to as β and the corresponding cone formed from the reflected rays will be called the "reflection cone". If not only a surface element, but a zone forming a band around the satellite surface has a reflective coating, the sunlight (as in Ref.3) is simultaneously reflected in the whole surface of the reflection cone (Fig.7), since, at any given moment, a reflecting surface element exists for every α_B'' which satisfies equation (13). In the following discussion, this case will be considered first. The results can without loss of generality, be applied to the rotation velocity and orbital motion of a satellite by suitable adjustment of the number of reflecting areas used in practice.

3.2 A sufficient condition for the avoidance of reflection flashes

If a station observes, from the earth, a flash of light, it must at the moment of observation, necessarily lie on the surface of the reflection cone and thus satisfy the condition:-

$$\cos \beta = \vec{X}_\theta \cdot \vec{X}_A = \frac{\vec{x}_B \cdot \vec{X}_A}{|\vec{x}_B|} \quad (14)$$

Since $\vec{x}_B = \vec{x} - \vec{x}_R$, writing in terms of the components, the following relationship holds:-

$$F(\vec{x}_B) = \frac{(x - x_R) X_A + (y - y_R) Y_A + (z - z_R) Z_A}{\sqrt{(x - x_R)^2 + (y - y_R)^2 + (z - z_R)^2}} - (X_\theta X_A + Y_\theta Y_A + Z_\theta Z_A) = 0. \quad \dots (15)$$

Now positions of the satellite and of its axis of rotation must be indicated for which the reflection cone by-passes the earth, and for which, therefore, no flashes of light can be observed anywhere on the earth's surface. Such a case is represented schematically in Fig.8. In the illustration chosen, the

axis of rotation and the centre of the earth lie in the plane of the paper. The axis of the reflection cone is shown by a dotted line and the lines of intersection of the plane of the paper and the reflection cone are drawn thickly. The sun is to be imagined in the direction of a surface line of the opposed cone - not indicated - associated with the reflection cone. The circle represents the section of the earth's sphere in the plane of the paper. As Fig.8 shows, the conditions under which the reflection cone by-passes the earth are dependent on \vec{x}_A , β and on the position of the vertex of the cone \vec{x} . They can be derived from the figure and are shown in detail in Table 1 where eight cases, (a) to (h), are considered.

If \vec{x} and \vec{x}_A are specifically expressed in components of the orbital system with the help of the angular directions, finally the required equation is obtained:-

$$\cos \mu = \cos \delta_A' \cdot \cos (u' - \alpha_A') \quad . \quad (21)$$

Fig.9 represents a case where the earth is not intersected by the reflection cone throughout an entire revolution of the satellite. For the sake of simplicity, the orbital path is illustrated as a circle ABCDA. During a revolution, the apex of the reflection cone moves with the satellite along this path whereas the shape of the cone (β) and its orientation in space remain constant. Firstly, the satellite is at point A, where case (e) applies. The corresponding condition

$$\sin (\mu - \beta) > \frac{R}{r} \quad (22)$$

for position A is:-

$$\sin (|\delta_A'| - \beta) > \frac{R}{r} \quad . \quad (23)$$

If the satellite moves from A to B, as u' increases, according to equation (21), μ also increases. At point B, $u' - \alpha_A' = 90^\circ$ and hence $\mu = 90^\circ$ also. Case (f) applies here, and the corresponding condition

$$\sin (90^\circ - \beta) > \frac{R}{r} \quad (24)$$

is satisfied, if condition (23) was also satisfied. If the satellite moves through B towards C, $\vec{x} \cdot \vec{x}_A < 0$ and μ increases from 90° to $(180^\circ - |\delta_A'|)$. $\sin (\mu - \beta)$ varies from $\sin (90^\circ - \beta)$ to $\sin (|\delta_A'| + \beta)$. Thus, for the orbital arc CB,

$$1 \geq \sin (\mu - \beta) > \sin (|\delta_A'| - \beta) > \frac{R}{r} \quad (25)$$

when the conditions for case (b) or (c) are obtained. Similar considerations apply also for the other half of the orbit. Condition (23) is thus a sufficient criterion for the absence of reflection flashes at all positions of the satellite.

3.3 Conditions for the appearance of light flashes

Whereas, for avoidance of reflection flashes, the condition that the reflection cone shall not intersect the earth is a sufficient criterion, equation (15) alone, on the other hand, does not guarantee the appearance of a reflection flash. For this, it is more important that four conditions should be fulfilled simultaneously.

- (1) The satellite must be illuminated by the sun.
- (2) The satellite must be above the horizon of the observer.
- (3) The sun must be below the horizon of the observer (dusk or night at the place of observation).

The fourth condition is identical with equation (15). It can be seen that this is necessary but not sufficient, since it describes only the geometry of the intersection of a cone (reflection cone) with the earth's sphere. If for example, this cone penetrates the earth, then even the penetration curve on the side of the earth turned away from the satellite satisfies equation (15); this fact, of course, has no physical significance. The first condition is illustrated by Fig.10. The earth's shadow is represented as a circular cylinder of radius R . In reality, the radius of the conical umbra of the earth at a distance of 1, 2 or 10 earth radii from the centre of the earth amounts to 0.995, 0.99 or 0.95 R respectively. If the satellite is in the earth's shadow, from Fig.10 the following apply simultaneously:-

$$\vec{x} \cdot \vec{X}_0 < 0 \quad (26)$$

$$R^2 > r^2 - (\vec{x} \cdot \vec{X}_0)^2 \quad (27)$$

The second condition is illustrated by Fig.11. If the satellite is above the horizon of the observer, then:-

$$\vec{x}_B \cdot \vec{x}_R > 0 \quad (28)$$

A more precise criterion, which makes it possible to exclude cases in which the satellite, by reason of insufficient height above the horizon, is observed only poorly, is the requirement of a certain minimum height. From detailed

considerations, and in accordance with Veis (1963)¹⁶, a minimum height of 15° is required here. Taking the corresponding, largest possible zenith distance ξ_{\max} (75°) the following relationship replaces equation (28):-

$$\vec{X}_B \cdot \vec{X}_R > \cos \xi_{\max} \quad (29)$$

The third condition requires that the sun should be below the horizon at the place of observation, and so the relationship

$$\vec{X}_B \cdot \vec{X}_\theta < 0 \quad (30)$$

holds (c.f. Fig.11). For the cases to be investigated more closely in this work, this requirement is more sharply defined and extended, in that the sun, at the place of observation, is at least 12° below the horizon (nautical twilight). With the required minimum zenith distance ξ_{\min} (102°), the following relationship results:-

$$\vec{X}_R \cdot \vec{X}_\theta < \cos \xi_{\min} \quad (31)$$

3.4 Programme for the calculation of flash curves

All points on the earth's surface, at which a reflection flash can be observed at the same time, together give a curve, which in future will be called the flash curve. It is that part of the penetration curve of the earth's sphere and the reflection cone which satisfies the conditions (1) to (3) given above. As the satellite travels round the orbit, as a rule the shape, length and geographical position of the flash curve change, or the flash curve disappears.

For calculating the flash curves obtained in real cases, a machine-code programme has been written for the Siemens 2002 digital computer. Its structure is shown in Fig.12 in a simplified form. The input values are those of the radius (a), the inclination (i), the ascending node (Ω) of the orbit, the celestial longitude of the sun (L) and the right ascension (α_A) and declination (δ_A) of the satellite axis. The calculation is limited to circular orbits.

After the start, the programme yielded for inspection the output data, the computed height of the satellite above the surface of the earth and also its period of revolution. The machine then calculated $\cos \beta$ from the positions of the sun and satellite axis previously found and set in the core store for the later calculations a table of values of trigonometrical functions, which are frequently needed. The main part of the programme calculated the position of the satellite (\vec{x}) for equally spaced (ΔT) times (T), checked whether

condition (1), (see 3.3) was satisfied and then, in the given case, sought for points on the earth at which reflection flashes could be observed. The sign of the function $F(\vec{x}_B)$, (see equation (15)) was thus checked at equally spaced $(\Delta\zeta)$ latitudes (ζ_k) , also for equally spaced $(\Delta\alpha)$ right ascensions (α_j) . When the sign changed, the zero of $F(\vec{x}_B)$ was found at the latitude in question, and hence the right ascension or the geographical longitude, for which condition (4), (see 3.3) was satisfied. Test calculations and the results showed that the values of latitude used for finding the zeros could lie several degrees apart, without impairing the feasibility of the technique through the zeros lying too close together. For each zero found, the programme checked that conditions (2) and (3) were satisfied and the printing of tabulated values was completed before the search was resumed. From these values, the geographical latitude, the right ascension related to the geocentric equatorial system, and the geographical longitude of the calculated points of a flash curve, related to a system rotating with the earth, were given for the corresponding time and position (T, u') of the satellite. All the intervals $(\Delta T, \Delta\zeta, \Delta\alpha)$, the limits of the section of the satellite orbit (u'_0, u'_{\max}) , and the region of the earth's surface considered $(\zeta_{\min}, \zeta_{\max}, \alpha_{\min}, \alpha_{\max})$ could be varied at will. It was therefore possible to carry out investigations either involving the whole earth or a small area of it, (e.g. Europe). Similarly, regions could be excluded in which it was certain that no light flashes would occur, in this case by appropriate choice of the limits of the areas investigated.

3.5 Results

In order to give an idea of the flash curves produced during a revolution, 133 examples were worked out on the Siemens 2002 digital computer. The input parameters used, $L, a/R, i, \Omega, \alpha_A, \delta_A$ and the information fed in by means of a code number for six different types are set out in Table 2. In most cases it was assumed that the sun was at the equinoctial point ($L = 0$ corresponding to $\alpha_\odot = \delta_\odot = 0$) since it cannot at any time be more than 23.5° above or below the plane of the equator and hence $L = 0$ represents an average value. Examples numbers 77 to 115, however, refer to other positions of the sun. In order to study the effect of the diameter of the satellite orbit, two larger groups of examples, for $a = 1.1R$ and $a = 2R$, were considered. Elliptical orbits were excluded from the discussion, since they would contribute no basically new results to the earlier fundamental research. For the inclination, $i = 60^\circ$ or 90° was chosen, in order that only those cases should be considered in which the satellite could be satisfactorily observed from our latitudes. By a systematic variation of Ω , it was ensured that widely different relative

positions of the orbital plane and the sun were covered. Finally, the effect of different positions of \vec{A} was investigated by systematically varying α_A and δ_A for otherwise similar satellite orbits and solar alignments.

The few examples in which there is no flash can be made qualitatively plausible by considering two limiting cases. One limiting case is illustrated in example number 9. Here \vec{X}_A coincides with \vec{X}_0 and only glancing light is reflected in the direction of $-\vec{X}_A$ onto the sunlight side of the earth. The other limiting case arises when \vec{X}_0 and \vec{X}_A lie in the plane of the orbit and the reflection cone degenerates to a plane, since $\beta = 90^\circ$. In this case, the satellite is to be found directly in the earth's shadow if the degenerate reflection cone meets the dark side of the earth. Since in examples numbers 3, 97 and 118, \vec{X}_0 lies exactly in the orbital plane, $\beta = 90^\circ$, and \vec{X}_A forms a small angle (15°) with the orbital plane, it is understandable that, under the more rigidly defined conditions of visibility (equations (29) and (31)) no flashes could be observed here.

Some typical flash curves are reproduced in Figs. 13 to 19. For purposes of illustration, the curves, taking into account the rotation of the earth, are plotted on a map of the earth. The curve parameter is the time in minutes (related to an arbitrary initial time). As a result of the rotation of the earth, the curves are repeated, after one revolution of the satellite, over other parts of the earth at the corresponding geographical latitudes. The centres of these areas are indicated by circles containing the number of the revolution concerned. It can be seen that for $a/R = 2$, considerably greater areas of the earth's surface are covered by flash curves during a revolution than when $a/R = 1.1$, where the distance between the vertex of the reflection cone and the earth's surface is relatively small. On the other hand, in the latter case, the number of repetitions per day is greater, due to the correspondingly small period of revolution of the satellite. The fact that the flash curves in Figs. 16 and 18 travel appreciably more slowly over the earth's surface can be attributed to the small deviation (15°) of the angle between \vec{X}_A and the orbital plane from a right angle. In the extreme case, where this angle is 90° and in addition, $\beta = 90^\circ$, all flash curves in the intersection circle between the orbital plane and the earth would coincide.

4 ACCURACY OF THE TECHNIQUE

4.1 Errors in the normal to the reflecting surface

The unit vector in the direction from the observer to the satellite can, in practice, be estimated to within an error of $\Delta\vec{X}_B$. Instead of \vec{X}_B , a false unit vector \vec{X}_B' which forms an angle ϵ_B with \vec{X}_B , is obtained. The normal vector \vec{n}' , calculated using \vec{X}_B' from equation (5), then also deviates from the true normal \vec{n} to the reflecting area. Let the angle between \vec{n} and \vec{n}' be ϵ_n ($0 \leq \epsilon_n < 180^\circ$). If $\vec{n} = \vec{X}_0 - \vec{X}_B$ and $\vec{n}' = \vec{X}_0 - (\vec{X}_B + \Delta\vec{X}_B)$ are substituted in the equation

$$\tan \epsilon_n = \frac{|[\vec{n}, \vec{n}']|}{\vec{n} \cdot \vec{n}'},$$

then

$$\tan \epsilon_n = \frac{|[\Delta\vec{X}_B, (\vec{X}_0 - \vec{X}_B)]|}{2 \cdot (1 - \vec{X}_0 \cdot \vec{X}_B) - (\vec{X}_0 - \vec{X}_B) \cdot \Delta\vec{X}_B}. \quad (32)$$

This general formula includes, moreover, the familiar case where \vec{X}_0 , \vec{X}_B and $\Delta\vec{X}_B$ lie in one plane and where, independent of the angle θ between \vec{X}_0 and \vec{X}_B , $\epsilon_n = \frac{1}{2} \epsilon_B$ is always true. It is known, however, that in certain circumstances the error ϵ_n of the calculated normal direction can be considerably greater than the original direction error ϵ_B of the observation. If, for example, $\Delta\vec{X}_B$ is perpendicular to the plane defined by \vec{X}_0 and \vec{X}_B , then, since $|\Delta\vec{X}_B| = 2 \sin \frac{\epsilon_B}{2}$ and $|\vec{X}_0 - \vec{X}_B| = 2 \sin \frac{\theta}{2}$, and since the second term in the denominator of equation (32) disappears, this equation becomes:

$$\tan \epsilon_n = \frac{\sin \frac{\epsilon_B}{2}}{\sin \frac{\theta}{2}}. \quad (33)$$

For a given value of ϵ_B , ϵ_n becomes greater as the angle between incident and reflected rays becomes more obtuse, i.e. as θ becomes smaller. In the case of glancing incidence, ($\theta = 0$), the technique finally becomes completely unusable.

If ϵ_B is sufficiently small, $\Delta\vec{X}_B$ can be replaced by the vector $\delta\vec{X}_B$, neglecting terms of order ϵ^2 ; this vector lies at right angles to \vec{X}_B and has the value $1 \cdot \epsilon_B$. Equation (32) then becomes:-

$$\tan \epsilon_n \approx \frac{|[\delta\vec{X}_B, (\vec{X}_0 - \vec{X}_B)]|}{4 \sin^2 \frac{\theta}{2} - \vec{X}_0 \cdot \delta\vec{X}_B}. \quad (34)$$

Here the numerator is always smaller than $2 \epsilon_B$ and the denominator is always larger than $4 \sin^2 \frac{\theta}{2} - \epsilon_B$, as long as $\epsilon < 4 \sin^2 \frac{\theta}{2}$. This is always the case in practical measurements for $\epsilon_B < 12^\circ$, since as explained in 3.3 on the grounds of technical observation requirements a minimum value of θ , $\epsilon_{\min} - \epsilon_{\max} = 27^\circ$ is required. Thus, for the estimation of the maximum error,

$$\tan \epsilon_n \leq \frac{\frac{\epsilon_B}{2}}{\sin^2 \frac{\theta}{2} - \frac{\epsilon_B}{4}} \quad (35)$$

In cases where, in addition to higher powers of ϵ_B , the linear term in ϵ_B in the denominator of equation (34), $\vec{X}_0 \cdot \delta \vec{X}_B \leq \epsilon_B$ can be neglected in comparison with $4 \sin^2 \frac{\theta}{2}$, a more rigorous formula for estimating the maximum error in the direction of \vec{n} can be written:-

$$\tan \epsilon_n \leq \frac{\frac{\epsilon_B}{2}}{\sin^2 \frac{\theta}{2}} \quad (36)$$

The error caused by neglecting the linear term in the denominator is less than 1% if $\theta > 27^\circ$ and $\epsilon_B < 7^\circ$.

4.2 Errors in the determination of the axis

Now we shall investigate the effect of errors in the direction of the two normals used (index 1,2) on the position of the axis vector \vec{X}_A , calculated from equation (8).

Using the correct normal vectors, first a vector lying along the satellite axis is obtained:-

$$\vec{x}_A = \sin \gamma \cdot \vec{X}_A \quad (37)$$

where γ is the angle between \vec{N}_1 and \vec{N}_2 . On the other hand, taking the normal vectors found by observation, which are subject to errors, $\vec{N}_1' = \vec{N}_1 + \Delta \vec{N}_1$ and $\vec{N}_2' = \vec{N}_2 + \Delta \vec{N}_2$,

$$\vec{x}_A' = \sin \gamma \cdot \vec{X}_A + [\vec{N}_1, \Delta \vec{N}_2] + [\Delta \vec{N}_1, \vec{N}_2] + [\Delta \vec{N}_1, \Delta \vec{N}_2] \quad (38)$$

The angle ϵ_A between \vec{x}_A and \vec{x}_A' represents the error in estimating the axial direction. Since

$$\tan e_A = \frac{|[\vec{x}_A, \vec{x}'_A]|}{\vec{x}_A \cdot \vec{x}'_A},$$

it follows that:-

$$\tan e_A = \frac{|[\vec{x}_A [\vec{N}_1, \Delta\vec{N}_2]] + [\vec{x}_A [\Delta\vec{N}_1, \vec{N}_2]] + [\vec{x}_A [\Delta\vec{N}_1, \Delta\vec{N}_2]]|}{\sin \gamma + (\vec{x}_A \vec{N}_1 \Delta\vec{N}_2) + (\vec{x}_A \Delta\vec{N}_1 \vec{N}_2) + (\vec{x}_A \Delta\vec{N}_1 \Delta\vec{N}_2)} \quad (39)$$

If only small errors in the normal directions ($|\epsilon_{N1}| \ll 1$, $|\epsilon_{N2}| \ll 1$) are considered, $\Delta\vec{N}_1$ and $\Delta\vec{N}_2$ can be replaced by $\delta\vec{N}_1$ and $\delta\vec{N}_2$, where $\delta\vec{N}_1$ has the value ϵ_{N1} and is perpendicular to \vec{N}_1 . If $\delta\vec{N}_1$ is divided into a component at right angles to the plane defined by \vec{N}_1 and \vec{N}_2 and a parallel component, then:-

$$\delta\vec{N}_1 = \epsilon_{N1}^\perp \vec{x}_A + \epsilon_{N1}^\parallel \vec{M}_1 \quad (40)$$

\vec{M}_1 is a unit vector at right angles to \vec{N}_1 in the $\vec{N}_1 \vec{N}_2$ plane. If this relationship is introduced into equation (39) and the quadratic terms in ϵ_N are negligible in comparison with the linear ones, then:-

$$\tan e_A = \frac{|\vec{N}_1 \epsilon_{N2}^\perp - \vec{N}_2 \epsilon_{N1}^\perp|}{\sin \gamma + \cos \gamma \cdot (\epsilon_{N2}^\parallel - \epsilon_{N1}^\parallel)} \quad (41)$$

Since, in general, nothing is known about the sign and relationship of the errors ϵ_{N1}^\perp and ϵ_{N1}^\parallel , the most unfavourable case will be assumed for the present, and the numerator in equation (41) be made as large as possible, or the denominator as small as possible. In addition, the components $\epsilon_{N1}^\perp, \epsilon_{N1}^\parallel$ may be replaced by the largest possible error, ϵ_N , in the normal direction. For the upper limit of the error of e_A one obtains:-

$$\tan e_A < \frac{|\epsilon_N| \cdot \sqrt{2(1 + |\cos \gamma|)}}{\sin \gamma - 2 \cdot |\epsilon_N \cos \gamma|} \quad ; \quad (42)$$

this is valid as long as $\sin \gamma > 2|\epsilon \cos \gamma|$. Thus, in agreement with intuition, the error in the calculated axial direction for a given error ϵ_N of the normal becomes smaller as γ approaches a right angle, and greater as the angle contained by \vec{N}_1 and \vec{N}_2 becomes more acute or obtuse. In the limiting case where $\gamma = 0$ or $\gamma = 180^\circ$, \vec{N}_2 lies in the direction or counter-direction of

\vec{N}_1 and the technique described for determining \vec{X}_A fails completely. An idea of the dependence of the maximum error ϵ_A of the axial direction on γ and ϵ_N can be obtained from the values shown in Table 4, which were calculated using equation (42).

Since the normal angle is of great significance where the accuracy of the method described here is concerned, in the following section formulae for the calculation and evaluation of γ will be derived, and some numerical examples given.

4.3 The normal angle

The angle ($0 \leq \gamma \leq 180^\circ$) between the two normals obtained from two observations is given directly by the scalar product:-

$$\cos \gamma = \frac{\vec{n}_1 \cdot \vec{n}_2}{|\vec{n}_1| \cdot |\vec{n}_2|} \quad (43)$$

If one substitutes for \vec{n}_1 and \vec{n}_2 using equation (5), then, after multiplying out the denominator it follows that:-

$$\cos \gamma = \frac{(\vec{X}_{O1} - \vec{X}_{B1}) \cdot (\vec{X}_{O2} - \vec{X}_{B2})}{2 \cdot \sqrt{(1 - \vec{X}_{O1} \cdot \vec{X}_{B1})(1 - \vec{X}_{O2} \cdot \vec{X}_{B2})}} \quad (44)$$

Thus, for each pair of observations, γ can be obtained without further difficulty.

If \vec{X}_O , \vec{X}_{B1} and \vec{X}_{B2} are each divided into a component parallel to \vec{X}_A and one perpendicular to the satellite axis (unit vectors \vec{N}_O , \vec{N}_{B1} , \vec{N}_{B2} , - see Fig.20) it follows that:- ($\vec{X}_{O1} = \vec{X}_{O2} = \vec{X}_O$)

$$\vec{X}_O = \sin \beta \vec{N}_O + \cos \beta \vec{X}_A \quad (45)$$

$$\vec{X}_{B1} = -\sin \beta \vec{N}_{B1} + \cos \beta \vec{X}_A \quad (46)$$

$$\vec{X}_{B2} = -\sin \beta \vec{N}_{B2} + \cos \beta \vec{X}_A \quad (47)$$

From this, by substituting in equation (5) one obtains:-

$$\vec{n}_1 = \sin \beta (\vec{N}_O + \vec{N}_{B1}) \quad (48)$$

$$\vec{n}_2 = \sin \beta (\vec{N}_0 + \vec{N}_{B2}) \quad . \quad (49)$$

The vectors $(\vec{N}_0 + \vec{N}_{B1})$ and $(\vec{N}_0 + \vec{N}_{B2})$ have the same direction as the normal unit vectors \vec{N}_1 and \vec{N}_2 respectively (Fig.21). By substituting equations (48) and (49) in equation (43), an equation analogous to (44) is obtained:-

$$\cos \gamma = \frac{(\vec{N}_0 + \vec{N}_{B1}) \cdot (\vec{N}_0 + \vec{N}_{B2})}{2 \cdot \sqrt{(1 + \vec{N}_0 \cdot \vec{N}_{B1})(1 + \vec{N}_0 \cdot \vec{N}_{B2})}} \quad . \quad (50)$$

If γ is a right angle ($\cos \gamma = 0$), it follows* that:-

$$\vec{N}_{B2} = -\vec{N}_{B1} \quad . \quad (51)$$

Equation (51) means that observations must be made at points on opposing generators of the reflection cone if $\gamma = 90^\circ$. If equation (51) is substituted in equation (46), then, by adding equations (47) and (46) a further form for the condition $\gamma = 90^\circ$ results:-

$$\vec{X}_{B2} = -\vec{X}_{B1} + 2 \cos \beta \vec{X}_A \quad . \quad (52)$$

As a rule, one is not able to obtain pairs of observations for which the observing stations lie exactly on opposing generators of the reflection cone. Often the generators lying opposite each other at a particular time do not meet the earth at all, so that it is possible to combine only those observations for which $|90^\circ - \gamma| > 0$. It is clear that γ becomes smaller as the generators of the reflection cone corresponding to the combined observations come closer together. In the limiting case (which has no practical significance), where the two observations are made on the same generator of the reflection cone, $\gamma = 0$.

If the angle between the generators is denoted by Γ , then

$$\cos \Gamma = \vec{X}_{B1} \cdot \vec{X}_{B2} \quad . \quad (53)$$

* The cases $\vec{N}_{B1} = -\vec{N}_0$ and $\vec{N}_{B2} = -\vec{N}_0$ are without practical significance, since here the observer would find that the bearing of the satellite coincided with that of the sun.

In order to derive a quantitative relationship between Γ and γ , the following equation is obtained directly from Fig.21, which represents a plane perpendicular to the satellite axis with the unit vectors \vec{N}_0 , \vec{N}_{B1} and \vec{N}_{B2} :-

$$\gamma = \frac{1}{2} (\vartheta_2 - \vartheta_1) \quad (54)$$

since the normals \vec{n}_1 and \vec{n}_2 bisect the angles ϑ_1 and ϑ_2 respectively. On the other hand, $(\vartheta_2 - \vartheta_1)$ is the angle between \vec{N}_2 and \vec{N}_1 . It thus follows that:-

$$\cos 2\gamma = \vec{N}_{B1} \cdot \vec{N}_{B2} \quad (55)$$

If one resolves \vec{N}_{B1} and \vec{N}_{B2} into components in the directions \vec{X}_{B1} and \vec{X}_{B2} respectively, and \vec{X}_A , using equations (46) and (47), then introduces the relationship given in equation (53), and notes, when evaluating the scalar product, that $\vec{X}_B \cdot \vec{X}_A = \cos \beta$, then the desired equation is obtained:-

$$\cos 2\gamma = \frac{\cos \Gamma - \cos^2 \beta}{\sin^2 \beta} \quad (56)$$

This equation shows that γ , starting with $\gamma = 0$ when $\Gamma = 0$, increases with increasing Γ and finally, for $\Gamma = 2\beta$, reaches the value $\gamma = 90^\circ$. The last result agrees with that obtained from equation (53), according to which for $\gamma = 90^\circ$, the observing stations lie on opposite generators of the reflection cone, i.e. in this case, the angle between \vec{X}_{B1} and \vec{X}_{B2} is 2β . Further, equation (56) shows that for a given value of Γ ($2\beta > \Gamma$), the angle between the normals increases as the vertex angle of the reflection cone decreases.

Numerical data, calculated from equation (56), concerning the relationship between Γ , β , and γ , are given in Table 5. The alternative solution $(180^\circ - \gamma_{\max})$, also obtained from equation (56), gives the same error ϵ_A as γ_{\max} when substituted in equation (42).

The maximum angle Γ_{\max} , which can be achieved with two simultaneous observations, is, (apart from the limitation $2\beta \geq \Gamma_{\max}$)

$$\Gamma_{\max} = 2 \arcsin \frac{R}{a} \quad (0 \leq \Gamma_{\max} < 180^\circ) \quad (57)$$

It is equal to the largest angle at which two stations could be observed simultaneously from the satellite. This angle has a value of 131° , 60° or 11.5° for orbital radii of $1.1R$, $2R$ or $10R$ respectively. The corresponding maximum angles between the normals, Γ_{\max} or $180 - \gamma_{\max}$, for $\beta = 45^\circ$, $\gamma_{\max} = 90^\circ$,

45° or 8°, and for $\beta = 90^\circ$, only 65.5°, 30° or 6°. When simultaneous* observations are made, from Table 4, for satellites with large orbital radii ($a/R > 2$), it can be expected that the estimation of \vec{X}_R will be insufficiently accurate.

The accuracy of \vec{X}_A is however satisfactory, even with distant satellites, if the earth, during each revolution, is intersected twice by the reflection cone, and one is not then dependent on the combination of "simultaneous" or "almost simultaneous" observations. This case is illustrated in Table 2 and denoted by the code number 4 or 5. If the generators of the reflection cone produced by the first group of flash curves form a sufficiently large angle with the generators resulting from the second series of flash curves, observations from two different series of flash curves at any time can be combined. Favourable combinations - leaving aside limitations imposed by conditions of visibility - are possible when the angle the satellite axis forms with the orbital plane is considerably smaller than β . If \vec{X}_A lies in the orbital plane, a sufficient number of opposing generators of the reflection cone meet the earth during one revolution even when $a \gg R$.

In order to obtain an idea of the values which γ can attain in practical cases by considering all conditions of visibility, positions of observing stations are indicated on Figs. 13 to 19, and γ is calculated for the combination of observations made by all pairs of such stations. The results are shown in Table 6. They show, in agreement with equation (57), that γ increases as the distance between the stations on the flash curves increases, i.e. as r becomes greater. Bearing this fact in mind, the angle γ was calculated for each pair of observations for 80 distinct cases from examples numbers 1-76 and 116-126. In 57 cases, for $a/R = 1.1$, this angle was greater than 45°, and in 21 cases even greater than 75°. On the other hand, for $a/R = 2$, with combinations from only one series of flash curves, γ remained at 30°, and with combinations of observations from two different series of flash curves γ was 70°. The conclusion that, for $a/R = 2$, values of $\gamma > 60^\circ$ can only be attained using combinations of observations from different sets of flash curves, agrees with the estimate made in equation (57).

4.4 Effect of the finite diameter of the sun's disc

In the discussion so far, the sun has been regarded, by implication, as a point-source of light. Since, however, the apparent diameter of the sun's disc is about 0.5°, the flash curves broaden into bands bounded by two reflection cones with semi-vertex angles β and $(\beta - 0.5^\circ)$. These cones will, in future,

* or an exact number of revolutions apart.

be referred to as limiting cones. If a satellite at a height of $H = R(a/R - 1)$ is at the zenith of the observer, who is in the range of one limiting cone, the distance of the other limiting cone from the observer on the earth's surface is found to be $b = H \tan (0.5^\circ)$. For $a/R = 1.1$ or $a/R = 2$, the corresponding width of the visibility band on the earth's surface is 5.6 or 55.5 km respectively. If the satellite moves in a direction perpendicular to the tangent to the visibility band over the place of observation, the band sweeps over the observing station in the shortest possible time. If the satellite's velocity is 7.5 or 5.6 km/sec in the example taken above, the approximate duration of the flash is 0.7 or 10 seconds. In both cases, the length of the corresponding flash trail seen by the observer is 0.5° .

As a rule, however, the satellite is not observed at zenith, nor does the visibility band sweep over the station in the way described above. Therefore, using the modified programme described in Section 3.4, two examples (Table 2, numbers 2 and 7) were computed between $\zeta = 47^\circ$ and $\zeta = 54.5^\circ$; the development of the visibility bands was evaluated, taking into account the earth's rotation and plotted on a map of Germany (Figs.22 and 23). In the case of Fig.22, the width of the band is about 12 to 13 km. Since the visibility band for $\zeta \approx 50^\circ$ sweeps over the surface of the earth with a velocity of about 6.5 km/sec, a flash time of about 2 seconds is obtained. The upper limit for the length of the flash trail seen by the observer can be found from this. It is equal to the angle which the satellite would cover during the period of a flash if it were at the zenith. In the case considered, this angle is about 1.4° .

In the example given in Fig.23, the width of the visibility band is approximately the same as that for Fig.22. However, it now sweeps over the station with a considerably smaller velocity of about 0.73 km/sec. This leads to a flash duration of about 17 seconds. The upper limit for the length of the observed flash trail is, in this case, circa 12° . If it is assumed that the mid-point of a flash trail can be estimated to an accuracy of $\pm 10\%$ of its length, the direction of \vec{X}_B can be estimated to within $\pm 0.14^\circ$ in the case illustrated by Fig.22, and in the very unfavourable example represented by Fig.23, still to within $\pm 1.2^\circ$.

In order to study more generally the behaviour of the reflection cone as it sweeps over an observing station, an auxiliary plane will now be considered. This plane, which, as a rule, intersects the earth's sphere, contains the place of observation B and, in addition, has \vec{x} as its normal (Fig.24). Let the height of the satellite above the auxiliary plane be h. In the following discussion, the co-ordinate system used will be the auxiliary plane system defined in Section 1.2.

Further, let the angle between \vec{X}_A and the plane be denoted by η . In the $(\vec{E}_1, \vec{E}_2, \vec{E}_3)$ system:-

$$\vec{X}_A = \begin{pmatrix} \cos \eta \\ 0 \\ \sin \eta \end{pmatrix} \quad (58)$$

and if the corresponding components of the vector from the origin of the $(\vec{E}_1, \vec{E}_2, \vec{E}_3)$ system to the observing station are indicated by x, y and o , then:-

$$\vec{x}_P = \begin{pmatrix} -x \\ -y \\ h \end{pmatrix} \quad (59)$$

All points in the plane which lie on the reflection cone must satisfy equation (14). In the $(\vec{E}_1, \vec{E}_2, \vec{E}_3)$ system, this becomes:-

$$\cos \beta = \frac{-x \cos \eta - h \sin \eta}{\sqrt{x^2 + y^2 + h^2}} \quad (60)$$

After squaring and combining the corresponding equations of the intersection curves in the auxiliary plane, we obtain:- for $|\eta| = \beta$ (parabola)

$$\left(\frac{y}{h}\right)^2 = -\frac{\sin 2\eta}{\cos^2 \beta} \left(\frac{x}{h} + \frac{\cos^2 \beta - \sin^2 \beta}{\sin 2\eta}\right) \quad (61)$$

For $|\eta| > \beta$ (ellipse)

$$\frac{\left(\frac{x}{h} + \frac{\frac{1}{2} \sin 2\eta}{\cos^2 \beta - \cos^2 \eta}\right)^2}{\left(\frac{\frac{1}{2} \sin 2\beta}{\cos^2 \beta - \cos^2 \eta}\right)^2} + \frac{\left(\frac{y}{h}\right)^2}{\left(\frac{\sin \beta}{\sqrt{\cos^2 \beta - \cos^2 \eta}}\right)^2} = 1 \quad (62)$$

For $|\eta| < \beta$ (hyperbola)

$$\frac{\left(\frac{x}{h} - \frac{\frac{1}{2} \sin 2\eta}{\cos^2 \eta - \cos^2 \beta}\right)^2}{\left(\frac{\frac{1}{2} \sin 2\beta}{\cos^2 \eta - \cos^2 \beta}\right)^2} - \frac{\left(\frac{y}{h}\right)^2}{\left(\frac{\sin \beta}{\cos^2 \eta - \cos^2 \beta}\right)^2} = 1 \quad . \quad (63)$$

If x and y are measured in units of h , the conics, as derived from equations (62) and (63), depend only on β and on the angle η at which the satellite axis is inclined to the auxiliary plane. In Fig.26 are shown, for different values of η , the curves resulting from the intersection of the auxiliary plane with, in each case, two limiting cones of semi-vertex angles $\beta = 60^\circ$ and $\beta = 59.5^\circ$. The geometrical position of all points which are common to the auxiliary plane and the earth's surface, and at which the satellite appears at a zenith distance ξ , must now be located in the h -normalised auxiliary plane representation. From Fig.24:-

$$\frac{R}{a} = \frac{\sin \angle BSP}{\sin \angle SBO} = \frac{s/\sqrt{s^2 + h^2}}{\sin \xi} \quad . \quad (64)$$

From this it follows that:-

$$\frac{s}{h} = \frac{\sin \xi}{\sqrt{\left(\frac{a}{R}\right)^2 - \sin^2 \xi}} \quad . \quad (65)$$

The position desired thus lies on a circle about the origin of the $(\vec{E}_1, \vec{E}_2, \vec{E}_3)$ system, which, in the illustration chosen, has a radius of s/h . For $\xi = 0^\circ$, s/h is always 0. If the satellite is at an elevation of 12° above the horizon, for $a/R = 1.1$ or 2.0 , the radius $s/h = 1.9$ or 0.56 . If the satellite is 30° above the horizon, the radius of the circle (shown in Fig.26) is $s/h = 1.28$ or 0.48 . Of all the stations on such a circle, only those which, in addition, lie between the two limiting cones, will see a flash. These points are to be found in the auxiliary plane between the two adjacent limiting curves which correspond to the parameter in question. Let the co-ordinates of one such station be, in the auxiliary plane system (Fig.25), $x_B = s \cos \psi_B$ and $y_B = s \sin \psi_B$. Then:

$$\vec{X}_B = \begin{pmatrix} -s \cos \psi_B \\ -s \sin \psi_B \\ h \end{pmatrix} \quad . \quad (66)$$

In order to evaluate the length of the flash trail seen by the observer at B, the auxiliary plane system is now regarded as being fixed in space, and the satellite moves from the point (0, 0, h) along its path in the direction indicated by ψ_d (Fig.25) by a small amount d, such that the component of its movement perpendicular to the auxiliary plane can be neglected. The change in position of the satellite, and therefore of the limiting curves in the auxiliary plane, is

$$\Delta \vec{X}_B = \begin{pmatrix} d \cos \psi_d \\ d \sin \psi_d \\ 0 \end{pmatrix} \quad (67)$$

The angle ϵ_d between the old and new directions from the observer to the satellite is given by:-

$$\tan \epsilon_d = \frac{|[\vec{X}_B, \Delta \vec{X}_B]|}{\vec{X}_B^2 + \vec{X}_B \cdot \Delta \vec{X}_B} \quad (68)$$

Finally, after substituting for the vectors in the form given above

$$\tan \epsilon_d = \frac{\frac{d}{h} \cdot \sqrt{1 + \left(\frac{s}{h}\right)^2 \sin^2 (\psi_B - \psi_d)}}{1 + \left(\frac{s}{h}\right)^2 - \frac{s}{h} \cdot \frac{d}{h} \cdot \cos (\psi_B - \psi_d)} \quad (69)$$

Using this formula, calculations were made to find the interval d by which the satellite can move in various directions relative to the auxiliary plane before the length of the flash trail observed in the sky reaches a value of 5° . The smallest tolerance values found, $(d/h)_{\min}$, are indicated by circles round B_1 and B_2 in Fig.26. They represent the case where the satellite moves perpendicular to the direction from which the flash is observed, so that no fore-shortening of the flash trail occurs.

Since, in the representation of the auxiliary plane, when the satellite moves by a further interval of d, the limiting curves are also displaced by a distance d in the auxiliary plane, the range of the angle ψ_d for which ϵ_d remains below 5° can be read directly from Fig.26. If, from B_1 or B_2 , one marks off in different directions ψ_d the circles of radius $(d/h)_{\min}$ shown, the condition $\epsilon_d < 5^\circ$ is satisfied for all radii which intersect one limiting curve. If it is further assumed that the mid-point of a flash trail can be estimated to an accuracy of $\pm 10\%$, the chosen example shows that the technique makes it

possible in most cases to estimate \vec{X}_B to within $\pm 0.5^\circ$. Only a range of 8° or 7° (about the tangent to the limiting curve) is unusable in the case of observing positions B_1 or B_2 .

These results are not significantly impaired if, instead of a complete reflecting ring on the surface of the satellite (c.f. 3.1) several individual plane mirrors are used, when the reflection flash is cut into several short single flashes. According to data in the bibliography^{2,4,15,17,18}, the rotational velocity of a spin-stabilized satellite lies between 6 and 0.2 rotations per second. In order to obtain about five single flashes per second for a total flash duration of about one second, between one and twenty-five equally spaced mirrors must be fixed to the casing of the satellite. The number of mirrors required for a longer duration of the total flash cycle is correspondingly smaller.

5 CONCLUSION

If mirrors are fixed to a rotating satellite, with their normals perpendicular to the axis of rotation, the satellite's orientation in space can be determined by means of observed flashes of reflected sunlight. This technique is distinguished by the relatively small expenditure on computation and instruments. As an evaluation of the possibilities of practical application, on the one hand, conditions are given under which the method fails. On the other hand, it was shown that the technique is at least as accurate ($\pm 0.5^\circ$) as familiar methods described in the literature, particularly when the angle between the satellite axis and the direction of the sun is between 45° and 90° , and for satellite orbits having semi-major axes of less than 2 earth radii. 133 numerical examples were worked out and quantitative data is given concerning the errors to be expected and their evaluation.

ACKNOWLEDGEMENT

I extend grateful thanks to my esteemed tutor, Professor H. Siedentopf, and to his provisional successor, Professor G. Mollenstedt, for their constant helpful interest. Sincere thanks are also due to Professor F. Lenz and Dr. D. Hablick for their critical perusal of the manuscript and for stimulating discussions.

Table 1

SUFFICIENT CONDITIONS FOR THE ABSENCE OF REFLECTION FLASHES
(REFLECTION CONE DOES NOT INTERSECT THE EARTH'S SURFACE)

β semi-vertex angle of reflection cone
 μ angle between radius vector \vec{x} and axis of cone \vec{X}_A
 $\vec{x} \cdot \vec{X}_A$ projection of the radius vector on the axis of the cone
 R radius of earth (c.f. Fig.8).

Case	Vertex of cone	Angular range	Conditions
a	$\vec{x} \cdot \vec{X}_A < -R$	$0 < \beta \leq 90^\circ$	no further conditions
b	$-R \leq \vec{x} \cdot \vec{X}_A < 0$	$\beta > \mu - 90^\circ$	$\sin (\mu - \beta) > \frac{R}{r}$
c	$-R \leq \vec{x} \cdot \vec{X}_A < 0$	$\beta < \mu - 90^\circ$	$1 > \frac{R}{r}$
d	$\vec{x} \cdot \vec{X}_A > 0$	$\beta > \mu$	$\sin (\beta - \mu) > \frac{R}{r}$
e	$\vec{x} \cdot \vec{X}_A > 0$	$\beta < \mu$	$\sin (\mu - \beta) > \frac{R}{r}$
f	$\vec{x} \cdot \vec{X}_A = 0$	$\mu = 90^\circ$	$\cos \beta > \frac{R}{r}$
g	$\vec{x} \cdot \vec{X}_A = r$	$\mu = 0$	$\sin \beta > \frac{R}{r}$
h	$\vec{x} \cdot \vec{X}_A = -r$	$0 < \beta = 90^\circ; \mu = 180^\circ$	$1 > \frac{R}{r}$

Note: I wish to thank Professor Lenz for the information that the areas in the plane of drawing, in which the vertex of the reflection cone must lie if no light flash is to occur, are defined by the three conditions:

$$(1) \quad \mu > \beta + 90^\circ \quad (16)$$

$$(2) \quad \beta < \mu \leq \beta + 90^\circ \quad (17)$$

$$\text{and} \quad \sin (\mu - \beta) > \frac{R}{r} \quad (18)$$

$$(3) \quad 0 < \mu < \beta \quad (19)$$

$$\text{and} \quad \sin (\beta - \mu) > \frac{R}{r} \quad (20)$$

and are illustrated particularly clearly in Fig.8(a).

Table 2

WORKED EXAMPLES

- a orbital radius, i inclination,
 α_A right ascension of the spin axis vector,
 δ_A declination of the spin axis vector,
 L celestial longitude of the sun,
Bl possibilities of observing reflection flashes:
0 = none,
1 = once per revolution in the northern hemisphere,
2 = once per revolution in the southern hemisphere,
3 = once per revolution in the vicinity of the equator,
4 = once in the northern and once in the southern hemisphere per revolution
5 = twice per revolution in the vicinity of the equator
() = test carried out only with the visibility restriction
 $\xi_{\max} = \xi_{\min} = 90^\circ$.

No.	L	$\frac{a}{R}$	i	Ω	α_A	δ_A	Bl
1	0	1.1	60	0	0	45	1
2	0	1.1	60	0	45	45	1
3	0	1.1	60	0	90	45	0
4	0	1.1	60	0	135	45	2
5	0	1.1	60	0	180	45	2
6	0	1.1	60	0	225	45	4
7	0	1.1	60	0	270	45	4
8	0	1.1	60	0	315	45	4
9	0	1.1	60	0	0	0	0
10	0	1.1	60	0	45	0	1
11	0	1.1	60	0	90	0	4
12	0	1.1	60	0	135	0	2
13	0	1.1	60	0	0	90	0
14	0	1.1	60	60	0	45	1
15	0	1.1	60	60	45	45	1
16	0	1.1	60	60	90	45	2
17	0	1.1	60	60	135	45	2
18	0	1.1	60	60	180	45	2
19	0	1.1	60	60	225	45	4
20	0	1.1	60	60	270	45	4
21	0	1.1	60	60	315	45	4
22	0	1.1	60	60	45	0	1
23	0	1.1	60	60	90	0	1
24	0	1.1	60	60	135	0	2
25	0	1.1	60	120	0	45	1
26	0	1.1	60	120	45	45	4

Table 2 (Contd)

No.	L	$\frac{a}{R}$	i	Ω	α_A	δ_A	B1
27	0	1.1	60	120	90	45	4
28	0	1.1	60	120	135	45	4
29	0	1.1	60	120	180	45	2
30	0	1.1	60	120	225	45	2
31	0	1.1	60	120	270	45	2
32	0	1.1	60	120	315	45	1
33	0	1.1	60	120	45	0	2
34	0	1.1	60	120	90	0	1
35	0	1.1	60	120	135	0	1
36	0	1.1	60	180	0	45	(1)
37	0	1.1	60	180	45	0	2
38	0	1.1	60	180	90	0	4
39	0	1.1	60	180	135	0	1
40	0	1.1	60	240	45	0	2
41	0	1.1	60	240	90	0	2
42	0	1.1	60	240	135	0	1
43	0	1.1	60	300	45	0	1
44	0	1.1	90	0	0	45	1
45	0	1.1	90	0	45	45	1
46	0	1.1	90	0	90	45	4
47	0	1.1	90	0	135	45	2
48	0	1.1	90	0	180	45	2
49	0	1.1	90	0	225	45	2
50	0	1.1	90	0	270	45	4
51	0	1.1	90	0	315	45	1
52	0	1.1	90	0	45	0	4
53	0	1.1	90	0	90	0	4
54	0	1.1	90	0	135	0	4
55	0	1.1	90	60	0	45	1
56	0	1.1	90	60	45	45	1
57	0	1.1	90	60	90	45	1
58	0	1.1	90	60	135	45	4
59	0	1.1	90	60	180	45	2
60	0	1.1	90	60	225	45	2
61	0	1.1	90	60	270	45	2
62	0	1.1	90	60	315	45	4
63	0	1.1	90	60	45	0	4
64	0	1.1	90	60	90	0	4
65	0	1.1	90	60	135	0	4
66	0	1.1	90	120	0	45	1
67	0	1.1	90	120	45	45	4
68	0	1.1	90	120	90	45	2
69	0	1.1	90	120	135	45	2
70	0	1.1	90	120	180	45	2
71	0	1.1	90	120	225	45	4
72	0	1.1	90	120	270	45	4
73	0	1.1	90	120	315	45	1
74	0	1.1	90	120	45	0	4
75	0	1.1	90	120	90	0	4
76	0	1.1	90	120	135	0	4

Table 2 (Contd)

No.	L	$\frac{a}{R}$	i	Ω	α_A	δ_A	Fl
77	90	1.1	60	0	0	45	(5)
78	90	1.1	60	0	45	45	(5)
79	90	1.1	60	0	90	45	(5)
80	90	1.1	60	0	135	45	(5)
81	90	1.1	60	0	180	45	(5)
82	90	1.1	60	0	225	45	(5)
83	90	1.1	60	0	315	45	(5)
84	90	1.1	60	0	0	0	(5)
85	90	1.1	60	0	45	0	(3)
86	90	1.1	60	0	90	0	(5)
87	90	1.1	60	0	135	0	(3)
88	90	1.1	60	0	0	90	(5)
89	90	1.1	60	60	0	45	(4)
90	90	1.1	60	60	90	45	(1)
91	90	1.1	60	60	135	45	(1)
92	90	1.1	60	60	180	45	(1)
93	90	1.1	60	120	0	45	(4)
94	90	1.1	60	120	135	45	(4)
95	180	1.1	60	0	0	45	(2)
96	180	1.1	60	0	45	45	(2)
97	180	1.1	60	0	90	45	0
98	180	1.1	60	0	135	45	(1)
99	180	1.1	60	0	180	45	(1)
100	180	1.1	60	0	225	45	(4)
101	180	1.1	60	0	270	45	(4)
102	180	1.1	60	0	315	45	(4)
103	270	1.1	60	0	0	45	(5)
104	270	1.1	60	0	45	45	(5)
105	270	1.1	60	0	90	45	(5)
106	270	1.1	60	0	135	45	(5)
107	270	1.1	60	0	180	45	(5)
108	270	1.1	60	0	225	45	(5)
109	270	1.1	60	0	270	45	(5)
110	270	1.1	60	0	315	45	(5)
111	270	1.1	60	0	0	0	(5)
112	270	1.1	60	0	45	0	3
113	270	1.1	60	0	90	0	(5)
114	270	1.1	60	0	135	0	(3)
115	270	1.1	60	0	0	90	(5)
116	0	2.0	60	0	0	45	1
117	0	2.0	60	0	45	45	3
118	0	2.0	60	0	90	45	0
119	0	2.0	60	0	135	45	2
120	0	2.0	60	0	180	45	2
121	0	2.0	60	0	225	45	2
122	0	2.0	60	0	270	45	4
123	0	2.0	60	0	315	45	1
124	0	2.0	60	0	45	0	1
125	0	2.0	60	0	90	0	4
126	0	2.0	60	0	135	0	2
127	0	2.0	90	0	0	45	(1)
128	0	2.0	90	0	45	45	(1)
129	0	2.0	90	0	90	45	(2)

Table 2 (Contd)

No.	L	$\frac{a}{R}$	i	Ω	α_A	δ_A	B1
130	0	2.0	90	0	135	45	(2)
131	0	2.0	90	0	225	45	(2)
132	0	2.0	90	0	270	45	(2)
133	0	2.0	90	0	315	45	(1)

Table 3

Dependence of the value of the directional error ϵ_n (minutes of arc) in the calculated normal to the reflecting surface on the error ϵ_B (minutes of arc) in the observed direction of the flash of light and on the angle θ (degrees) between the direction of the sun \vec{X}_\odot and the direction from the observer to the satellite (\vec{X}_B). (Using equation (35).)

$\epsilon_B \backslash \theta^\circ$	30°	50°	70°	90°	110°	130°	150°	170°
1	7.472	2.800	1.210	1.000	0.752	0.609	0.534	0.504
5	37.52	14.03	7.607	5.004	3.727	3.045	2.681	2.520
10	75.45	28.11	15.23	1.001	7.460	6.093	5.363	5.042
15	113.7	42.24	22.87	15.03	11.20	9.143	8.048	7.566
30	231.1	85.00	45.90	30.13	22.43	18.31	16.11	15.15
45	351.9	128.3	69.07	45.29	33.69	27.50	24.20	22.75
60	476.0	172.0	92.39	60.52	45.00	36.72	32.30	30.36
75	603.2	216.3	115.9	75.81	56.34	46.00	40.42	38.00
90	733.2	261.0	139.5	91.17	67.71	55.22	48.57	45.64
105	865.8	306.3	163.2	106.6	79.13	64.51	56.73	53.31
120	1000	352.0	187.2	122.1	90.57	73.82	64.90	61.00
180	1554	539.3	184.3	184.7	136.7	111.3	97.81	91.88
240	2110	733.3	383.6	248.2	183.4	149.2	131.6	123.9
300	4751	933.0	485.0	312.8	230.7	187.4	164.5	154.4

Table 4

Dependence of the angular error ϵ_A (minutes of arc) of the satellite axis on the directional error ϵ_N (minutes of arc) of the normals to be used in the calculation and on the angle γ (or $180^\circ - \gamma$) between these normals.

$\epsilon_N \backslash \gamma$	10°	20°	30°	40°	50°	60°	70°	80°	90°
1	11.5	5.77	3.87	2.93	2.37	2.00	1.74	1.56	1.41
5	58.3	29.0	19.4	14.7	11.9	10.0	1.73	7.78	1.07
10	118	58.5	39.0	29.4	23.8	20.1	17.5	15.6	14.1
15	181	88.5	58.8	44.3	35.8	30.2	26.2	23.4	21.2
30	381	181	120	89.6	72.0	60.6	52.6	46.8	42.4
45	600	279	182	136	109	91.4	79.2	70.3	63.6
60	841	381	246	183	146	122	106	93.9	84.8
75	1104	488	313	231	184	154	133	118	106
90	1388	599	381	280	222	185	160	141	127
105	1692	716	451	330	261	217	187	165	148
120	2013	838	523	381	301	250	214	189	170
180	3357	1377	833	595	464	382	325	285	254
240	4526	1987	1175	826	635	518	438	381	338
300	5365	2640	1548	1071	816	659	553	478	422

Table 5

Angle Γ (degrees) between two generators of the reflection cone as a function of β (degrees) and γ (degrees). From equation (56).

$\gamma \backslash \beta$	10°	20°	30°	40°	50°	60°	70°	80°	90°
5	1.74	3.42	5.00	6.42	7.66	8.66	9.40	9.85	10.0
10	3.46	6.81	9.96	12.8	15.3	17.3	18.8	19.7	20.0
15	5.15	10.2	14.9	19.2	22.9	25.9	28.2	29.5	30.0
20	6.81	13.4	19.7	25.4	30.4	34.5	37.5	39.4	40.0
25	8.42	16.6	24.4	31.5	37.8	42.9	46.8	49.2	50.0
30	9.96	19.7	29.0	37.5	45.0	51.3	56.1	59.0	60.0
35	11.4	22.6	33.3	43.3	52.1	59.6	65.2	68.8	70.0
40	12.8	25.4	37.5	48.8	59.0	67.7	74.3	78.6	80.0
45	14.1	28.0	41.4	54.1	65.6	75.5	83.3	88.3	90.0
50	15.3	30.4	45.0	59.0	71.9	83.1	92.1	98.0	100
55	16.4	32.5	48.4	63.5	77.7	90.4	101	108	110
60	17.3	34.5	51.3	67.7	83.1	97.2	109	117	120
65	18.1	36.1	53.9	71.3	87.9	103	117	126	130
70	18.8	37.5	56.1	74.3	92.1	109	124	136	140
75	19.3	38.6	57.8	76.8	95.5	114	130	144	150
80	19.7	39.4	59.0	78.6	98.0	117	136	152	160
85	19.9	39.8	59.8	79.6	99.5	119	139	158	170
90	20.0	40.0	60.0	80.0	100	120	140	160	180

Table 6

Angle between the normals (γ) from combinations of observations from observing stations indicated in Figs.13 to 19.

Figure No.	Example No.	Station 1	Station 2	γ°
13	117	a	b	33
14	2	a b c a e h f i a	b c d d g k h d k	11 37 30 78 76 74 22 59 77
15	125	a c a	b d d	22 25 55
16	122	a c b	b d c	27 28 61
18	7	a b a	b c c	24 33 57
19	112	a b a	b c c	39 37 76

REFERENCES

<u>No.</u>	<u>Author</u>	<u>Title, etc.</u>
1	W. R. Bandeen W. P. Manger	Angular motion of the spin axis of the TIROS I Meteorological Satellite due to magnetic and gravitational torques. J. Geophys. Res. <u>65</u> , 2992, (1960)
2	J. Boehm	Mechanical system, design engineering and packaging of Explorer VII in Juno II Summary Project Report Vol.I (Explorer VII satellite). N.A.S.A. Technical Note D 608, (1961)
3	R. J. Davis R. C. Wells F. L. Whipple	On determining the orientation of a cylindrical artificial satellite. Astronautica Acta, III, 232, (1957)
4	R. C. Doolittle L. I. Miller I. S. Ruff	Geographic location of cloud features in final Report on the TIROS I Meteorological Satellite System. N.A.S.A. Technical Report R-131, (1962)
5	R. H. Giese	Attitude determination from specular and diffuse reflection by a cylindrical artificial satellite. Smithsonian Institution Astrophysical Observatory, Research in Space Science, Special Report 127, (1963)
6	R. H. Giese	Zur optischen Bestimmung der räumlichen Orientierung rotierender künstlicher Satelliten. (Concerning the optical estimation of the space orientation of rotating artificial satellites.) Raketentechnik und Raumfahrtforschung VII, 141, (1963)
7	N. H. Hatcher E. F. Germann, Jr.	Study of a proposed infrared horizon scanner for use in Space Orientation Control Systems. N.A.S.A. Technical Note D-1005, (1962)
8	D. W. Hill	Calculation of the spin axis orientation of the TELSTAR Satellites from optical data. Bell System Tech. Journ. <u>42</u> , 2943, (1963)

REFERENCES (Contd)

<u>No.</u>	<u>Author</u>	<u>Title, etc.</u>
9	R. T. Hutchison R. A. Swift	Results of the TELSTAR Satellite Space Experiments in TELSTAR I. N.A.S.A. Sp.32, Vol.2, (1963)
10	B. K. Lunde	Horizon sensing for attitude determination. Goddard Memorial Symposium, Washington D.C., (1962)
11	R. J. Naumann	Recent information gained from Satellite Orientation Measurement. Planetary and Space Science, <u>7</u> , 445, (1961)
12	R. J. Naumann	An investigation of the observed torques acting on Explorer XI. Goddard Memorial Symposium, Washington, D.C., (1962)
13	R. J. Naumann	Observed torque producing forces acting on satellites (Ed. M. Roy) Dynamics of Satellites. Berlin, Göttingen, Heidelberg, (1963)
14	P. Notni H. Oleak	Die rotation der trägerrakete von Sputnik III. (The rotation of the rocket of Sputnik III.) (1958 Delta 1). Publication of Sternwarte Babelsberg XIII, Vol.4, (1959)
15	J. R. Scull	The application of optical sensors for lunar and planetary space vehicles. JPL Technical Report 32-274, Pasadena (1962)
16	G. Veis	Optical tracking of artificial satellites. Space Science Reviews <u>2</u> , 250, (1963)
17	R. H. Wilson	Rotational magnetodynamics and steering of space vehicles. N.A.S.A. Technical Note D 566, (1961)
18	R. H. Wilson	Rotational decay of satellite 1960 Eta 2 (Solar Radiation I). XII International Astronautical Congress, Washington, D.C. (1961)

REFERENCES (Contd)

<u>No.</u>	<u>Author</u>	<u>Title, etc.</u>
19	W. P. Zessewich	Über den Lichtwechsel der sowjetischen Erdsatelliten. (Concerning the variation of exposure to light of the soviet earth satellites.) IAU - Tagung, Moskau, (1958)
(Textbook)	R. M. L. Baker M. W. Makemson	An Introduction to Astrodynamics, New York, London, 1960
(Textbook)	A. Bohrmann	Bahnen künstlicher Satelliten. (Orbits of artificial satellites.) Mannheim, 1963
(Textbook)	T. Thomson	Introduction to Space Dynamics, New York, London, 1961

ILLUSTRATIONS

- Fig.1 The equatorial system
- Fig.2 The orbital system
- Fig.3 Vectors used particularly frequently
Sonne = sun
- Fig.4 Determination of the normal to the reflecting surface
Beobachter = observer
Richtung zur sonne = direction to sun
- Fig.5 "Tumbling" motion
- Fig.6 "Spin" motion
- Fig.7 Definition of reflection cone
Lichtkegel = cone of light
- Fig.8 } Conditions for the absence of reflection flashes
- Fig.8(a) }
- Fig.9 Illustration of one case when reflection cones by-pass the earth throughout a revolution of the satellite
Reflexionskegel = reflection cone
Bahnebene = orbital plane
Erde = earth
- Fig.10 Flashes of light observable; the satellite is illuminated by the sun
Sonnenlicht = sunlight
Erdschatten = earth's shadow

ILLUSTRATIONS (Contd)

- Fig.11 Flashes of light observable; the satellite is above the horizon of the observer
 zur Sonne = to sun
- Fig.12 Programme calculating flash curves
- Fig.13-19 Examples of computed flash curves
- ζ geographical latitude
 λ geographical longitude
 a radius of orbit
 R radius of earth
 i inclination
 L celestial longitude of the sun
 α_A right ascension of the satellite axis
 δ_A declination of the satellite axis
 Tag = day
 Nacht = night
- Fig.20 See text 4.3
- Fig.21 See text 4.3
- Fig.22 Position of visibility bands (curve parameter: time in minutes)
 Example 2, Table 2
- Fig.23 Position of visibility bands: example 7, Table 2
- Fig.24 Position of auxiliary plane
- Fig.25 See text 4.4
- Fig.26 Lines of intersection of the limiting cones with the auxiliary plane

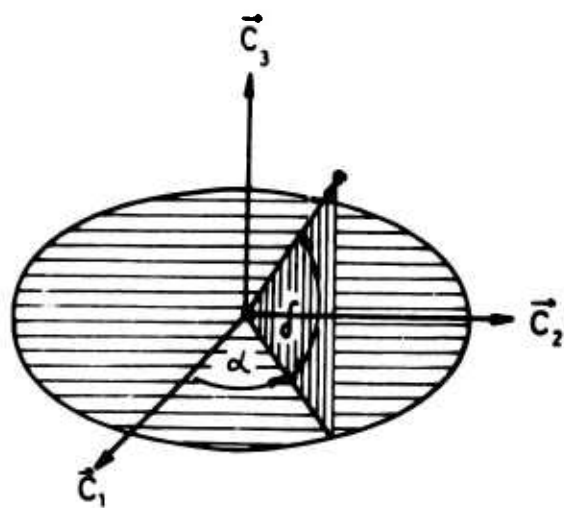


Fig.1

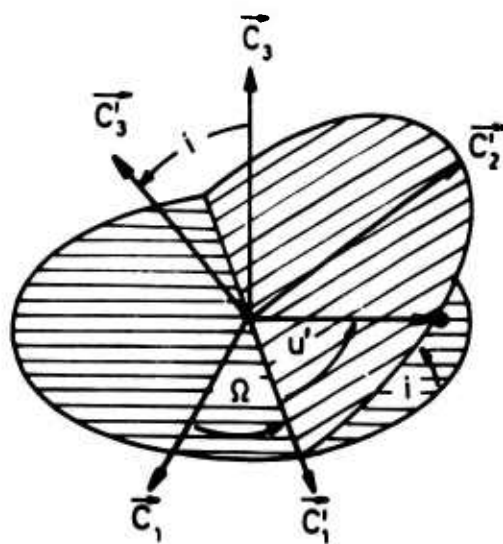


Fig.2

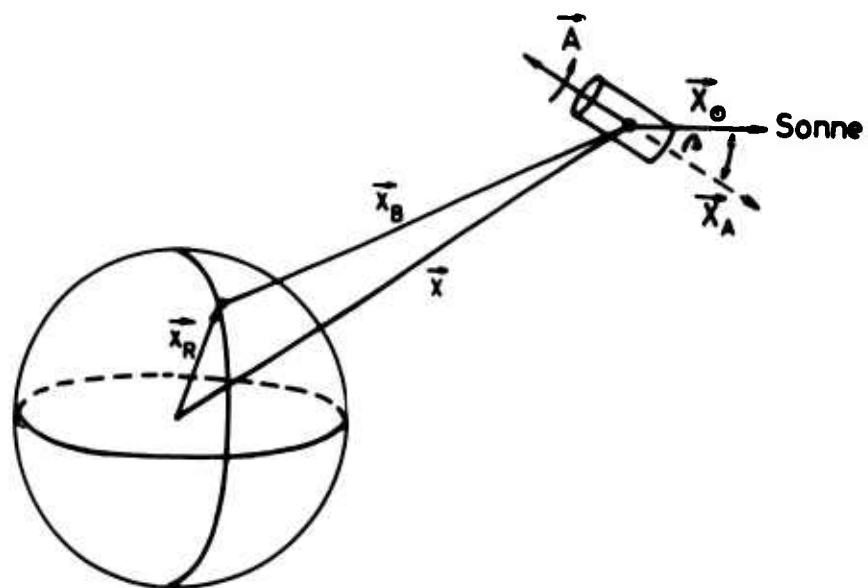


Fig.3

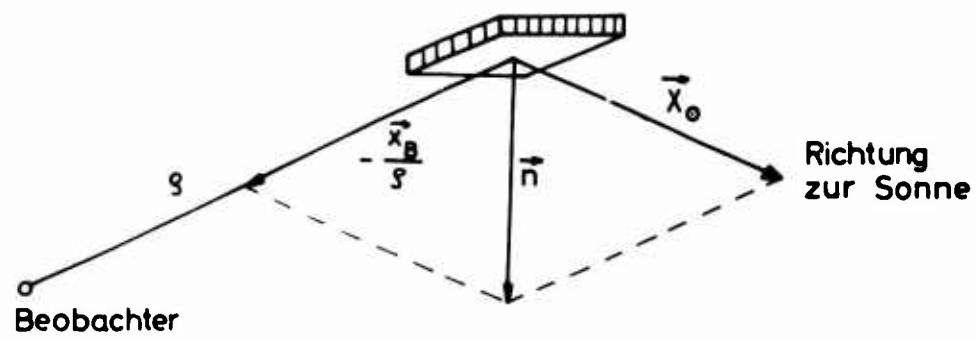


Fig.4

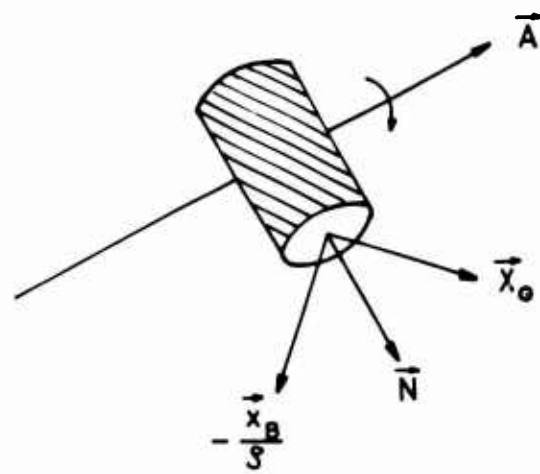


Fig.5

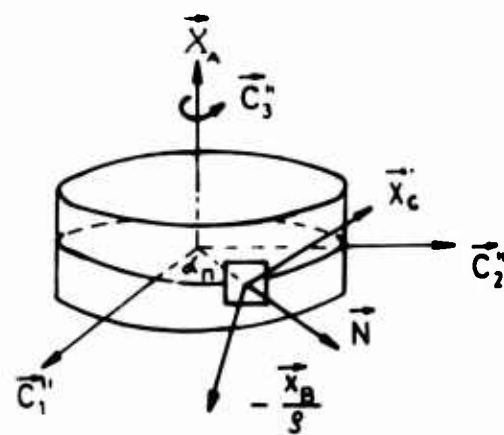


Fig.6

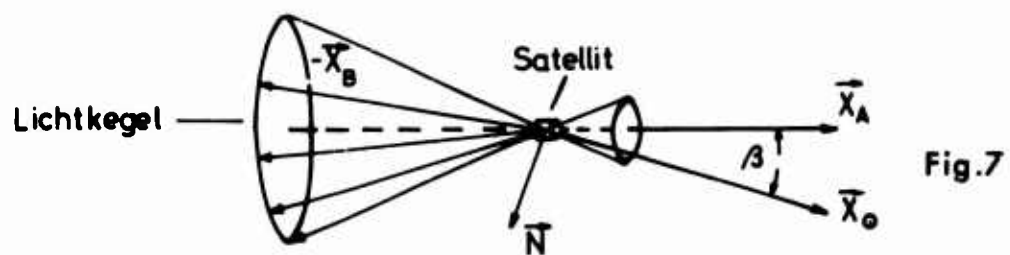


Fig.7

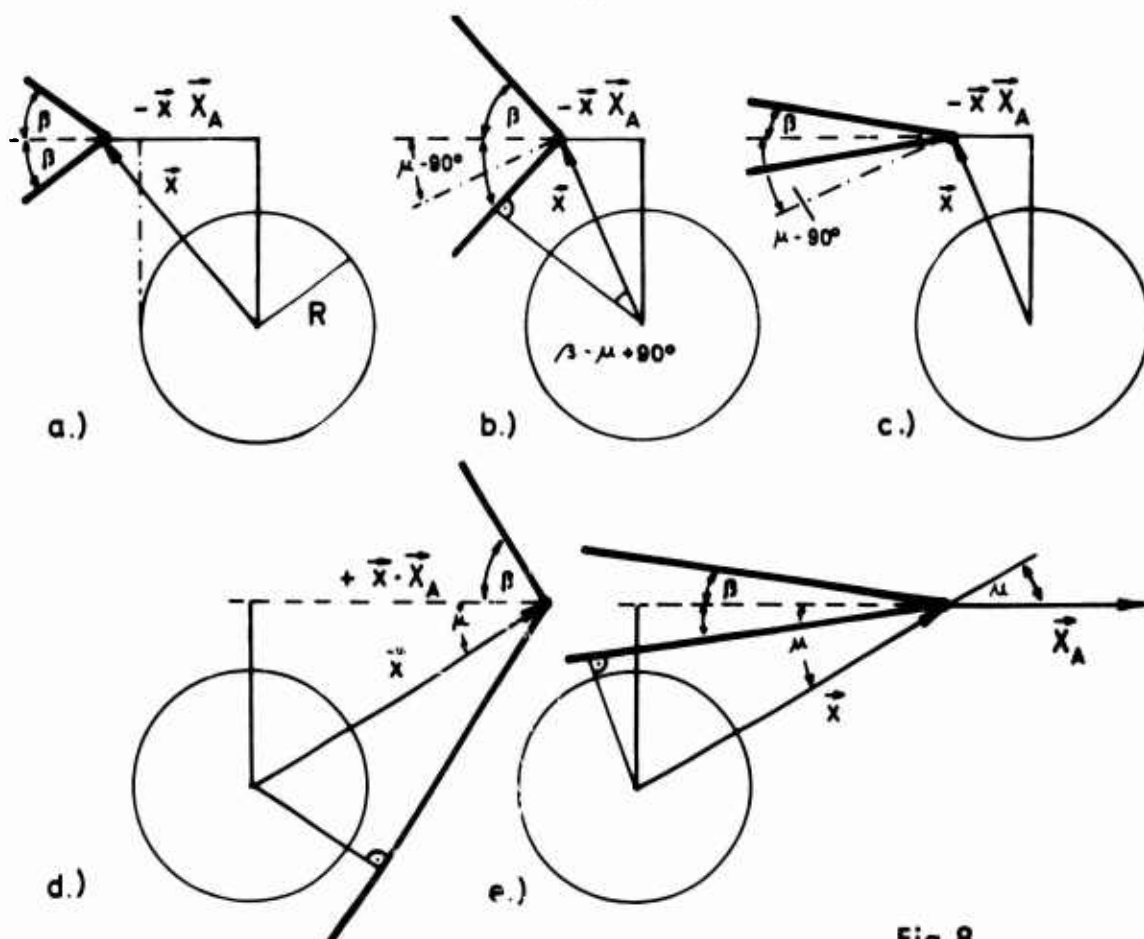


Fig.8

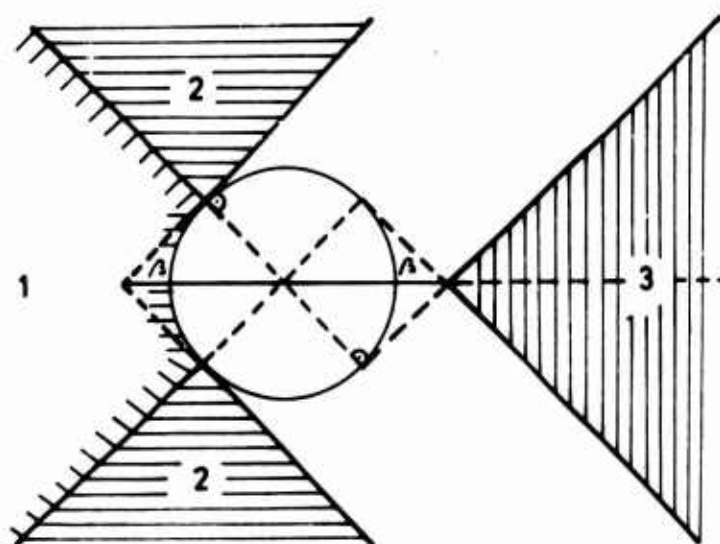


Fig.8a

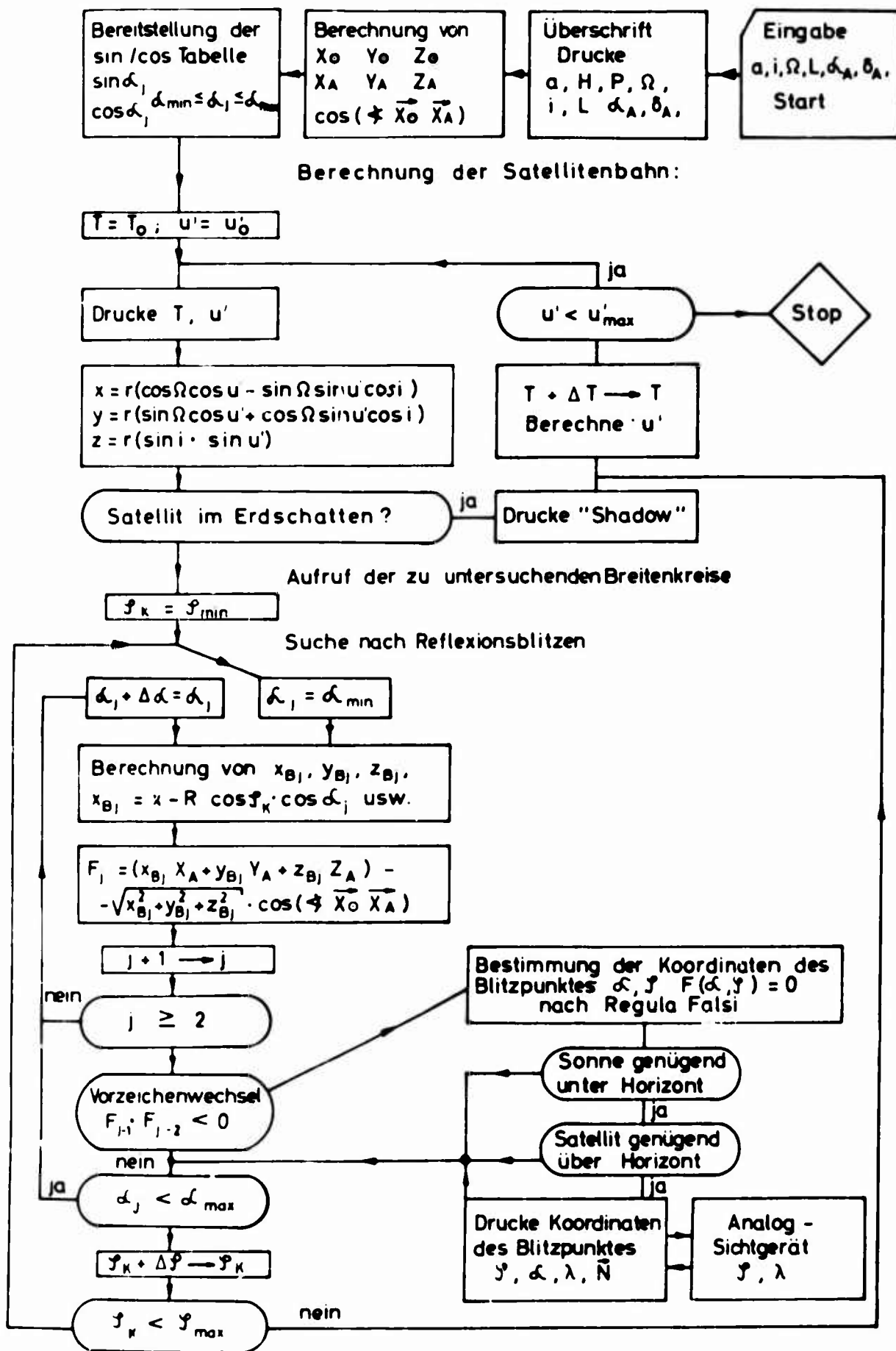


Fig.12

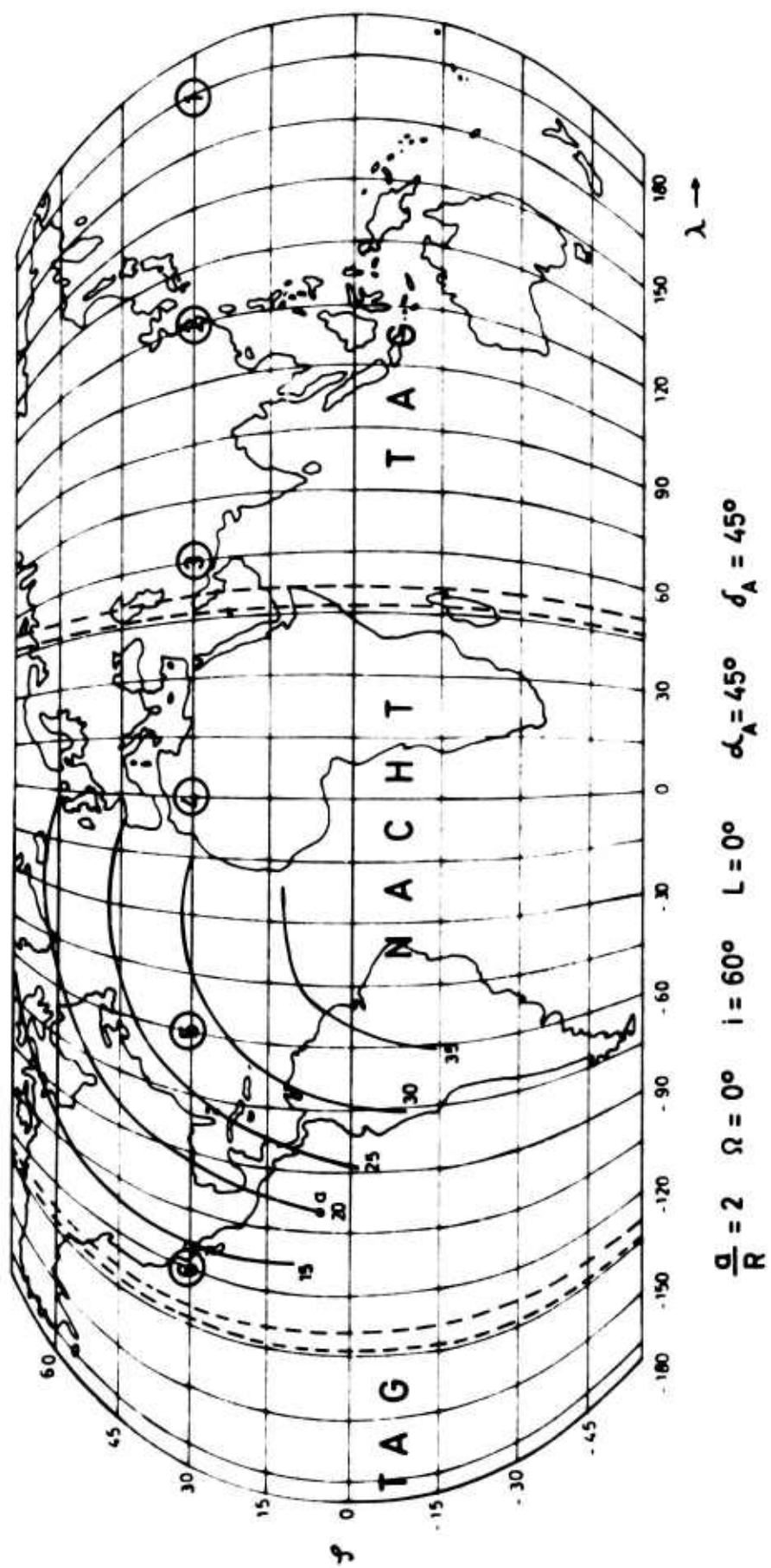


Fig.13

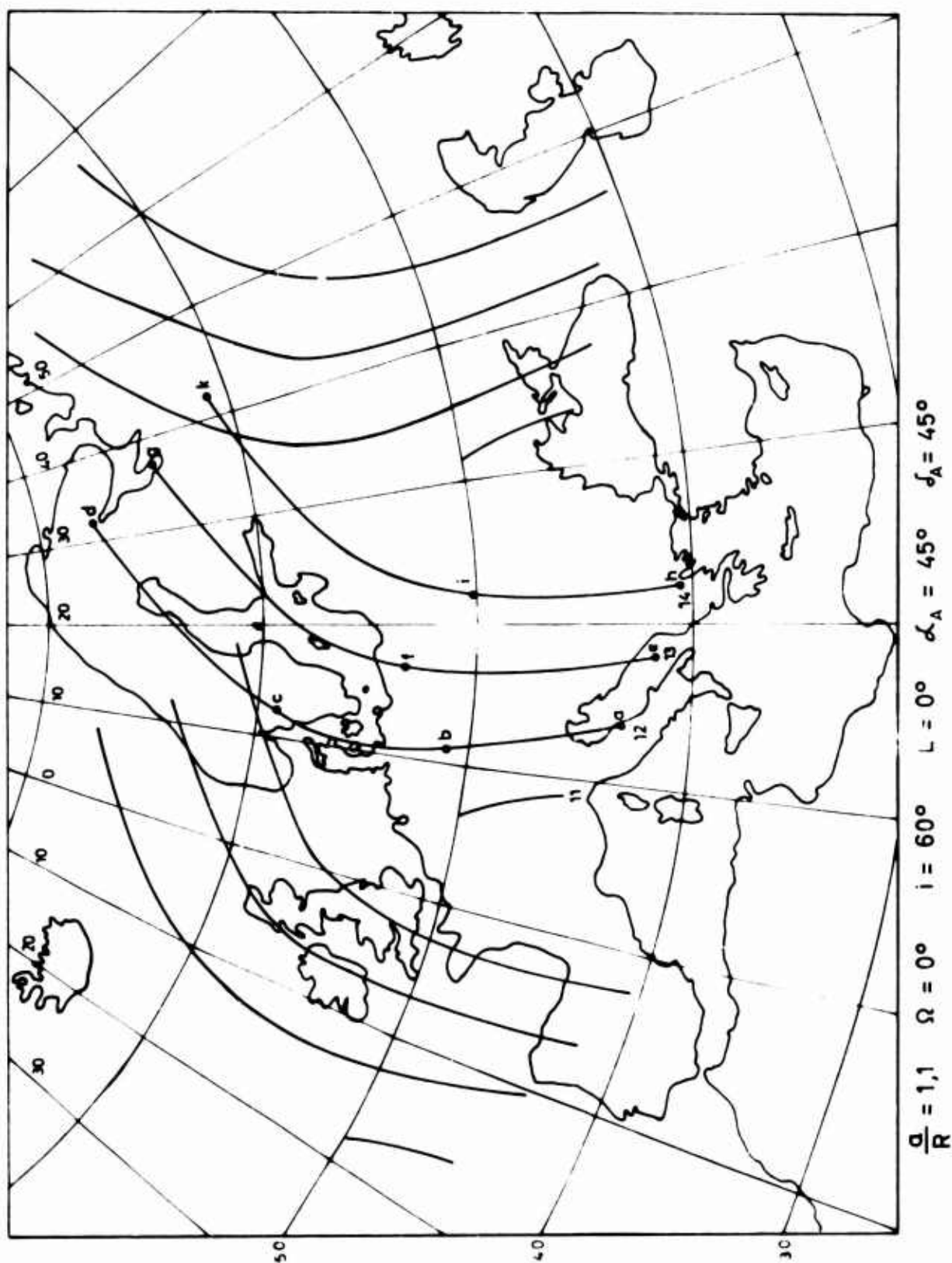
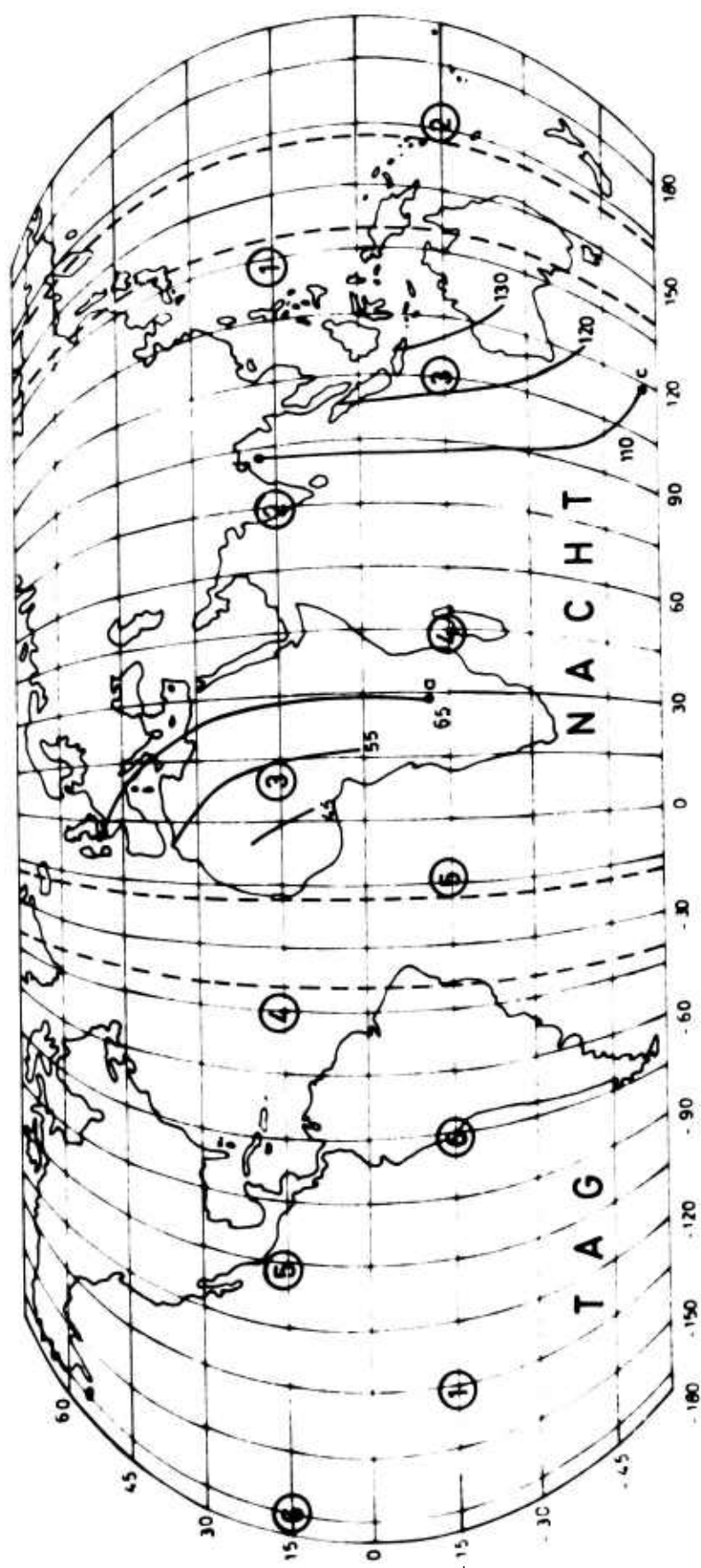
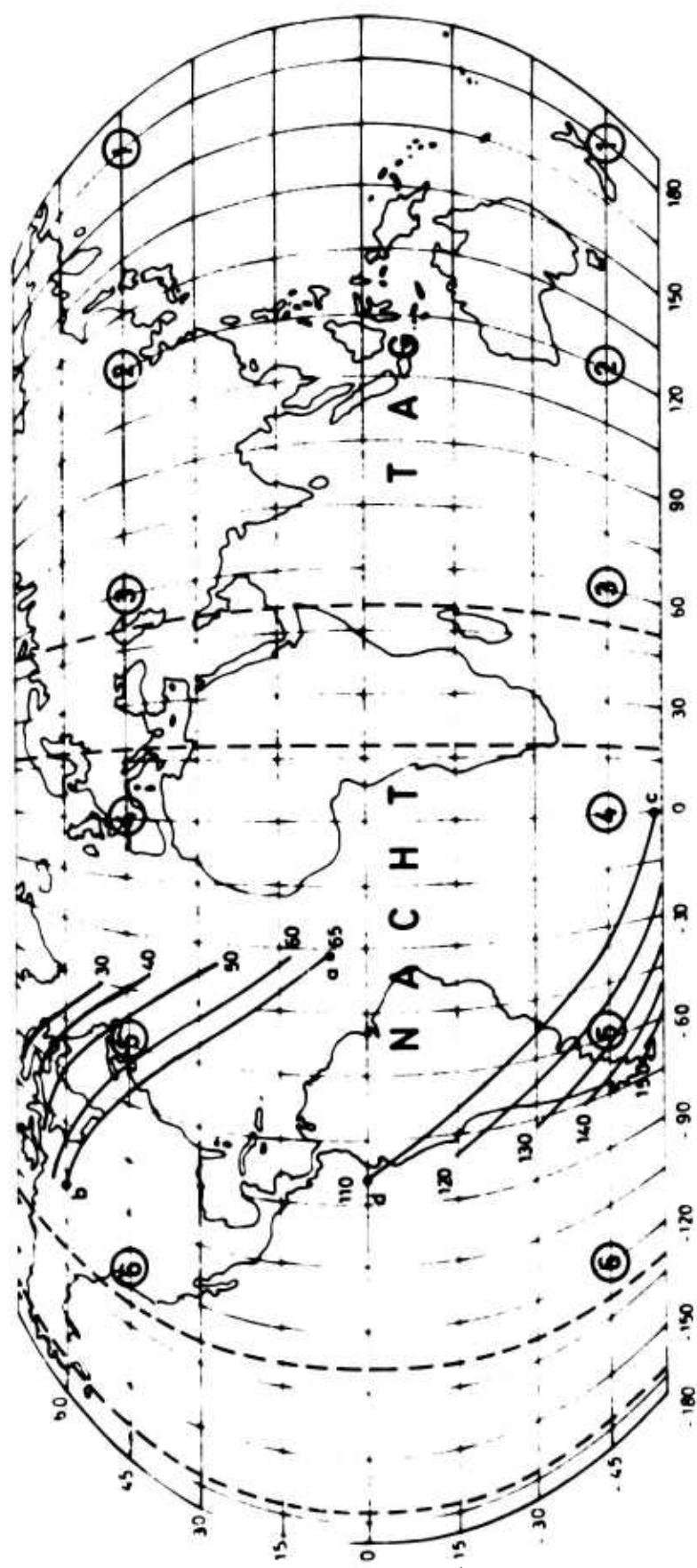


Fig.14



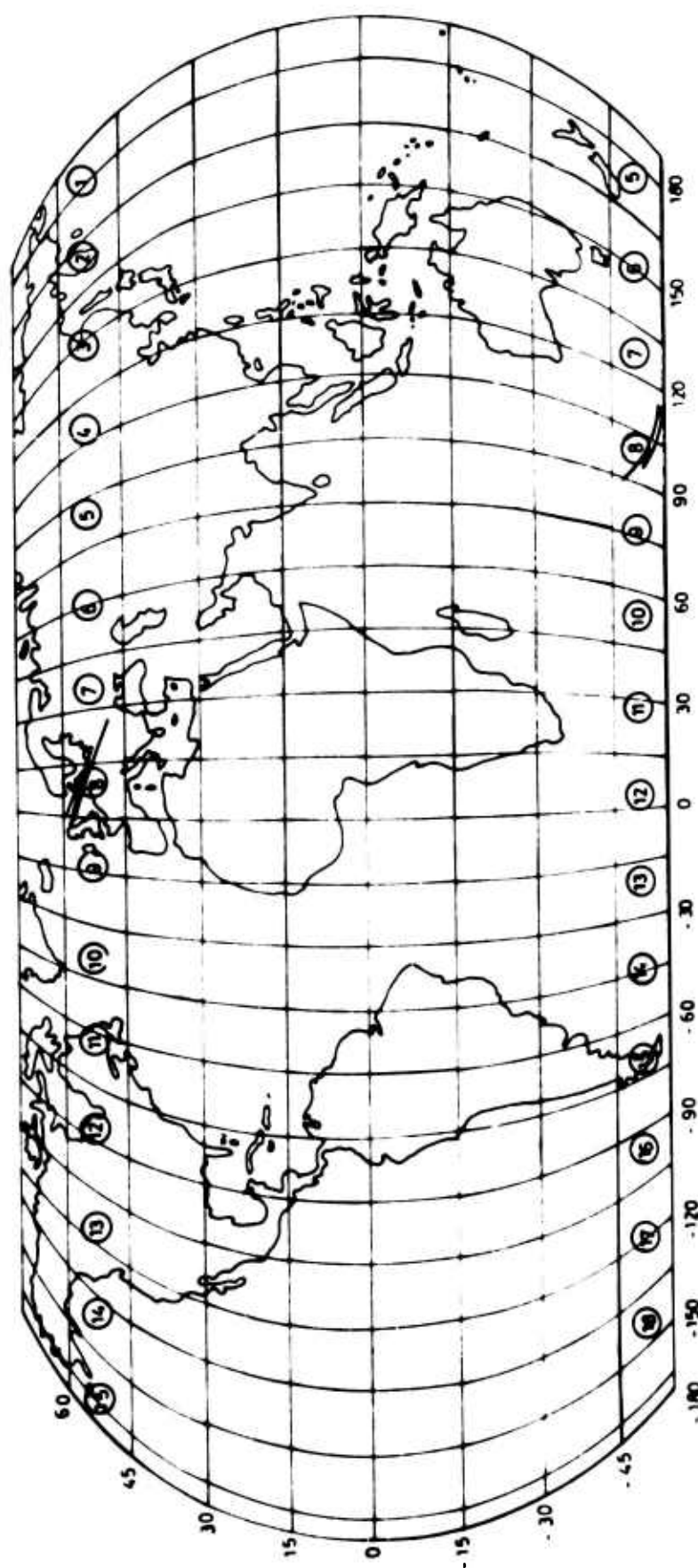
$$\frac{a}{R} = 2 \quad \Omega = 0^\circ \quad i = 60^\circ \quad L = 0^\circ \quad \alpha_A = 90^\circ \quad \delta_A = 0^\circ$$

Fig.15



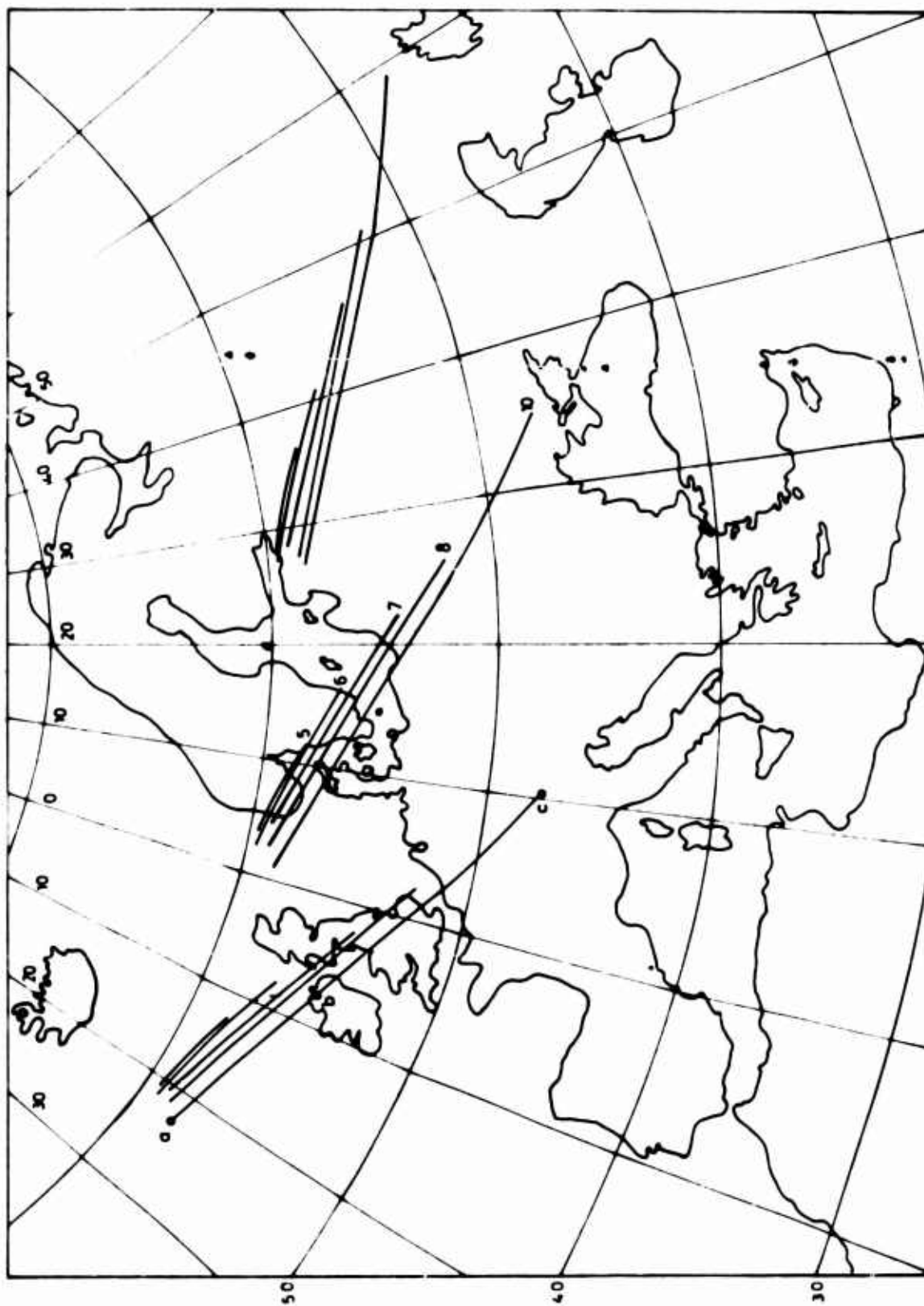
$$\frac{a}{R} = 2 \quad \Omega = 0^\circ \quad i = 60^\circ \quad L = 0^\circ \quad \alpha_A = 270^\circ \quad \delta_A = 45^\circ$$

Fig.16



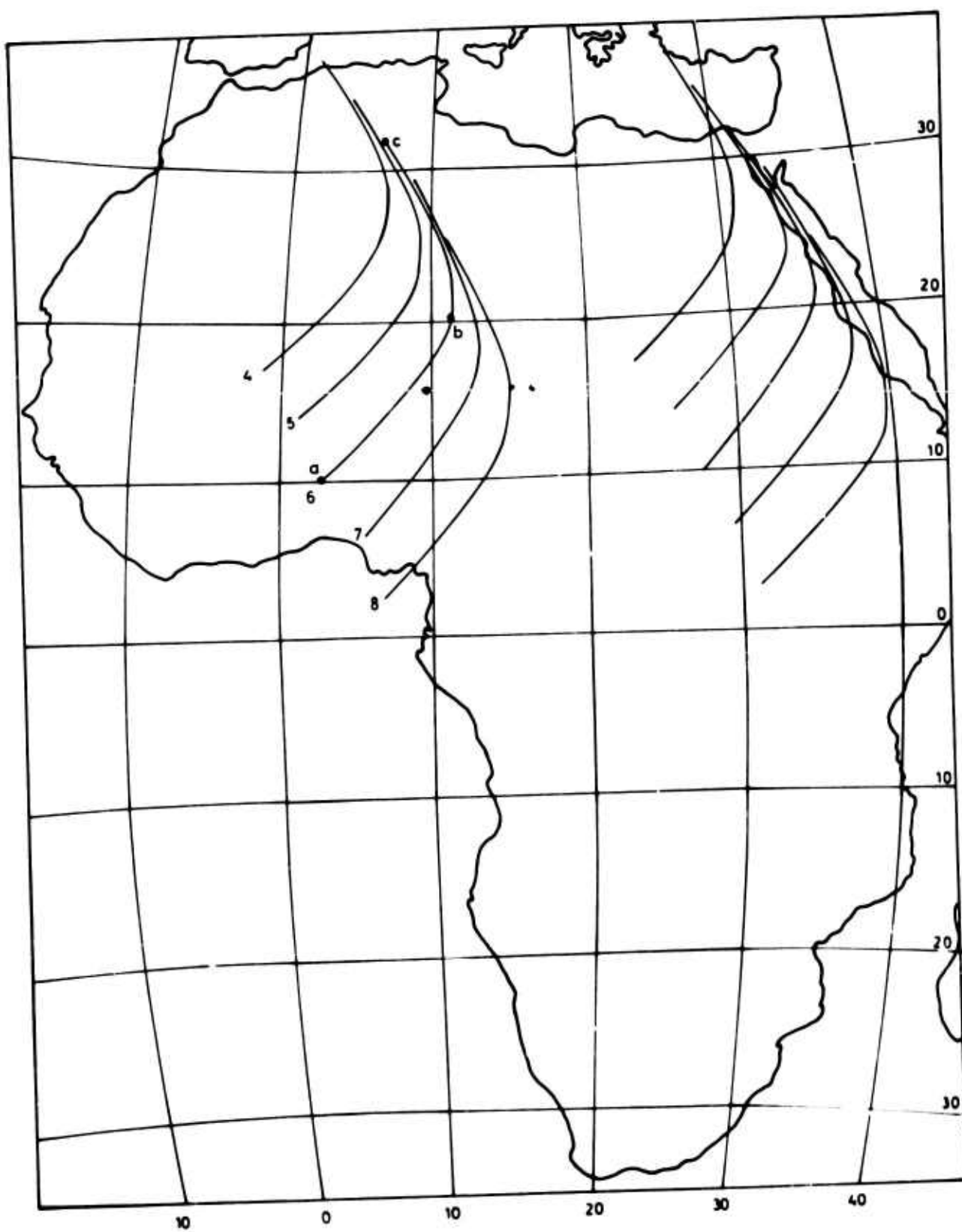
$$\frac{a}{R} = 1,1 \quad \Omega = 0^\circ \quad i = 60^\circ \quad L = 0^\circ \quad \alpha_A = 270^\circ \quad \delta_A = 45^\circ$$

Fig.17



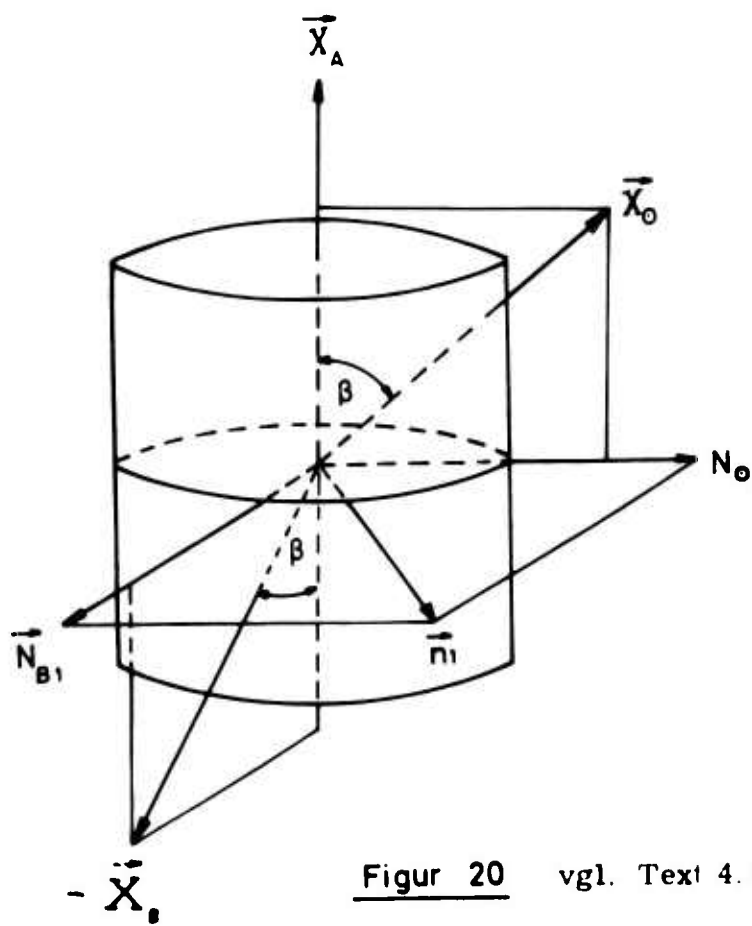
Figur 18 $\frac{a}{R} = 1,1$ $\Omega = 0^\circ$ $i = 60^\circ$ $L = 0^\circ$ $\alpha_A = 270^\circ$ $\delta_A = 45^\circ$

Fig.18



$$\frac{a}{R} = 1,1 \quad \Omega = 0^\circ \quad i = 60^\circ \quad L = 270^\circ \quad \alpha_A = 45^\circ \quad \delta_A = 0^\circ$$

Fig.19



Figur 20 vgl. Text 4.3

Fig.20

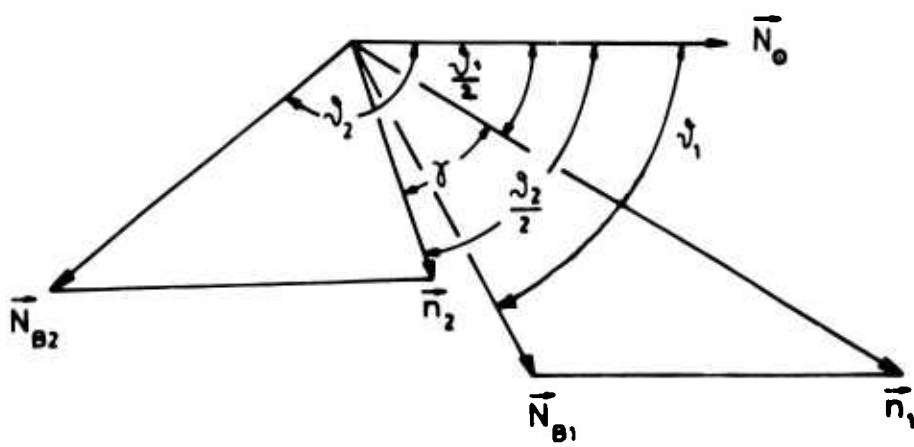
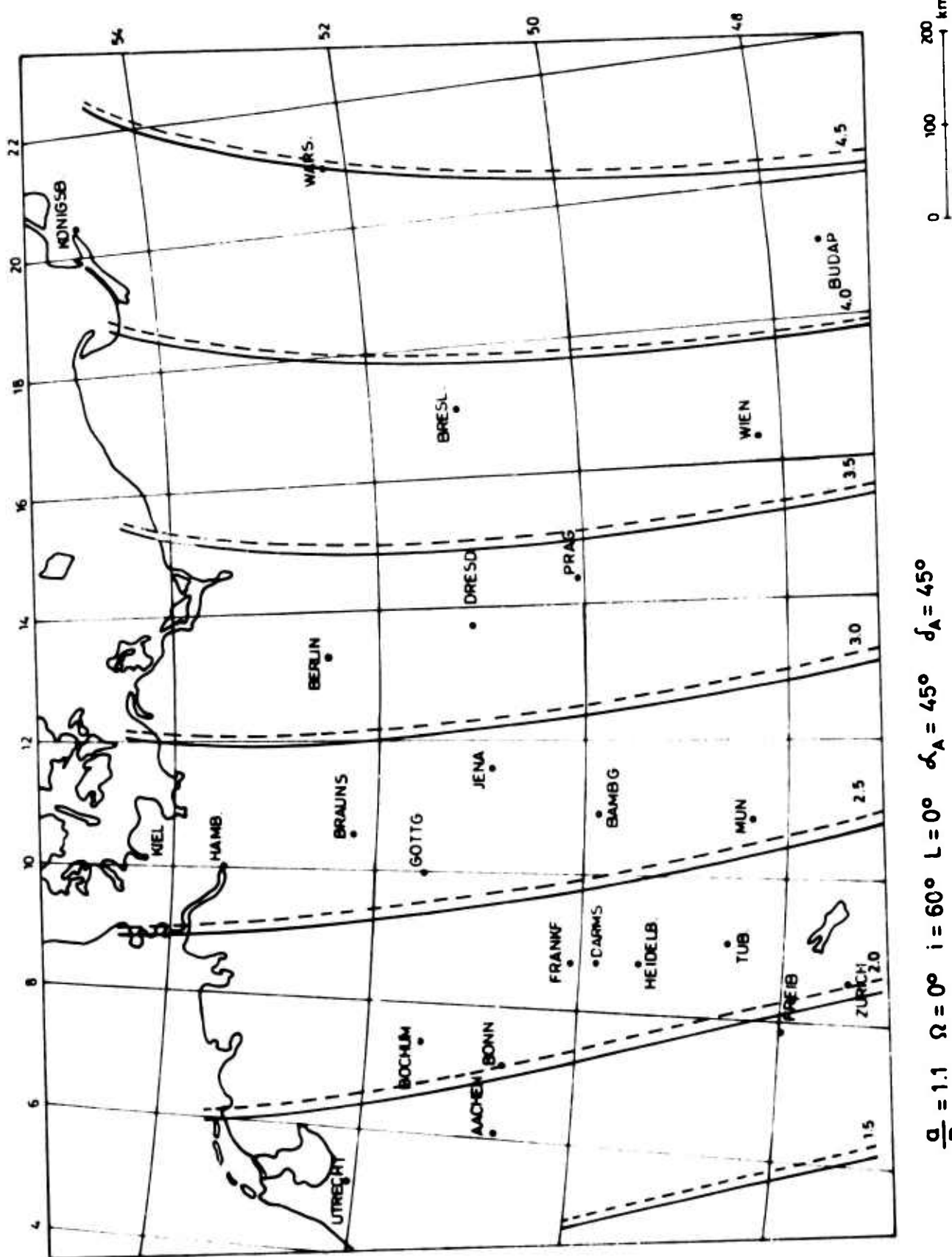
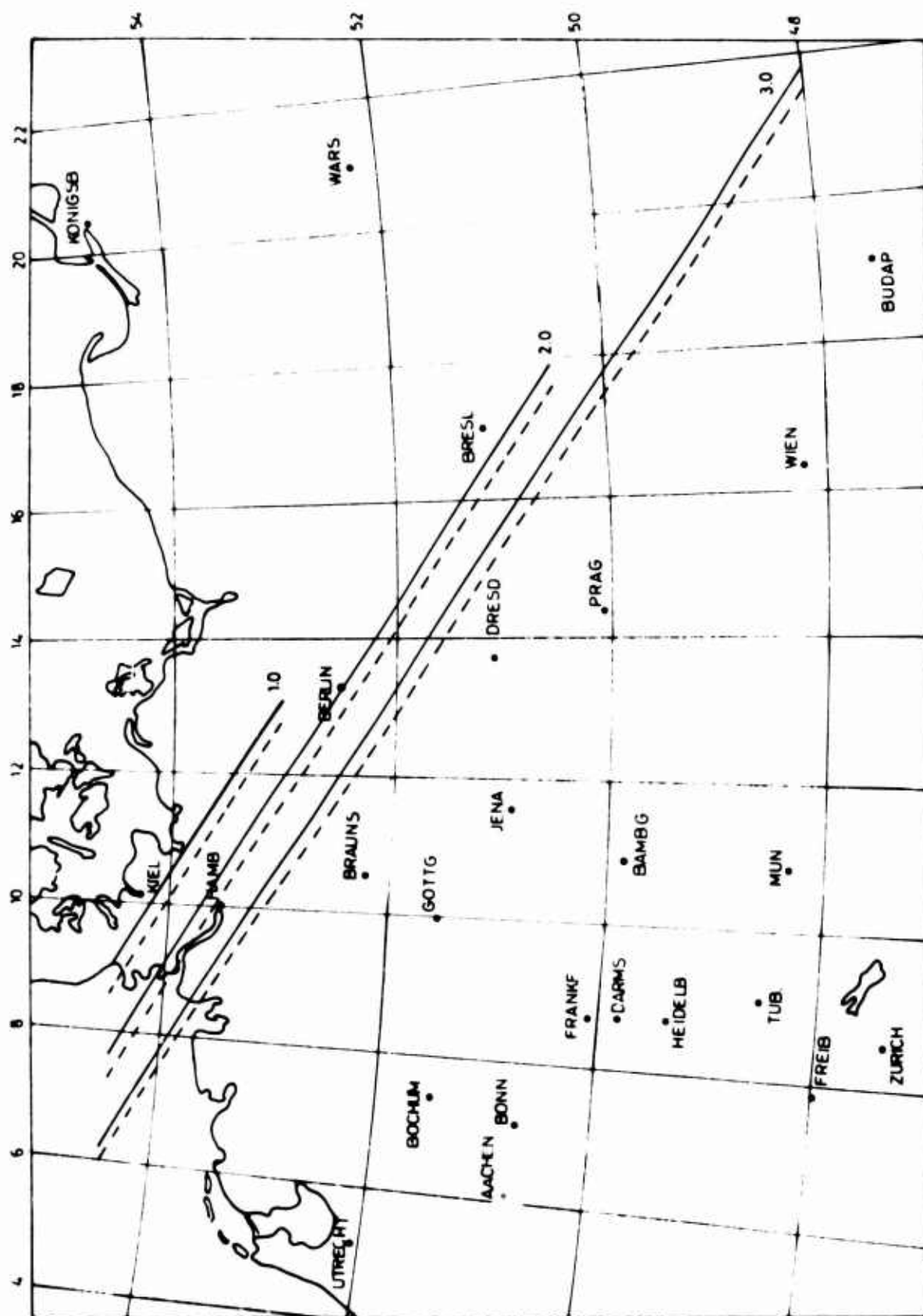


Fig.21





$$\frac{a}{R} = 1.1 \quad \Omega = 0^\circ \quad i = 60^\circ \quad L = 0^\circ \quad \alpha_A = 270^\circ \quad \delta_A = 45^\circ$$

Fig.23

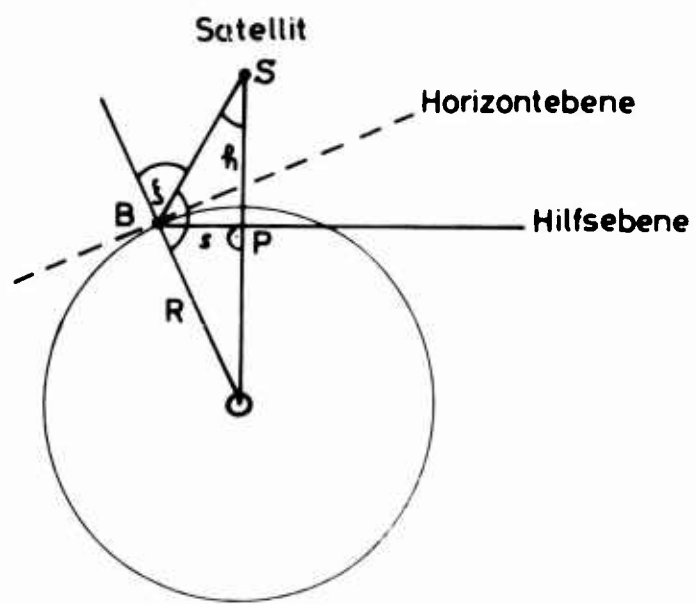


Fig.24

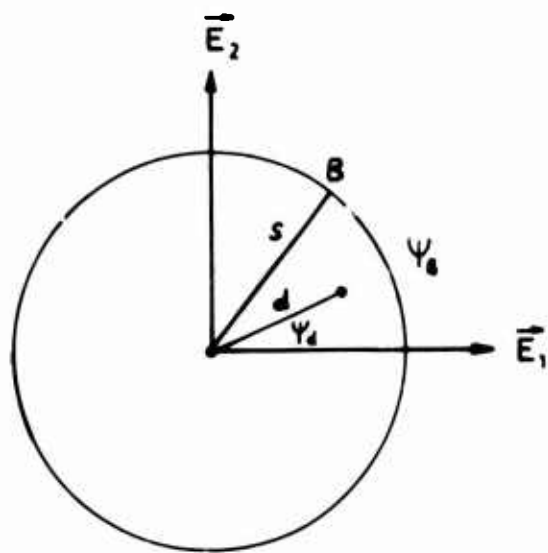


Fig.25

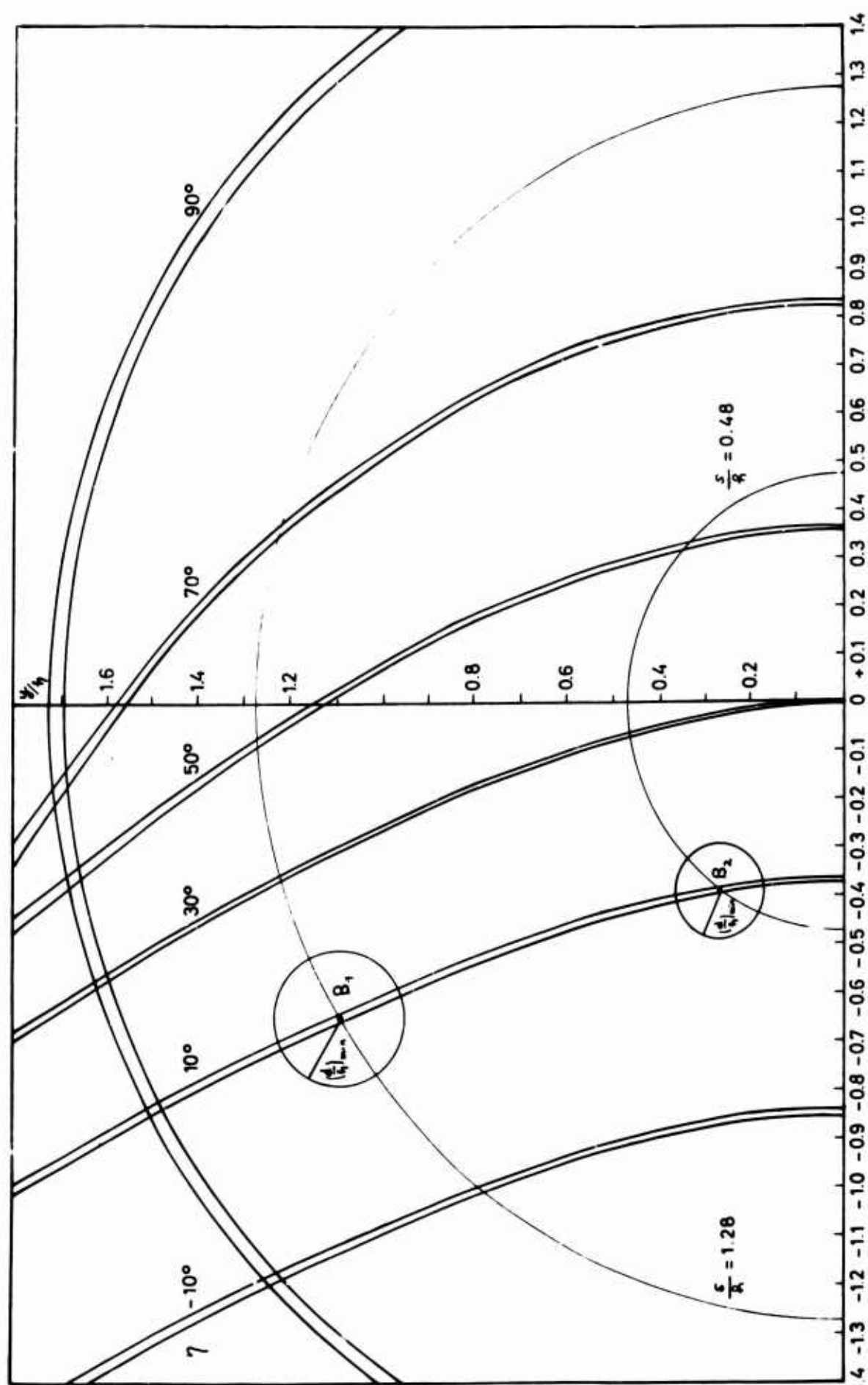


Fig.26

OPTICAL STUDIES OF SPACECRAFT
FROM THE CLOUDCROFT FACILITY

E. T. TYSON
Electro-Optical Site
Cloudcroft, New Mexico

ABSTRACT

OPTICAL STUDIES OF SPACECRAFT FROM THE CLOUDCROFT FACILITY

E. T. TYSON

Data, consisting primarily of resolved and quasi-resolved images, are collected with a 48-inch telescope whose effective focal length can be varied between 312 and 6000 inches. Although image recording has been tried using vicon, image orthicon, and direct photography, none of these methods has been found to match the eye of a trained observer for signal separation from noise and adaptability to rapid and extreme brightness fluctuations.

A 16-mm movie made from a video tape recording of a Saturn S-IVB stage was shown, which provided an example of resolution quality, and the effect of large fluctuations in brightness.

THE DESIGN AND OPERATION OF SOME DEVICES
FOR PHOTO-ELECTRIC AND PHOTOGRAPHIC
REGISTRATION OF ARTIFICIAL SATELLITES

Kenneth Fea
University of London
London, England

ABSTRACT

THE DESIGN AND OPERATION OF SOME DEVICES FOR PHOTO-ELECTRIC AND PHOTOGRAPHIC REGISTRATION OF ARTIFICIAL SATELLITES

Kenneth Fea

Photoelectric techniques are applied to satellite position measurement, where precision is comparable to that of the highest quality Baker-Nunn photographic techniques. The method described employs a 6-inch $f/8$ objective with a 10-inch tri-alkali photocathode behind an M-shaped linear slit system. Satellite images trail across the slits producing pulses in the photoelectric output. Intervals between pulses are related to image position through the M pattern. Simultaneous photography and photoelectric sensing of stars is used for equipment calibration. Resulting satellite positions are measurable to one arc second.

RESULTS OF PHOTOMETRIC AND POLARIMETRIC
MEASUREMENTS OF VARIOUS SATELLITES
USING NASA'S MOBILE PHOTOMETRIC OBSERVATORY

Richard H. Emmons and Raymon J. Preski
Goodyear Aerospace Corporation
Akron, Ohio

RESULTS OF PHOTOMETRIC AND POLARIMETRIC MEASUREMENTS OF
VARIOUS SATELLITES USING NASA'S MOBILE PHOTOMETRIC OBSERVATORY*

Richard H. Emmons⁺ and Raymond J. Preski⁺

Goodyear Aerospace Corporation
Akron, Ohio

1. INTRODUCTION

Under contracts NAS1-6189 and NAS1-6436 with the National Aeronautics and Space Administration (NASA) Langley Research Center, Goodyear Aerospace Corporation has obtained and analyzed multicolor photometric measurements of the Echo I, Echo II and PAGEOS I balloon-type satellites, to establish a time-history of their approximate size, figure and their surface reflectance, specularity and polarization as functions of wavelength. These observations were made using NASA's Mobile Satellite Photometric Observatory which was developed for the Langley Research Center by Goodyear Aerospace Corporation under Contract NAS 1-5580.

2. INSTRUMENTATION

The mobile observatory's new, cryogenically-cooled UBURI photometer head, shown in Figure 1, provides up to four simultaneous intensity signal channels with two pairs of matched S-20 and S-1 photomultipliers, arranged to beam-share and simultaneously photometer both the target field and the adjacent sky. For the photometric mode, matched pairs of field stops from 30 arc seconds to 4 arc minutes are provided. UVB color filters are time-shared on the S-20 detectors, while VRI filters are time-shared on the S-1 detectors. Polarimetric measurements may alternatively be made in each of these colors by re-positioning both the single 2-minute arc central field stop and the stowed Wollaston prism into the light path, and then manually rotating the entire photometer head on a

* This work is supported by the Langley Research Center (NASA), Hampton, Va., under Contract NAS1-6436.

⁺ Space Systems and Analytics Division, Goodyear Aerospace Corporation, Akron, Ohio.

precision bearing through seven keyed 36-degree steps. UVB polarimetric measurements can also be made automatically by repositioning the stowed achromatic half-wave plate into the optical path and initiating its automatic 36-degree stepped rotations. Signals indicating the intensities, amplifier gains, color filters, and half-wave plate orientations are fed, together with radio time signals, to a recorder in the instrumentation room.

Figure 2 presents the normalized response curves and effective wavelengths for the standard UBVRI color bands. These five bands span about 70 percent of the solar energy. The availability of hundreds of photometric reference stars which have been repeatedly measured in these colors permits highly accurate calibration of the UBVRI satellite observations.

The principle by which sunlit spherical satellite's specularly may be determined from the photometric observations is presented in the following equations.

Illuminance ratios of spherical satellites:

$$\begin{aligned} \text{Specular: } \frac{F_{sp}}{E_o} &= \text{Antilog} (-0.4m) = 1/4 \frac{E_s}{E_o} \left(\frac{R}{D} \right)^2 \\ \text{Diffuse: } \frac{E_d}{E_o} &= \text{Antilog} (-0.4m) = 2/3 \frac{E_s}{E_o} \left(\frac{R}{D} \right)^2 f(\psi) \\ f(\psi) &= \frac{1}{\pi} \left[\sin \psi + (\pi - \psi) \cos \psi \right] \end{aligned}$$

Regression equation for determining specularly:

$$\begin{aligned} \text{Antilog} (-0.4m) &= 1/4A + 2/3B f(\psi) \\ \text{Specularity} &= \frac{A}{A + B} \end{aligned}$$

The first two equations (from Tousey, Reference 1) predict the extra-atmospheric stellar magnitude, m (or illuminance ratios, $\frac{E}{E_o}$) of 100 percent reflecting specular and diffuse spheres of radius R and distance D . The phase function, $f(\psi)$ (from Russell, Reference 2) gives the dependence of the illuminance upon phase angle for a perfectly diffuse sphere, whose surface reflects in accordance with Lambert's cosine law. By eliminating the common factors in these equations, the regression equation is found which weighs and sums the specular and diffuse components in relation to the processed satellite observations (Reference 3). Prior to performing this regression analysis, the

satellite's reduced magnitudes are corrected for Earth albedo and normalized to a uniform distance and the instantaneous phase angles are computed. After the best-fit solution is obtained for the two weighting coefficients (specular (A) and diffuse (B)) the "specularity", as a fraction of the total reflected light, is found simply by evaluating $\frac{A}{A + B}$.

For spherical satellites that are found to be highly specular, the small diffuse component of the reflected sunlight can be computed and subtracted from the illuminance. This net "specular magnitude" can then be employed in the theory to determine either the satellite's reflectance or radius of curvature, or parametrically, both.

3. OBSERVATIONS AND RESULTS

The first observations with NASA's Mobile Satellite Photometric Observatory were made during the summer of 1966 from Palomar Mountain, California, from a peak opposite that occupied by the famous 200-inch Hale telescope. The mobile observatory's original single channel UVB photometer was used there to observe both the Echo I and PAGEOS satellites, the latter during the first 60 days of its orbital life (Reference 4). Upon completion of the new UVBRI photometer and polarimeter these satellites were re-observed, as well as Echo II, from the desert floor near Yuma, Arizona, in the winter of 1967. Table I presents the results of all these photometric observations, together with some early (1964) visual-band results for Echo I.

The principal findings from the visual-band photometric data for the three satellites are summarized in Table II.

The measured color indices, in stellar magnitudes, are presented in Table III together with the reference solar values. The ultraviolet deficiency in the light reflected from Echo I and PAGEOS is as expected, and appears to increase with time.

Figure 3 presents PAGEOS' indicated mean and extreme radii of curvature versus 1966 date, from the Palomar observations. The effect of the first contact with the Earth's shadow on July 14 is clearly shown. The relative stability regained in early August, after six weeks in orbit, may be associated with the loss of most or all of the more volatile inflation gases.

Figure 4 presents the visual band polarimetric determinations versus phase angle. The solid curve is the theoretical curve for bare aluminum. There seems to be an indication here that Echo II may have lost some of its amorphous phosphate thermal balance coating.

4. REFERENCES

1. Tousey, R., "Optical Problems of the Satellite," Journal Optical Society of America, Volume XLVII, Page 261. (1957).
2. Russell, H. N., "On the Albedo of the Planets and Their Satellites," Astrophysical Journal, Volume XLIII, Page 173 (1916).
3. Emmons, R. H., "An Indicated Specular Degradation Rate for Aluminized Mylar Surfaces in Near-Earth Orbit From Recent Photometric Observations of the Echo I Satellite," GER-11521, Rev. A, Goodyear Aerospace Corporation, 17 June 1964, (Abstracted in Astronomical Journal, Volume 69, No. 8, Page 540, October 1964).
4. Emmons, R. H., Rogers, C. L., and Preski, R. J., "Photometric Observations of Artificial Satellites for Determining Optical and Physical Characteristics. I," The Astronomical Journal, Volume 72 No. 8, pp. 939-944, October 1967.

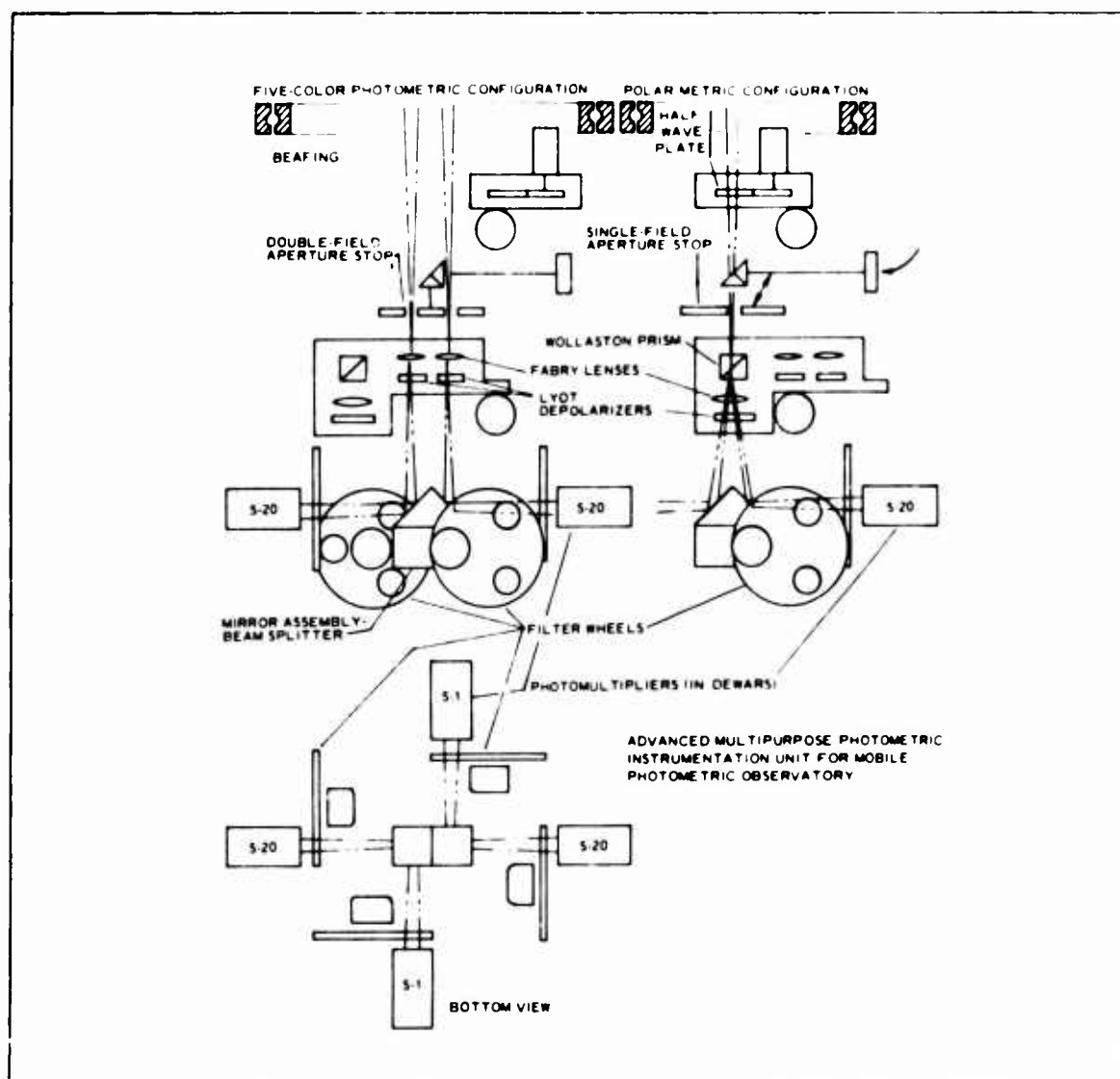


FIGURE 1. DIAGRAM OF THE FIVE-COLOR PHOTOMETER

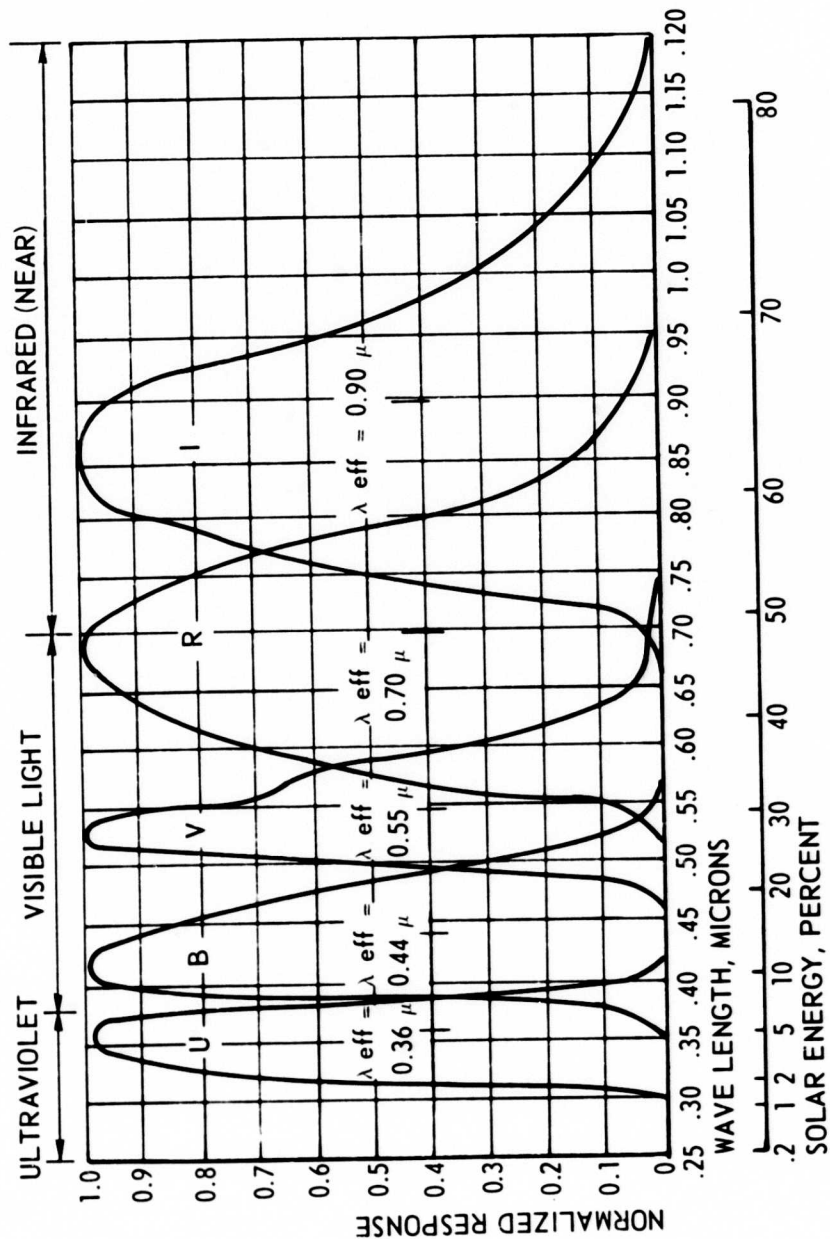


Figure 2 - Normalized Response Curves and Effective Wavelengths for the standard UBVR Color Bands

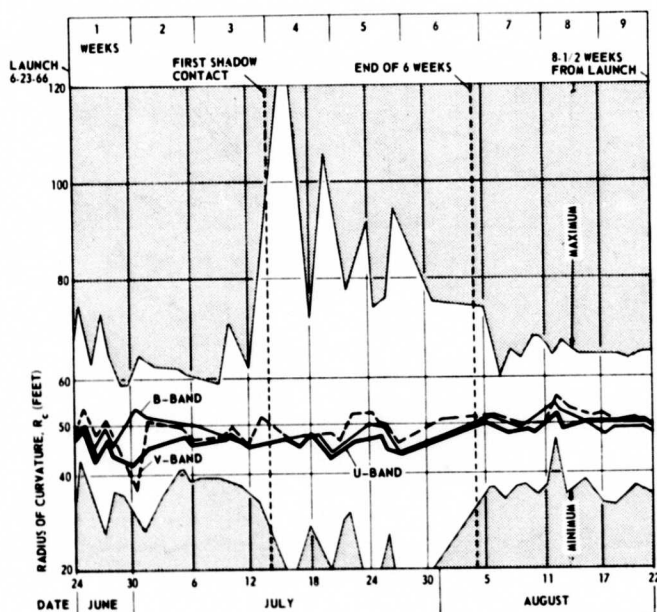


Figure 3 - PAGEOS' INDICATED MEAN AND EXTREME RADII OF CURVATURE VERSUS 1966 DATE, FROM PALOMAR OBSERVATIONS

V - BAND POLARIMETRIC OBSERVATIONS

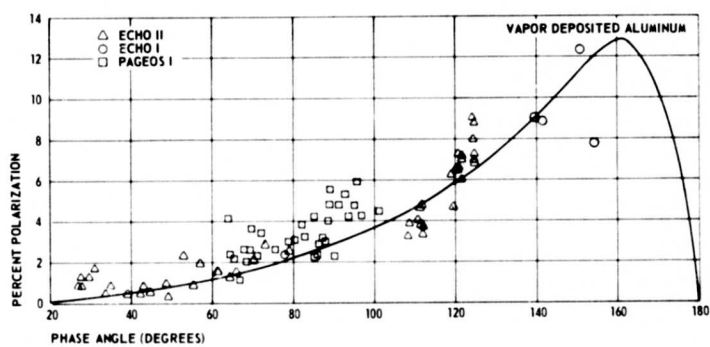


Figure 4 - Visual Band Polarimetric Determinations
versus Phase Angle

TABLE I. ANALYSIS OF PHOTOMETRIC OBSERVATIONS

Parameter	Color									
	V			B		U		V _{s-1} 3/67	R 3/67	I 3/67
	5/64	8/66	3/67	8/66	3/67	8/66	3/67			
Average radius of curvature (ft)*										
PAGEOS I	. . .	50.6	49.6	50.4	49.1	48.6	46.5	48.7	49.5	50.7
Echo I	51.1	50.7	50.1	50.6	49.8	48.2	47.5	50.0	50.1	52.6
Echo II	67.5	. . .	67.6	. . .	66.6	. . .	67.7	68.4
Standard deviation of radius of curvature (ft)*										
PAGEOS I	. . .	5.0	6.4	5.1	6.1	5.1	6.4	6.3	6.9	8.3
Echo I	6.5	4.6	5.6	4.6	7.4	4.7	7.6	5.8	6.0	7.4
Echo II	8.6	. . .	12.0	. . .	11.7	. . .	8.0	7.1
Total reflectance (for design radius of curvature)										
PAGEOS I	. . .	0.91	0.87	0.90	0.85	0.83	0.75	0.84	0.84	0.88
Echo I	0.92	0.91	0.89	0.91	0.87	0.81	0.78	0.89	0.87	0.95
Echo II	0.66	. . .	0.62	. . .	0.68	. . .	0.63	0.68
Indicated specularity										
PAGEOS I	. . .	0.98	0.95	0.99	0.95	0.99	0.99	0.89	0.87	0.84
Echo I	0.96	0.96	0.96	0.99	0.82	0.98	0.87	0.92	0.91	0.81
Echo II	0.74	. . .	0.65	. . .	0.87	. . .	0.93	0.87

* Based on laboratory-measured reflectances of surface materials.

TABLE II. PRINCIPAL FINDINGS FROM
VISUAL BAND PHOTOMETRIC DATA

Characteristic	Satellite		
	PAGEOS I	Echo I	Echo II
Mean diameter (ft)	99 ± 1	100 ± 1	135 ± 2
General surface waviness σR_c (ft)	$\pm 6 \pm 1$	$\pm 6 \pm 1$	$\pm 10 \pm 2$
Total reflectance	0.89 ± 0.02	0.90 ± 0.02	0.65 ± 0.10
Indicated specularity	0.95 ± 0.02	0.96 ± 0.02	0.75 ± 0.10

TABLE III. COLOR INDEXES

Color index	Reference solar value	Measured values					
		PAGEOS I		Echo I		Echo II	
		1966	1967	1966	1967	1966	1967
U-V	0.70	0.81	0.85	0.83	0.86	0.65	0.65
B-V	0.64	0.66	0.66	0.65	0.70	0.71	0.71
R-V	-0.52	. . .	-0.54	. . .	-0.49	-0.47	-0.47
I-V	-0.78	. . .	-0.87	. . .	-0.84	-0.78	-0.78

AN APPROXIMATE METHOD OF ESTIMATING
THE REFLECTION CHARACTERISTICS
OF A SPHERICAL SATELLITE

D. E. Smith
Radio and Space Research Station
Ditton Park, Slough, Bucks, England

AN APPROXIMATE METHOD OF ESTIMATING THE REFLECTION
CHARACTERISTICS OF A SPHERICAL SATELLITE

by

D. E. Smith

Summary

The sunlight reflected from a spherical satellite is assumed to be composed of an amount that is specularly reflected and an amount that is diffusely reflected. It is shown that the amount of reflected sunlight falling on a unit area a great distance from the satellite is directly related to the amount that is specularly reflected and by inference to the amount that is diffusely reflected. The apparent stellar magnitude of the satellite is used to estimate the fraction of solar radiation scattered by the satellite that is specularly reflected. The method has been applied to the Echo 2 satellite.

1. Introduction

The orbits of large balloon satellites, such as Echo 1, Echo 2 and Pageos, are subject to perturbations by the forces of solar radiation pressure acting on the satellite. These perturbations are proportional to the area-to-mass ratio of the satellite and to a dimensionless quantity, often termed the "reflection coefficient". This coefficient is a measure of the energy transferred from the photons to the satellite and depends on whether the incident radiation is absorbed or reflected; and if reflected, whether the reflection is specular or diffuse⁽¹⁾. For example, if the satellite is a perfect sphere and specularly reflecting, so that the incident radiation falling on the satellite is reflected with equal intensity in all directions, this quantity is unity. If, however, all the incident radiation is uniformly diffusely reflected from the satellite the "reflection coefficient" is about 1.44.

For the accurate computation of solar radiation pressure perturbations of a satellite orbit it is obvious that a knowledge of the way sunlight is reflected from the satellite is essential. In addition, a knowledge of the way light is reflected can be an indication of the condition of the surface of the satellite.

In the present study the amount of sunlight reflected from a spherical satellite of known radius and falling on a unit area at a large but known distance from the satellite is investigated as a function of the fraction of the incident sunlight that is reflected specularly. It is assumed that a fraction α of the incident radiation is reflected and that α is composed of α_s , the specular albedo and α_d , the diffuse albedo. It is assumed that the fraction $1 - \alpha$ is absorbed.

2. Specular Reflection

Let I be the intensity of solar illumination of a unit area normal to the direction of the sun and F the total radiation falling on a spherical satellite of radius a , then

$$F = \pi a^2 I \quad (1)$$

If the satellite is a perfect specular reflector, all the incident radiation is reflected uniformly over the entire unit sphere. The flux of radiation reflected specularly in a unit solid angle is therefore

$$\frac{F}{4\pi}$$

and the intensity of illumination, E_s , of a unit area distance r from the satellite (where r is considerably greater than a , the radius of the satellite) is given by

$$E_s = \frac{F}{4\pi r^2} = \frac{1}{4} \left(\frac{a}{r}\right)^2 I \quad (2)$$

If only a fraction α_s of the incident radiation is specularly reflected, then

$$E_s = \frac{\alpha_s F}{4\pi r^2} = \frac{\alpha_s}{4} \left(\frac{a}{r}\right)^2 I \quad (3)$$

3. Diffuse Reflection

A spherical coordinate system centred on the satellite can be constructed such that the fundamental reference plane contains the sun and the eye of the observer, and the normal to the reference plane is the polar axis of the spherical system. (see Fig. 1).

Let the angle between the sun and the observer, distant r from the centre of the satellite, as measured in the reference plane be θ and any point on the satellite be designated by λ , the longitude measured in the reference plane from the satellite-sun line, and φ , the latitude of the point with respect to the reference plane. An elementary area, ds , is therefore given by

$$ds = a^2 \cos \varphi \, d\varphi \, d\lambda \quad (4)$$

The solar radiation (dF) falling on ds is

$$dF = I a^2 \cos \varphi \cos \beta \, d\varphi \, d\lambda \quad (5)$$

where β is the angle between the normal to ds and the sun and from spherical trigonometrical considerations in Fig. 1, we have

$$\cos \beta = \cos \varphi \cos \lambda \quad (6)$$

and therefore

$$dF = I a^2 \cos^2 \varphi \cos \lambda \, d\varphi \, d\lambda \quad (7)$$

If the radiation falling on the elementary area ds is diffusely reflected according to a general function $f(\gamma)$ where γ is the angle between the normal to ds and the observer (see Fig. 1), then the intensity of illumination, dE_p , of a unit area at the observer, distance r from the satellite (r considerably greater than a), is

$$dE_D = \frac{\alpha_D}{r^2} \cos \gamma f(\gamma) dF \quad (8)$$

where α_D is the diffuse albedo. The total diffusely reflected solar radiation, E_D , falling on a unit area distance r from the satellite is, therefore, given by the integral of dE_D over that part of the satellite that is illuminated and can be seen from the unit area. Thus

$$E_D = \int_{\varphi = -\frac{\pi}{2}}^{\varphi = \frac{\pi}{2}} \int_{\lambda = \theta - \frac{\pi}{2}}^{\lambda = \frac{\pi}{2}} d\tau \quad (9)$$

$$= \alpha_D I \left(\frac{a}{r}\right)^2 \int_{\varphi = -\frac{\pi}{2}}^{\varphi = \frac{\pi}{2}} \int_{\lambda = \theta - \frac{\pi}{2}}^{\lambda = \frac{\pi}{2}} \cos^2 \varphi \cos \lambda \cos \gamma f(\gamma) d\varphi d\lambda \quad (10)$$

From Fig. 1 we can obtain

$$\cos \gamma = \cos \varphi \cos (\theta - \lambda) \quad (11)$$

and hence

$$E_D = \alpha_D I \left(\frac{a}{r}\right)^2 \int_{\varphi = -\frac{\pi}{2}}^{\varphi = \frac{\pi}{2}} \int_{\lambda = \theta - \frac{\pi}{2}}^{\lambda = \frac{\pi}{2}} \cos^3 \varphi \cos \lambda \cos (\theta - \lambda) f(\gamma) d\varphi d\lambda \quad (12)$$

(a) perfect diffuser

If the surface of the satellite is a uniformly diffuse reflector, the luminance is the same in all directions and $f(\gamma)$ takes its simplest form, that is, a constant. We may then write

$$f(\gamma) = k_1 \quad (13)$$

where k_1 is unknown and needs to be evaluated.

The total illumination on the surface of a hemisphere of radius r with ds at the centre is equal to the total radiation diffusely reflected ($\alpha_D dF$) from ds . We therefore have

$$\alpha_D dF = \int_{\text{hemisphere}} dE_D r^2 \sin \gamma d\gamma d\psi \quad (14)$$

where ψ is the longitude of a point on the surface of the hemisphere as shown in Fig. 2. From equations 8 and 14 we obtain

$$\alpha_D dF = \int_{\psi=0}^{\psi=2\pi} \int_{\gamma=0}^{\gamma=\frac{\pi}{2}} \alpha_D \sin \gamma \cos \gamma f(\gamma) dF d\gamma d\psi$$

and hence

$$2\pi \int_{\gamma=0}^{\gamma=\frac{\pi}{2}} \sin \gamma \cos \gamma f(\gamma) d\gamma = 1 \quad (15)$$

when $f(\gamma) = k_1$, we obtain from equation 15

$$k_1 = \frac{1}{\pi} \quad (16)$$

Performing the integration in equation 12 we obtain

$$E_D = \frac{2Ia^2}{3\pi r^2} \alpha_D \left[(\pi - \theta) \cos \theta + \sin \theta \right] \quad (17)$$

The above equation gives the total diffusely reflected radiation falling on a unit area distance r from the satellite and angle θ from the sun when the surface of the satellite is a uniform diffuser.

(b) imperfect diffuser

In general, $f(\gamma)$ is not constant and the luminance is therefore not the same in all directions. Let us consider the case of

$$f(\gamma) = k_2 \cos \gamma \quad (18)$$

From equation 15, we obtain

$$k_2 = \frac{3}{2\pi} \quad (19)$$

and from equations 11 and 12

$$E_D = \frac{3Ia^2}{2\pi r^2} \alpha_D \int_{\varphi = -\frac{\pi}{2}}^{\varphi = \frac{\pi}{2}} \cos^4 \varphi d\varphi \int_{\lambda = \theta - \frac{\pi}{2}}^{\lambda = \frac{\pi}{2}} \cos \lambda \cos^2 (\theta - \lambda) d\lambda \quad (20)$$

which leads to

$$E_D = \frac{3Ia^2}{16r^2} \alpha_D (1 + \cos \theta)^2 \quad (21)$$

This equation gives the total diffusely reflected radiation falling on a unit area when the reflection follows a $\cos \gamma$ law.

4. Apparent Brightness of Satellite

In general, the radiation reflected from a satellite will be composed of radiation that is specularly reflected and radiation that is diffusely reflected. Thus if E_0 is the total reflected radiation falling on a unit area at a distance r from the satellite we have

$$E_0 = E_s + E_D \quad (22)$$

Further, if we assume that a fraction α of the incident radiation is reflected, specularly and diffusely, and β is the fraction of α that is specularly reflected, then

$$\alpha_s = \alpha\beta \quad (23)$$

$$\alpha_D = \alpha(1 - \beta) \quad (24)$$

If the type of diffuse reflection is known and values of E_0 are obtained from say, a photo-electric photometer measurement, we can derive a value for ξ . For the Echo 2 balloon satellite (1964-04A), which we shall assume to be perfectly spherical, we have $a = 20.5$ metres ⁽²⁾. When $r = 1000$ km, we therefore have from equation 3

$$\frac{E_s}{I} = 1.051 \times 10^{-10} \times \alpha_s \quad (25)$$

and from equation 17

$$\frac{E_D}{I} = 0.892 \times 10^{-10} \times \alpha_D \left[(\pi - \theta) \cos \theta + \sin \theta \right] \quad (26)$$

when the satellite is a perfect diffuser, that is $f(\gamma) = \frac{1}{\pi}$, and from equation 21

$$\frac{E_D}{I} = 0.788 \times 10^{-10} \times \alpha_D \left[1 + \cos \theta \right]^2 \quad (27)$$

when $f(\gamma) = \frac{3}{2\pi} \cos \gamma$. Thus, from equations 22 to 27, we have

$$\frac{E_0}{I} \times 10^{10} = 1.051 \alpha \xi + 0.892 \alpha (1 - \xi) \left[(\pi - \theta) \cos \theta + \sin \theta \right] \quad (28)$$

when $f(\gamma) = \frac{1}{\pi}$, and

$$\frac{E_0}{I} \times 10^{10} = 1.051 \alpha \xi + 0.788 \alpha (1 - \xi) \left[1 + \cos \theta \right]^2 \quad (29)$$

when $f(\gamma) = \frac{3}{2\pi} \cos \gamma$.

The variation of $\frac{E_0}{\alpha I}$ with θ for $\xi = 0, 0.5$ and 1 is shown in Fig. 3. For values of θ , phase angle, greater than $\frac{\pi}{2}$ there is only a small difference between the two sets of curves. For small values of θ the difference is larger and for constant θ increases as ξ decreases. It is interesting to note that the graphs show that for $\theta = 0$, $\frac{E_0}{\alpha I}$ is about 3 times larger for completely diffuse reflection ($\xi = 0$) than for a completely specular reflection ($\xi = 1$).

On May 30th, 1966 the Echo 2 satellite was tracked by the U.S.A.F. at the Wright-Patterson Air Force Base, Ohio using a photo-electric photometer⁽³⁾.

The measurements obtained at Ohio on this pass have been compared with the theory outlined in this and previous sections of this paper and used to estimate a value of $\frac{1}{4}$, the fraction of scattered radiation that was specularly reflected.

The transit of Echo 2 at about 0420 U.T. on May 30th, 1966 passed almost overhead of Ohio, rising in the north and entering eclipse in the south. Measurements of the apparent stellar magnitude were made continuously for over five minutes. The magnitude changed steadily throughout this time and showed no violent oscillation or jumps and the transit appeared to be a very suitable one for comparing with the analysis already described.

Six values for the apparent stellar magnitude, at minute intervals, were taken from the photometer measurements and corrected for atmospheric extinction and range. The extinction correction, Δm_e , was calculated on the basis of 0.5 stellar magnitude per air mass (measured at Ohio at the time of the observations) from the equation

$$\text{Extinction correction, } \Delta m_e = 0.5 / \sin E \text{ magnitudes} \quad (30)$$

where E is the elevation of the satellite. The range correction was calculated for a standard range of 1000 km on the basis that the brightness of the satellite varied inversely as the square of the range. The apparent magnitude (m) of an object is defined in terms of the brightness (B), as follows⁽⁴⁾

$$m = -2.5 \log_{10}(B) \quad (31)$$

Thus, two brightness values (suffixes 0, 1) are related in apparent magnitude by

$$m_1 - m_0 = 2.5 \log_{10} \left(\frac{B_0}{B_1} \right) \quad (32)$$

and since

$$\frac{B_0}{B_1} = \left(\frac{\rho_1}{\rho_0} \right)^2 \quad (33)$$

where ρ_0 , ρ_1 are the ranges of the object, we have

$$m_1 - m_0 = 5.0 \log_{10} \left(\frac{\rho_1}{\rho_0} \right) \quad (34)$$

If m_1 is the stellar magnitude at a range of 1000 km ($= \rho_1$) and m_0 is the stellar magnitude at the observed range (ρ_0), then

$$\text{range correction, } \Delta m_r = 5.0 \log_{10} \left(\frac{\rho_0}{\rho_1} \right) \quad (35)$$

and the corrected apparent stellar magnitude (m_c) is therefore given by

$$m_c = m_0 - \Delta m_e - \Delta m_r \quad (36)$$

Details of the satellite pass, the observed magnitudes of the satellite, the corrections applied and the values of m_c are shown in Table 1.

TABLE 1. Details of Echo 2 observed from Ohio on May 30th, 1966

Time (U.T.)	m_0	E (degs)	ρ_0 (km)	Phase θ (degs)	Δm_e	Δm_r	m_c
0418	+ 0.82	31.6	1825	112	+ 0.95	+ 1.31	- 1.44
0419	+ 0.07	42.5	1533	104	+ 0.74	+ 0.93	- 1.60
0420	- 0.63	57.9	1304	94	+ 0.59	+ 0.58	- 1.80
0421	- 1.12	77.0	1162	80	+ 0.51	+ 0.33	- 1.96
0422	- 1.24	81.1	1136	64	+ 0.51	+ 0.28	- 2.03
0423	- 1.10	61.6	1277	53	+ 0.58	+ 0.53	- 2.21

The sources of error in the values of m_c arise from errors in the observed magnitude (m_0), the extinction correction (Δm_e) and the range correction (Δm_r).

The noise in the photo-electric photometer recording had an overall width of about 0.2 magnitudes and was approximately constant throughout the record. The central value taken from the record had a standard deviation of about 0.05 magnitudes.

The error in the extinction correction is primarily due to any error in the measured value of 0.5 magnitudes per air mass. The accuracy of this figure is probably of the same order as the accuracy of the satellite magnitude, that is, 0.05 magnitudes but for the extinction correction the error is systematic. Assuming a figure of 0.05 magnitudes the systematic error of the extinction correction lies between 0.05 and 0.1 magnitudes, depending on the elevation. Additional errors in the extinction correction arising from errors in the computed elevation of the satellite, which ^{is} believed to be accurate to about 0.2 degrees, can be shown to be negligible.

The accuracy of the computed range of the satellite is thought to be better than 10 km and is a systematic error rather than a random error because the relative accuracy of one predicted range with another is probably of the order of 1 km. A systematic error of 10 km introduces a systematic error in the range correction of 0.03 to 0.04 magnitudes, depending on the range. The error in m_c , the corrected stellar magnitude, is therefore composed of a standard deviation of about 0.05 magnitudes and a possible systematic error between 0.09 magnitudes and 0.12 magnitudes, depending on the elevation and range of the satellite.

The effect of a systematic error on the corrected stellar magnitude is a reduction or an increase of all the values by approximately the same amount. Thus, a systematic error will change the individual values of m_c but the shape of the magnitude versus phase curve will be largely unaffected.

The theoretical apparent stellar magnitude (m_t) can be obtained from the theoretical brightness of the satellite in the following way. From equation 32, we obtain

$$m_t = M + 2.5 \log_{10} \left(\frac{E_0}{I} \right)$$

where M is the apparent stellar magnitude of the sun (equal to $-26.78^{(4)}$), E_0 is the intensity of illumination of a unit area, distant r , by sunlight reflected from the satellite and I is the intensity of illumination of direct sunlight.

Thus

$$m_t = -1.78 - 2.5 \log_{10} \left(\frac{S_0}{I} \times 10^{10} \right) \quad (37)$$

The values of m_c are shown in Figures 4 and 5 superimposed on curves of m_t for $S = 0, 0.5, 0.6$ and 1.0 when $\alpha = 1$. The standard deviation of each value of m_c is indicated by the length of the vertical lines above and below the point. The systematic error is not shown. Curves of m_t when $\alpha \neq 1$ are identical in shape to those for $\alpha = 1$ but are displaced so as to decrease the theoretical magnitude. A comparison of the slope of the observed points with the theoretical curves can provide an estimate of S , the fraction of scattered sunlight that is specularly reflected.

An inspection of Figure 4, in which the theoretical curve is based on $f(\gamma) = \frac{1}{\pi}$, suggests that S lies in the range 0.5 to 0.6 and Figure 5, based on $f(\gamma) = 3 \cos \gamma / 2\pi$, suggests that S probably lies in the range 0.55 to 0.65 . In addition, there is some indication that there is better agreement between the observed and theoretical values in Figure 4 than in Figure 5, suggesting that the fraction of sunlight that is diffusely reflected is being reflected nearly uniformly in all directions.

It is important to remember that the assumption that the satellite is perfectly spherical may not be entirely true and, if not, could introduce systematic errors. Errors of several percent from this source cannot be ruled out.

Neglecting these possible errors, the present study suggests that S , the fraction of scattered solar radiation that is reflected specularly lies in the range 0.50 to 0.65 , say

$$S = 0.57 \pm 0.07 \quad (38)$$

6. Summary and Conclusions

The apparent brightness of a spherical satellite is shown to be a measure of the fractional part of the scattered solar radiation that is specularly reflected. Expressions have been derived for the amount of reflected radiation falling on a unit area for specular reflection and for two models of diffuse reflection.

It has been assumed that, in general, a fraction α of the solar radiation incident on the satellite is reflected and is composed of a fraction α_s that is specularly reflecting and a fraction α_d that is diffusely reflected.

The theoretical stellar magnitude of the Echo 2 satellite at a range of 1000 km has been compared with the observed magnitude (corrected for this range) for different phase angles and has indicated that about 57 percent of the solar radiation scattered by Echo 2 is specularly reflected, the remaining 43 percent being diffusely reflected.

Any major deterioration in the surface of the satellite or extensive small scale changes in the shape, such as wrinkling, will almost certainly affect the reflection characteristics of the satellite and therefore its apparent brightness as a function of range and phase. The present paper has described a simple method of estimating these reflection characteristics from ground based measurements of the apparent stellar magnitude which might be used as a measure of the deterioration (if any) of the surface of the satellite.

Acknowledgements

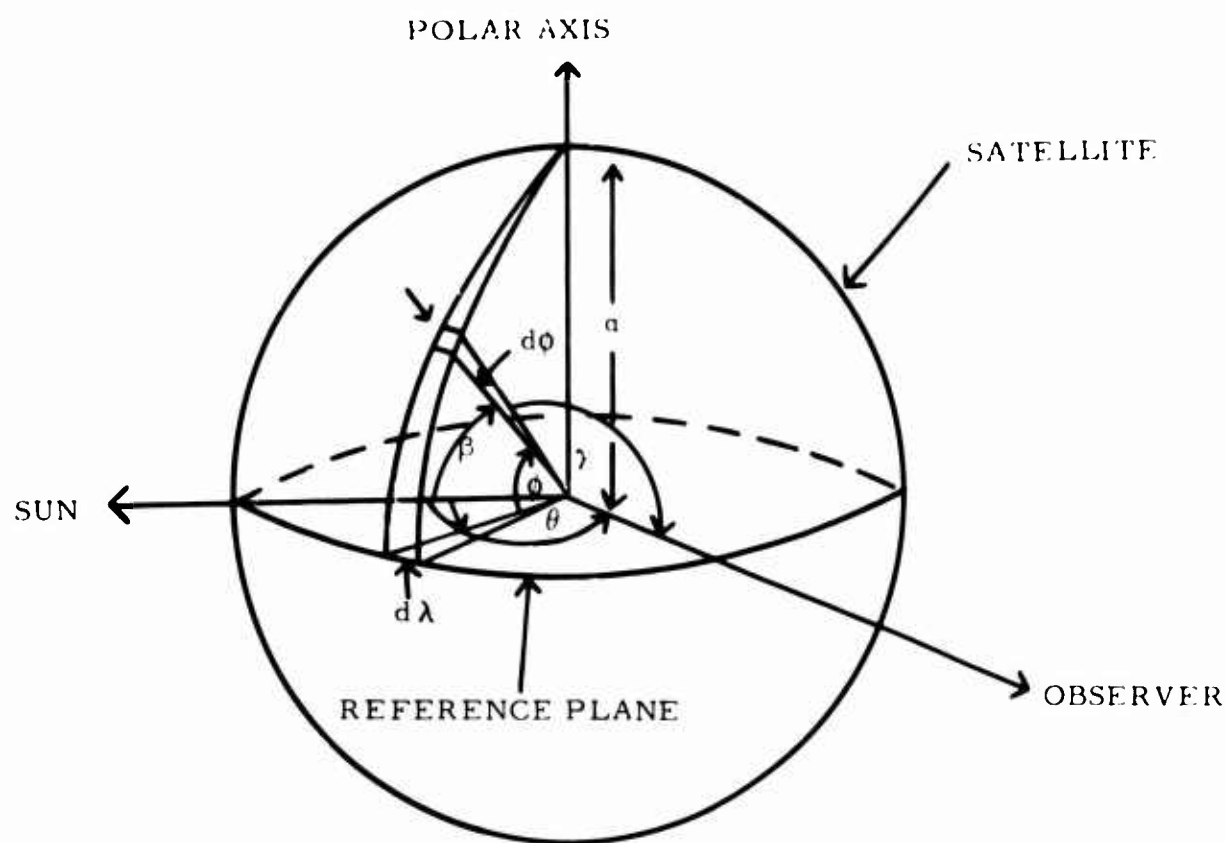
The author would like to thank Drs. Kissell and Vanderburgh of the General Physics Research Laboratory, Aerospace Laboratory, U.S.A.F., Wright-Patterson Air Force Base, Ohio who provided the photo-electric photometer record of Echo 2 without which this work could not have been undertaken and for several useful discussions during the course of the work.

The work described was carried out at the Radio and Space Research Station of the Science Research Council and is published with the permission of the Director.

References

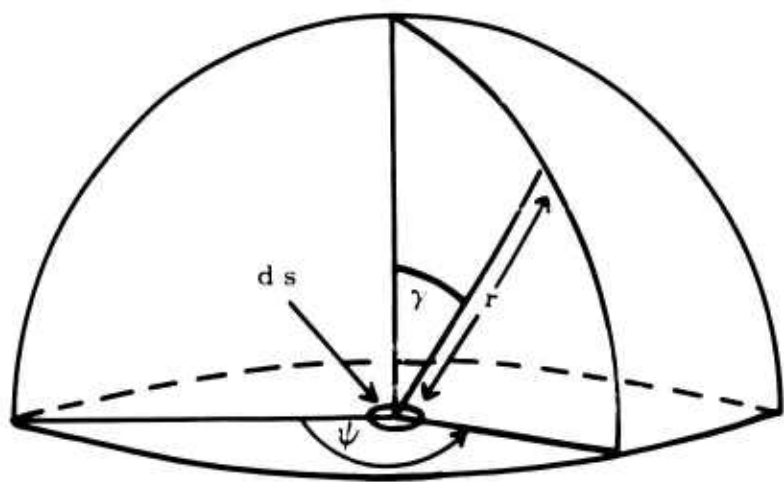
1. W. J. O'Sullivan, C. W. Coffee, and G. M. Keating,
"Space Research III", North-Holland Publishing Co., p.89, (1963).
2. D. G. King-Hele and E. Quinn,
Planet Space Sci., 13, 707 (1965)
3. K. Kissell and R. C. Vanderburgh,
Private communications.
4. C. V. Allen,
"Astrophysical Quantities", The Athlone Press, (1955).

FIGURE 1



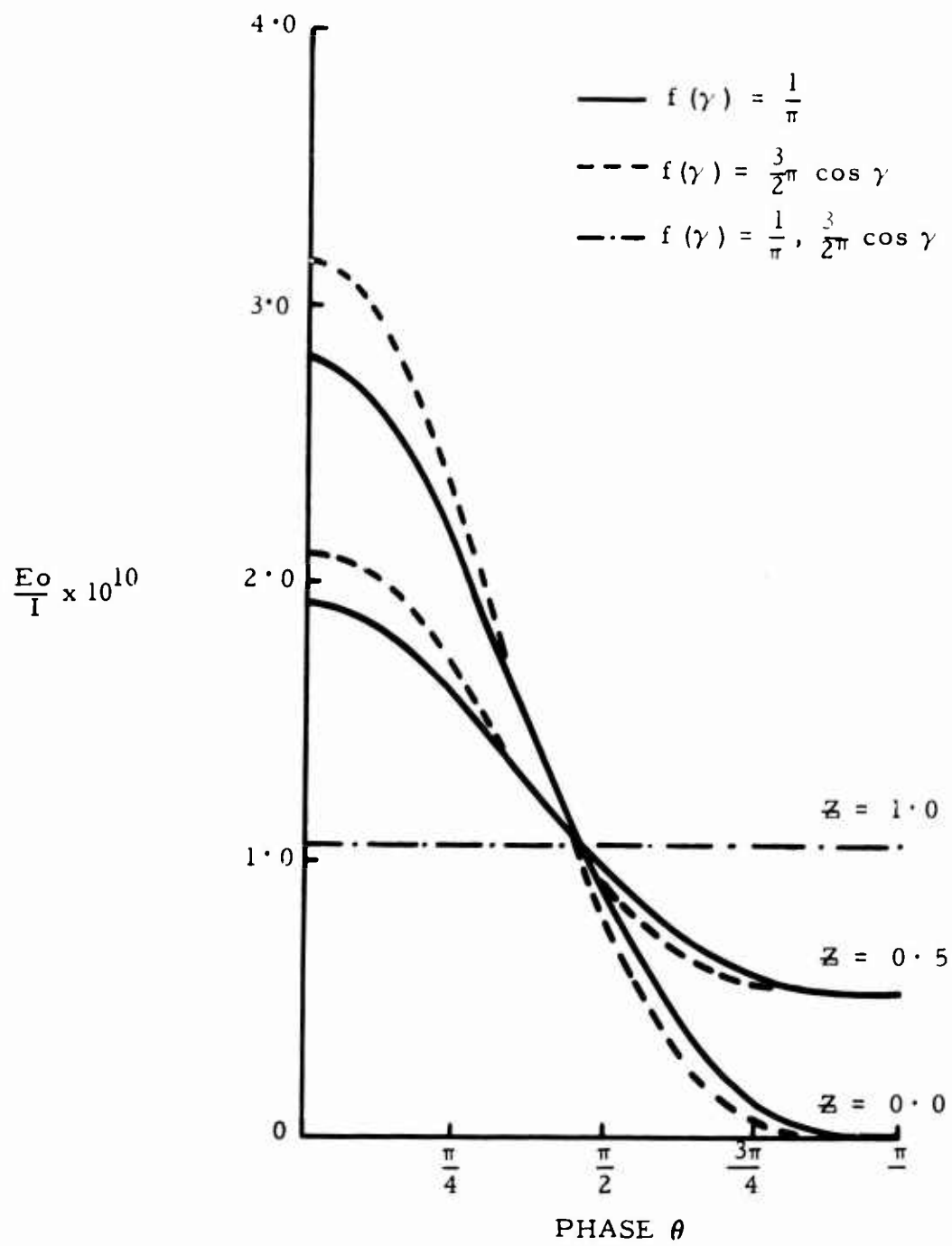
COORDINATE SYSTEM FOR DIFFUSE REFLECTION

FIGURE 2



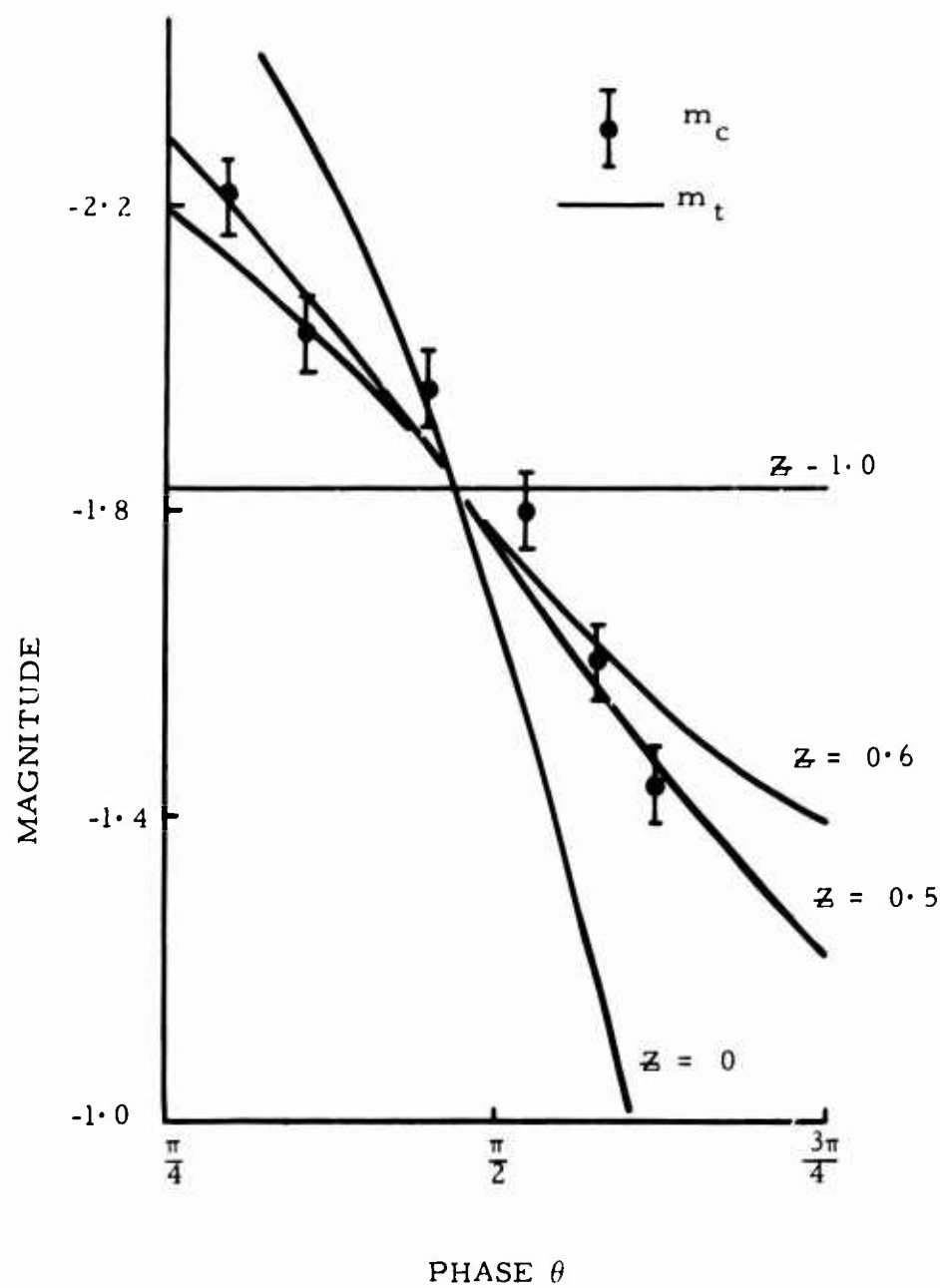
HEMISPHERE ABOUT THE ELEMENTRY AREA, ds .

FIGURE 3



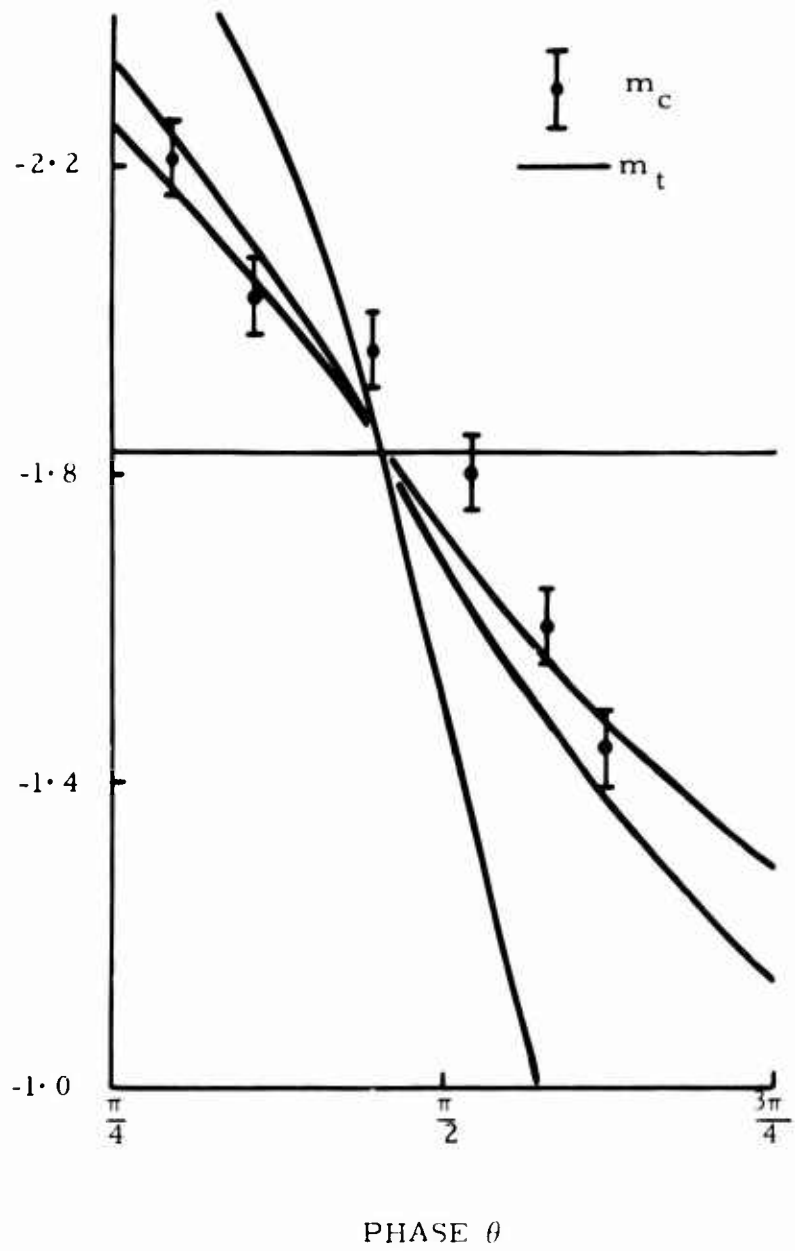
THEORETICAL VARIATION OF REFLECTED
RADIATION FROM ECHO 2 WITH PHASE

FIGURE 4



OBSERVED AND THEORETICAL MAGNITUDES
OF ECHO 2 FOR $\gamma = 1, f(\gamma) = \frac{1}{\pi}$

FIGURE 5



OBSERVED AND THEORETICAL MAGNITUDES
 OF ECHO 2 FOR $= 1, f(\gamma) = \frac{3}{2\pi} \cos \gamma$

DESIGN OF TELESCOPE OPTICAL
SYSTEMS FOR VISUAL OBSERVATIONS
OF ORBITING SATELLITES

Arthur S. Leonard
University of California
Davis, California

DESIGN OF TELESCOPE OPTICAL SYSTEMS
FOR
VISUAL OBSERVATIONS OF ORBITING SATELLITES

By
Arthur S. Leonard*

The first telescopes used for visual satellite tracking were designed as Richest-Field⁽¹⁾ instruments. The purpose of a "Richest-Field" telescope is to afford spectacular views of the heavens, and to show the greatest possible number of Milky Way stars at one view.

The intention of the design of the Richest-Field telescope is to provide an optimum combination of a wide field of view and reaching to fairly faint stars. This is just about what is needed for a satellite tracking instrument, so it is not at all surprising that the Richest-Field design was selected for the first satellite telescopes.

Standard specifications for Richest-Field design are an objective of $f/4$ to $f/6$ focal ratio and a wide-angle eyepiece to give 3.39 power per inch of aperture of the objective. Arguments put forth in the earliest published articles on this design indicate that these specifications were derived almost entirely from theoretical considerations and assumptions which seemed reasonable at the time.

Many Richest-Field telescopes have been built, and their builders have attested to the spectacular views which they afford; but there appears to have been little systematic experimental testing to ascertain whether or not these specifications lead to a truly optimum design. It is the

* Lecturer in Mechanical Engineering, Department of Mechanical Engineering, University of California, Davis.

writer's opinion that they are in rather serious error on two points. First, the optimum specific magnification (magnifying power per inch of aperture of the objective) should be somewhere between 5- and 10- power per inch, depending on the individual's feelings for what he sees in the eyepiece of his telescope, rather than at the earlier published value of 3.39; and second, an increase in the focal ratio of the objective system from the $f/4 - f/6$ range to the $f/12 - f/17$ range will give a significant improvement in the sharpness of star images over a large fraction of the field of view.

Limiting Magnitude versus Specific Magnification

One of the assumptions made in setting up the earlier specifications was that the limiting magnitude of a telescope is determined by aperture alone and is entirely independent of its magnifying power. A more recent experimental investigation into this matter⁽²⁾ has shown that limiting magnitude is very much a function of magnifying power as well as light gathering power. For example, an increase in magnification from 3.39 to 10 power per inch will increase the limiting brightness of a small telescope by 1.9 stellar magnitudes. The reason for this is that the ability of the eye to detect a faint star image depends not only on the amount of light in that image, but also on the apparent brightness of the surrounding background. The brightness of the star image is dependent almost entirely on the light gathering power of the objective while the brightness of the surrounding background presented to the eye varies inversely as the square of the specific magnification.

Although the impression which a given view will make on a person will probably be different for different observers, it is the writer's feeling

that the relatively milky background presented by a specific magnification of 3.39 power per inch generally detracts from the beauty of the view. Eight-to-ten-power per inch gives a much darker background and greater contrast between the stars and background. Even at 11.3 power per inch, which the writer is using for satellite tracking, the background illumination offered by the darkest part of the sky on the darkest night is still sufficient to make cross-wires of 0.006-inch diameter easily visible in the eyepiece without any supplemental illumination.

One of the implied assumptions used in writing the specifications for the Richest-Field telescope is that it will be used mainly on clear dark nights. Satellite tracking, on the other hand, must be carried out on as many occasions as possible; and, as any experienced satellite observer knows, this means working in full moon light, strong twilight, and with light fog or clouds in the sky. Thus the specifications which yield the best Richest-Field instrument are not necessarily the best prescription for a satellite tracking telescope. As the background illumination is increased, higher magnification is of increasing value in revealing faint objects. Also, averted vision is very helpful in attracting an observer's attention to a faint moving object, but this works only if the apparent background illumination is fairly low. It won't be of any help in broad daylight. For these reasons a satellite telescope should be designed with a higher magnifying power than a Richest-Field.

If a satellite appears well above threshold brightness in the field of view, high angular velocity does not interfere appreciably with its being seen. If it is near limiting brightness, however, a high apparent velocity

increases the probability of its being missed by the observer. For this reason as magnifying power is increased a value is soon reached above which there is little net gain to be realized by going higher. From long experience observing faint satellites with a 6-inch refractor and other smaller telescopes, it is the writer's opinion that 10 power per inch is just about optimum specific magnification for telescopes up to 6-inches aperture. Experiments with higher magnification have indicated that there is little to be gained by going above about 15 power per inch. On the other hand, if the satellite is so bright that high magnification is unnecessary to make it easily visible under the existing sky conditions and if its angular velocity is fairly high, a lower power is to be preferred. If the angular velocity of the satellite is so high that it will cross the field of view in less than about two seconds, some loss in accuracy of the observations may result. Under such circumstances a lower magnification should be used, assuming, of course, that the lower magnification will not render the satellite invisible to the observer's eyes. On the other hand, if the satellite is very high and moving very slowly, an increase in magnification can easily lead to a more accurate observation.

Eyepiece Aberrations versus Focal Ratio of Objective

The specification for the focal ratio of the objective of the Richest-Field telescope was probably set as a matter of convenience rather than from any consideration of what effect it might have on the over-all performance of the instrument. To obtain a specific magnification of 3.39 power per inch with a conventional f/15 refractor objective would require an eyepiece of 4.42-inch focal length. For the amateur telescope makers who built the first Richest-Field telescopes, such an eyepiece was -- and still is --

difficult to obtain; and, if available, would be a relatively costly item. So, they followed the route of least resistance and made or purchased objectives to match their eyepieces. An eyepiece of 15-inch focal length -- which is about as large as can be readily obtained -- requires an $f/5.085$ objective to give a specific magnification of 3.39 power per inch.

In the center of field of view, some of our best eyepiece designs can handle an $f/5$ cone of rays without serious aberration; but as we go away from the center, even the best designs get into rather serious trouble. The very low power employed in the Richest-Field telescope helps to reduce the apparent magnitude of these aberrations, but, as the original designer says: "Marginal definition must be a little inferior to central in every Richest-Field telescope, --".

This loss in performance toward the outer part of the field of view can be reduced to negligible proportions by simply increasing the focal length of both the objective and eyepiece. Although this will require larger and more costly eyepieces, to obtain a magnification of 10 power per inch with a standard $f/15$ objective requires an eyepiece of only 1.5-inch focal length.

The following example is presented in order to explain in detail why this improvement in optical performance comes about when we increase the focal lengths of the objective and eyepiece. Consider two telescopes, 1 and 2, which are of identical optical design throughout. They are of the same aperture and magnification; but 2 has a longer focal length than 1, and the radii of curvature of all its surfaces are greater than those in 1 by the same ratio. Both telescopes are pointed in the same direction, but we are looking at a star some distance off the axes of the telescopes. At

corresponding points in each telescope the cones of rays from the star will be of the same diameter; and the angles of incidence of the central rays at corresponding optical surfaces will be the same in both instruments.

We will assume that the design of the objective is such that virtually no aberration is produced by either objective and all the observed errors are produced in the eyepieces. Consider the various aberrations produced at the first surface of the eyepiece in each instrument. Spherical aberration is given by the following expression:

$$w_s = C_s \frac{d^4}{R^3} \tag{1}$$

where w_s is the maximum wave-front aberration in the same units as the other linear dimensions, C_s is a number which depends on the geometry of the rays and the index of refraction of the glass, d is the diameter of the cone of rays, and R is the radius of curvature of the lens surface.

Since C_s and d will be the same for both instruments, the ratio of spherical aberration produced by this first surface in the two instruments will be:

$$\frac{w_{s2}}{w_{s1}} = \frac{R_1^3}{R_2^3} \tag{2}$$

This indicates that the ratio of the spherical aberration produced by the two eyepieces will be inversely proportional to the cubes of the radii of curvature of the lenses and this will be inversely proportional to the cubes of the focal lengths of their objectives.

First-order coma⁽³⁾ will be given by:

$$w_c = C_c \frac{d^3}{R^2} \quad (3)$$

where w_c is the maximum wave-front aberration due to coma, and C_c is a constant which depends on the geometry of the rays and the index of refraction. Therefore, the ratio of coma produced by the two eyepieces will be inversely proportional to the squares of the focal lengths of the objectives.

First-order astigmatism is given by:

$$w_s = C_s \frac{d^2}{R} \quad (4)$$

This means that the ratio of astigmatism produced by the two eyepieces will be inversely proportional to the first power of the ratio of the focal lengths.

Chromatic aberration varies in a way similar to astigmatism, so it too will be inversely proportional to the focal lengths of the objectives.

Thus in telescope 2, with its longer focal length, all of these eyepiece aberrations will be reduced. If we go to an objective of long enough effective focal length, all of these aberrations can be reduced to negligible amounts. The only eyepiece aberration not affected by this increase in focal length will be field curvature. In a well-designed eyepiece this defect is not serious, so we can practically eliminate all eyepiece aberration by simply going to an objective and eyepiece of long enough focal length.

Conclusions

In designing a telescope for satellite tracking the focal ratio of the objective system should be made as high as $f/15$ if at all possible. A refractor is to be preferred over a reflector because with the former it is usually possible to design an internal system of light baffles which will give a darker, more contrasty field than with a reflector. In order that the instrument should be able to operate near its maximum performance over a wide range of observing conditions, and satellite brightness and speed, a good selection of eyepieces should be provided which will provide good coverage over a range of specific magnification from about 5- to 20-power per inch of aperture. For telescopes of more than 6-inches aperture the range of specific magnification should be lowered somewhat from these figures.

References

1. Ingalls, Albert G., Editor Amateur Telescope Making Advanced, Scientific American, Inc. New York, New York, 1954, pp 623-647

2. Leonard, Arthur S., "Limiting Magnitudes of Visual Telescopes" Proc. 19th Annual Convention of Western Amateur Astronomers, Long Beach, California, August 16 - 19, 1967

3. Leonard, Arthur S., "First Order Tilt Aberrations in Mirrors and Lenses" Proc. 17th Annual Convention of Western Amateur Astronomers, University of Nevada, Reno, Nevada, August 19 - 21, 1965.

THEORY AND OBSERVATION OF THE ROTATIONAL
MOTION OF THE PEGASUS SATELLITES

Robert L. Holland and Matthew B. Barkley
NASA Marshall Space Flight Center
Huntsville, Alabama

THEORY AND OBSERVATION OF THE ROTATIONAL MOTION OF THE PEGASUS SATELLITES

Robert L. Holland and Matthew B. Barkley
Space Sciences Laboratory
National Aeronautics and Space Administration
Marshall Space Flight Center
Huntsville, Alabama

Abstract

New theoretical results are derived which predict the principal effect of the gravitational and magnetic torques on the rotational motion of an orbiting triaxial rigid body. Three integrals are derived by the averaging principle of Kryloff-Bogoliuboff to determine the motion of the rotational angular momentum vector. The results are compared with the observations of the rotational motion of the Pegasus satellites.

Introduction

The rotational and translational motion of a rigid body are generally coupled. Because the coupling effect is negligible in most applications in celestial mechanics, the two problems may be treated separately. They are, however, analogous in many respects. For example, if there are no external torques acting in the two-body problem of two-point masses, then the orbital angular momentum vector is constant, and the motion of the bodies is called "free Keplerian." Likewise, if there are no external torques acting in the rotational problem of a rigid body, then the rotational angular momentum vector is constant and the motion of the rigid body is called "free Eulerian." If the primary body in the translational two-body problem is triaxial or oblate, then the principal effect is that the time-averaged orbital angular momentum vector follows periodic paths of motion. Likewise, it is shown in this paper that if the orbiting rigid body is triaxial or oblate, then again the principal effect is that the time-averaged rotational angular momentum vector follows periodic paths of motion.

Beletskii⁽¹⁾ and Colombo⁽²⁾ have studied the symmetrical rigid body rotational problem (i. e., two moments of inertia are equal) in a circular orbit. Colombo published two integrals of this problem analogous to the first two derived in this paper except that they refer to a different coordinate system.

This paper extends the work to asymmetrical bodies; in addition, a method is also indicated, but not developed, for an extension to eccentric orbits.

The more specialized problem of the rotational motion of a symmetrical rigid body moving in a fixed orbit about another body has been treated successfully in the astronomical literature for the case of the rotational motion of the earth under the influence of the gravitational attraction of the sun and moon; this is the luni-solar precession problem.

The more general problem of the motion of a triaxial rigid body in a regressing orbit about another body, which

is treated here, reduces to the aforementioned symmetrical problems if the rigid body is assumed to be a figure of revolution in a fixed orbit about the primary mass.

Theory

Formulation of Differential Equations for Rotational Motion

The Newtonian gravitational torque about the center of mass of a small triaxial rigid body orbiting a spherical primary mass may be written⁽³⁾

$$\underline{N} = \frac{3mG}{R^3} \underline{R} \times (\underline{S}) \underline{R} \quad (1)$$

where m is the mass of the primary, G is the universal gravitational constant, \underline{R} is the vector from the center of mass of the small rigid body, m' , to the center of mass of the primary mass, m (Fig. 1).

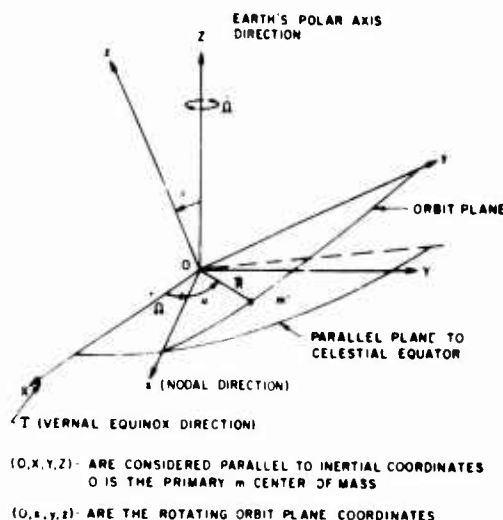


Figure 1. Geometry of Equatorial and Orbit Plane Coordinate Systems

The symbol R is the magnitude of \underline{R} , and (\underline{S}) is the moment of inertia matrix of m' with respect to any particular coordinate system which may be arbitrarily chosen for the convenience of the particular problem or analyst.

From Newton's second law for rotational motion, the torque given in equation (1) may be equated to the time rate of change of the angular momentum vector (i. e.,

$$\text{i. e., } \frac{d\underline{L}}{dt} = \underline{N} \text{ in an inertial coordinate system. If it is}$$

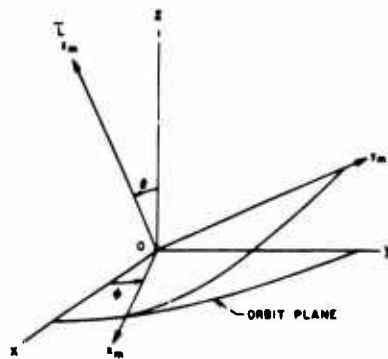
desirable to know the motion of the angular momentum vector, \underline{L} , in a rotating system, the equation of motion becomes

$$\frac{d\bar{L}}{dt} + \bar{\omega} \times \bar{L} = \bar{N} \quad (2)$$

where $\bar{\omega}$ is the angular velocity vector of the rotating coordinates.

If the rotating coordinates are chosen to coincide with the principal moment of inertia axes of the small rigid body, equation (2) becomes Euler's dynamical equations. These equations have known periodic solutions if the torque \bar{N} is zero.

This free Eulerian motion is usually defined by the periodic Euler angles, Θ_m, ϕ_m, ψ_m , in a coordinate system which has its polar axis along the constant vector \bar{L} (Figs. 2 and 3).



(0, x, y, z) ARE SAME AS DEFINED IN FIGURE 1
(0, x_m, y_m, z_m) ARE COORDINATES DEFINED WITH x_m ALONG THE \bar{L} VECTOR THIS IS REFERRED TO AS THE MOMENTUM COORDINATE SYSTEM

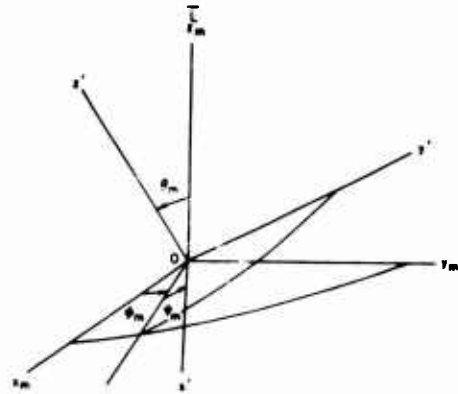
Figure 2. Geometry of Momentum and Orbit Plane Coordinate Systems

In the present problem, the torque is not zero; hence \bar{L} is not a constant of the motion.

It is convenient for the purposes of this study to choose rotating coordinates so that the polar axis z is normal to the orbit plane of m' about m and the x axis is in a direction parallel to the line of nodes (Fig. 1). In this coordinate system, the angular velocity vector in equation (2) is

$$\bar{\omega} = \begin{pmatrix} 0 \\ \dot{\Omega} \sin i \\ \dot{\Omega} \cos i \end{pmatrix} = \begin{pmatrix} 0 \\ -A \\ -B \end{pmatrix} \quad (3)$$

where $\dot{\Omega}$ is the rate of change of the right ascension of the ascending node and i is the inclination of the orbit plane to the celestial equator. These quantities will be assumed to be constant so that A and B are constants. A circular orbit will also be assumed so that R will be a constant.



(0, x_m, y_m, z_m) ARE SAME AS DEFINED IN FIGURE 2
(0, x', y', z') ARE THE RIGID BODY COORDINATES ALONG THE PRINCIPLE MOMENT OF INERTIA AXES

Figure 3. Geometry of Principal Body and Momentum Coordinate Systems

Now equation (2) may be interpreted as the perturbation equation for the variation of \bar{L} which is a constant of the motion in the torque-free Eulerian motion.

From equations (1) and (2)

$$\frac{d\bar{L}}{dt} = \frac{3mG}{R^3} \bar{R} \times (S) \bar{R} - \bar{\omega} \times \bar{L} \quad (4)$$

where all the vectors and (S) are now referred to the rotating orbit plane coordinates defined in Figure 1.

The matrix (S) may be obtained by a transformation from the principal axis of m' to the rotating coordinates (Figs. 2 and 3)

$$(S) = (T) (I') (T)^T \quad (5)$$

where (T) is the transformation matrix from the principal axes to the rotating orbit plane coordinates. $(T)^T$ is the transpose of (T), and (I') is the diagonal moment of inertia matrix for m'

$$(I') = \begin{pmatrix} I_1' & 0 & 0 \\ 0 & I_2' & 0 \\ 0 & 0 & I_3' \end{pmatrix}$$

The matrix (T) may be written as the product of two matrices (M) and (B). The matrix (M) is the transformation matrix from the momentum vector coordinate system to the rotating orbit plane coordinate system (Fig. 2). The matrix (B) is the transformation matrix from the rigid body principal axes to the momentum coordinate system (Fig. 3).

The matrices (M) and (B) are

$$(M) = \begin{pmatrix} \cos \phi & -\cos \Theta \sin \phi & \sin \Theta \sin \phi \\ \sin \phi & \cos \Theta \cos \phi & -\sin \Theta \cos \phi \\ 0 & \sin \Theta & \cos \Theta \end{pmatrix} \quad (6)$$

And (B) =

$$\begin{pmatrix} \cos \Theta_m \cos \phi_m \cos \psi_m & \sin \Theta_m \cos \phi_m \cos \psi_m & \sin \Theta_m \sin \phi_m \cos \psi_m \\ \cos \Theta_m \sin \phi_m \cos \psi_m & \sin \Theta_m \sin \phi_m \cos \psi_m & -\sin \Theta_m \cos \phi_m \cos \psi_m \\ \sin \Theta_m \cos \phi_m \sin \psi_m & \sin \Theta_m \sin \phi_m \sin \psi_m & \cos \Theta_m \cos \phi_m \sin \psi_m \end{pmatrix} \quad (7)$$

The reason for splitting the transformation into two matrices is to separate the Euler angles, Θ_m , ϕ_m and ψ_m , which define the orientation and Eulerian motion of the rigid body with respect to the momentum coordinate system, from Θ and ϕ which define the position and motion of \bar{L} with respect to the rotating orbit plane coordinate system.

From the preceding definitions it is clear that

$$(T) = (M) (B) \quad (8)$$

Combining equation (4) with equations (5) and (8), the equation of motion may be written

$$\frac{d\bar{L}}{dt} = \frac{3mG}{R^3} \bar{R} \times (M) (B) (I') (B)^T (M)^T \bar{R} - \bar{\omega} \times \bar{L} \quad (9)$$

This equation is now in the form desired for the application of the "averaging principle" of Kryloff and Bogoliuboff⁽⁴⁾.

Formulation of the Differential Equations for the Averaged Rotational Motion

For the application of the Kryloff-Bogoliuboff theory to equation (9), it is necessary to assume that the rotational kinetic energy is large compared to the gravitational potential energy. This is necessary so that the chosen dependent variables (L_x , L_y , L_z) = \bar{L} of the perturbed problem will vary slowly during a period T of any of the periodic parameters, Θ_m , ϕ_m , ψ_m , or u of the unperturbed problem. The symbol u is the argument of latitude of the orbiting rigid body. This assumption is very important from a theoretical point of view because it has the effect of separating librational theories for bodies such as the moon from rotational theories such as for the earth. The problem considered here is in the rotational category.

Under the above assumption, the first approximation of Kryloff-Bogoliuboff states that

$$\frac{d\bar{L}}{dt} \approx \frac{\bar{L}(t+T) - \bar{L}(t)}{T} = \frac{1}{T} \int_t^{t+T} \frac{d\bar{L}}{dt} dt \quad (10)$$

The previous section was devoted to formulating the differential equations in terms of periodic parameters, Θ_m , ϕ_m , ψ_m , and u from the unperturbed problem so that the averaging operations indicated by equation (10) could be applied.

The averages were performed independently with respect to the angles ψ_m , ϕ_m and u; therefore, no resonance conditions must exist and the Eulerian motion must be nearly uniform.

From Figure 1

$$\bar{R} = \begin{pmatrix} R \cos u \\ R \sin u \\ 0 \end{pmatrix} \quad (11)$$

Then,

$$\bar{R} \times (S) \bar{R} = \begin{pmatrix} S_{22} R^2 \sin u \cos u + S_{33} R^2 \sin^2 u \\ -S_{11} R^2 \cos^2 u - S_{22} R^2 \sin u \cos u \\ S_{11} R^2 \cos^2 u + S_{22} R^2 \sin u \cos u - S_{33} R^2 \sin^2 u \end{pmatrix} \quad (12)$$

where S_{ij} are elements of (S).

The average over u is

$$\frac{1}{2\pi} \int_0^{2\pi} \bar{R} \times (S) \bar{R} du = \frac{1}{2} R^2 \begin{pmatrix} S_{22} \\ -S_{21} \\ 0 \end{pmatrix} \quad (13)$$

The last component is zero because of the symmetry of (S).

Now equation (9) becomes

$$\frac{d\bar{L}}{dt} = \frac{3mG}{2R^3} \begin{pmatrix} S_{22} \\ -S_{21} \\ 0 \end{pmatrix} - \bar{\omega} \times \bar{L} \quad (14)$$

The averages are carried out over ψ_m and ϕ_m in the same manner, that is, by expressing S_{22} and S_{21} in terms of Θ_m , ϕ_m , ψ_m , Θ and ϕ by equations (5), (6), (7) and (8), then averaging over ϕ_m and ψ_m .

The result is

$$\frac{d\bar{L}}{dt} = \frac{K}{L^3} (\hat{\Omega} \cdot \bar{L}) (\hat{\Omega} \times \bar{L}) - \bar{\omega} \times \bar{L}$$

Where

$$K = -\frac{3mG}{8R^3} (I_1 + I_2 - 2I_3) (1 - 3 \cos^2 \Theta_m) \quad (15)$$

L is the magnitude of \vec{L} and $\hat{\Omega}$ is a unit vector normal to the orbit plane, that is, $\hat{\Omega} = (0, 0, 1)$. This is the form of the differential equation for describing the averaged motion of \vec{L} (to be discussed in the next section).

The preceding formulation may also be used to determine the effect of an eccentric orbit. The trigonometric terms and R which involve u must be written as a Fourier expansion of the mean anomaly M and the averages carried out over a period of M .

The spin and precession are assumed to be about I_3 in the above definition of K . This choice places no restrictions on the generality because no assumption has been made regarding the relative magnitudes of the moment of inertia.

Periodic Solutions

From equation (15), it is evident that

$$\vec{L} \cdot \frac{d\vec{L}}{dt} = \frac{1}{2} \frac{d}{dt} (\vec{L} \cdot \vec{L}) = \frac{1}{2} \frac{d}{dt} (L^2) = 0$$

Therefore

$$L^2 = L_x^2 + L_y^2 + L_z^2 = \text{const.} \equiv C_1 \quad (16)$$

which is a first integral of the motion and states that the averaged magnitude of the angular momentum is constant

Now equation (16) may be used to write equation (15) in terms of the direction cosines of \vec{L} . Denoting these by

$$\frac{\vec{L}}{L} \equiv (x, y, z) \quad (17)$$

Then

$$x^2 + y^2 + z^2 = 1 \quad (18)$$

Combining equations (17), (18) and (3) with equation (15), the differential equations (15) become

$$\begin{aligned} \dot{x} &= \frac{K}{L} zy + Az - By \\ \dot{y} &= -\frac{K}{L} zx + Bx \\ \dot{z} &= -Ax \end{aligned} \quad (19)$$

From the last two equations

$$\dot{y} = \frac{K}{AL} z\dot{z} - \frac{B}{A} \dot{z}$$

which may be integrated to

$$y = \frac{K}{2AL} z^2 - \frac{B}{A} z + C_2 \quad (20)$$

This is a second integral of the motion. The first integral states that the motion of the end point of \vec{L} takes place on the surface of a sphere. This second integral states that the motion takes place on the surface of a parabolic cylinder. Therefore, the motion takes place on the curve (or path) formed by the intersection of the sphere, equation (18), with the parabolic cylinder, equation (20).

This result is sufficient to infer that the motion is periodic; however, the third integral given below also implies periodicity.

From the last equation in (19) combined with equations (18) and (20)

$$z = -A \sqrt{1 - \left(\frac{K}{2AL} z^2 - \frac{B}{A} z + C_2 \right)^2} - z^2$$

or

$$-A dt = \frac{dz}{\sqrt{1 - \left(\frac{K}{2AL} z^2 - \frac{B}{A} z + C_2 \right)^2} - z^2} \quad (21)$$

Integrating equation (21) gives

$$-At + C_3 = \int \frac{dz}{\sqrt{1 - \left(\frac{K}{2AL} z^2 - \frac{B}{A} z + C_2 \right)^2} - z^2} \quad (22)$$

which is immediately recognized as an elliptic integral and implies that z is a periodic function of time.

This concludes the proof that the averaged motion of the angular momentum vector of a rigid body under the gravitational perturbation of an oblate body is periodic, described by the above three integrals.

The Permanent Magnetic Torque. When a rigid body in orbit in the earth's magnetic field possesses a magnetic moment M_L along \vec{L} , a torque, given by

$$\vec{N}_m = M_L B_N \left[\frac{1}{2} \hat{k}^* \times \hat{L}^* - \frac{3}{2} (\hat{k}^* \cdot \hat{\Omega}^*) (\hat{\Omega}^* \times \hat{L}^*) \right] \quad (23)$$

is experienced [5], where $M_L B_N \equiv C_m$ is the constant magnetic couple and \hat{k}^* is a unit vector along the Z^* inertial axis. An earth-centered dipole representation of the magnetic field is assumed.

When equation (23) is resolved onto the rotating orbit plane coordinates, written out in component form, and combined with equation (15), the result is merely to change the definitions of the constants A and B . That is, instead of equations (19) we have

$$\begin{aligned}\dot{x} &= \frac{K}{L} zy + A_m z - B_m y \\ \dot{y} &= -\frac{K}{L} zx + B_m y \\ \dot{z} &= -A_m x\end{aligned}$$

where

$$A_m = \left(1 + \frac{C_m}{2\Omega L}\right) A$$

and

$$B_m = \left(1 - \frac{C_m}{\Omega L}\right) B \quad (24)$$

Therefore, the three integrals remain unchanged except for replacing A and B with A_m and B_m .

Observations of the Pegasus Satellites

Figure 4 is a plot of y versus z obtained from numerical integration of equation (15), the second integral of motion given by equation (20) and experimental observations obtained from the artificial earth satellite Pegasus I during the month of May, 1965.

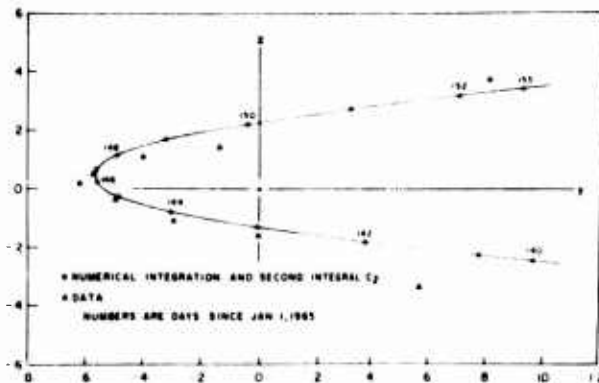


Figure 4. Motion of Rotational Angular Momentum Vector - Pegasus I Satellite - Rectangular Coordinates y vs. z

Figure 5 is a plot of the spherical coordinates ϕ versus θ , again obtained from the present theory, numerical integration and Pegasus I.

The agreement with the experimental observations and numerical integrations is further evidence that the first order theory developed here describes the physical situation quite adequately.

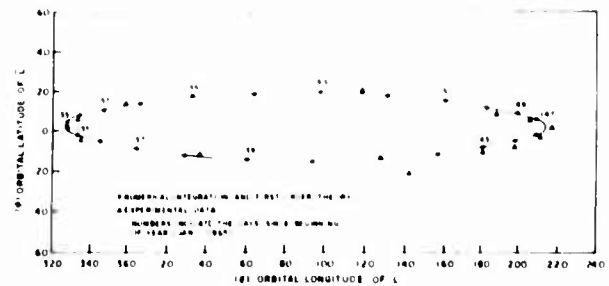


Figure 5. Motion of Rotational Angular Momentum Vector - Pegasus I Satellite - Spherical Coordinates ϕ vs. θ

Figure 6 is a conceptual sketch of the various paths which the momentum vector may follow in the orbit plane coordinates. The particular path which the momentum vector takes depends on the physical characteristics of the body and the initial conditions. It may be of practical astronomical significance to note that both of these conditions may be controlled passively.

All three of the Pegasus satellites followed different types of paths.

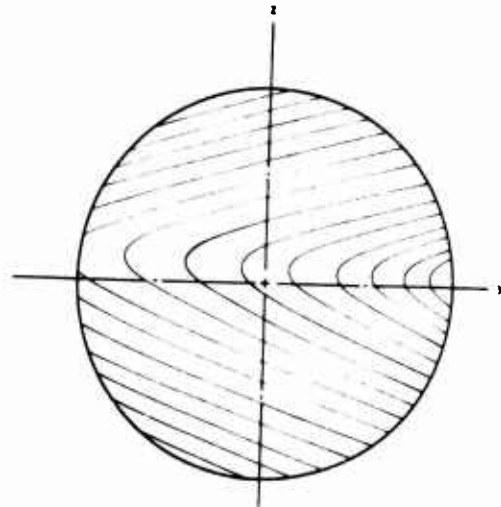


Figure 6. Conceptual Sketch of Possible Paths of Motion

This method has been applied to the luni-solar precession problem and the results agreed with the well known classical theory.

References

1. Beletskii, V. V.: Artificial Earth Satellites. Vols. 1 and 3, Plenum Press, 1961.
2. Colombo, G.: On the Motion of Explorer XI Around its Center of Mass. Torques and Attitude Sensing in Earth Satellites. Academic Press, 1964.
3. Holland, Robert L.: A First Order Theory and Applications for the Rotational Motion of a Triaxial Rigid Body Orbiting an Oblate Primary. Thesis, University of Alabama, Huntsville Center, 1967.
4. Kryloff, N.; and Bogoliuboff, N.: Introduction of Non-Linear Mechanics. Princeton University Press, 1947
5. Kraus, John D.: Electromagnetics. McGraw-Hill, 1953, p. 161.

Acknowledgements

The author would like to thank Dr. Hans J. Sperling, Aero-Astrodynamics Laboratory, Marshall Space Flight Center, for his patience in reviewing the manuscript and for his many helpful suggestions. Grateful acknowledgment is given to Dr. Charles A. Lundquist, Smithsonian Astrophysical Laboratory, who first suggested the application of the averaging principle.

ATTITUDE DETERMINATION OF THE
ARIEL III SATELLITE

R. B. Bent **
Radio and Space Research Station
Ditton Park, Slough, Bucks, England

**Now associated with Wolf Research and Development, Bladensburg,
Virginia.

Attitude determination of the Ariel III satellite

by

R. B. Bent

S.R.C., Radio and Space Research Station, Ditton Park, Slough, Bucks.

Ariel III, the third U.K./U.S. satellite, was successfully placed into orbit on May 5th 1967 with apogee and perigee approximately 600 km and 500 km respectively and inclination 80° . It had been suggested some time before launch that the spin axis direction required for the interpretation of data from some of the experiments could be monitored by observing fluctuations in the telemetry A.G.C. recordings as the satellite rotated; this method had been adopted for the Ariel II satellite ⁽¹⁾ but the analysis proved difficult and as the telemetry polar diagrams for Ariel III were found to be nearly circular this technique was regarded as unpromising. An alternative method was therefore proposed similar to that used on Telstar ⁽²⁾, namely observing the glints of solar reflections from the solar cell panels and from special mirrors placed on the spacecraft. Solar aspect sensors already included in the payload, would determine the angle between the spin axis of the satellite and the direction of the sun thus defining a conical surface containing the spin axis. To position the spin axis on this cone another frame of reference would be required and the mirror glints would define this. The method was adopted successfully for Ariel III and spin axis direction to better than $\pm 2^\circ$ has been calculated together with coning angle and spin rate.

Six echelon mirrors each with an effective reflecting surface at 30° to the spin axis direction were placed around the body of the spacecraft which was launched with a spin rate of 30 r.p.m. When the spin axis is correctly related to the directions of the sun and the observer there are three reflections per second from the mirrors, similarly the body solar cells reflect glints at a rate of six per second with the appropriate directions to the spin axis and the double sided boom solar cells at a rate of two per second. As an example, with the sun's direction normal to that of the spin axis there are glints at angles of 25, 60, 90 and 155

degrees to the spin axis direction. The mirrors are rhodium plated and have a 76% reflection for normally incident light in the visible spectrum whilst the solar cells have a reflectivity of 20% for normal light. If the mirrors had been optically flat only 2 or 3 glints would have been detected during a pass over an observer on the earth since the sun's reflection would illuminate, at any instant, an area of only 5 km diameter, so it was decided to manufacture them flat to only 1° thereby giving a $2\frac{1}{2}'$ dispersion of the sun's image. According to calculations, about ten 7 m.sec. glints of first magnitude would be observed at a ground station in a period of about four seconds from mirror reflections whilst glints from the solar cell panels, which had greater surface irregularities, would each have about 25 m.sec. duration with their glint train lasting for at least 15 sec and the most intense magnitude glint being also first magnitude. As the eye has an integration period longer than the individual glint duration these glints appear to be about two magnitudes lower to the eye, although photographic and photo-electric devices record the magnitude correctly. An experiment carried out in the laboratory showed that the mirror glints would be easily visible to the human eye through binoculars of magnification 10 although reasonably accurate predictions of the azimuth and elevation of observation would be required. Owing to the number of reflecting surface angles some glints would be visible on each pass over any station provided the sun was at least about 10° below the horizon and the satellite was illuminated by the sun.

A number of organisations agreed to co-operate in the observations and they are listed below along with the type of equipment employed.

1. National Aeronautics and Space Administration (NASA) - Worldwide network of
MOTS* cameras
 2. Smithsonian Astrophysical Observatory (SAO) - Worldwide network of Baker-Nunn
cameras
 3. United States Air Force (USAF) - Baker-Nunn cameras
 4. Royal Observatory Edinburgh - Kinetheodolites at Edinburgh and
Malta
 5. Aerospace Research Laboratories U.S.A.F. - Photoelectric camera at Ohio
(ARL)
 6. N.A.S.A. Optical Facility - Photoelectric camera at Washington
- *M.O.T.S. - Minitrack Optical Tracking System 176

Two teams of amateur observers controlled by the S.A.O. Moonwatch group and R.S.R.S. were also alerted. As it is difficult to predict the position along the orbit where glints are expected at a particular station the photoelectric cameras that are capable of tracking the spacecraft from horizon to horizon are the most satisfactory recording system.

echelon mirror and Figure 2 shows them
Figure 1 is a photograph of an / mounted on the satellite. They could be adjusted in angular position, and alignment tests were carried out on a flight satellite. The spacecraft was vibrated to the level expected during lift off and the resulting change in alignment was only $1/6^\circ$. The final flight model alignment was carried out just prior to launch when the spacecraft doors had been screwed down for the last time and the full dispersion characteristics of each mirror were determined. The mirrors were found to exhibit different dispersion characteristics, and it is possible on analysis of ground photoelectric photometry records to indicate which mirror has led to a particular flash.

Since launch there have been many reports of glint observations from satellite tracking cameras and amateur observers all over the world. A sample record from a Baker-Nunn camera in stationary mode is shown in Fig. 3 in which the satellite travels from right to left. The camera shutter was opened just after the satellite entered the field of view. Some remarkable photoelectric records from the Aerospace Research Laboratories, Ohio have led to the calculation of the satellite's coning angle, which is the angle between the geometric and dynamic axes, and have shown it to be less than 1° . There is an r.m.s. error in analysed spin axis direction of about 2° which is no doubt caused by an inability to identify the peak magnitude in the glint train either on photographs or during visual observations by amateurs. The photoelectric data from Ohio however have allowed this peak magnitude position to be determined to an accuracy of about $1/6$ sec. of time. This type of recording is therefore to be recommended in any future use of the optical glint technique. Such a recorder, with azimuth and elevation angle indicates correct to 0.1° enables the spin axis direction to be measured to better than $\pm 1^\circ$ and the coning angle to $\pm 0.1^\circ$. Furthermore, a series of measurements

of the glints is sufficient to measure these angles without the use of solar aspect sensors, particularly when more than one set of glints can be observed on a single pass. By this means the use of telemetry channels for transmitting solar aspect data is avoided.

The results of spin axis direction during the first 115 days are shown in Fig. 4, the day of the year being marked periodically on the curve with launch occurring on day 125.

The coning angle of the satellite which is the angle between the geometric axis and the dynamic axis around which the satellite spins has been determined to be $0.6^\circ \pm 0.1^\circ$. As the satellite passes over an observer it moves in a manner displayed in Fig. 5 where θ is the coning angle. If the observer was monitoring glints photoelectrically his record should show some modulation in magnitude due to the fact that the reflecting surfaces are aligned to the geometric axis. Considering first the simple case of reflections from the solar cell panels which are fixed parallel to the geometric axis we have the following sequence of events illustrated by Fig. 5. Whenever the satellite is in position A (nose up), the same panel, say P_A , will be in the position to give specular reflections. The succession of reflections from P_A will pass through a maximum intensity with a given geometrical arrangement. Owing to the coning action other panels will give maxima at different times. At the other extreme for example, P_B will give maxima intensities later than Panel P_A , and the time displacement between the conditions of maximum intensity is a measure of the coning angle θ .

Figure 6 shows the intensities of the successive reflections from all 12 panels. From the record, taking every 12th reflection, the intensity variation from a single panel can be plotted, and Fig. 7 shows these variations in each case. The curves marked 6 and 12 relate to the extreme positions of the satellite as indicated in Fig. 5, and the time difference between them enables the coning angle to be calculated.

The dispersion from the solar cells is large compared with that from the 60° mirrors fixed to the spacecraft and the corresponding period of time when

reflections occur from the mirrors is therefore shorter. Similar but more accurate results from these mirrors are displayed in Figs. 8 and 9.

By considering reflections from the body solar cell panels it is expected that monitoring the time at which each panel reflects the sun with maximum intensity against its solar cell panel number a resulting graph will follow a sine curve. Such a curve has been plotted in Fig. 10 from the results shown in Fig. 7 and it is quite remarkable how accurately these points follow a sine curve. This would indicate that the short term scintillation of the solar reflections are extremely small. Another example illustrating this point is shown in Fig. 11 where the magnitude v time plot of two adjacent solar cell panels shows almost perfect individual symmetry. The difference in magnitudes between the adjacent panels is caused by the different number of solar cells on alternate panels of the spacecraft as can be seen in Fig. 2.

Thanks are due to N.A.S.A., S.A.O., U.S.A.F. and the Royal Observatory, Edinburgh, for their continuing help in monitoring glints from the satellite, in particular Drs. Kissel and Vanderburgh of the Aerospace Research Laboratories of the Wright Patterson Air Force Base, Ohio and also to the many amateur observers for their valued assistance. The British Aircraft Corporation also deserve special mention for their co-operation in carrying out the installation and mechanical tests on the mirrors in a period of only two months just prior to launch. Acknowledgements are due to the Science Research Council who have been responsible for the management and financial support of the Ariel III international co-operative project.

Dr. D. E. Smith of R.S.R.S. co-operated in the planning of the experiment in detail and developed the mathematical techniques needed in the data analysis. He has also organised the visual observations made by many of the amateur observers.

The work described was carried out at the Radio and Space Research Station of the Science Research Council and this paper is published with the permission of the Director.

References

1. C. C. Harvey - Results from U.K.-2 satellite. Annales D'Astrophysique, Tome 28, No. 1 (pp. 248-254) 1965.
2. J. S. Courtney-Pratt, J. H. Hett, J. W. McLaughlin - Optical Measurements on Telstar. Bell Telephone System Monograph 4575, 1963.

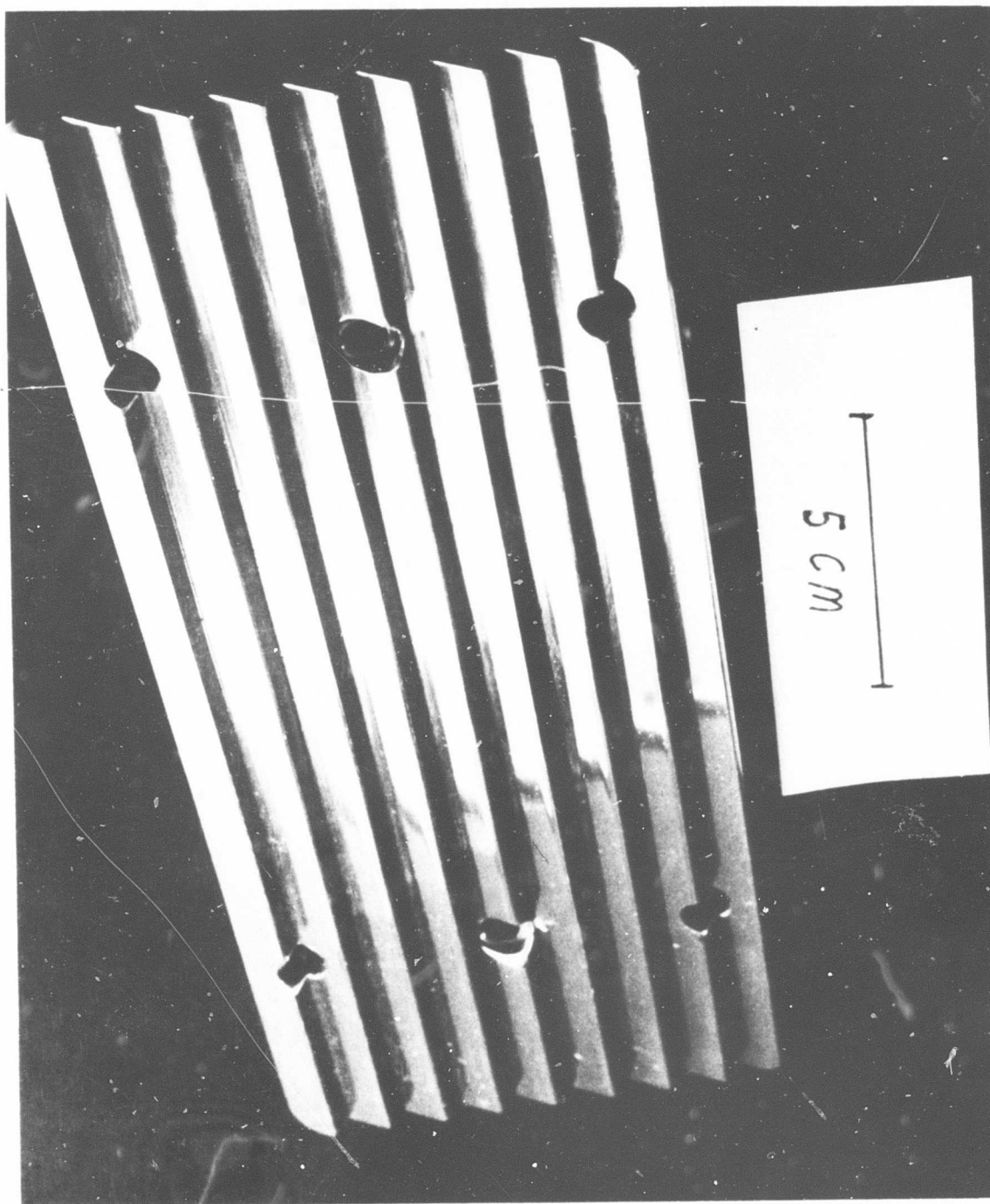


Figure 1. Photograph of an echelon mirror

(copy of figure 2 not available)

Figure 2. Echelon mirrors mounted on satellite.



GLINTS FROM BODY SOLAR CELLS ON ARIEL III

Photographed by S.A.O. Baker-Nunn camera at Island

Lagoon, Australia, 14 May 1967

Figure 3 - Record of satellite traveling from right to left.

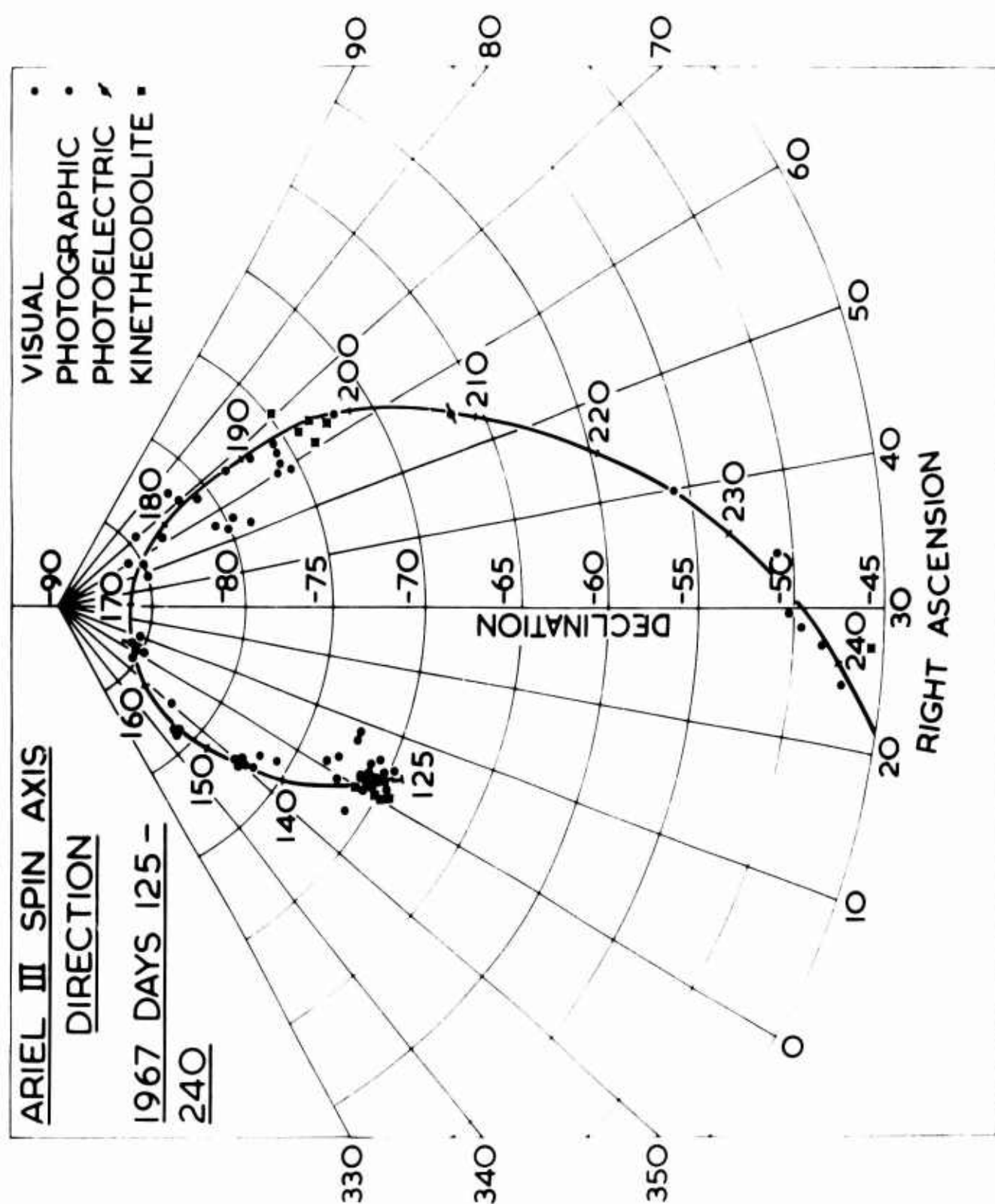


Figure 4 - Results of spin axis direction during the first 115 days

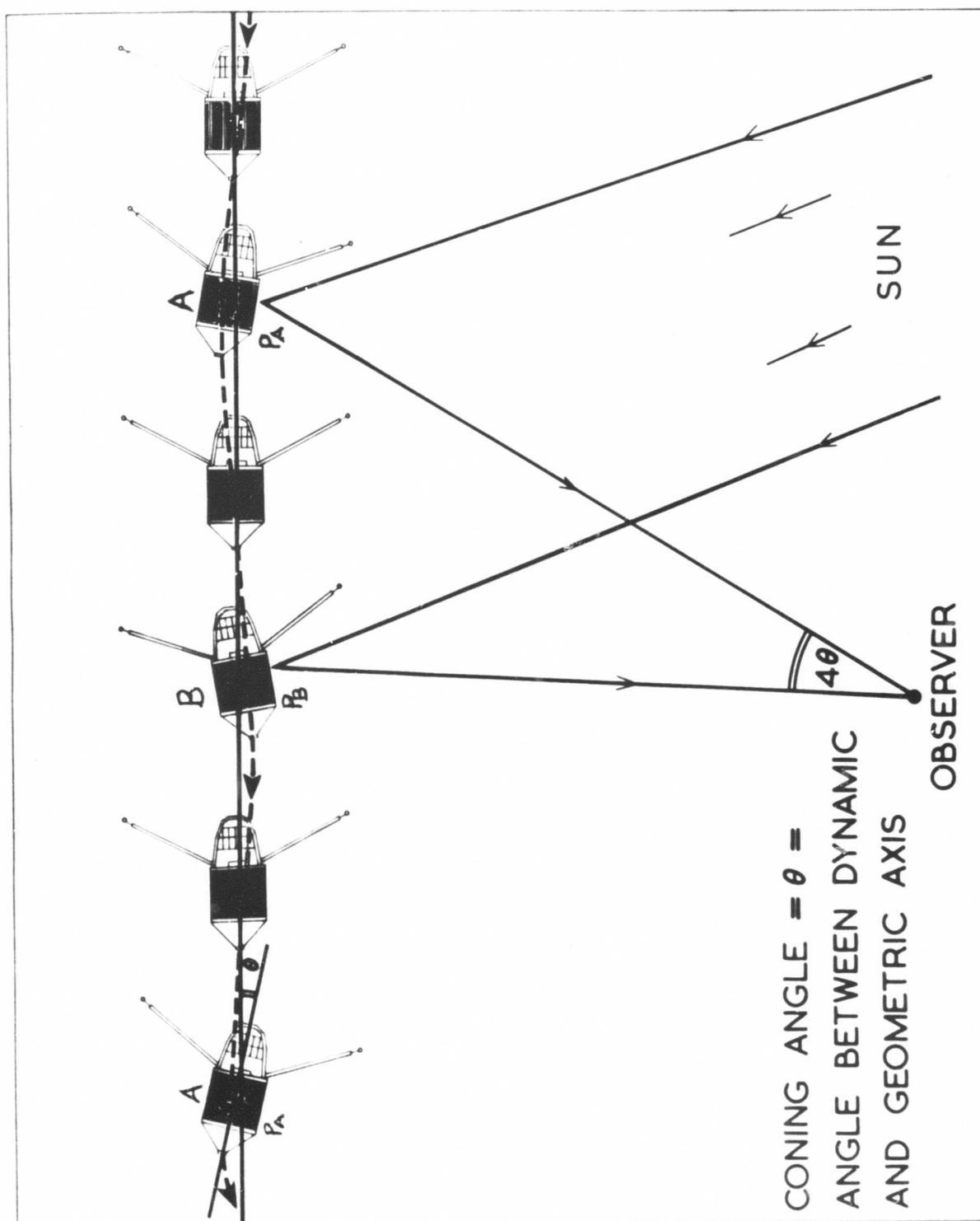


Figure 5 - Illustration of a Sequence of Events

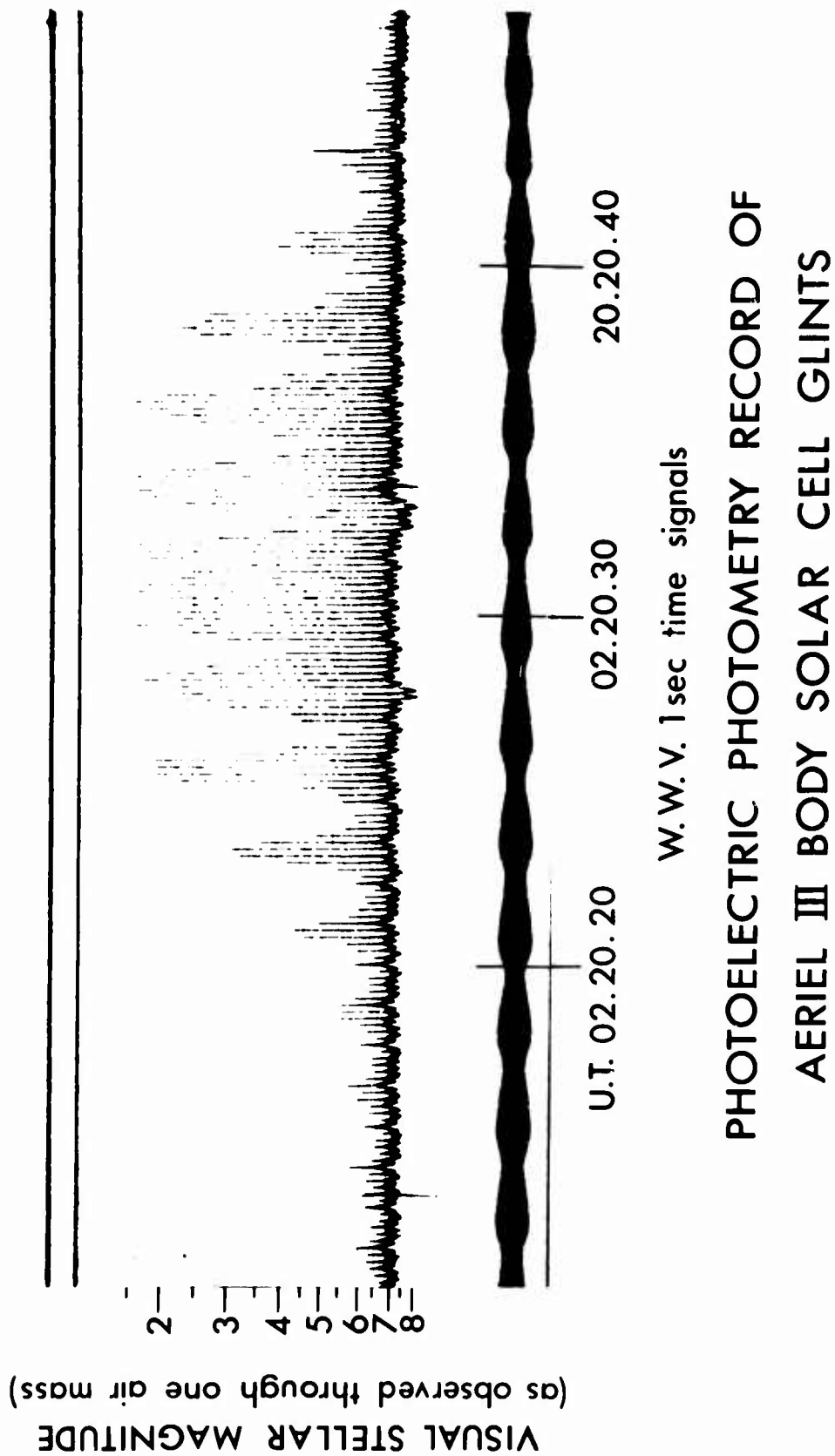


Figure 6 - Intensities of Successive Reflections
 from all 12 panels

Taken by the Aerospace Research Laboratories, U.S.A.F. at the Wright-Patterson
 Air Force Base, Ohio, U.S.A. on 17 July 1967.

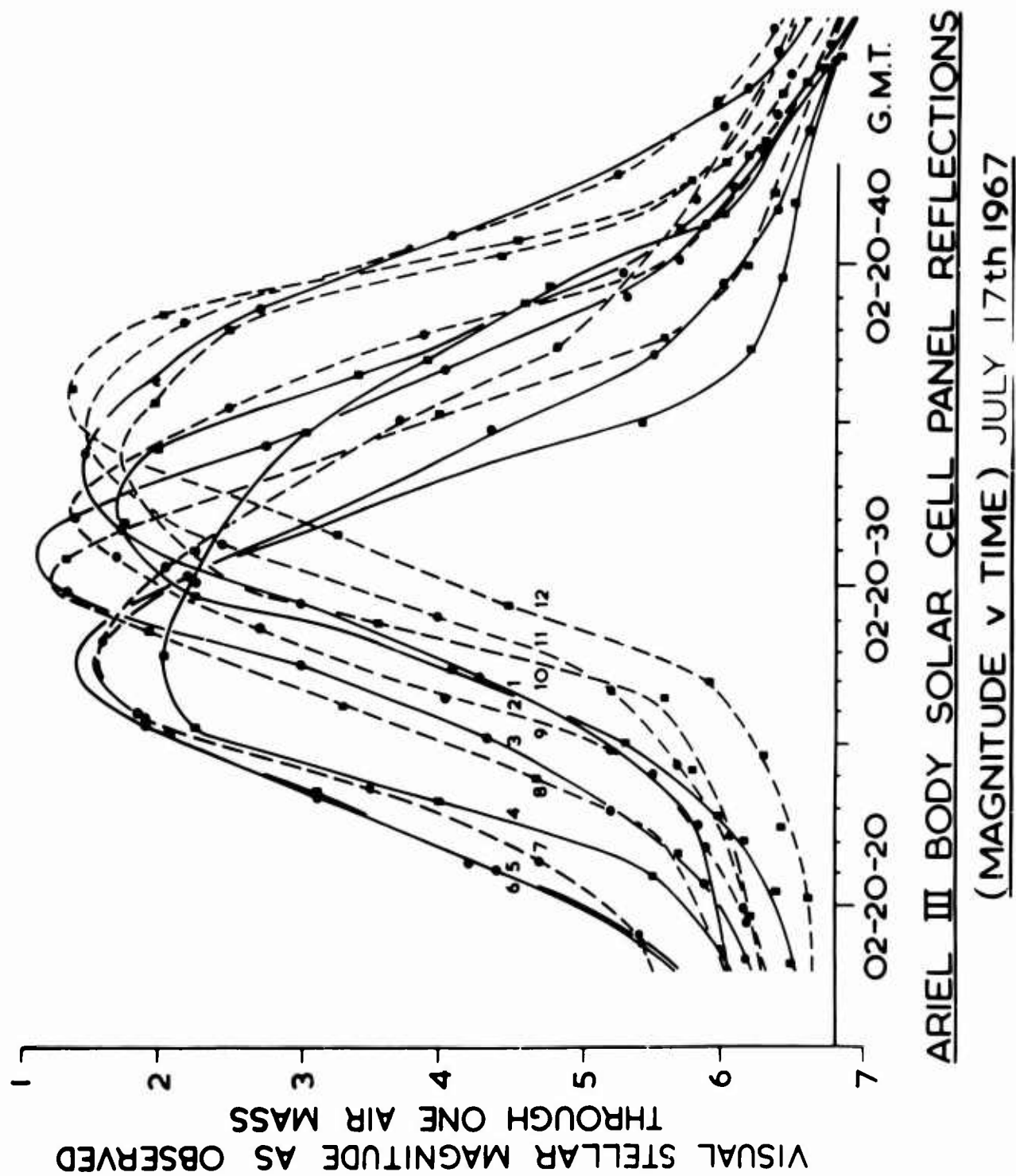


Figure 7 - Plotting of intensity variations

(Copies of Figures 8 & 9 not available)

Figures 8 and 9 - Reflections from 60° Mirrors

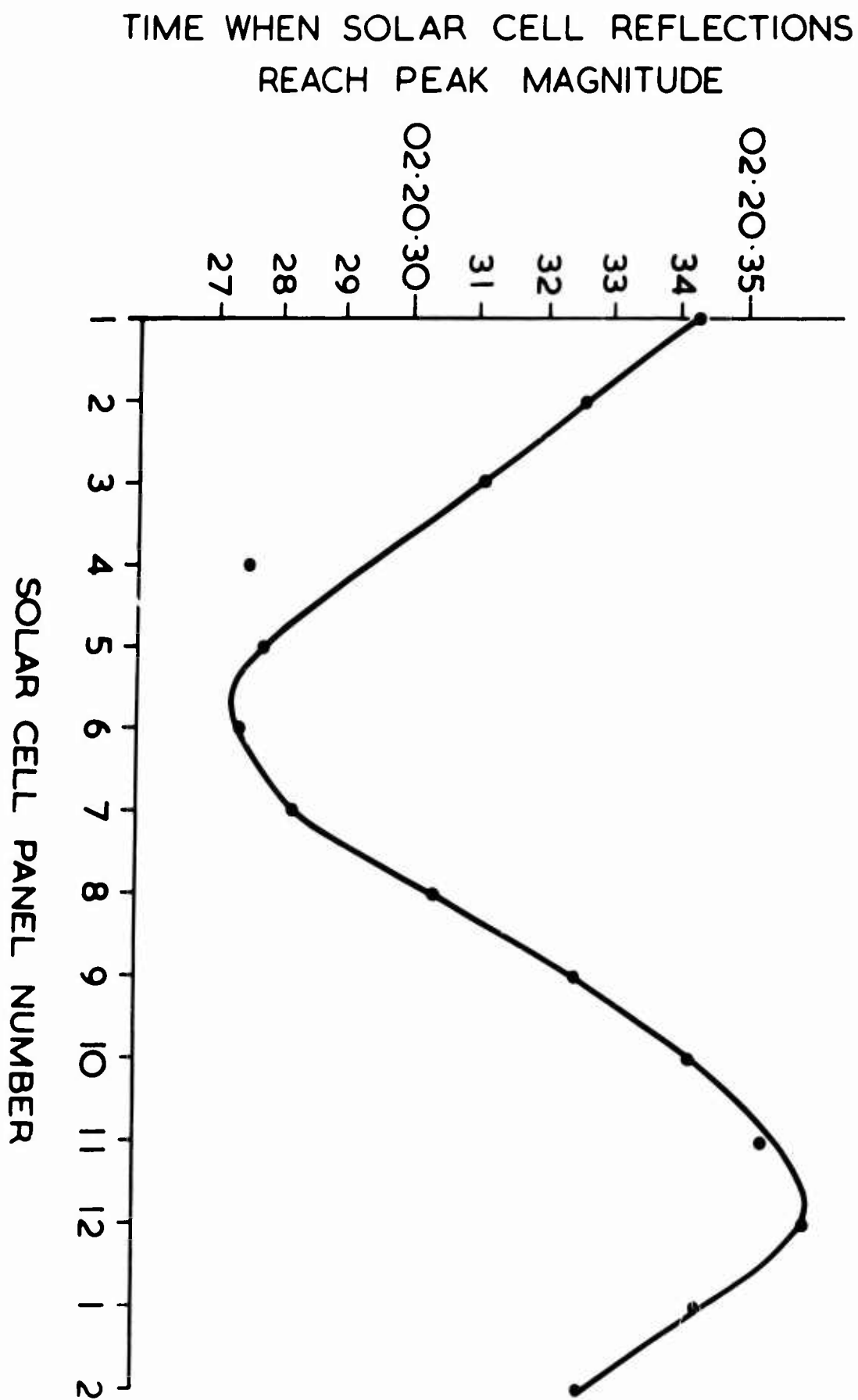
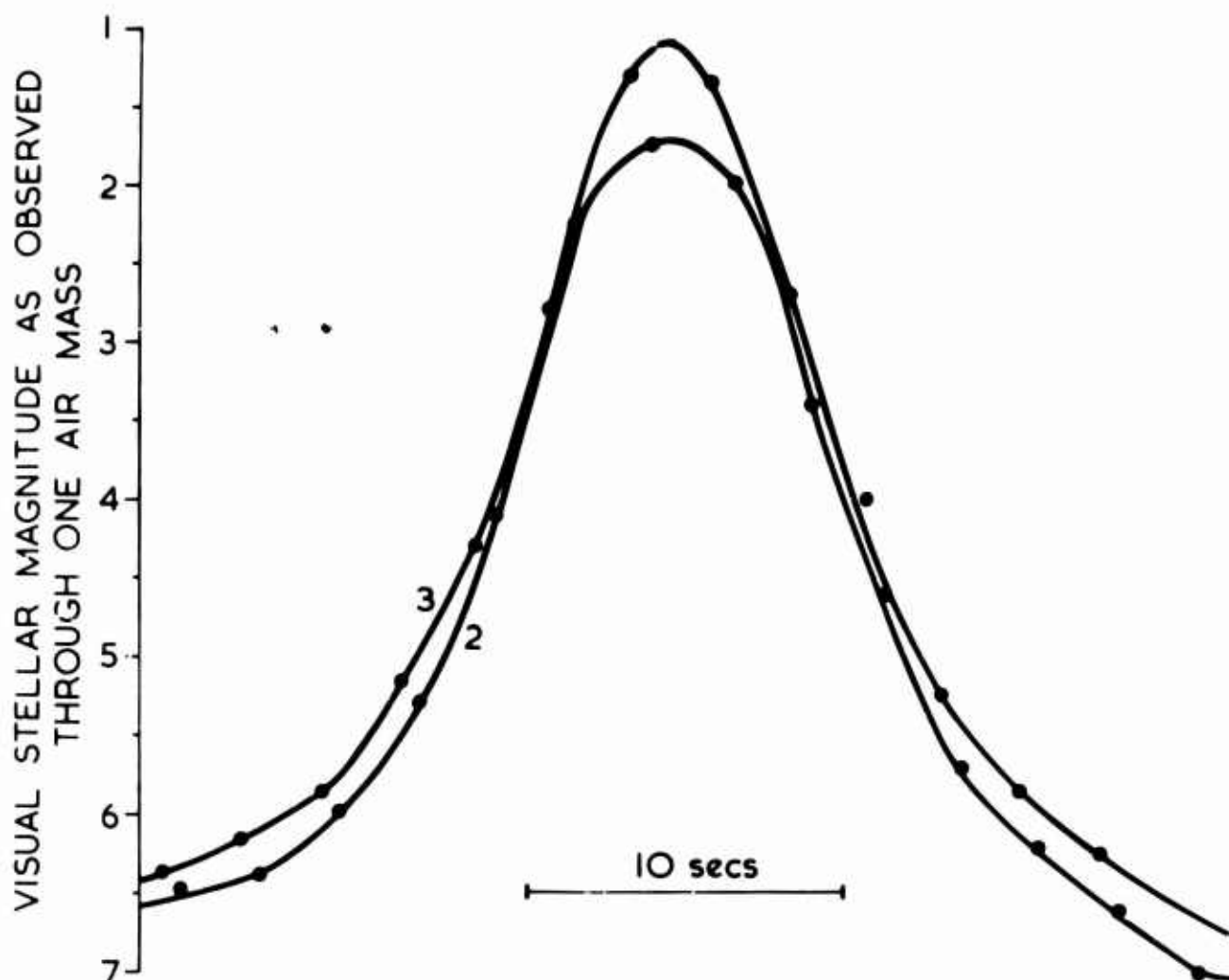


Figure 10 - Sine Curve of Sun Reflections



REFLECTIONS FROM TWO ADJACENT SOLAR CELL
PANELS ON ARIEL III

(MAGNITUDE v TIME PLOT FROM A.R.L. PHOTOELECTRIC
 PHOTOMETRY RECORD JULY 17th 1967.)

Figure 11 - Curve showing magnitude v time plot

CZECHOSLOVAKIA CONTRIBUTION ON THE
SATELLITE PHOTOMETRY

F. Link
Astronomical Institute, Ondrejov, Czechoslovakia

Czechoslovakia Contribution on the Satellite Photometry

F. Link

Astronomical Institute, Ondrejov, Czechoslovakia

1. INTRODUCTION

Our work at the Ondrejov Observatory (Dept. of the Upper Atmosphere) has been concerned with the balloon satellites, and the photometry of satellite eclipses in order to explore the upper atmosphere.

A by-product of this work is the study of satellite light curves outside the eclipses. The form of the light curves depends on surface properties of these satellites and, therefore, I think that some of our results may be of interest for the participants of this symposium.

2. PHOTOMETRY OF SATELLITES

We have used a two-color photoelectric photometer in recording the light curves of the satellite transits. The scheme of each half of the photometer consists (Fig 1) of:

- a. an achromatic objective: 50 mm diameter and 40 cm focal length.
- b. a field stop C giving 0.75° of the sky followed by a Fabry lens L which forms the image of the objective on the photocathode FK of the multiplier EMI 6094.
- c. a wheel F containing the color filters.
- d. a radioactive luminiscent capsule R as the light standard.
- e. a pen recorder with paper speed of 3 mm per sec.

In the latest version we have adopted, instead of two separate recorders, one high speed Ripp recorder micrograph. The photocurrents of both photometers are connected alternately by an astronomical clock (each three seconds) to this recorder; in this manner we obtain two superposed light curves whose interruptions are exactly timed.

The whole photometer has an altitude/azimuth mounting. The tracking is performed manually with the observer using both hands - one hand acting to push or pull in azimuth and the other to set altitude by soft striking of a guiding bar. With some training it is possible to track all the balloon satellites by this method.

3. ROTATION OF SATELLITES

All three balloon satellites Echo I, II and Pageos I display light fluctuations which may be interpreted in terms of rotation. On the light curves one can find the repetition of many details. Their time separation gives directly the length of the photometric period, T_{ph} , which is of course slightly different from the sidereal period, T_{sid} , because of the combination of rotation with the topocentric revolution of the satellite.

In the most simple case, when the orbit of the satellite is placed in the plane containing also the sun and the observer and the spin axis is perpendicular to this plane, we have the following relation (2, 3):

$$T_{ph} = T_{sid} \left(1 + \frac{\Delta}{720^\circ} \right)$$

where Δ is the topocentric angle described by the satellite during one photometric rotation. It is assumed that the balloon surface produces a specular reflection and that the brightness fluctuations result from local irregularities in the surface figure.

In the above relation the topocentric angle Δ increases with decreasing topocentric distance of the satellite, i.e., toward the zenith. Our formula gives, therefore, the possibility to fix the sense of the rotation by the use of the following rule:

"If the photometric period of rotation increases toward the culmination, the sense of rotation is direct, i.e., identical with the sense of revolution, and vice versa."

4. EXPERIMENTAL RESULTS

The main results obtained for the three balloon satellites are as follows:

ECHO I (1960 Iota I)

The light curves have a very irregular shape with many periodic details, enabling good determinations of the rotation period. From November 1964 to February 1967 the length of the period has dropped from 0.93^m to 0.66^m (2, 4). The internal accuracy of these determinations is as high as $\pm 0.003^m \pm 0.2s$; the main uncertainty is due to the systematic differences between the photometric and sidereal periods which, of course, change from one transit to another.

The form of the light curves seems to be determined mainly by the relative position of the three bodies: sun, satellite, observer, since we have found nearly the same form of the light curve (Fig 2) after an interval of 5 months. This shows also the constancy of the satellite form during this time interval. The sense of the rotation is found to be retrograde. In fact, we found for the differences of the photometric periods (horizon - zenith) the following results:

+ 0.414 ^m	in 41 cases
- 0.129 ^m	in 29 cases
zero	in 16 cases

ECHO II (1964 - 04A)

In 1964 we observed many interesting light curves showing (as in Fig 3) the existence of discontinuities due to antennae or similar systems on the opposite sides of the balloon. From September 1964 to August 1965, the rotation period had slowed from 1.52^m to about 2.3^m. After this date a lack of details on the light curves makes the determination of the rotation quite difficult.

PAGEOS (1966 - 56A)

The light curves always show many details, but their repetition is not obvious, in contrast to Echo I. In the summer of 1966, the sidereal rotation period was between 12-13^m(4). Some of the autumn 1966 curves display a series of light flashes of great amplitude (Fig 4). At the end of March 1967, the period seems to have fallen to about 6^m.

In every case the use of Pageos as a geodetic satellite would not have been too easy because of the large fluctuation of the light.

5. ECLIPSES OF ECHO 2

As the eclipses of the satellites lie outside the scope of this symposium, let me mention only briefly some work accomplished at Ondrejov Observatory.

The photometric theory of satellite eclipses had been already developed in 1961 (5,6) on the basis of our 30-year-old lunar eclipse theory. The computation of an ephemeris supplements this work (7). Finally, to aid in solutions of satellite eclipse problems, we have published a set of very convenient Tables (8) giving the density of the shadow for Echo II eclipses in every possible case between 30° N and 70° N latitude.

Up to the present time we have measured several tens of eclipse curves of Echo 2. Their final reduction depends on the exact orbital elements which will soon be (we hope) available from the Smithsonian Astrophysical Observatory. Some preliminary attempts in this direction on two eclipses are very promising (9).

BIBLIOGRAPHY

1. F. Link and G. Tacharov, BAC 17 (1966) 151.
2. F. Link, BAC 17 (1966) 16.
3. F. Link, Space Research 6 (1966) 1004.
4. F. Link, L. Neuzil, and G. Zacharov, Space Research 8 (1968)

5. F. Link, Space Research 2 (1961) 70.
6. F. Link, BAC 13 (1962) 1.
7. F. Link, BAC 16 (1965) 112.
8. F. Link and L. Neuzil, BAC 18 (1967) 359.
9. F. Link

FIGURES

- Figure 1 Two-color photoelectric photometer.
- Figure 2 Light curves of Echo 1 in 5-month interval. Similarity of both curves but change of the period ($0.93^m-0.82^m$).
- Figure 3 Light curves of Echo 2
3-4 Mid September 1964 (rot. per. 1.57^m)
47-49 end of October 1964 (rot. per. 1.68^m)
72-79 beginning of May 1965 (rot. per. 2.0^m)
- Figure 4 Portion of Pageos light curve (1966 X. 22) showing several flashes.

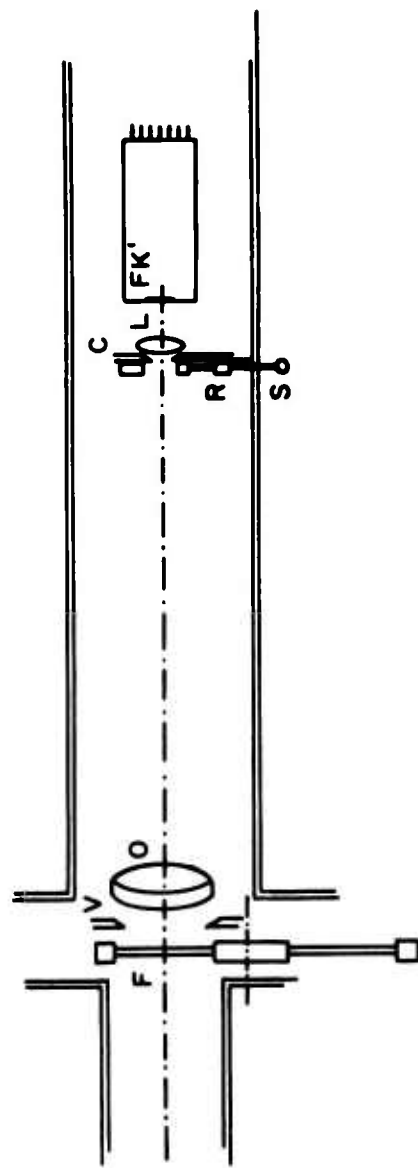


Figure 1. Two-color photoelectric photometer.

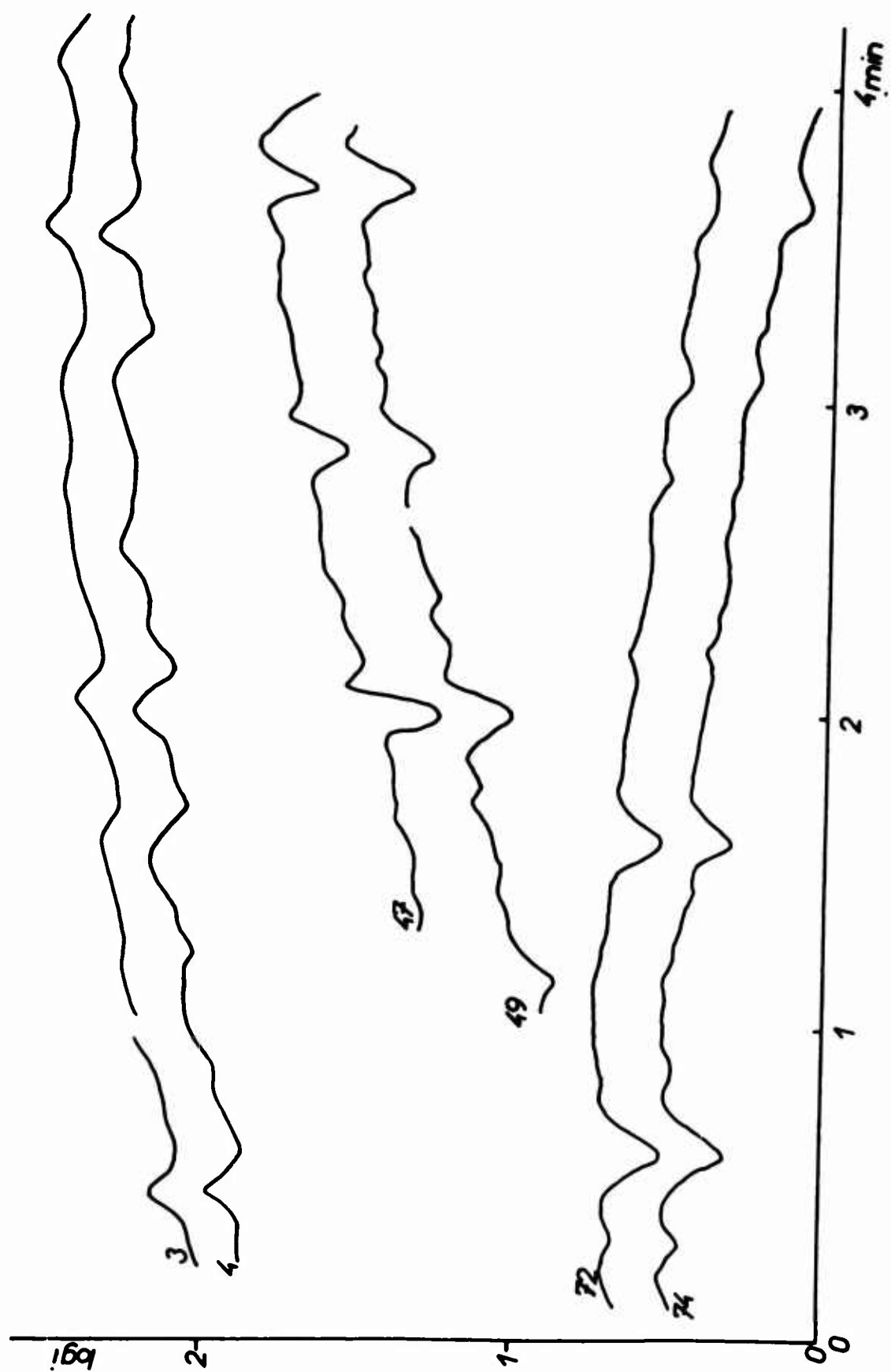


Figure 2. Light curves of Echo 1 in 5-month interval. Similarity of both curves but change of the period ($0.93^m - 0.82^m$).

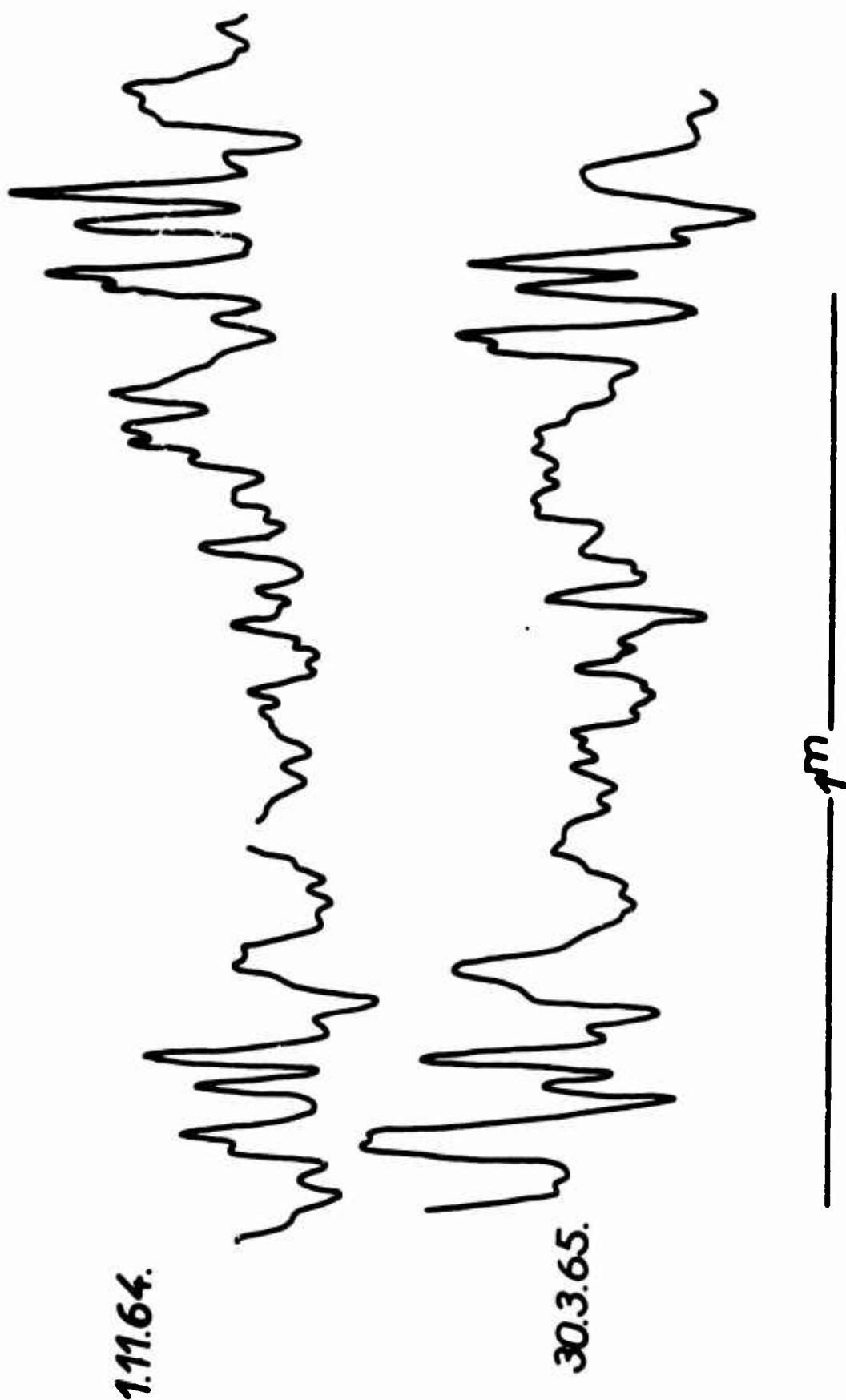


Figure 3 - Light curves of Echo 2
 3-4 Mid-September 1964 (rot. per. 1.57m)
 47-49 end of October 1964 (rot. per. 1.68m)
 72-79 beginning of May 1965 (rot. per. 2.0m)

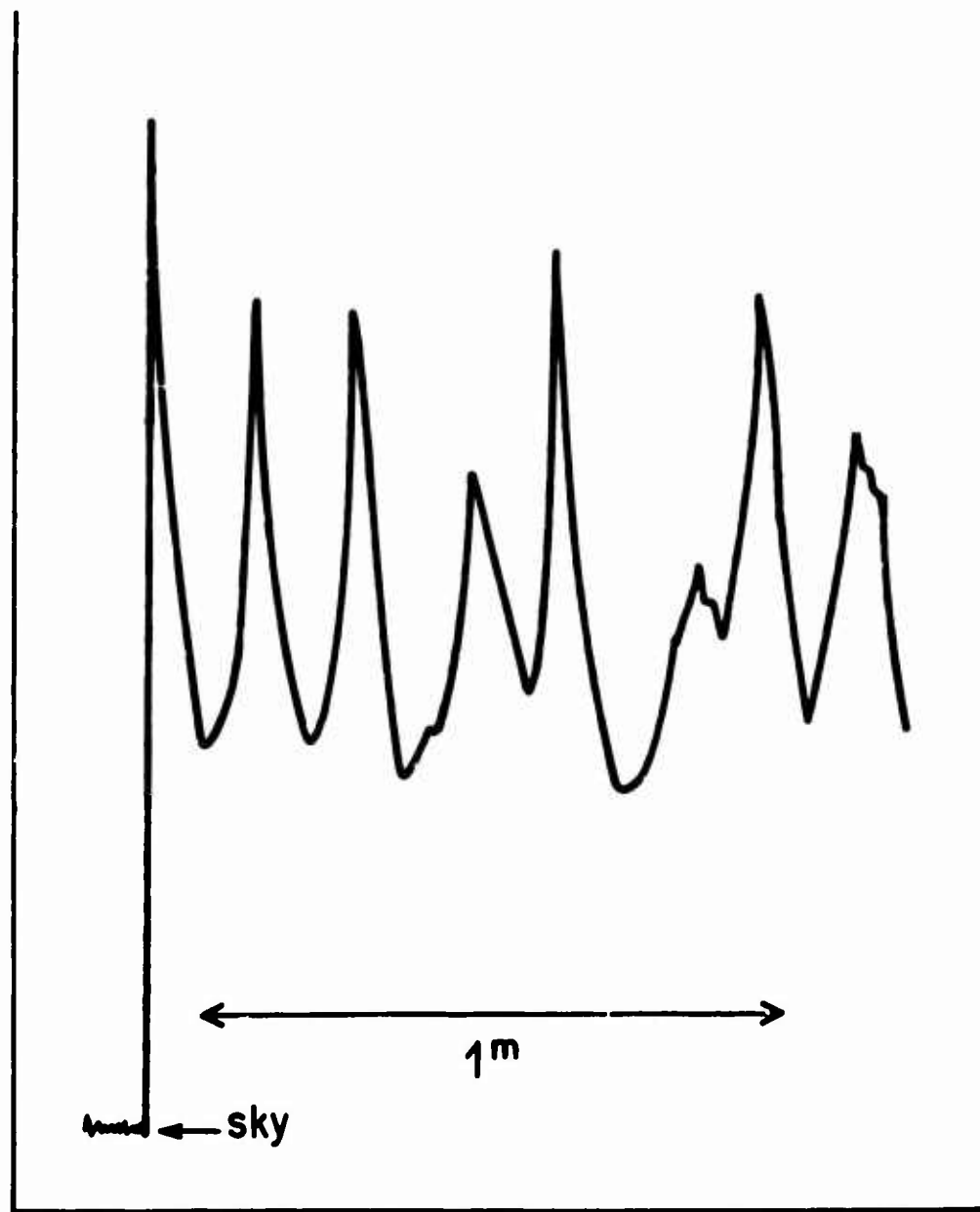


Figure 4. Portion of PAGEOS light curve (1966 X. 22) showing several flashes.

WIDE BAND (VISUAL SPECTRUM) PHOTOELECTRIC
PHOTOMETRY OF PAGEOS DURING ITS FIRST
FIFTEEN MONTHS IN ORBIT

Richard C. Vanderburgh
General Physics Research Laboratory

Project 7114

ABSTRACT

Photoelectric photometry, displayed as continuous lightcurves on a logarithmic scale, are presented with sufficient detail to enable the reader to ascertain their phenomenological character and general quality. Selected portions of these lightcurves are presented and discussed in greater detail to enhance the understanding of the physical processes important in the optical scattering of spacecraft and in the collection of data. Calibration techniques and data reduction methods are outlined, with commentary on the significance of short and long term brightness fluctuations. A portion of the data is analyzed and attention is drawn to the types of information which is extractable and which may be of interest to geodesists, PAGEOS project scientists and engineers, fabricators of future balloon-satellites, and investigators of satellite dynamics. The earliest records indicate that a spheroid of about fifteen meters radius was deployed, the radius being nearly uniform. The most recent record strongly suggests a shrinking of the original sphere to a prolate spheroidal shape during its fifteen months in orbit. Intermediate records indicate varying but generally increasing degrees of surface anomaly. These data comprise the most extensive and definitive information at optical wavelengths known to exist for the PAGEOS satellite, and were collected at the Aerospace Research Laboratories' Sulphur Grove (Ohio) Observatory.

INTRODUCTION

As part of the program on photoelectric photometry of orbiting spacecraft carried out at the Aerospace Research Laboratories since early 1962, the PAGEOS spacecraft was singled out for study for several reasons. These include the intent (1) to study the spin history from deployment until a condition of steady state was reached, (2) to study the scattering properties of the object, both diffuse and specular if possible, for comparison with those of Echo I (its prototype) and Echo II, (3) to study the buildup of brightness fluctuations following relaxation of the internal inflation pressure, and (4) to use this object for measurement of eclipse phenomena as measured near its apogee for comparison with eclipse measurements of the nearer Echos I and II. Another inflation-deployed spacecraft, OV1-8 (1966-63A) was scheduled for launch the following month and was also to be observed from soon after initial injection for the same reasons.

The anticipation of a spin build-up was predicated on the previous optical measurements at ARL and at Ondrejov, Czechoslovakia by F. Link (Ref. 1) of inflatable spacecraft, namely Echo I (1960 Ioto 1), Explorer 9 (1961 Delta 1), DASH 2 (1963-30D), Explorer 19 (1963-53A), Echo II (1964-04A), and Explorer 24 (1964-76A), all indicated that a state of rotational motion at surprisingly rapid rates was the eventual equilibrium state for all of these vehicles although the rotation of Echo II has dropped to a very low level. Table I gives rotation rates inferred from optical photometry on these spacecraft on various dates of observation when definite periodic brightness variations were discerned. Included are data on OV1-8. Early Echo II data based on radio measurements of the Goddard Space Flight Center are also included, as reported by Mar and Vigneron of the Defense Research Telecommunications Establishment of Canada.

Photoelectric data on the PAGEOS spacecraft were obtained as early as 6^h20^m after inflation, i. e., after 2.1 orbits of the earth near the beginning of Rev 3. Additional early data were obtained on Rev 11 and Rev 27. These data were obtained at the ARL OPOS Observatory at Sulphur Grove, Ohio. Observing equipment² consisted of a 4-axis mounted 24" Cassegrain telescope shown in Figure 1 employing a logarithmic-feedback photometer³ using a specially selected RCA 7029 photomultiplier which has an S-17 photocathode. The detector was used without filter; the resulting broad-band photometry thus covered the wavelength range from 310 to 600 millimicrons. Data were recorded on an FM tape recorder. Aided manual tracking maintained the target in a two arc-minute diameter aperture. Stars were recorded for brightness comparisons, and reference voltages recorded as a brightness scale.

Selected oscillograms are shown in Figures 2-7. These are time-compressed copies produced by a light-beam galvanometer recorder, and read from right to left. One data channel records photometer output, another time pulses recorded directly from the WWV radio transmissions.

Table I. Rotation Rates of Inflation-Deployed Spacecraft Data are apparent rotational periods derived by optical photometry at the ARL OPOS Observatory unless otherwise noted.

Vehicle	Date (U. T.)	Rotational Period Seconds	Vehicle	Date (U. T.)	Rotational Period Seconds
Echo I	8 July 62	177.0	Echo II	14 April 64	101.0**
	1 Nov 64	56.5*		24 May 64	99.0**
	30 Mar 65	53*		23 July 64	99.8**
	30 June 67	38.0		1 Sept 64	97.6**
	11 Sept 67	37.7		13 Sept 64	93.8*
Explorer IX	2 May 63	2.66		1 Nov 64	100.8*
	15 June 63	2.67		9 Nov 64	100.0
1963-30D Dash 2				12 Nov 64	102.0
	2 Oct 66	59.3		21 Nov 64	98.0
	7 Nov 66	61.3		30 Apr 65	122*
	16 Dec 66	62.7		19 Mar 66	139.0
Explorer XIX				28 May 66	135.5
	Oct 64			29 Apr 67	840
	July 66				
	25 Oct 66	6.39		27 Aug 66	4.11
	23 Nov 66	6.40		16 Dec 66	4.31
	30 June 67	7.25	Explorer XXIV	29 April 67	4.52
				20 Oct 67	4.9
				18 July 66	26.3
				20 July 66	24.2
				26 July 66	21.0
				5 Aug 66	19.25
				27 Oct 66	14.58
				29 Jan 67	13.03
				28 April 67	9.85
				15 Oct 67	6.95

* F. Link, B.A.C. Vol. 12 (1966) No. 1 (Reference 1).

** J. Mar and F. R. Vigneron, COSPAR-IAU-IUTAM Symposium of 20-23 April 1965 (Reference 9).

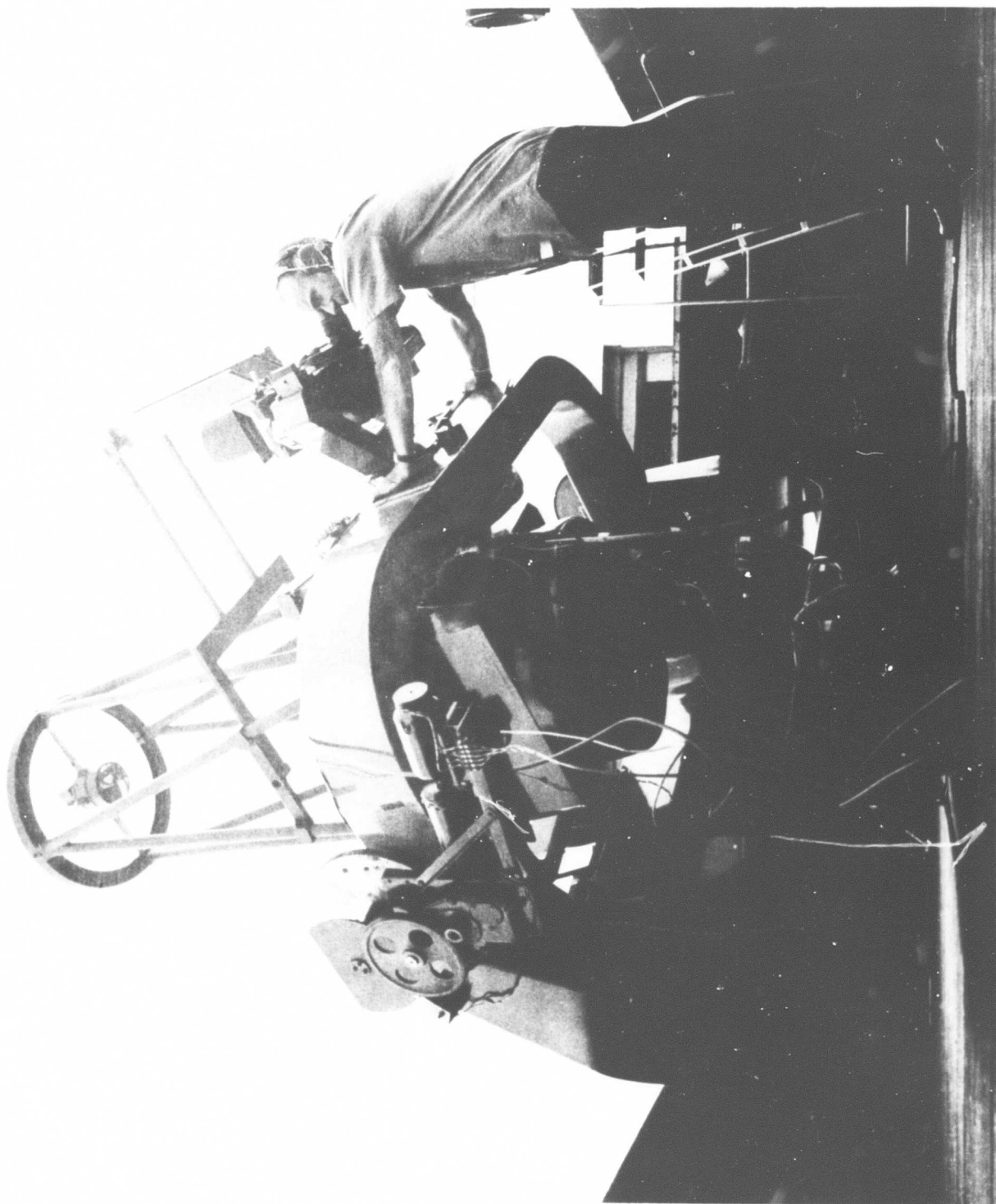


Figure 1 - The 61-cm Satellite Tracker on 4-Axis Mount

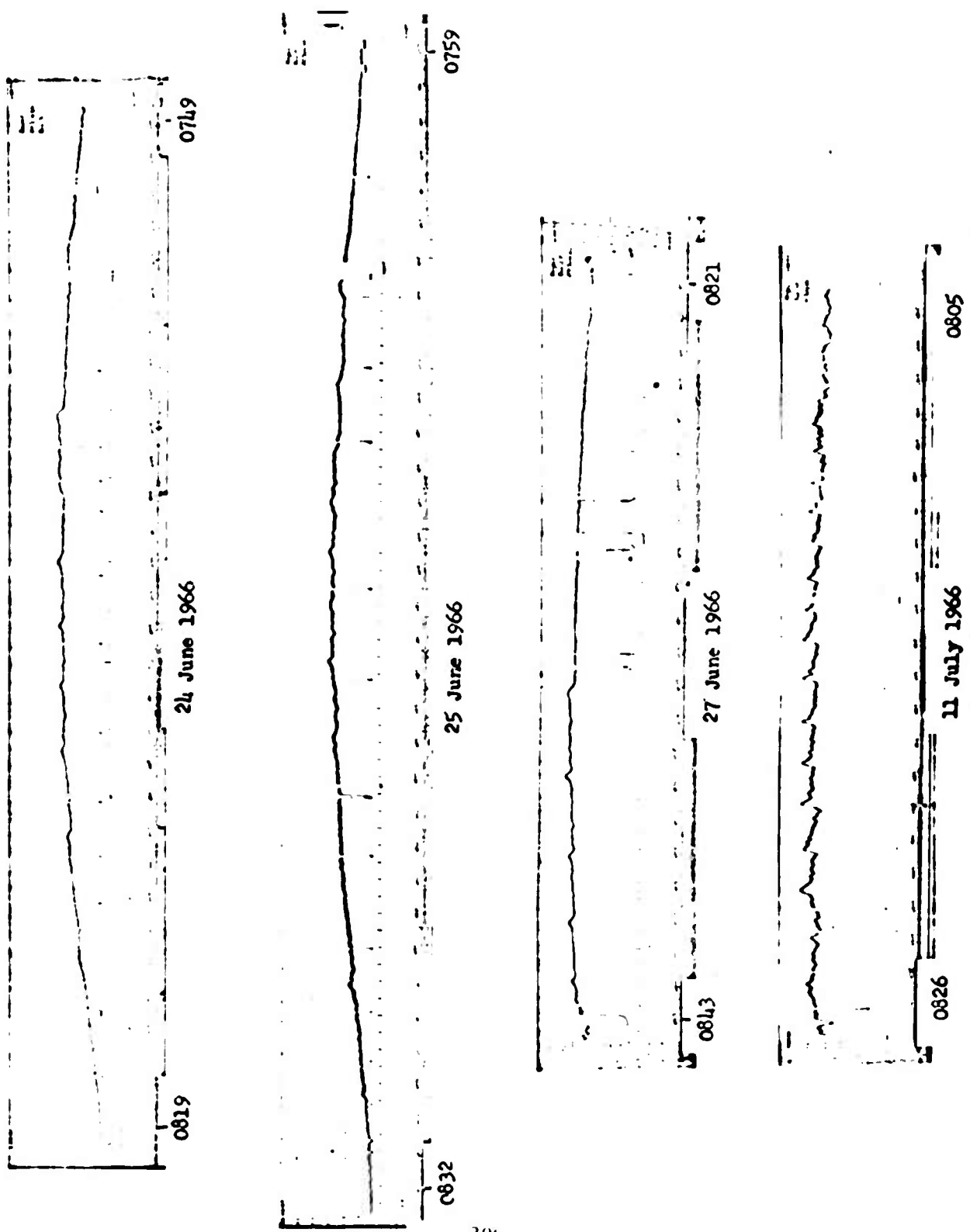


Figure 2: PAGEOS Lightcurves 24 June 1966 - 11 July 1966

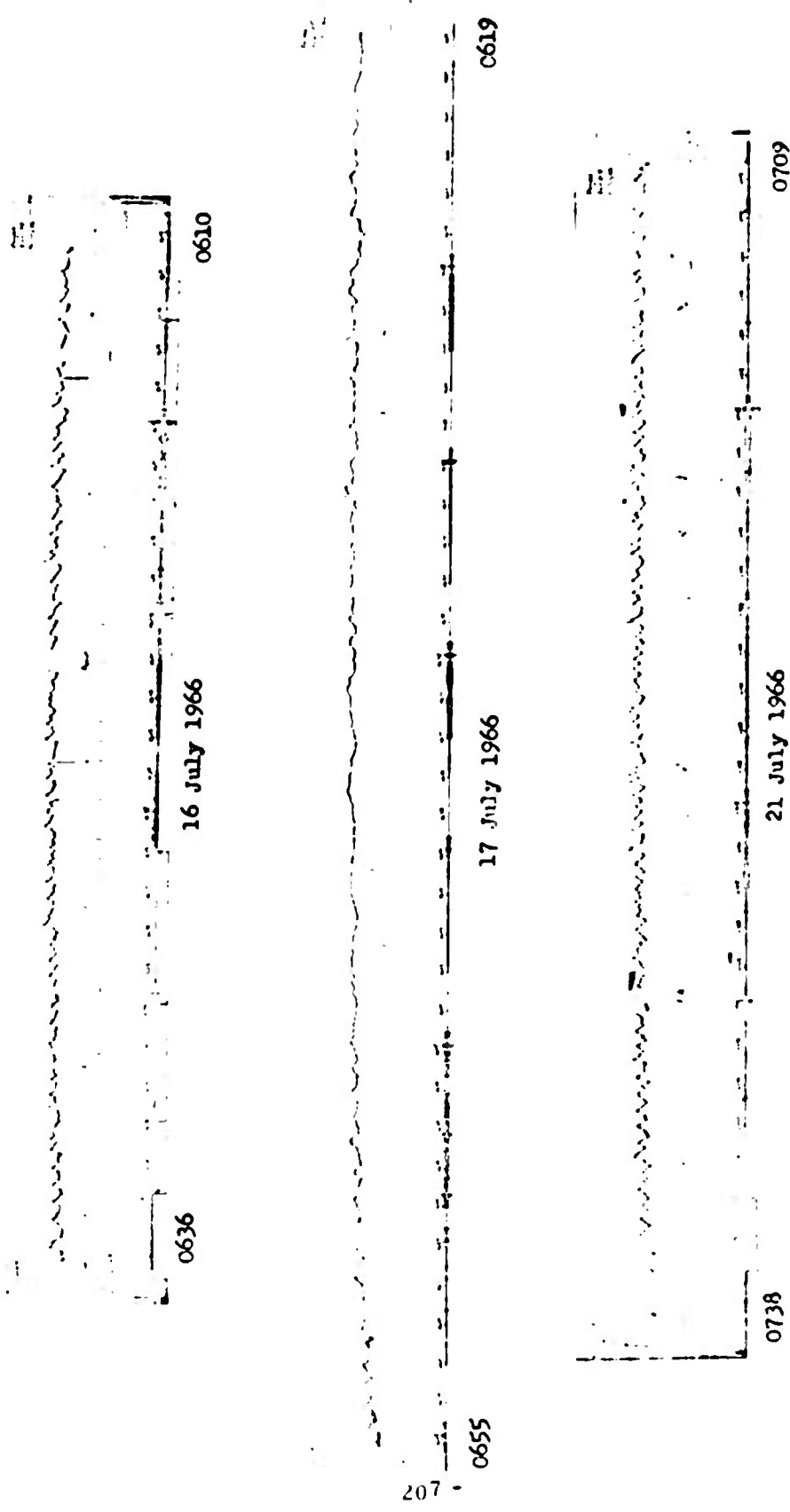


Figure 3: PAGEOS Lightcurves 16 July 1966 - 21 July 1966

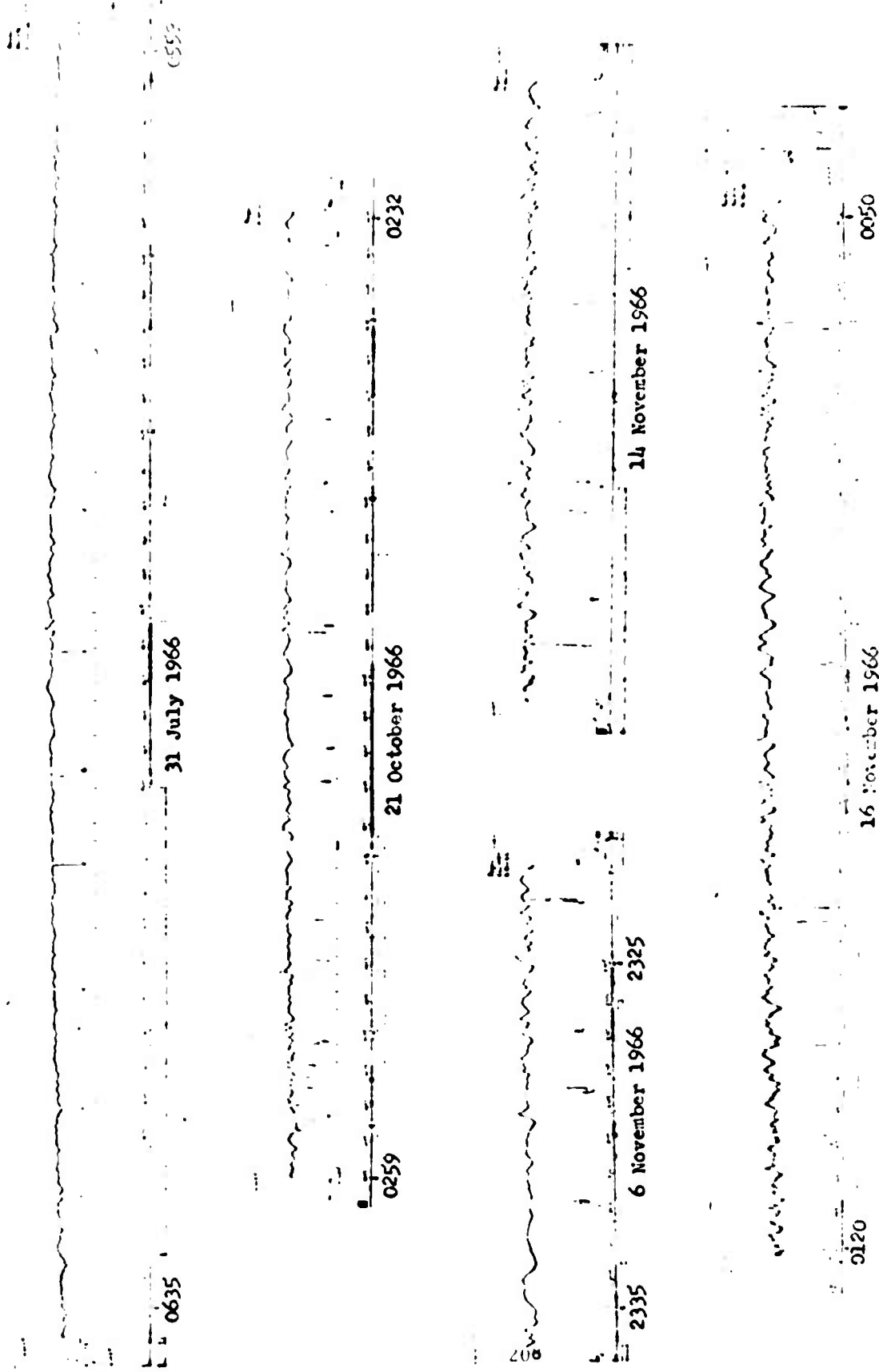


Figure 4: PACEOS Lightcurves 31 July 1966 - 15 November 1966

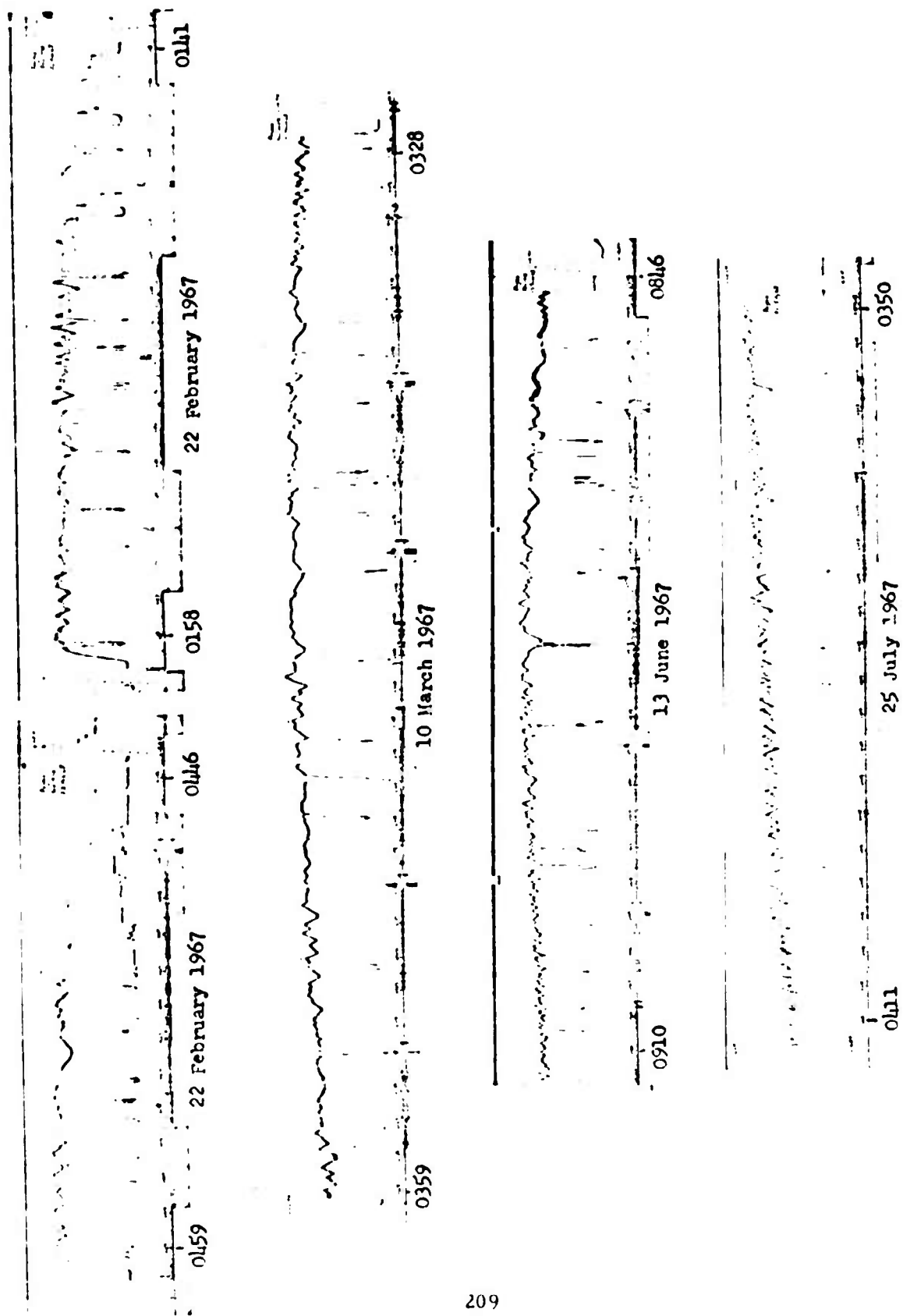


Figure 5: PACEDS Lightcurves 22 February 1967 - 25 July 1967

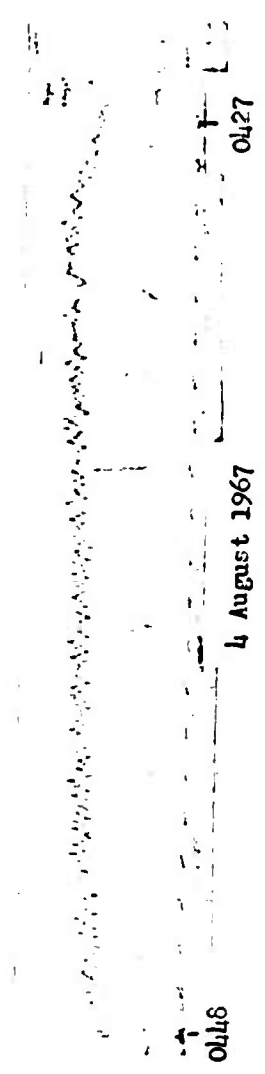
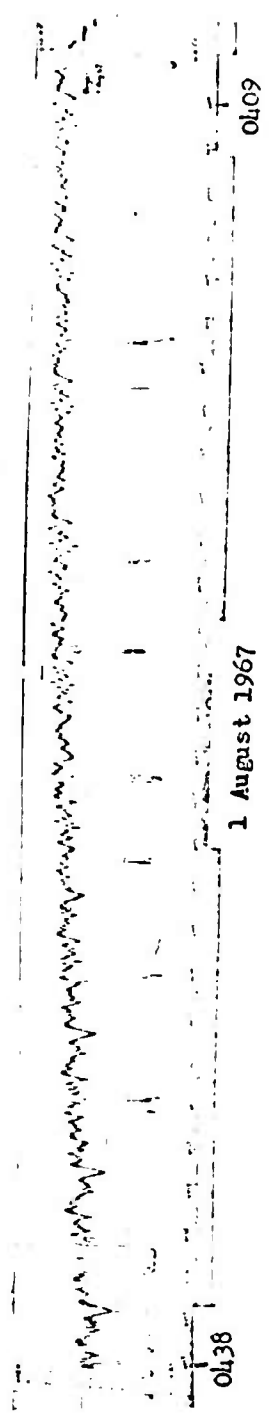
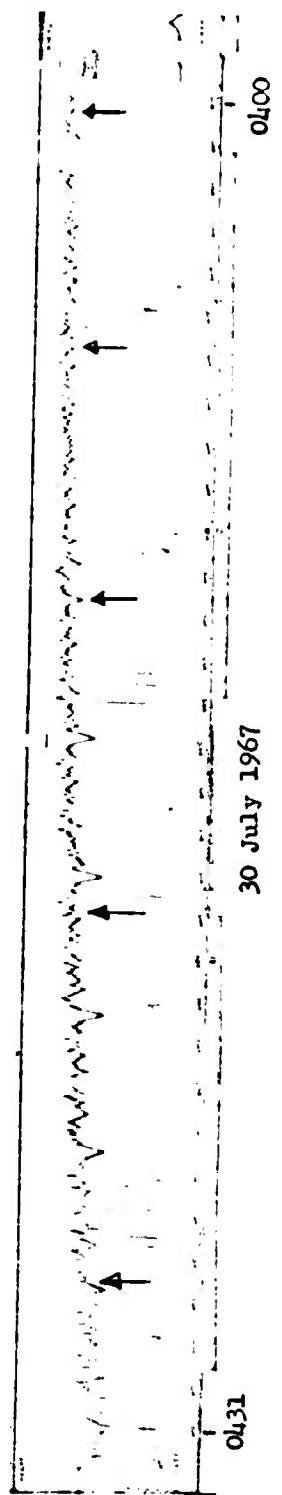
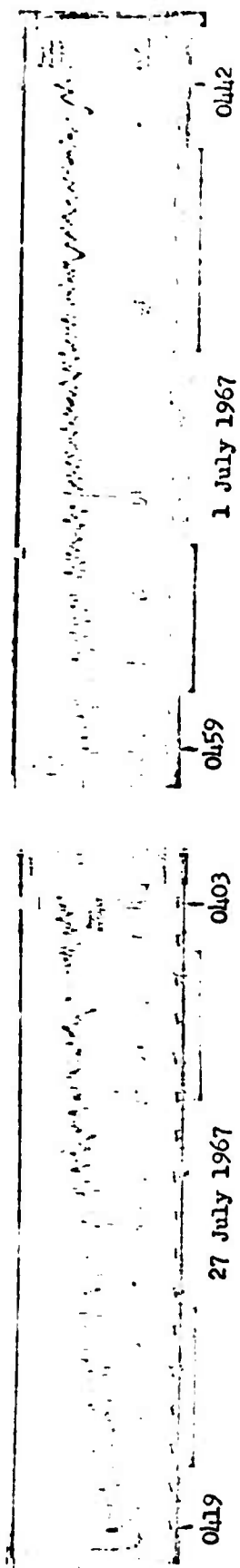


Figure 6: PAGEOS Lightcurves 1 July 1967 - 4 August 1967

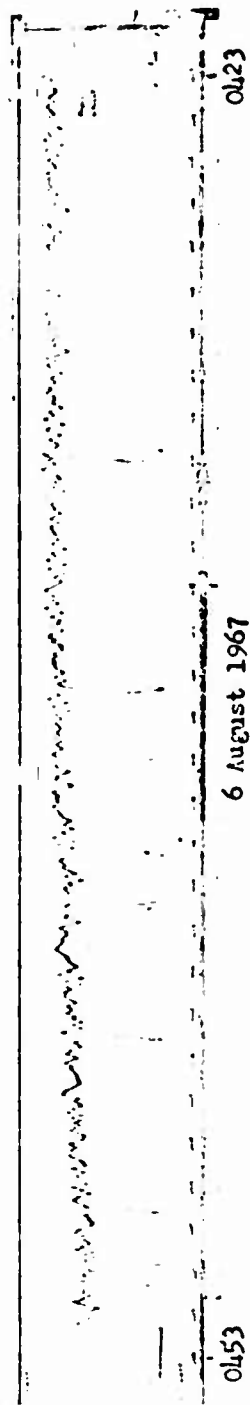
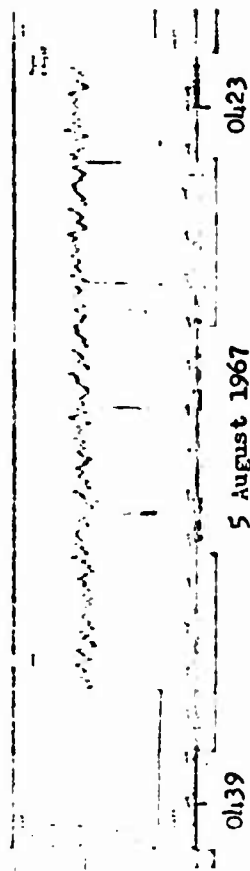


Figure 7: PAGEOS Lightcurves: 5 August 1967 - 25 August 1967

Occasional brightness drops between satellite and dark indicate sky brightness as accepted by the field aperture. Deeper drops indicate the dark current level of the photomultiplier. In the earlier records these are effected at 30-second intervals by a timer.

Brightness Calibration

A star calibration technique is used to measure photometer response and atmospheric transmission. Selected stars are observed photometrically, and the corresponding output voltage (deflections) recorded. Figure 8 is a plot showing the results of star calibration conducted on 27 June 1966. The groups of stars defining the zenith curve were observed near the zenith, and their published visual magnitude is plotted versus photometer output voltage, with corresponding corrections applied to the measured output voltages to account for these small zenith distances. This curve thus represents output voltage as inferred through one air-mass, as a function of extra-atmospheric visual stellar magnitude. Values for the visual stellar magnitudes have been taken from recently published catalogs^{4,5} prepared from modern conventional photoelectric photometry. G-type stars (matching the sun's energy distribution) were used, although for the bright region only the blue star Vega was accessible at this sidereal time. In this case, a color correction was applied to obtain a simulation of a G star of zero magnitude. From this approach, absolute brightness is measurable to .05 to .5 magnitudes depending upon observed brightness and sky quality. The observed brightness range for all the recorded PAGEOS transits lies along the linear portion of the response curve, so short term fluctuations were subject to minimum measurement error. On Revs. 27 and 3566 conditions were excellent and the absolute errors believed less than 0.1 magnitude.

Analysis of the Brightness Data

Physical interpretation of brightness data requires separation of the received brightness into specular and diffuse components. While pre-launch laboratory measurements by NASA⁶ established the initial values of the scattering components quite precisely (See Table II),

Table II. Initial Reflectivity of PAGEOS

R _{specular}	0.862 ± 0.0046
R _{diffuse}	0.029 ± 0.0046
R _{total}	0.891 ± 0.0032

These values are weighted to represent the solar spectrum within the range 3,600 Å to 7,000 Å. (Reference 6)

there is sufficient uncertainty concerning effects of the orbital environment to warrant verification, especially after the satellite has been in orbit for some time. This is possible for an approximately spherical

satellite by comparison of selected average brightness values over a wide range of phase angle (the angle at the satellite formed by sun and observer vectors). Given a suitable change in illumination geometry, a diffuse contribution exceeding 5% should be detectable from the recorded brightness data. Because of the short-term brightness fluctuations, primarily random in nature, characteristic of most of the data, it is difficult to determine localized average brightness values. However, experimental conditions for the transits yielding the 27 June 1966 and 30 July 1967 records cover a large range of phase angle and occurred on nights of good photometric quality. Reduction of these data shows that the diffuse contribution was less than 5 percent on Rev. 27 and has remained at least that low during the first 13 months in orbit. It seems reasonable to infer that since specularity has remained high, there has been little microscopic surface degradation, i.e., a dulling of the shiny surface would have increased the diffuse component. This bound on the constancy in reflectance properties is in accord with the conclusions reached by Emmons, et.al.,⁹ based on strongly averaged data after 2 months in orbit and inferred by defining a specularity index as the ratio of specular to specular plus diffuse scattering.

Table III presents positional parameters, absolute brightness, and inferred radii of curvature as functions of time, for selected transits. The positional parameters were computed from Smithsonian orbital data and the mean anomaly adjusted by local position checks generally by photoelectrically observed near occultations. Observed brightness was converted to absolute brightness from the usual relation¹⁰

$M = m - 25 \log\left(\frac{R}{1000}\right)^2$ where M is the absolute magnitude for 1000

kilometers slant range, and m the observed magnitude (corrected for extinction). Radii of curvature were calculated by simultaneous application of the specular reflection and diffuse scattering expressions:¹¹

$$E_{sp} = \frac{E_s r_{sp} b^2}{4R^2} \quad (3)$$

$$E_d = \frac{2E_s r_d b^2}{3\pi R^2} [\sin \phi + (\pi - \phi) \cos \phi] \quad (4)$$

where E_s is the incident solar flux¹² 13.21×10^4 (lumens/m²), b the radius of the satellite (meters), R the distance from observer to satellite (meters), ϕ the phase angle (formed at the satellite by observer and the sun vectors), E_{sp} the specular contribution, E_d the diffuse contribution of satellite brightness (lumens/m²), and r_{sp} and r_d the specular and diffuse reflectivity, respectively. Using the laboratory data of Table II for the specular and diffuse reflectivity: i.e., assuming only slight departures from the predeployment values:

Table III. Reduction of PAGEOS Photometric Data to Absolute Magnitude and Radius of Curvature, Revs 3, 11, 27, 217, and 3566.

Rev 3									
24 June 66									
Point	UT	Alt	Az	Slant Range (Km)	Phase Angle ϕ	Visual Mag. at 1000 Km (No Extinction)		Apparent Sphere Radius (Meters)	
						Max	Min	Max	Min
* 1	0757:35	36°	084°	5520	106°	-1.94	-1.33	23.4	17.7
* 2	0759:42	37°	075°	5470	111°	-1.69	-1.31	20.9	17.4
* 3	0801:55	37°	065°	5470	116°	-1.79	-1.44	21.8	18.6
* 4	0803:50	37°	055°	5500	120°	-1.68	-1.45	20.8	18.7
* 5	0805:38	35°	048°	5600	124°	-1.57	-1.32	19.7	17.5
* 6	0807:35	33°	040°	5740	127°	-1.54	-1.29	19.5	17.3
Rev 11									
25 June 66									
* 1	0808:32	41°	091°	5300	103°	-0.90	-0.57	14.5	12.4
* 2	0811:57	43°	073°	5180	111°	-1.32	-1.10	17.6	15.9
* 3	0815:44	42°	054°	5260	118°	-1.18	-1.00	16.5	15.1
* 4	0816:33	41°	050°	5300	120°	-1.40	-1.12	18.3	16.0
Rev 27									
27 June 66									
1	0820:18	23°	139°	6350	74°	-1.38	-	17.8	-
2	0821:04	25°	138°	6220	75°	-0.80	-	13.6	-
3	0824:00	32°	132°	5740	79°	-0.93	-	14.5	-
4	0828:15	43°	119°	5180	88°	-0.98	-	14.9	-
* 5	0833:10	53°	092°	4810	99°	-1.36	-0.96	17.8	14.8
* 6	0835:40	54°	073°	4780	105°	-1.45	-0.99	18.6	15.0
* 7	0838:04	52°	055°	4840	111°	-1.19	-0.82	16.5	13.9
* 8	0840:04	49°	044°	4970	116°	-1.22	-0.84	16.8	14.1
9	0841:00	47°	040°	5040	119°	-0.95	-	14.8	-
* 10	0841:51	45°	035°	5110	121°	-1.28	-1.06	17.3	15.6

* Indicates brightness enhancement point

Table III (continued)

21 July 66

Rev 217

Point	UT	Alt	Az	Slant Range (Km)	Phase Angle φ	Apparent Vis. Mag. (No extinction)	Visual Mag. at 1000 Km (No extinction)	Apparent Sphere Radius (Meters)
1	0711:43	50°	128°	5020	61°	1.03	-2.47	29.2
2	0711:51					2.92	-0.58	12.2
3	0717:00	66°	085°	4590	78°	1.11	-2.20	26.1
4	0717:14					3.12	-0.19	10.3
5	0723:48	49°	025°	5030	106°	3.20	-0.31	11.0
6	0724:07					1.26	-2.25	26.9

15 Sep 67

Rev 3566

1	0233:46	33°	217°	6910	75°	3.43	- .85	13.9
2	:56	34°	217°	6890	75°	4.78	+ .51	7.5
3	0234:10	35°	218°	6860	75°	3.40	- .85	13.9
4	0235:27	38°	220°	6750	75°	3.43	- .77	13.4
5	:42	38°	220°	6730	75°	5.42	+ 1.22	5.4
6	0236:01	39°	221°	6690	75°	3.12	-1.07	15.4
7	0237:15	42°	223°	6625	75°	3.20	- .97	14.7
8	:27	42°	224°	6615	75°	4.58	+ .42	7.8
9	:42	43°	224°	6600	75°	3.28	- .87	14.1
10	0238:56	45°	227°	6540	76°	3.32	- .82	13.7
11	0239:12	45°	228°	6525	76°	5.24	+ 1.11	5.6
12	:32	46°	228°	6510	76°	2.96	-1.17	16.1
13	0240:45	48°	232°	6455	77°	3.08	-1.04	15.2
14	:58	49°	232°	6450	77°	4.45	+ .33	8.1
15	0241:14	49°	233°	6440	77°	3.19	- .93	14.4
16	0242:27	51°	238°	6395	77°	3.20	- .90	14.2
17	:43	52°	238°	6390	78°	5.15	+ 1.05	5.8
18	0243:05	52°	240°	6380	78°	2.70	-1.40	17.9

Table III (continued)

15 Sep 67

Point	UT	Alt	Az	Slant Range (Km)	Phase Angle ϕ	Apparent Vis. Mag. (No extinction)	Visual Mag. at 1000 Km (No extinction)	Apparent Sphere Radius (Meters)
19	0244:16	54°	245°	6350	78°	2.89	-1.20	16.3
20	:29	55°	246°	6345	79°	4.36	+ .27	8.3
21	:45	55°	248°	6340	79°	3.05	-1.03	15.1
22	0245:58	57°	254°	6320	80°	3.14	- .94	14.5
23	0246:14	57°	255°	6315	80°	4.85	+ .77	6.6
24	:33	57°	256°	6310	80°	2.70	-1.37	17.7
25	0247:47	59°	263°	6300	81°	2.77	-1.30	17.1
26	:59	59°	264°	6295	81°	4.16	+ .10	9.0
27	0248:15	59°	266°	6295	81°	3.05	-1.01	15.0
28	0249:29	59°	267°	6290	81°	3.16	- .90	14.2
29	:44	60°	268°	6290	82°	4.52	+ .46	7.7
30	:59	60°	275°	6290	83°	2.90	-1.16	16.0
31*	0250:30	61°	280°	6305	84°	2.68	-1.37	17.6
32*	0253:00	61°	290°	6350	86°	3.20	- .89	14.2
33*	0256:28	57°	308°	6495	90°	3.16	- .99	14.8

216
(Max)

*These points are estimated smoothed values.

$$r_{sp} = .862$$

$$r_d = .029 \text{ and recalling}$$

that absolute stellar magnitudes are extra atmospheric values at 1000 km distance,

$$E = \frac{E_s b^2}{10^{12}} [0.216 + 0.0062 (\sin \phi + [\pi - \phi] \cos \phi)] \quad (5)$$

where E is the total brightness contribution.

$$b = \sqrt{\frac{\text{or} \quad 7.56 \times 10^6 E}{0.216 + 0.0062 [\sin \phi + (\pi - \phi) \cos \phi]}} \quad (6)$$

The conversion of absolute stellar magnitude to lumens/ m^2 is accomplished by the expression:

$$E = \frac{2.65 \times 10^{-6}}{2.512^M} \quad (7)$$

Thus from the measured value E and the computed value ϕ the radius of curvature could be calculated, assuming constant reflectivity. The absolute values of the calculated radii of curvature are, of course, only as good as the brightness measurements and the degree to which the assumed reflectivity coefficients represent the optical properties of the satellite surface. Figure 9 gives a graphical solution of Eqns. (6) and (7) in the range of brightness of importance in this paper, where ϕ was essentially constant. From Figure 9, it may be noted that an absolute brightness uncertainty of 0.05 magnitudes produces a radius of curvature uncertainty of 0.3 meters in the neighborhood of the nominal 15 meter radius. In this same region, a brightness uncertainty as large as 0.5 magnitudes would produce an apparent radius of curvature uncertainty of 3.7 meters. However, as noted above, short term relative brightness fluctuations are independent of absolute values, and thus their measurement carries the minimum error. The absolute brightness values in Table III for 24 and 25 June 1966 are probably subject to errors up to ± 0.5 magnitudes as the result of poor sky conditions; for the other three dates, tabulated absolute magnitudes are almost certainly good to ± 0.1 magnitudes or better.

Rotational History of PAGEOS

Rotation of the satellite about its center of mass is detectable from some of the brightness data. Figure 10 is a plot of apparent spin rates, and

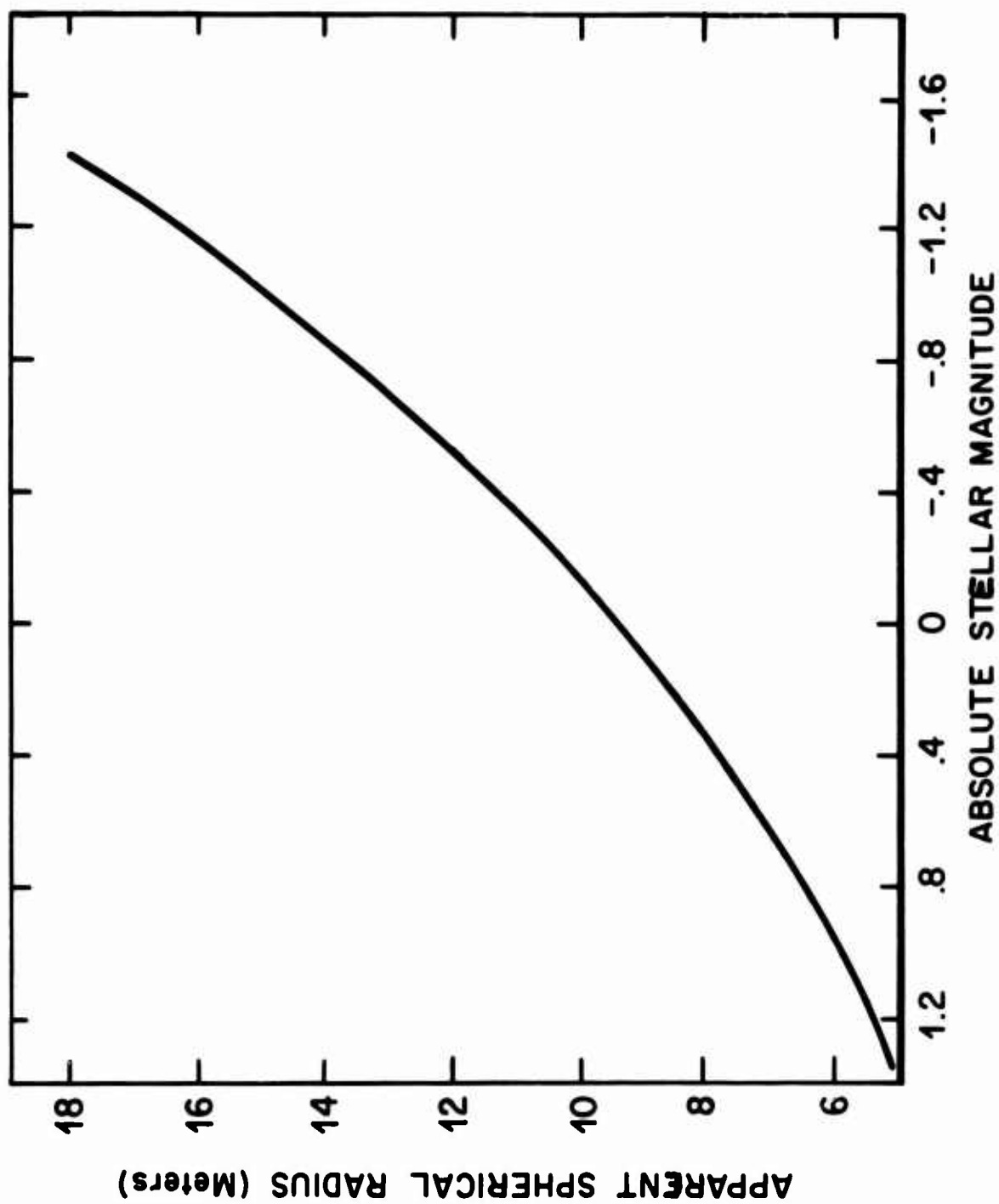


Figure 8: Apparent Spherical Radius from Stellar Magnitude Transit of
15 September 1967

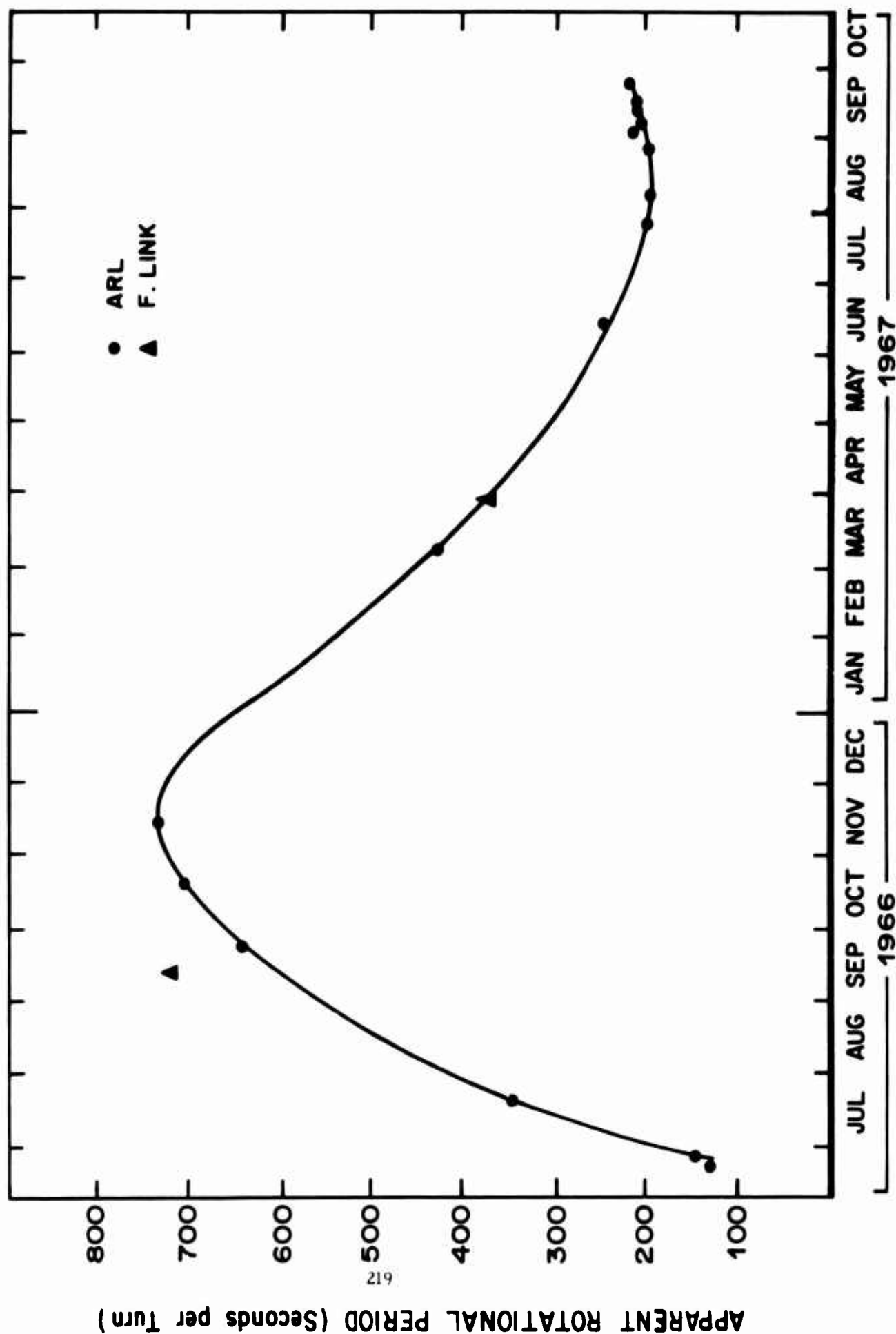


Figure 9 - The apparent spin of PAGEOS

indicates that PAGEOS has spun up from a low rate of about 0.083 revolutions per minute in the fall of 1966 to a high of about 0.325 rpm in the summer of 1967. The first three points, showing an apparent fast spin at launch are based on brightness fluctuations whose periodicity may be multiples of the true period although these points join the others smoothly. Periodic patterns on later records were sufficiently detailed to allow determination of spin rates with a high degree of confidence. Two additional points were obtained from independent optical measurements,⁸ and as the plot shows, one is in close agreement with the ARL data while the other is slightly off the apparent curve. Since the discrepancy occurs at a time when the period was longest, it is most likely due to differences in observing geometry, i.e., use of apparent period to infer sidereal period plus contributing shifts of reference points for the apparent rotation. In any case, it is evident that the rotational period did decrease from a maximum of about 730 seconds per turn to a minimum of about 195 seconds per turn in 245 days. This represents a change in kinetic energy:

$$\Delta K = \frac{I \omega_2^2}{2} - \frac{I \omega_1^2}{2} \quad (1)$$

where I is the moment of inertia, ω_1 the minimum angular velocity and ω_2 the maximum angular velocity. For PAGEOS $I = \frac{2}{3} (\text{mass})^* (\text{radius})^2 = 8375 \text{ Kg-m}^2$; $\omega_1 = 8.6 \times 10^{-3} \text{ radians/second}$ $\omega_2 = 3.22 \times 10^{-2} \text{ radians/second}$. Thus $\Delta K = 4.04 \text{ joules}$. The average torque required to produce this energy change is

$$\begin{aligned} \tau &= I \alpha \\ \text{where } \alpha &= \frac{\omega_2 - \omega_1}{245 \text{ days}} = \frac{2.36 \times 10^{-2} \text{ radians/sec}}{2.12 \times 10^7 \text{ seconds}} \quad (2) \\ &= 9.30 \times 10^{-6} \text{ newton-meters} \end{aligned}$$

These indicated small values for energy change and torque suggest that rotation of PAGEOS about its center of mass and the observed rate changes could have been caused by solar radiation pressure, the earth's magnetic field, or both. The analysis of Echo II rotation in Reference 9 anticipates a radiation pressure torque of 8×10^{-5} newton meters due to thermal shape distortions.

* In the above calculation a mass value⁶ of 54.08 kg was used.

Determination of the PAGEOS Figure

The light curve of 15 September 1967, showing the largest and most periodic brightness fluctuations yet recorded, was selected for detailed reduction. Figure 11-A shows the entire light curve at approximately the same scale as in Figures 2 through 7. The obvious periodicity, shown in the expanded section (Figure 11-B), results almost certainly from the large specular brightness component. The specular highlight which contributes to the specular component is only an area subtending a 0.25-degree arc at the center of the sphere, i.e., an area some 7 cm in diameter. This implies that the brightness values represented by the section AA (one rotation) were produced by the virtual image of the sun as it mapped out a thin band nearly circumscribing the satellite, i.e. a trace some 4-8 cm wide and 96 meters in path length which nearly joins back on itself as the satellite rotates under the solar image. Figure 11-C is a polar plot of corresponding radii of curvature, assuming constant, pre-launch reflectivity values. A first-order smooth joining of these curvatures produces the apparent cross section of Figure 11-D. At this scale, the small curvature fluctuations between the deep minima are not discernible, although the measured data definitely show a preponderance of small surface anomalies on one side as compared with the other. The prolate spheroidal shape that this cross section implies, holds only if the observe band is close to being the maximum circumference of the actual figure. Cross sections of less peripheral measurement (whose planes do not pass through the figure center) imply greater localized curvature distortions to be consistent with observed radii of curvature.

There are, of course, other possible interpretations of the brightness fluctuations recorded on September 15th. However, those that come to mind seem less probable than the prolate spheroid model. If the satellite is spherical, the deep brightness minima might be accounted for by loss of specularly-reflective surface area from regions on the sphere subtending nearly 60 degrees at the center of the sphere and opposite each other, or by loss of reflectivity due to skin wrinkling. It seems unlikely that the first of these mechanisms for reduction of specular scattering would obtain locally rather than generally over the entire sphere since it involves removal or degradation of the aluminized layer on a sub-macroscopic scale. The second of these is certainly admissible if one postulates two opposed spherical caps with progressively wrinkled zones as the virtual solar image approaches the poles of the caps. It is felt beyond the scope of this paper to analyze the nature of the wrinkling to yield a smoothly increasing change from a scattering distribution of a purely specular form to one which is quasi-diffuse in form. The difficult concept is the statistical distribution of the macroscopic specular elements which must redirect the light in a diffuse distribution such that another zone of wrinkles does not reinforce the central virtual image. The end caps also must subtend an included angle of some 60 degrees, i.e. they are 16 meters in diameter much larger than the one-meter

diameter polar caps of the PAGEOS construction which are the areas of unique character on the vehicle where stresses might develop at opposite points on the nominal sphere.

This wrinkle mechanism is much more complex and constrictive in its character than the assumption that the vehicle has distorted to a spheroid, but it cannot be ruled out. On the other hand the spheroid could result from stresses produced by satellite spin. Of non-spherical shape possibilities, the prolate spheroid is the most nearly spherical consistent with measured brightness fluctuations. Whatever shape and/or surface condition is responsible for producing the deep brightness minima, it persisted for at least the twenty days between the 25 August and 15 September (1967) records, but may have existed considerably longer.

Conclusions

From the generally constant brightness on the early orbits and the good agreement of the measured brightness to that expected for a 100-foot sphere, successful deployment of PAGEOS and its full inflation were achieved. The brightness irregularities evident only six hours after deployment indicate definite departure of the deployed vehicle from a smooth sphere. It should be noted that the slow 0.25 magnitude fluctuations observed on Rev. 3 are consistent with the conclusions of the Smithsonian Astrophysical Observatory¹⁴ that the vehicle inflation was perfect, based on apparent constancy of the trailed image at 01^h28^m26^s, (20 seconds after complete inflation). The photographic record is simply not capable of showing such small modulations in brightness of a trailed image. The data presented here suggest initial rotation of PAGEOS about its center of mass, and show what appears to be a rate of change pattern. The gradual evolution in late June and early July 1966 of the relatively small initial brightness discontinuities into the major ones of mid-July indicates that these deformations of the balloon material were due to evolution of stresses in the skin rather than due to the sublimed inflation material as suggested by others.⁷ However, the discontinuities of form were most drastic some two to ten days after the satellite grazed the earth's shadow for the first time and thus skin temperatures would have dropped to as low as -100°C and allowed either the benzoic acid or anthraquinone inflation gases, if any remained, to solidify and accrete on the skin. Reference 6 contains an estimate that the inflation gases should essentially be lost by revolution 80 (4 July 1966), based on a projected thermal history. However, such thermal shocking of the plastic as would have occurred in this temperature cycling would also have intensified mechanical stress redistribution. This point probably deserves more study.

From the relatively large amplitude of the atmospheric scintillation, as well as from the lack of a phase angle effect, one can conclude that the vehicle appears as a bright stellar point and hence is a highly specular convex form, like Echo I, and unlike Echo II or the 4-meter Explorer balloon satellites or even the 9-meter USAF evaporative grid-sphere

(1966-63A), all of which exhibit diffuse scattering characteristics and show lower levels of scintillation as would be expected of objects subtending angular extents of 0.5 to 5 arc seconds.

The one practical complication which the brightness variations of the PAGEOS vehicle might produce is a difficulty in continuous detection of the vehicle near its maximum slant range for ballistic cameras of limited aperture, such as the BC-4 and MOTS cameras. This is almost certain to be true since the minimum brightness events will correspond to approximately stellar magnitude + 4.8 at the slant ranges of 10,000 km which are expected later in its life (Ref. 6). Alternately, the occurrence of bright maxima might produce camera images which are larger than the 40-60 microns desired for best determination of the image location. The computation of nominal exposure time and camera aperture to be used at a given site on each transit will prove to be less satisfactory than would have been possible without the brightness variations.

It would appear that for the purpose of remote satellites intended to have a brightness which is both large and nearly invariant (except for predictable phase angle variations) a diffusely-scattering inflatable sphere would be the best design. This type of vehicle would also suffer the least from atmospheric scintillation. The image displacement from the center of mass due to the phase effect might prove less troublesome than the brightness variations of random rather than predictable character. The maximum image displacement of PAGEOS is only some 1.0 arc seconds at a 2400 km slant range and the image size only some 2 arc seconds, comparable if not smaller than the seeing disc for all but the best of observing sites. However, if a collapsible satellite is required with a specular surface to produce a nearly-constant point-like source, the use of some of the new polyurethane "memory-stressed" foams might be used to establish sphericity to a predictable tolerance.

It has been shown that continuous monitoring by broad-band photo-electric photometry with due care to obtain continuity of record and accuracy of calibration, is a particularly useful data source in providing information concerning PAGEOS' size, form, surface characteristics, and rotation about its center of mass. Other workers have shown that additional information concerning surface characteristics is available by use of narrow-band and polarimetric sensing,^{7,13} but unless these ancillary data are sensed simultaneously (through the use of beam splitters or additional telescopes), continuity of the often complicated brightness fluctuation patterns is lost by the interruptions in the record. This is even more important if the vehicle is rapidly rotating and/or non-spherically symmetrical as in the case of most payloads and all upper stage rockets.

REFERENCES

1. F. Link "Sur la Rotation des Satellites Echo I and II," Bulletin of the Astronomical Institutes of Czechoslovakia, Vol. 17 (1966), No. 1, pp. 16-21.
2. K. E. Kissell and R. C. Vanderburgh "Photoelectric Photometry — A Potential Source for Satellite Signatures", Proceedings of the First GISAT Symposium held at the Mitre Corporation, December 1965, pp. 341-364. ARL Technical Report 66-0162.
3. K. E. Kissell and E. T. Tyson, "Rapid-Response Photometry of Satellites," A. J., 69, 8, 547 (A).
4. O. J. Eggen, "Colors, Luminosities, and Motions of the Nearer G-Type Stars" Astron. J. 69, 8, pp. 570-609 (1964).
5. B. Iriarte, H. L. Johnson, R. I. Mitchell, and W. K. Wisniewski, "Five-Color Photometry of Bright Stars" Sky and Telescope, XXX, No. 1, pp. 21-31.
6. David E. Bowker, "PAGEOS Project, Compilation of Information for Use of Experimenter," NASA TM X-1344, March 1967.
7. R. H. Emmons, C. L. Rogers, Jr., R. J. Preski, Photometric Observations of Artificial Satellites for Determining Optical and Physical Characteristics, I. Astron. J. 72, No. 8, pp. 939-944 (1967).
8. F. Link, Private communication concerning Czechoslovakian photometry of PAGEOS.
9. J. Mar and F. R. Vigneron, "Passive Spin Propulsion of Large Flexible Spherically-Shaped Satellites by the Solar Radiation Field COSPAR-IAU-IUTAM Symposium Trajectories of Artificial Celestial Bodies" Paris, 20-23 April, 1965, Proceedings-Jean Kovalevsky, Editor, Springer-Verlag, Berlin (1966).
10. S. Macko, Satellite Tracking, John F. Rider, New York (1962) p. 125.
11. J. B. Zirker, F. L. Whipple and R. J. Davis, "Time Available for the Optical Observation of an Earth Satellite," Scientific Uses of Earth Satellites, Univ. of Mich. Press, Ann Arbor, (1956), pp. 23-28.
12. H. L. Johnson, "Lunar and Planetary Observatory Contributions" Vol. 3, pp. 52-57, 15 May 1965.
13. R. H. Emmons and R. J. Preski, "Five Color Photometric Measurements of Near-Earth Satellites" Goodyear Aerospace Corporation Report SP-5656, 30 June 1967.

14. W. Kirchhoff and J. Latimer, "South Africa Baker-Nunn
Photography of the PAGEOS-A Inflation and Apogee Burn of the
AGENA D" Smithsonian Astrophysical Observatory Special Report
No. 243, 30 June 1967.

ACKNOWLEDGEMENTS

The author would like to express his thanks to personnel at the NASA Geodetic Operation Control Center, Goddard Space Flight Center for their timely assistance in providing launch and early orbital parameters, making it possible to find and photometer PAGEOS at the ARL OPOS Observatory at the first possible opportunity.

Appreciation goes to K. E. Kissell for encouraging the attempts at interpretation of many of the observed brightness fluctuations and for discussions of alternate methods.

Thanks go to Dr. F. Link for having kindly made available the results of his photoelectric photometry of PAGEOS and the ECHO balloons as a useful independent comparison source.

Unclassified

Security Classification

DOCUMENT CONTROL DATA - R & D		
(Security classification of title, body of abstract and indexing annotation must be entered when the overall report is classified)		
1. ORIGINATING ACTIVITY (Corporate author)		2a. REPORT SECURITY CLASSIFICATION
University of Miami Miami, Florida		UNCLASSIFIED
		2b. GROUP
		ARP-4
3. REPORT TITLE		
Proceedings of University of Miami Symposium on Optical Properties of Orbiting Satellites		
4. DESCRIPTIVE NOTES (Type of report and inclusive dates)		
Scientific. Final.		
5. AUTHOR(S) (First name, middle initial, last name)		
Kenneth E. Kissell, and Douglas Duke		
6. REPORT DATE	7a. TOTAL NO. OF PAGES	7b. NO. OF REFS
May 1969	231	0
8a. CONTRACT OR GRANT NO	9a. ORIGINATOR'S REPORT NUMBER(S)	
F33615 67C 1870		
b. PROJECT NO	9b. OTHER REPORT NO(S) (Any other numbers that may be assigned this report)	
7114-00-11		
c. DOD Element 61102F		
d. DOD Subelement 681301	ARL 69-0078	
10. DISTRIBUTION STATEMENT		
This document has been approved for public release and sale; its distribution is unlimited.		
11. SUPPLEMENTARY NOTES		12. SPONSORING MILITARY ACTIVITY
TECH OTHER		Aerospace Research Laboratories(ARP) Wright-Patterson AFB, Ohio 45433
13. ABSTRACT		
This final technical report was prepared under Contract F33615 67C 1870, University of Miami, Florida. The symposium covered herein was accomplished on Project 7114 under the technical cognizance of Dr. Kenneth E. Kissell, Director of the General Physics Research Laboratory, Aerospace Research Laboratories.		

DD FORM 1 NOV 65 1473

Security Classification

14	KEY WORDS	LINK A		LINK B		LINK C	
		ROLE	WT	ROLE	WT	ROLE	WT